

https://dspace.org/

3D geophysical modelling used for structural interpretation in southern Mali and northeastern Guinea, West Africa

Yossi, Mamadou

2017

http://hdl.handle.net/10539/23530

Yossi, Mamadou (2017) 3D geophysical modelling used for structural interpretation in southern Mali and northeastern Guinea, West Africa, University of the Witwatersrand, Johannesburg, <http://hdl.handle.net/10539/23530>

Downloaded from a DSpace repository. https://dspace.org/

3D geophysical modelling used for structural interpretation in southern Mali and northeastern Guinea, West Africa

Mamadou YOSSI

Person number: 565434

A dissertation submitted to the Faculty of Science, University of the Witwatersrand, Johannesburg, in fulfilment of the requirements of the Master degree in Science

2015



DECLARATION

I declare that this dissertation is my own work. It is being submitted for the Master of Science Degree in Science in the University of the Witwatersrand, Johannesburg. It has not been submitted before for any degree or examination in any other University.



Mamadou YOSSI

25 of August 2015

ACKNOWLEDGMENTS

I would like to extend my gratitude to the following people who have motivated, guided and helped me when I was completing this work:

Special thanks to Mr Jean David of SAGAX AFRIQUE Ltd for supplying the dataset and co-supervision of this work, and sponsorship of the project.

My supervisor, Prof. Kim A.A. Hein of the University of the Witwatersrand Johannesburg is thanked for her thorough and constructive comments. I am grateful for the assistance of Dr Musa Manzi for accommodation, input into my work, and patient discussions of the research results.

Also many thanks to Dr Chris Wijns who guided my steps to WITS University.

Many thanks to John Paine for use of the full package of the SCICOMAP software for free.

I will lastly thank my wife and daughter (Yossi Laya DOLO, Salimata YOSSI and Idrissa YOSSI) for their patience and encouragement during all this time.

TABLE OF CONTENTS

Declaration *2*
Acknowledgements *3*
Table of contents *4*
List of Figures *6*
List of Tables *15*
Abstract *16*

CHAPTER 1: Introduction **17**
1.1 Preamble 17
1.2 Location and physiography 18
1.3 Objective 19
1.4 Hypothesis 20
1.5 Thesis organisation 21
1.6 List of Abbreviations 21

CHAPTER 2: Regional setting **26**
2.1 West Africa Craton 26
2.2 Regional geology setting 26
2.2.1 Archaean Kénema-Man domain 26
2.2.2 Palaeoproterozoic Baoulé-Mossi domain 26
2.3 Architecture and geological setting of southern Mali and northeast Guinea 28
2.4 Geophysical interpretation in regional scale and direct modelling 29

CHAPTER 3: Methodology on geophysical inversion and image processing techniques **35**
3.1 Introduction 35
3.2 Data constraints 36
3.3 Geophysical data processing and attribute extraction 37
3.4 Fact geology attribute extraction 38
3.5 Geophysical modelling 39
3.6 Geophysical inversion 42
3.7 Data and image processing techniques 43
3.7.1 Vertical continuation *44*
3.7.2 Vertical derivative *45*
3.7.3 Analytic signal amplitude *45*
3.7.4 The vertical integral applied on the analytic signal *46*
3.7.5 Tilt Angle filter *47*
3.7.6 Automatic gain control *47*

CHAPTER 4: Geophysical attributes and geological fact data extraction **58**
4.1 Attribute extraction from geophysical maps 58
4.1.1 Upward continuation *59*
4.1.2 Magnetic First Vertical Derivative *60*
4.1.3 Bouguer anomaly First Vertical Derivative 62
4.1.4 Analytic signal 62
4.1.5 Application of vertical integral to the analytic signal *63*
4.1.6 Tilt angle *64*
4.1.7 Automatic Gain Control (AGC) *64*
4.1.8. The attribute map from geophysical data *64*
4.1.9 Potassium map *65*
4.1.10 Thorium map *65*
4.1.11 Uranium map *65*

4.2. Confidence level zone of the study area 66
4.3. Geological fact data extraction 66
4.4. Geophysical and structural architecture 66
4.4.1 Geophysical map of the study area *66*
4.4.2 Structural map of the study area *67*

CHAPTER 5: Geophysical modelling **87**
5.1 Introduction 87
5.2 Forward modelling 87
5.2.1 Profile AA' *88*
5.2.2 Profile BB' *89*
5.2.3 Profile CC' *89*
5.2.4 Synthesis of forward modelling *90*
5.3 Inversion modelling 91
5.3.1 Inversion zone 1 *92*
5.3.2 Inversion zone 2 *92*
5.3.3 Inversion zone 3 *93*
5.3.4 Inversion zone 4 *93*
5.3.5 Inversion zone 5 94
5.3.6 Inversion zone 6 *95*
5.3.7 Geological synthesis of inverse modelling *96*

CHAPTER 6: Key area **115**
6.1. Introduction 115
6.2. Geophysical processing 115
6.3. Key study area 1- southern part of Yanfolila shear zone 116
6.4. Key study area 2- southern part of Banifing shear zone 117
6.5. Key study area 3- southern part of Yanfolila belt 119
6.6. Synthesis 120

CHAPTER 7: Discussion **130**
7.1. Geophysical context 130
7.2. Geological context and implications 131
7.3. Understanding the geology using inversion modelling 132
7.4. New interpretation of the study area 133

CHAPTER 8: Conclusions 138

REFERENCES **140**

APPENDICES **148**

Appendix A: Gravity method theory 148
Appendix B: Magnetic method theory 150
Appendix C: Gravity data station points 155
Appendix D: UBC-GIF inversion algorithm 157
Appendix E: Comparison between unconstraint inversion and constraint inversion with the bound model in the study area 161

LIST OF FIGURES

(N.B., Chapter figures are presented at the end of each chapter for convenience)

Figure 1.1: The location of the study area in the West Africa Craton. The Bouguer anomaly data from the Office de la Recherché Scientifique et Technique Outre-Mer (1952, 1987) for the study area. 1: Morocco, 2: Mauritania, 3: Algeria, 4: Senegal, 5: Mali, 6: Burkina Faso, 7: Niger, 8: Guinea, 9: Sierra Leone, 10: Liberia, 11: Ivory Coast, 12: Ghana, 13: Togo, 14: Benin, 15: Nigeria. KKI: Kedougou-Kenieba Inlier; the magenta coloured box indicates the study area in WAC (Modified after Tshibubudze, 2015).

Figure 1.2: The Palaeoproterozoic Baoulé-Mossi domain of West African Craton. The study area is defined in pink. Partial country borders are indicated by the green line. Southern Mali and northeast of Guinea cover a geographical extent of 440km x 260km (modified after Hirdes and Davis, 2002).

Figure 1.3: The study area divided into map sheets. The study area is outlined in pink, the 1:200 000 map sheets in green, and the main river systems in blue. The map shows the Yanfolila, Bamako east and west, Bougouni, Tienko Tingrela, Massigui and Nielle sheets in Mali, and Kankan, Siguiri, Sirakoro, Falama and Faraba sheets in Guinea overlying the West Africa map with main provinces close to the study area (modified from the Institut Géographique National, France, 1993).

Figure 2.1: The stratigraphy of the Palaeoproterozoic of Baoulé-Mossi domain in the eastern part of the study area, modified from Baratoux et al. (2011).

Figure 2.2: The study area is divided into basins and volcano-sedimentary belts in overlay of the geological map modified from SIGAfrique (2000) and Miller et al. (2013). ME: magmatic event; VS: Volcano sediment; and: andesite; bas: basalt; pyr: pyroxene; and: andesite; ub: ultra-basic; ryo: rhyolite; kom:

Figure 2.3: The Siguiri basin bordered by Yanfolila belt, and including the Bougouni-Kekorobasin, Banifing shear zone, Massigui belt, Bagoe basin, Kolondieba shear zone, Syama belat and Syama-(Bananaso)shear zone (modified after Girard et al., 1998 and Miller et al., 2013).

Figure 2.4: The different domains and basins in the eastern part of the study area. The image show the Banifing shear zone which separates the Bougouni and Bagoe basins. It shows also the Syama-(Bananaso) fshear zone separating the Kadiana-Mandinani domain and Kadiolo domain. The Bagoe and Kadiana-Manakoro belts are also highlighted (modified after Girard et al., 1998; Bentley et al., 2000; Miller et al., 2013).

Figure 3.1: The methodology workflow diagram outlining the fundamental steps taken in the development of the 3D geophysical modelling in this study.

Figure 3.2: The georeferenced coordinates of petrophysical data; red for magnetic susceptibility and blue for density. The green line marks the international borders between Mali, Guinea to the west, and the Ivory Coast to the south.

Figure 3.3: The framework schema outlining the interaction between forward and inverse modelling.

Figure 3.4: The total magnetic field map (left) compared to the upward continuation at 500m (right). Certain wavelengths of the total magnetic field are eliminated as shown with the upward continuation.

Figure 3.5: The Bouguer anomaly map (left) compared with the upward continuation at 1000m (right).

Figure 3.6: The total magnetic field (left) compared to the first derivative map (right). The Yanfolila-Kalana shear zone is clearly evident in the first derivative map but invisible in the total magnetic field map.

Figure 3.7: The first derivative map (left) compared with the second derivative map (right). The black circles highlight that the more the derivative is applied, the more noise increases.

Figure 3.8: Analytic signal map to the right, and the total magnetic field to the left. The Yanfolila belt, folds and dykes present well in the analytic signal relative to the total magnetic field.

Figure 3.9: The vertical integral of the analytic signal map of the Banifing shear zone to the left compared to the total magnetic field to the right. The arrows mark points of comparison.

Figure 3.10: A map of the vertical integral applied of the analytic signal to the left for the Yanfolia region, compared to the analytic signal to the right. The Yanfolila belt and Yanfolila shear zone are compared in the two images.

Figure 3.11: The tilt angle of the total magnetic field of the Banifing shear zone to the left compared to the first derivative of the total magnetic field image to the right. The arcuate Fatou Shear Zone in the southeast is easy to resolve on the tilt angle image than with first derivative image.

Figure 3.12: The tilt angle of the total magnetic field of the Banifing shear zone to the left compared to total magnetic field image to the right. The portion of Banifing Shear Zone is well defined in the tilt angle map. Also the crosscutting relationship between east-west trending dykes and the Banifing Shear Zone become easy to resolve with tilt angle filter.

Figure 3.13: The first derivative of Bouguer anomaly image to the left compared to the tilt angle of the Bouguer anomaly to the right. The black arrows of the figures show the different comparison point and the usefulness of the tilt angle against first derivative with gravity data.

Figure 3.14: The Automatic Gain Control map of the total magnetic field for the Yanfolila-Kalana region to the left, compared to the analytic signal of total magnetic field to the right. The horizontal arrow shows the continuity of a lineament at the bottom of Yanfolila belt which is not clear with analytical signal. The vertical arrow highlights the intersection between Yanfolila Kalana Shear Zone and an east-west trending dykes. This intersection was enhanced by using the AGC.

Figure 4.1: Image of the total magnetic intensity map of the study area. The inclination of the zone is -0.528, the declination -6.107.

Figure 4.2 Image of the Bouguer anomaly map of the study area using colour shaded with the sun inclination =25; Declination = 125; vertical scale = 10 000.

Figure 4.3: Image of the upward continuation of the TMI presenting weakly defined NE trending lineaments. The image resolves the different magnetic zones, and a series of east-west trending lineaments that are interpreted as dolerite dykes that are greater than 270 km long. Northeast to north-northeast trending first-order scale lineaments in the west and east of the study area were interpreted as the Yanfolila-Kalana Shear Zone and Banifing Shear Zone, respectively, and are coincident with shear zones mapped at surface. The identification of these lineaments on the upward continuation map indicates that the structures extend at depth. The study area is thus characterised by a heterogeneous distribution in magnetic minerals

Figure 4.4: Image of the upward continuation of the Bouguer anomaly \ using colour shaded with inclination = 25, declination = 125 and vertical scale = 10 000. The image presents the different gravity zones. The low gravity intensity zone located in southwest of the study area is coincident with low intensity magnetic (or high magnetic mineral content) on TMI map. They region was assigned to the TTG suite granitoids Archaean Kenema-Man domain by Feybesse et al. (1999) and Lahondère et al (1999a). The low density zone in the south-southeast was assigned to the Bougouni and Bagoe basin by Kušnir et al. (1989) and Girard et al. (1998), and is dominated by shale, sandstone and greywacke, and intercalated volcano-sedimentary rocks, and/or numerous TTG suite granitoids. The A high density zone in the northwest coincides with a low magnetic susceptibility zone and is assigned to the Siguiri Basin that is composed of siltstone, mudstone and subordinate arkoses, with pelitic schists.

Figure 4.5: Image of the first derivative map of the TMI. The red arrows correspond to a series of NNE to NE lineaments. The blue arrows are interpreted as sites of folds; the grey corresponds to the NS lineament. Black arrows mark the location of a series of east-west trending dolerite dykes.

Figure 4.6: Image of the first vertical derivative map of the Bouguer anomaly, resolves NE to NNE trends in the data set (red arrows); black arrows and black lines indicate NW trending lineaments; the green arrow marks the trace of north-south trending lineaments in the data; the blue arrow is interpreted as a fold.

Figure 4.7: Image of the analytic signal map showing N to NE trending lineaments (red arrow and black lines); the white arrows show circular features interpreted as plutons; the grey arrows marks the position of folds. The black arrows indicate the position of east-west trending dykes

Figure 4.8: Image of the application of the vertical integral on the analytic signal. The N to NE trending lineaments are presented by red arrows. The blue arrows correspond to the folded greenstone

belts. The white arrows mark the position of circular features that are interpreted as intrusions. The black arrows once again mark east-west trending lineaments and are interpreted as dykes.

Figure 4.9: Image of the tilt angle of the magnetic total field map. Dykes are marked by black arrows; main shear zones are marked by red arrows; significant intrusions in white; blue is interpreted as a fold.

Figure 4.10: Image of the tilt angle of the Bouguer anomaly map presents many of the same features as seen in Figure 4.9, including NW trending faults (black), NE trending fault (red).

Figure 4.11: Image of the automatic gain control of the total magnetic field indicating first-order scale structures (red arrows), and possible outliers of greenstone belts and their relationship to other attributes (white).

Figure 4.12: Image of the automatic gain control of the Bouguer anomaly. Red arrows indicate the main interpreted shear zones as indicated previously. NW trending faults are marked in black. NE faults are shown as dotted black lines. The blue arrow marks the position of a fold, as marked on other images.

Figure 4.13: Geophysical attributes showing interpreted attributes of first and order structures in the study area, with key areas 1-3 and profiles A-A', B-B' and C-C' indicated.

Figure 4.14: The potassium map of the study area from radiometric data. The red correspond to the high levels of potassium, and the blue to the low level or drainage systems.

Figure 4.15: The thorium map of the study derived from radiometric data. The red colours of this image correspond to the high zone of thorium, the blue zone to the low thorium zones.

Figure 4.16: The uranium map of the study area from radiometric data. For this image, the red are high level of uranium and blue the low.

Figure 4.17: A schematic pseudo lithology map showing lithological attributes extracted from the combination of magnetic susceptibility and density datasets. The figure interprets rock type according to their susceptibility and density mineral content. The key inversion zones described in the following chapters are indicated in blue. The figure shows the AA', BB' and CC' profiles in orange.

Figure 4.18: The georeferenced fact geological data extracted from Claessens et al. (1988) and Feybesse et al. (2006a). The image shows the structures elements and their dip values (in degree).The fact data are located in the inversion zones 1 to 6 in Chapter 5. There is a general lack of fact geology data for the study area, and structural notation is not consistent across the mapped regions.

Figure 5.1: Experimental model of dyke using magnetic data from published petrophysical data. Body 1 corresponds to the low magnetic susceptibility (sedimentary rocks or certain volcano sediment rocks). The profile is given by 'a', while 'b' corresponds to the model constructed.

Figure 5.2: Experimental model of a fault using gravity data from published petrophysical data. Body 1 corresponds to low density; bodies 2 and 3 correspond to the high densities; the fault is affected by erosion that reports as an irregularity in the profile between bodies 2 and 3. The letter a: represent the profile, b; correspond to the model constructed.

Figure 5.3: Forward model of the Transect AA' showing Profile AA'. The red curve is the calculated data and the black curve corresponds to the data measured. Bodies 1, 2, 3, 4, 5, 6 correspond to the different rocks type of the profile.

Figure 5.4: The forward model image of the Transect BB' showing the model for Profile BB'. The red curve is the calculated data and the black curve corresponds to the data measured. The bodies 1, 2, 3, 4, 5 correspond to the different rocks type of the profile.

Figure 5.5: The forward model of the Transect CC' showing the Profile CC' model. The red curve is the calculated data and the black curve corresponds to the data measured. The bodies 1, 2, 3, 4, 5, 6 correspond to the different rocks type of the profile.

Figure 5.6: The 3D inversion model of magnetic and gravity data for zone 1. The Yanfolila shear zone and the secondary splay shear are easily resolved. The shear zone is characterised by two parallel trends and the presence of a close upright symmetric fold (brown) in the south on the inversion. A number of southeast trending splay shears are also evident.

Figure 5.7: Inversion section of magnetic data combined with magnetic and gravity isosurface of zone 1. The image describes the dip of Yanfolila shear zone with the section. The shear zone dip steeply west in the south, and steeply east in the centre and north of the inversion model. Secondary southwest trending splay shears dip subvertically to steeply west. The shears bound high susceptibility rock volumes, and in the centre of the inversion, form a left-handed (anticlockwise) sigmoid volume that is consistent with sinistral displacement in the plane of the Yanfolila shear zone.

Figure 5.8: Inversion section of gravity data combined with magnetic and gravity isosurface of susceptibility and density of zone 1.

Figure 5.9: The inversion image of magnetic and gravity data from zone 2. The image presents the trend of structures and rock volumes in 3D. High density rock volumes are located in the western region of the inversion adjacent to the Mandina-Yanfolila fault. The model also confirms the presence of this zone at depth. High susceptibility rock volumes generally trend north-northeast and are bounded by shears.

Figure 5.10: Inversion section of magnetic data combined with magnetic and gravity isosurface of zone 2. The image describes the various dip orientations of Yanfolila Shear Zone in section. The majority of high susceptibility rocks dip steeply east, as do their bounding shear zones.

Figure 5.11: Inversion section of gravity data combined with magnetic isosurface of zone 2. The image shows the depth information of rock densities of zone 2. High density rock volumes occur at

depth in the region of the Yanfolila shear zone, but these are (apparently) not crosscut by the shears.

Figure 5.12: The inversion result image of magnetic and gravity data from zone 3. The image shows the trend of rock volumes in 3D including the Yanfolila Fault, Yanfolila, belt and east-west trending dyke. The model resolves generally north to north-northeast rock volumes. The north trending rock volume in the east corresponds with the position of the Yanfolila belt. The north-northeast trending rock volume in the west corresponds with the position of the Yanfolila fault. An east-west trending dolerite dyke is clearly evident in the inversion model and crosscuts the Yanfolila fault and Yanfolila belt.

Figure 5.13: Inversion sections of magnetic data combined with magnetic and gravity isosurfaces of zone 3. The image describes the rocks geometry in section to give an overall 3D model of the region. The Yanfolila fault dips steeply west.

Figure 5.14: Inversion section of gravity data combined with magnetic and gravity isosurfaces of zone 3. The image shows depth information of rock densities, and high susceptibility rock volume top-depth as black lines.

Figure 5.15: Inversion section of magnetic data combined with magnetic isosurface of zone 3 as viewed from the east. The image shows the dyke geometry with the magnetic sections. The dyke dips steeply to the south in the east, but rolls-over to dip steeply north in the west. High susceptibility values are located at approximately 300m depth for the dyke.

Figure 5.16: The inversion result of magnetic and gravity data for zone 4. The image shows the trend of rock structures and rock volumes with the magnetic and gravity isosurfaces. Structures include the Banifing shear zone and secondary splay shears, and the Menakoro fault, as well as an east-west trending dyke.

Figure 5.17: Inversion sections of magnetic data combined with magnetic and gravity isosurface of zone 4. The image describes the Banifing shear zone and rocks geometry in section as viewed from the south. Northwest trending rock volumes in the Bougouni belt dip sub-vertically to steeply west, while north trending rock volumes dip steeply east

Figure 5.18: The inversion section of gravity data combined with magnetic isosurface of zone 4. The image shows the depth information of rock densities of zone 4. Also the density of Banifing shear zone can be determined from the gravity inversion sections.

Figure 5.19: Inversion section of magnetic data combined with magnetic isosurface of zone 4 as viewed toward the west. The image shows the geometry of east-west trending dyke with a clear dip to the north to vertical. The thick sedimentary cover above the dyke is attributed to low susceptibility values at surface.

Figure 5.20: The inversion image of magnetic and gravity data from zone 5. The image shows the trend of magnetic and gravity isosurfaces and also structures and rock volumes. The structures

include the Banifing shear zone and secondary splay shears. The overall shear trend can be defined as northeasterly, but internal north-northeast trending rock volumes form right-handed (clockwise) sigmoids that are consistent with dextral displacement in the plane of the Banifing shear zone. Two areas of high density values (brown) are resolved in the inversion model and correspond to gneissic rocks.

Figure 5.21: Inversion sections of magnetic data combined with magnetic isosurfaces for zone 5. The image describes the Banifing shear zone (BSZ) and rock geometries that are steeply dipping.

Figure 5.22: The inversion section of gravity data combined with magnetic and gravity isosurfaces for zone 5. The image shows the depth information of rock densities of zone 5. Also the density of Banifing shear zone and secondary splay shears can be determined in the gravity inversion sections.

Figure 5.23: The inversion model of magnetic and gravity data from zone 6. The image shows the trend of structures and rock volumes in 3D, and the isosurface of magnetic and gravity data. The Koumantou-Morila fault is interpreted as are the Banifing shear zone and splay shears.

Figure 5.24: Inversion sections of magnetic data combined with magnetic and gravity isosurfaces of zone 3.

Figure 5.25: The inversion section of gravity data combined with magnetic isosurfaces of zone 6. The image shows the depth information for rock densities in Zone 6.

Figure 6.1: The geological and structural interpretation map of the study area showing the key areas as red rectangles. The volcano-sedimentary belts are indicated in green. Key structures and dyke are also indicated.

Figures 6.2: The magnetic inversion isosurface of key area 1. The image shows four isosurfaces (orange, green, pink and red).

Figures 6.3: The gravity inversion isosurface of key area 1 showing three level of isosurface (blue, orange and red).

Figure 6.4: The magnetic susceptibility section combined to the isosurface of key zone 1 and is the same as Figure 5.7 for Inversion zone 1. The image shows the dips of the Yanfolila Shear Zone (YSZ) and the secondary splay shear. The structures and rocks volume trend is shown in the figure. The magnetic sections and depth of rocks volume and structures are displayed.

Figure 6.5: The gravity inversion section combined with magnetic and gravity isosurfaces of key zone 1. The image shows the dip and trend of shear zones from magnetic sections. Compare with Figure 5.8 for Inversion Zone 1.

Figure 6.6: The combination of magnetic and gravity sections with magnetic and gravity isosurfacesfor key zone 1 for Inversion Zone 1. The image shows the trend of structures and rock volumes. The number 1, 3 and 5 correspond to the magnetic section; 2 and 4 are the gravity inversion sections.

Figures 6.7: The magnetic and gravity inversion isosurface of key area 2 for Inversion zone 4. The image presents three density isosurface in blue, orange and red, and three magnetic susceptibility isosurface (orange, pink and red) .The images shows high susceptibility and high density values at depth.

Figure 6.8: The isosurface showing the trend of different rock volumes and structures in the key area 2. Compare with Figure 5.16 for Inversion Zone 4. The secondary splay shear and Banifing shear zone can be identified with the figure. An accommodation zone outlined in pink o and transfer faults in blue can be identified.

Figure 6.9: The section of inversion for gravity and magnetic data showing the dip of dyke viewed from east. The numbers 1, 3, 4, 5, 7 are related to the magnetic sections, the numbers 2 and 6 correspond to the gravity sections.

Figure 6.10: The magnetic isosurface combined with magnetic sections for key zone 2. The image shows the trend of the Banifing shear zone (BSZ) and secondary splay shears; also the trend of Menankoro fault is highlighted. The change of dip can be observed for the BSZ and Menankoro fault from south to north. The dip of secondary splay shear is defined. Also the merging point of secondary splay shear and BSZ is well highlighted.

Figure 6.11: The magnetic and gravity inversion isosurfaces of key area 3. The gravity inversion isosurface present three of isosurface in blue, orange and red. The magnetic inversion present three level of isosurface (orange, pink and red). The coincidence of gravity inversion isosurface and magnetic isosurface can be identified at depth in term of rock volumes.

Figure 6.12: Magnetic and gravity isosurfaces showing the trend of rock volumes for key area 3 according to the rock densities and susceptibilities. An east-west trending dyke is highlighted in green.

Figure 6.13: The section of inversion for gravity and magnetic data showing the dip of rock at depth. The numbers 1, 3, and 5 are related to the magnetic sections, and 2 and 4 correspond to the gravity sections.

Figure 6.14: The magnetic inversion section combined with the magnetic isosurface showing the trend and dip of a dyke.

Figure 7.1: The interpreted structural map of the study area using magnetic, gravity and radiometric data in combination and using fact data as a constraint. The image shows the probably displacement sense of shear zone and faults using the combination of geophysical images processing, forward and inverse modelling with fact and petrophysical data as constraint.

Figure 7.2: The interpreted structural map of the study area using magnetic, gravity and radiometric data. The image show folds (marked in blue), greenstone belts (marked in green) and dykes (marked in pink) using geophysical processing images, modelling with fact and petrophysical data as constraint.

Figure 7.3: The image shows the different type of rock in the key area 1. The section 2 and 3 correspond to the gravity section, the numbers 1 and 4 correspond to the magnetic sections. Basalt is located at depth in the northwest of the model. The southern part of the key area resolves volcano-sedimentary rocks at depth.

LIST OF TABLES

Table 3.1: The confidence level of structures in the study area.

Table 3.2: The density and magnetic susceptibility values of certain rocks and minerals.

Table 3.3: The georeferenced coordinate of physical property data measured in the study area rocks.

Table 5.1: Profile AA' parameters

Table 5.2: Profile BB' parameters

Table 5.3: Profile CC' parameters

ABSTRACT

This study presents the combined processing, integration and inverse modelling of magnetic and gravity data for first-order crustal scale structures in southern Mali and northeast of Guinea. Southern Mali and northeast Guinea form part of the Palaeoproterozoic Baoulé-Mossi domain, which is part of the West African craton (WAC). The current understanding of the geology region is limited to exploration camp-scale studies with limited borehole investigations, and regional interpretations of historic geophysical datasets. In this study geophysical modelling is used to attempt to advance the understanding of the geology at depth. The combination of geophysical methods is an optimization that can support geophysical interpretations and contribute to the determination of the geological and structural characteristics that are important in understanding the subsurface geology.

Geophysical inversion modelling broadly resolved geology and structures under thick sedimentary cover (850-1100, thick) that is interpreted as comprising basinal sediments of the Taoudenni basin, or Cretaceous ferricrete. Geological constraints reduced the non-uniqueness, but could not control the quality. Nonetheless, the architecture, geometry and form of structures and dykes were predicted when compared with experimental analogue models as being a reasonable predictive tool for the behaviour of structures and dykes at depth. The use of surface physical properties added more information to the inversion modelling, but was very limited.

The enhancement of magnetic and gravity data, using filters, defined tip damage zones for first-order scale Yanfolila and Banifing shear zones that host gold mineralisation for example, at the Morila gold mine, and Kalana, Kodieran mines and Komana prospects. Second-order structures were also defined including in the tip damage zones of the Siguiri, Fatou and Syama shear zones, and the Manakoro fault, Madina-Yanfolila fault and Madina fault.

1.0. INTRODUCTION

1.1. Preamble

Airborne magnetic and gravity methods are used in geological exploration to obtain information about subsurface geology under sedimentary cover and where access is difficult for geological mapping. These methods are now possible because of the evolution in the 1980s of airborne geophysics to assist regional geological mapping (Jessell, 2001). Airborne magnetic and gravity methods can be used to identify rocks and major structures by applying filter enhancements, image processing and interpretation methods (modelling). The delineation of subsurface structures such us first-order scale crustal structures is one of the main roles of geophysical modelling interpretation techniques.

Geophysical data surveys are interpreted in two ways:

1. Qualitative interpretations describe the data surveyed. They explain anomalies as geological and structural attributes. Qualitative interpretations are a good way to map geological features such as dykes, the boundary of rock units, intrusions, shear zones, faults and others discontinuities. The qualitative interpretation is improved and potentially constrained by applying geological data from the area of study. The qualitative interpretation is a mathematical manipulation of geophysical data (Mickus, 2008).
2. Quantitative interpretations can estimate geological features in terms of their depth, geometry, and block displacements. Quantitative interpretations facilitate the construction of conceptual geological models that can better explain geological phenomena in the sub-surface, and using existing geological information (if available). Forward modelling and inverse modelling are the two methods used in geophysical quantitative interpretations.

Geophysical modelling provides a conceptual description of the sub-surface; it begins with simple models that may produce analytical or numerical representations. This stage is direct or forward modelling (analytical modelling), and the construction of a model from the data surveyed is inverse modelling (numerical modelling). Simple models can be used to focus the selection of geophysical methods for future data collection.

According to Wijns (2004), numerical modelling is affected by two factors:

1. The *misfit (distance)* corresponds to the accumulation of errors between the initial and final model and is equal to the sum of errors from the beginning of the collection of data to the production of the model.
2. The *input parameters*. These parameters take into account the geometry, physical properties, approximate depth, and thickness of any weathering profile (regolith). These factors affect the ability to interpret the final model that explains phenomena at depth. To be realistic and consistent in geophysical modelling, it is necessary to combine and integrate information from

both geological and geophysical surveys (Lelievre, 2009).

The objective of geophysical modelling is to respond to the uncertainty and a non-uniqueness of solutions resulting from inverse modelling, and to constrain them. The main problem of inversion is the fact that an infinite numbers of geophysical solutions can fit the same geophysical data, thus creating ambiguity when choosing a reliable model that matches and responds well to the real distribution of subsurface properties among a multitude of other solutions.

Also most geological structures are not well defined with high confidence by only one geophysical method, which therefore requires a combination of several geophysical methods to constrain structures and geological domains. The combination of geophysical methods is an optimization that supports the geophysical interpretation and contributes in determining the geological elements that are important in developing and understanding the subsurface geology. The limitation in optimisation is the cost of applying multiple geophysical techniques and methods.

With this in mind, this project uses a combination of geophysical methods for geophysical modelling by integrating the available geological data to build a 3D geophysical model of the study area, and to interpret geological structures and geological domains. Geophysical attributes and geological fact data are extracted from a given set of company and published geological-geophysical survey data. Specifically, the aims are to: (1) establish tectonic domains in the south of Mali and northeast of Guinea in West Africa for rocks which are generally considered to the Palaeoproterozoic in age; (2) to determine if structures (for example, shears and faults), beneath sedimentary cover have the potential to host gold mineralization; and (3) constrain a strato-tectonic history for the study area from extracted geophysical attributes.

Furthermore, this study makes comparisons between gold-bearing structures that crop out at surface at the Syama Mine, Komana prospect, Morila mine and Kalana mine in the southwest of Mali, with those undercover in order to search for potential gold exploration targets at depth across the study area.

1.2. Location and Physiography

The study area covers the south of Mali and the northeast of Guinea in West Africa (Figure 1.1). Geologically, the study area is situated in the Palaeoproterozoic Baoulé-Mossi domain of the West African craton (Figure 1.2).

The study area is bounded by 10° 13TSf to 12° 47TSf latitude, and 9° 60W to 5° 55W longitude. It covers an area of 114,750 km^2 mostly across the province of Sikasso in Mali, and Sirgui in Guinea. It includes the 1:200,000 map sheets of Yanfolila, Tienko, Bougouni, Bamako East, Bamako West, Tingrela, Massigui and Nielle in Mali, and the 1:200,000 map sheets of Siguiri, Sirakoro, Faraba, Kankan and Falama in Guinea (Figure 1.3) (IGN, 1993).

The topography in the east of the study area is dominated by a set of slightly inclined plateaus, with low mountains and extensive plains. In the west of the study area, the topography is dominated by tabular sandstone massifs and cliffs that attain an elevation of 900m. Undulating plains occur between the massifs at 400 to 450m elevation above sea level.

Hydrographically, the Guinean portion of the study area hosts a number of rivers that have their sources in the elevated plateaus of Guinea. These rivers include the Banifing River, Niger River (at Kouroussa, Siguiri) and its tributaries that include Sankarani, Fie, Tinkisso (at Faranah), Mafou, Dion and Niandan (in Kissidougou) and Milo (in Kankan). In Mali, the study area is traversed by the tributaries of the Niger River including the Sankarani in the north that debouches into the Niger River upstream of the city of Bamako, and the Bani River that joins the Niger River at Mopti after collecting waters from the Baoulé, Bagoe and Banifing rivers.

1.3. Objective

Much of the geological studies completed at the scale of the study area are actually based on the interpretations of historic magnetic and radiometric data, or satellite images such as Landsat and Aster (c.f., Lahondère et al., 1999a, 1999b; Egal et al., 2002; Feybesse et al., 2006a). For the larger part of the West African craton, there are in fact very few geological studies that combine geophysical methods apart from those designed specifically for mineral exploration and research. Studies that combine geophysical methods include those by Hasting (1982), Ritz (1984), Bonvalot et al. (1991), Toft et al. (1992), Tidjani et al. (1993), Mickus (2008), Hein (2010), Baratoux et al. (2011), Metelka et al. (2011), Perrouty et al. (2012), Miller et al. (2013), and Tshibubudze (2015). Regardless, there is often limited integration of geological data with the geophysical interpretations; rather the geophysics constrains the regional geological interpretations. In fact, the majority of these studies have needed to collect large primary geological datasets to be significant, but large primary datasets do not exist across large parts of the Palaeoproterozoic of the West Africa craton, and certainly not in the study area in southern Mali and western Guinea. Nonetheless, some studies have relevance to the study area in southern Mali and western Guinea including those by (1) Baratoux et al. (2011) and Metelka et al. (2011) who interpreted the geology of southwest Burkina Faso on the eastern margin of the study area, and (2) a regional compilation by Miller et al. (2013) based on data by SIGAfrique's interpretation of magnetic data that forms the basis for geological constraints in the south of Mali and into the northeast of Guinea.

The main aim of this project is to define and interpret the volcano-sedimentary belts of the study area, batholiths, and regional structures that correspond to known zones of gold mineralisation, and to improve the resolution of mapped units and structures at the first-order scale. Using 3D geophysical modelling the general aims included;

1. Undertake an advanced processing of combined geophysical and radiometric data, satellite images and topographic data to develop an interpretative geological map that can be compared with published geological maps to measure similarities and differences.
2. Identify structures, geological domains and the architecture of basins, and the basement in key belts.
3. Integrate geological data with geophysical data to derive parameters for inversion modelling.
4. Perform 3D inversions of geophysical data that are constrained by the available (scant) geological information.
5. Test optimum inversion parameters.
6. Produce a 3D model of the study area (or key localities) that could help to interpret deep regional geological structures and domains and perhaps suitable exploration targets.

1.4. Hypothesis

Geophysical modelling is not able to determine the exact geology in a complex zone, particularly if there is no geological information known for the area of study (Mickus, 2008; Lelievre, 2009). A geophysical model can only be used to characterise the subsurface geology, and to expand and verify the geological information already available, which can be confirmed with drilling of boreholes.

Geological information is qualitative and/or quantitative. It includes petrophysical, borehole, lithological, geochemical, structural, and relative and absolute geochronology data. This information is collected from studies that precede modelling. Importantly geophysical models must be validated against the geological models to measure the usefulness of geophysical modelling for targeting in regions of geological difficulty, or under sedimentary cover. Geological and petrophysical data is needed to constrain models derived from inverse modelling.

Petrophysical data from WAXI (2013) and geological fact data for the study area has been extracted from maps and plans presented by Girard et al. (1998), Bentley et al. (2000), Standing (2006) and Feybesse et al. (2006a) without extracting the accompanying interpreted data (to avoid bias). Together with rock physical property data, the extracted fact data has been used to constrain the geophysical inversion model to:

1. Identify structures under sedimentary cover.
2. Evaluate which physical property data has more influence on the geophysical data inversion in the study area.
3. Establish tectonic domains.
4. Attempt a tectonic history based on relative chronology of geological events.
5. Characterise those structures under sedimentary cover that could control gold mineralization in the volcano-sedimentary belts, and local batholiths and plutons.

1.5. Thesis organisation

This thesis is divided into eight chapters including the Introduction.

Chapter 2 presents the regional geology of the study area.

Chapter 3 presents a review of geophysical methods used and modelling processes, and the methodologies used. This chapter also describes the image processing sequence used in this study and data constraints, Geophysical modelling and inversion methodologies are explained.

Chapter 4 presents the results of attribute extraction from geophysical maps and geological data, to define zones of high confidence that became the loci for geophysical modelling. Fist pas geophysical and structural maps of the study area where generated.

Chapter 5 is based on presentation of the results forward and inversion modelling in 2D and 3D. Forward modelling took place along three transects in zones of high confidence that were established in Chapter 4. Inversion modelling expanded on these transects to take in 6 regions of inversion study. A geophysical synthesis of inversion modelling is presented in this chapter.

Chapter 6 reports on the results obtained when the limitations of inversion modelling (beyond the depth of drilling) are addressed using published experimental analogue models to control the quality of inversion (using surface petrophysical data) at depth for structures and dykes. Three key areas were selected as laboratories of study.

Chapter 7 presents a limited discussion, but summarises the geological context, and how to understand the results of the inversion experimentation. It presents an new interpretations for the study area.

The conclusions are summarised in Chapter 8.

1.6. List of abbreviations

BRGM:	*Bureau de Recherché Géologique et Minière*
CGS:	Centimetre Gram and Second
DMA:	Defence Mapping Agency (USA)
DNRGH:	*Direction National de la Recherché Géologique et des Hydrocarbures*
DNGM:	*Direction Nationale de la Géologie et des Mines*
GRAV:	Gravity or Gravimetric
GPS:	Global Positioning System
IGN:	*Institut Géographique National (France)*
MAG:	Magnetic

ORSTOM:	*Office de la Recherché Scientifique et Technique Outre-Mer*
TMI:	Total Magnetic Intensity
TTG:	Tonalite Trondhjemite Granodiorite
UBC-GIF:	University of British Columbia – Geophysical Inversion Facility
WAC:	West Africa Craton

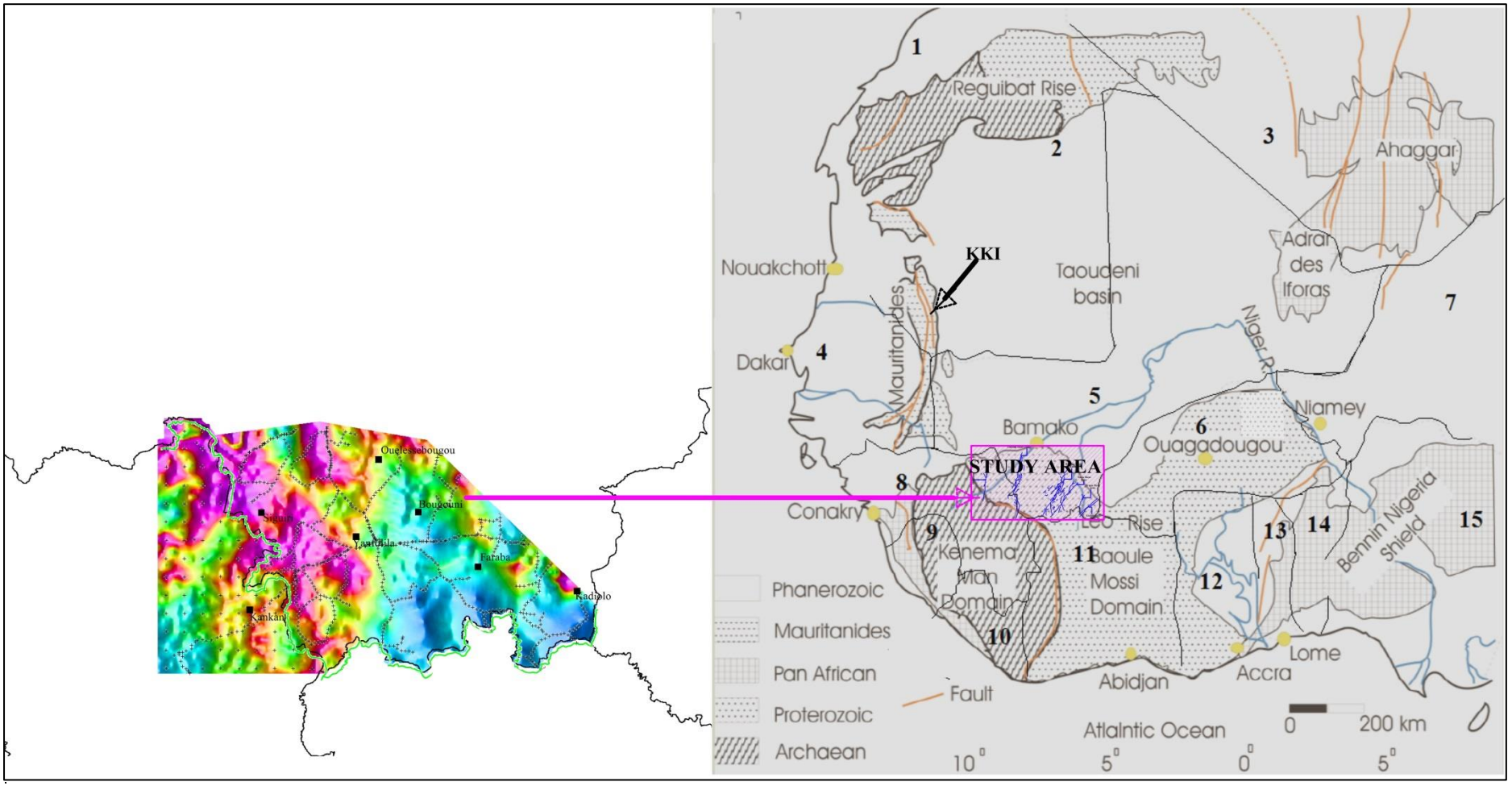

Figure 1.1*: The location of the study area in the West Africa Craton. The Bouguer anomaly data from the Office de la Recherché Scientifique et Technique Outre-Mer (1952, 1987) for the study area. 1: Morocco, 2: Mauritania, 3: Algeria, 4: Senegal, 5: Mali, 6: Burkina Faso, 7: Niger, 8: Guinea, 9: Sierra Leone, 10: Liberia, 11: Ivory Coast, 12: Ghana, 13: Togo, 14: Benin, 15: Nigeria. KKI: Kedougou-Kenieba Inlier; the magenta coloured box indicates the study area in WAC (Modified after Tshibubudze, 2015).*

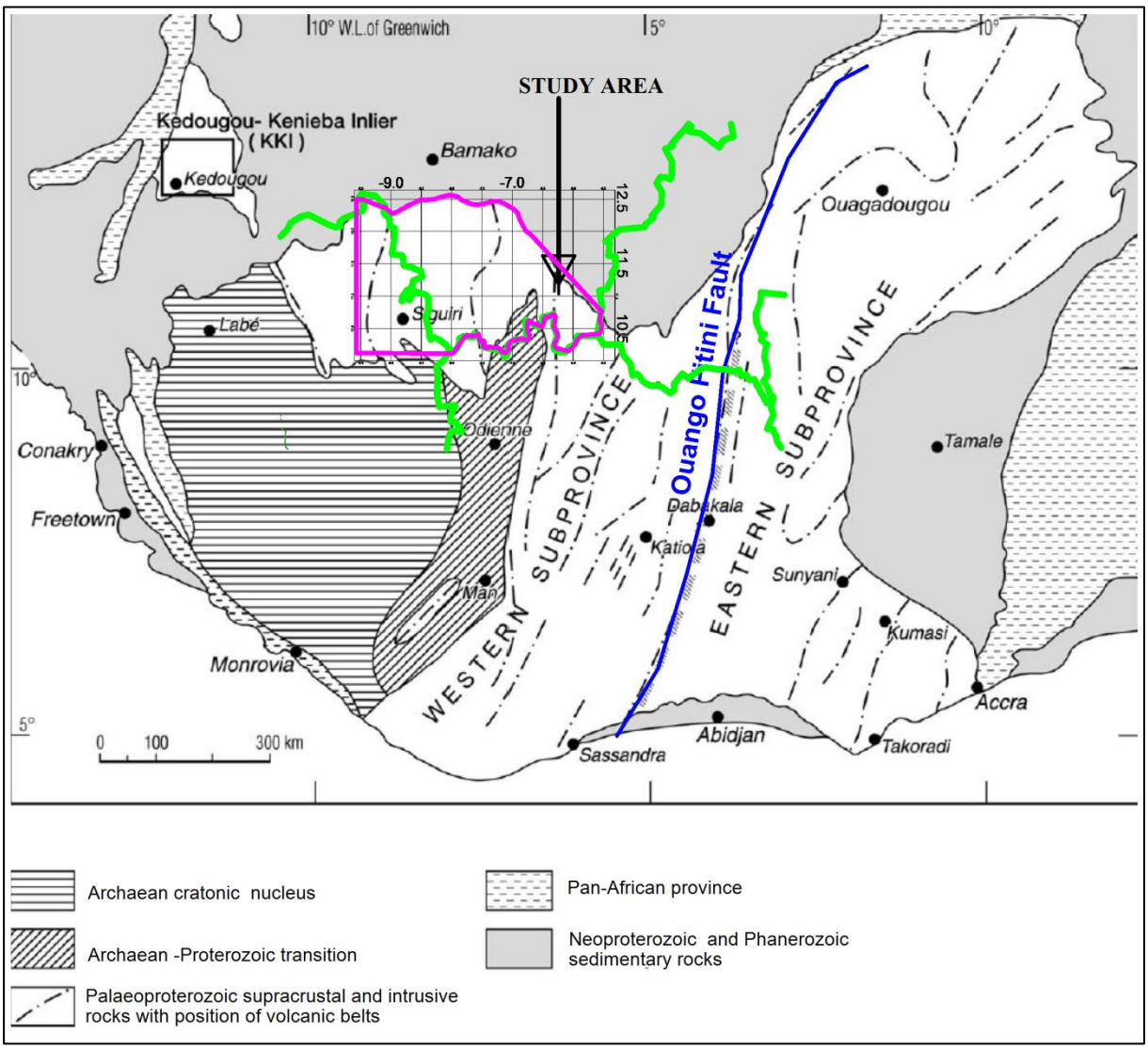

***Figure 1.2**: The Palaeoproterozoic Baoulé-Mossi domain of West African Craton. The study area is defined in pink. Partial country borders are indicated by the green line. Southern Mali and northeast of Guinea cover a geographical extent of 440km x 260km (modified after Hirdes and Davis, 2002).*

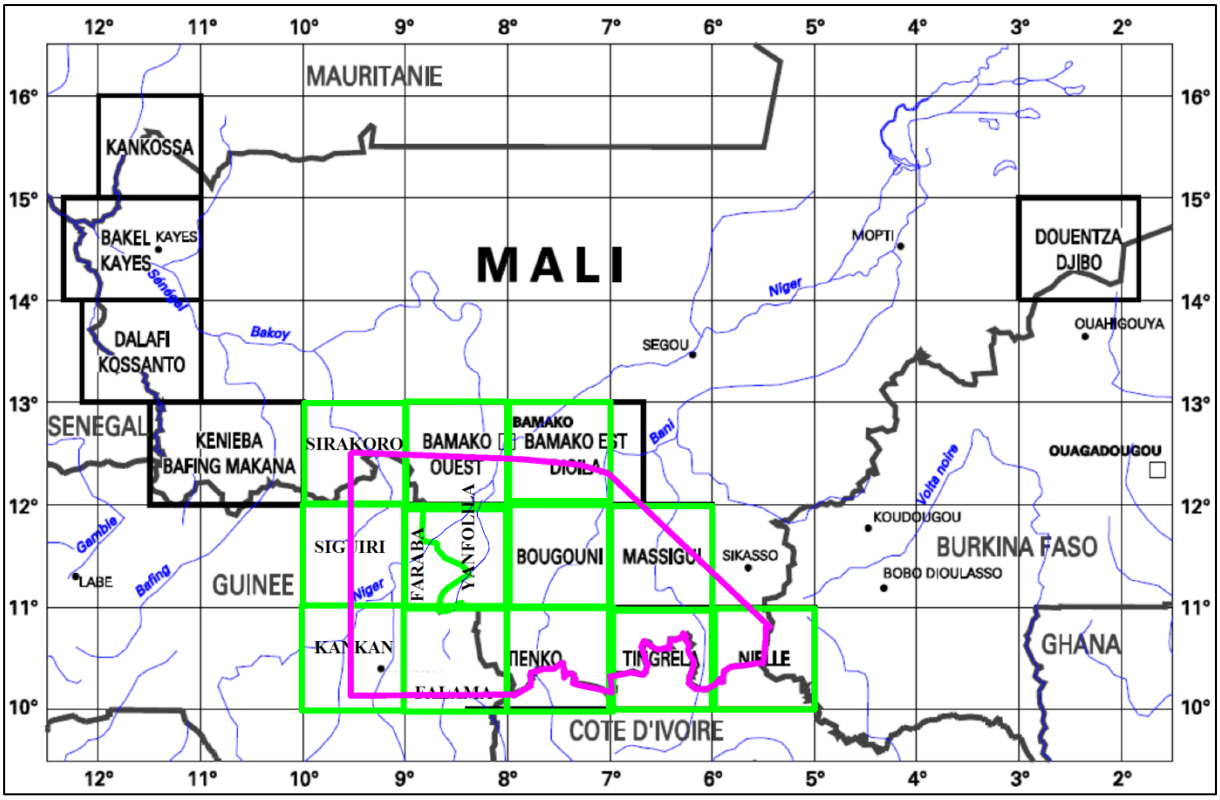

Figure 1.3*: The study area divided into map sheets. The study area is outlined in pink, the 1:200 000 map sheets in green, and the main river systems in blue. The map shows the Yanfolila, Bamako east and west, Bougouni, Tienko Tingrela, Massigui and Nielle sheets in Mali, and Kankan, Siguiri, Sirakoro, Falama and Faraba sheets in Guinea overlying the West Africa map with main provinces close to the study area (modified from the Institut Géographique National, France, 1993).*

2.0. REGIONAL SETTING

2.1. West African Craton

The West African Craton includes the Reguibat Shield in the north of the craton and the Leo Man Shield in the south (Figure 1.1). These shields represent two nuclei that formed in two stages of crustal evolution in West Africa (Naba, 2007). The shields are overlain by three main sedimentary basins; the Tindouf basin in the north, the Taoudenni basin in the centre, and the Volta basin in the southeast of the craton.

The West African craton is considered as stable since the end of the Palaeoproterozoic at approximately 1.8 Ga (Kušnir, et al., 1999). The Leo-Man Shield includes the Archaean Kenema-Man domain in the west and the Palaeoproterozoic Baoulé-Mossi domain in the east. The Palaeoproterozoic Kayes and Kedougou-Kenieba inliers are situated in the west of the craton between the Reguibat and Leo-Man shields. The Baoulé-Mossi domain is made up of linear greenstone belts composed of metamorphosed plutono-volcanic, volcaniclastic and sedimentary rocks, and TTG suite granitoids (Lompo, 2010).

2.2. Regional geological domains of craton

2.2.1. The Archaean Kenema-Man domain

The Kenema-Man domain crops out in the countries of Sierra Leone, Liberia and Guinea. The domain was marked by deformation of sub-domains in the Leonean and Liberian orogenies at approximately 2.7 Ga. The Kenema-Man domain is made up of the pre-Leonean granitic-gneiss basement that is Archaean in age. The degree of regional metamorphism observed in the Kenema-Man domain attains amphibolite to granulite facies (Bessoles, 1977). The Leonean is composed of tonalite-granodiorite plutons and batholiths equivalent to TTG suite granitoids (Egal et al., 1999a). In contrast, the Liberian is characterized by granite, monzogranite, tonalite or granodiorite (Lahondère et al., 1999b).

2.2.2. Palaeoproterozoic Baoulé-Mossi domain

The region of study for this research lies in the Palaeoproterozoic Baoulé-Mossi domain in southern Mali and northeastern Guinea. The study area is composed of metamorphosed clastic, volcanic and volcaniclastic sequences assigned to the Birimian Supergroup (Davis et al., 1994; WAXI, 2013). The Tarkwa Group (detrital U-Pb zircon; 2133 ± 4 Ma) of Pigois et al. (2003) and Perrouty et al. (2012) unconformably overlies the Birimian Supergroup (Tunks et al., 2004).

The lithological composition and structural architecture of the Baoulé-Mossi domain has been discussed and described by Milèsi et al. (1992), Feybesse and Milèsi (1994), Hirdes et al. (1996), Egal et al. (2002), Lahondère et al. (2002), Hein et al. (2004), Naba et al. (2004), Feybesse et al. (2006b), Roddaz et al. (2007), Lompo (2009, 2010), Hein (2010), Baratoux et al. (2011) and Tshibubudze and Hein (2013). The greenstone belts are composed of metamorphosed volcano-plutonic rocks of the calc-alkaline series (TTG suite), ultramafic-basalt-andesite units, and sedimentary and volcano-sedimentary rocks. TTG suite batholiths and granitoids are generally composed of tonalite, granodiorite, trondhjemite and monzogranite.

Two models have been proposed for the tectonic evolution of the granite-greenstone belts in the Baoulé-Mossi domain. Lompo (2010) and Vidal (2009) interpreted a dome and basin geometry for formation of the crust, while Baratoux et al. (2011) assigned major crustal thickening phase to nappe-stacking along orogeny-parallel thrust faults.

The structural style of the Baoulé-Mossi domain has been described by Davis et al. (1994), Hirdes et al. (1996) and Hirdes and Davis (2002). Historically, the domain is interpreted as having formed during (1) an accretion orogeny resulting from a collision of island arcs and oceanic plateaus with an Archaean craton, and (2) a phase of transcurrent tectonics characterized by regional scale faults (Lompo, 2010) and also a tectonic evolution of oceanic crust and continental crust with Archaean basement (Hirdes and Davis, 2002). However, subsequent studies of the Baoulé-Mossi domain have identified 3 major deformation events, namely;

1. Deformation, during the Tangaean Event (also referred to as Eburnean I or Eoeburnean in Ghana) at approximately 2190-2140Ma (D1), as recognised in the northeast of Burkina Faso by Tshibubudze et al. (2009), Hein (2010) and Tshibubudze and Hein (2013), and in Ghana by Allibone et al. (2002) and De Kock et al.(2011, 2012). This event corresponds to oceanic arc-backarc accretion tectonics (Tshibubudze and Hein, 2013) from a subduction slab, or the mafic lower crust (Baratoux et al., 2011).
2. Deformation which corresponds to the Eburnean Orogeny (D2) at approximately 2130-1980Ma (Feybesse et al., 2006b; Hein, 2010; Baratoux et al., 2011; Tshibubudze and Hein, 2013). D2 is divided in D2A that is characterised by compressive tectonics, and D2B that is transpressive with formation of strike-slip faults. The shift from D2A to D2B is generally associated with significant gold mineralisation in the Baoulé-Mossi domain.
3. D3 deformation during the Wabo-Tampelse Event (Hein, 2010) either in the late-Eburnean or the Pan African Orogeny (Baratoux et al., 2011).

The structures produced from these tectonic events are characterized by the development of:

1. In D1 - NW to NNW-trending fold-thrust belts, and NW-trending mylonite zones, shear zones and F1 folds (Hein, 2010; Perrouty et al., 2012; Tshibubudze and Hein, 2013).

2. In D2 - Regional folds that trend NNE, sinistral-reverse shear zones, a penetrative schistosity, and dextral strike-slip faults (Feybesse et al., 2006b; Hein, 2010); north to NE-trending transcurrent faults that affect all lithologies and localized at the contact zones between the granites and greenstones (Baratoux et al., 2011).
3. In D3 - Formation of WNW-trending dextral-reverse thrusts, east-west trending folds (Hein, 2010) and shallow north or south dipping thrust faults (Baratoux et al., 2011) during the Wabo-Tampelse Event.

The Baoulé-Mossi is unconformably overlain by the Neoproterozoic sediments of the Taoudenni basin and Quaternary formations, particularly laterite that unconformably overlies a third of the continent of Africa (Kušnir et al., 1986, Brown et al., 1994; Egal et al., 1999a; Feybesse et al., 2006a).

2.3. Architecture and geological setting of southern Mali and northeast Guinea

The study area in southern Mali and northeast Guinea is composed of, metamorphosed sedimentary units of the Birimian Supergroup, including greywacke, siltstone and conglomerate that are intercalated with volcanic rocks (Liegeois et al., 1991) and these are intruded by TTG suite plutons and batholiths. The rocks are grouped from west to east into the Siguiri, Bougouni, and Bagoe basins (Figure 2.2). The Siguiri and Bougouni basins are separated by the Yanfolila shear zone. The Bougouni and Bagoe basins are separated by the Banifing shear zone. The western margin of the Bagoe belt is defined by the Siguiri volcano-sedimentary belt and Siguiri shear zone. The Massigui and Bougouni volcano-sedimentary belts lie wholly within the Bougouni basin in the northeast and southeast, respectively (Girard et al., 1998; Randgold, 2008). The northwest trending Kadiana-Madinani volcano-sedimentary belt lies wholly within the Bagoe belt but in the southwest. The Kadiana-Madinani belt may be the extension of the Bougouni belt.

The Siguiri basin is dominated by the Siguiri-Kankan Formation in Guinea and is composed of siltstone, mudstone and subordinate arkoses, with pelitic schist (Egal et al., 1999a, 1999b; Lahondère et al., 1999a, 1999b). These sediments are intercalated with pyroclastites or tuffs that are composed of rhyolite and quartz lithic fragments (Lahondère et al., 2002). Yanfolila granites in Mali were intruded on the eastern margin of the Siguiri belt (Figure 2.3).

The Yanfolila volcano-sedimentary belt and several outliers are composed of massive mafic volcanic rocks (Girard et al., 1998; Parker and Wilkinson, 2011). The Yanfolila belt is crosscut by the north-trending Yanfolila shear zone (Figure 2.2) (Randgold, 2008).

The Bougouni basin (also locally called the Bougouni-Kerekoro basin) is situated between the Yanfolila and Banifing shear zones (Figures 2.2, 2.3). The basin is intruded by a TTG suite

batholiths and granite plutons (Girard et al., 1998, Miller et al., 2013). The basin is composed of shale, sandstone, greywacke, and intercalated volcano-sedimentary rocks (Feybesse et al., 2006a; Parker and Wilkinson, 2011). The northeast-trending Massigui belt in the Bougouni basin is composed of porphyry rhyodacites with basalt, breccia and conglomerate units (Kušnir et al, 1989; Girard et al., 1998).

The Banifing shear zone separates the Bougouni basin in the west from the Bagoe basin to the east (Figure 2.4). According to Bessoles (1977), the northwest trending Bagoe belt is the western extension of the Bondiali-Bagoe-Diaoula belt in the Ivory Coast that splits to form the Bagoe belt in Mali and the Banfora belt in Burkina Faso. The eastern margin of the Bagoe basin (also referred to as the Kadiana-Madinani domain) is the Syama belt (Girard et al., 1998). The Kadiolo domain lies to the east of the Syama Shear Zone (Standing, 2006). The Bagoe basin (Kadiana-Madinani domain) is interpreted by Bentley et al. (2000) as a back-arc basin that was accreted onto the Kadiolo terrane during the peak of the Eburnean orogeny (ca. 2.2-2.0 Ga).

The Syama belt can be divided into sedimentary sequences of the Tarkwa Group in the east, and volcano-sedimentary rocks of the Birimian Supergroup to the west (Girard et al., 1998). The north-northeast-trending Syama-Bananso Shear Zone crosscuts the Syama belt (Standing, 2006; Ballo et al., 2016).

Metamorphism in the study zone is characterised by regional and contact metamorphic mineral assemblages. Regional metamorphism is characterised by mineral assemblages to middle to upper greenschist mineral assemblage (Tunks et al., 2004). Contact metamorphism is characterised by amphibolite facies observed in the contact aureole of granitoids.

2.4. Geophysical interpretations at the regional scale and direct modelling

This study uses large-scale geophysical airborne data for interpretation by modelling of southern Mali and northeast Guinea, as a case study region, where there is currently limited geological data. Regional-scale geophysical studies in the study area are considered with respect to regional-scale studies conducted in Burkina Faso by Mickus (2008) and Metelka et al. (2011), and in the Gawler craton in Australia by Stewart and Berts (2010). A large scale gravimetric analysis study was conducted in Burkina Faso by Mickus (2008). The goal was to control the relation between the gravimetric anomalies and metal deposits. This study highlighted the use of the geophysical datasets in direct modelling, which is also the goal of this research in the study area.

The studies of Metelka et al. (2011) from the west of Burkina Faso demonstrated the importance of airborne geophysical data interpretation in reconstruction of the geology of southwest Burkina Faso where for the most part, there is little outcrop. It was possible to map lithologies and structures to obtain a better understanding of the subsurface geology.

The study in the Gawler craton in Australia by Stewart and Berts (2010) was based on the analysis of shear zones with interpretation of the geophysical data by direct modelling. Geological data were used as a constraint in building the forward model. These results demonstrated that interpretations by forward modelling, across large regions with little or absent outcrop, can be extremely useful when building tectonic models.

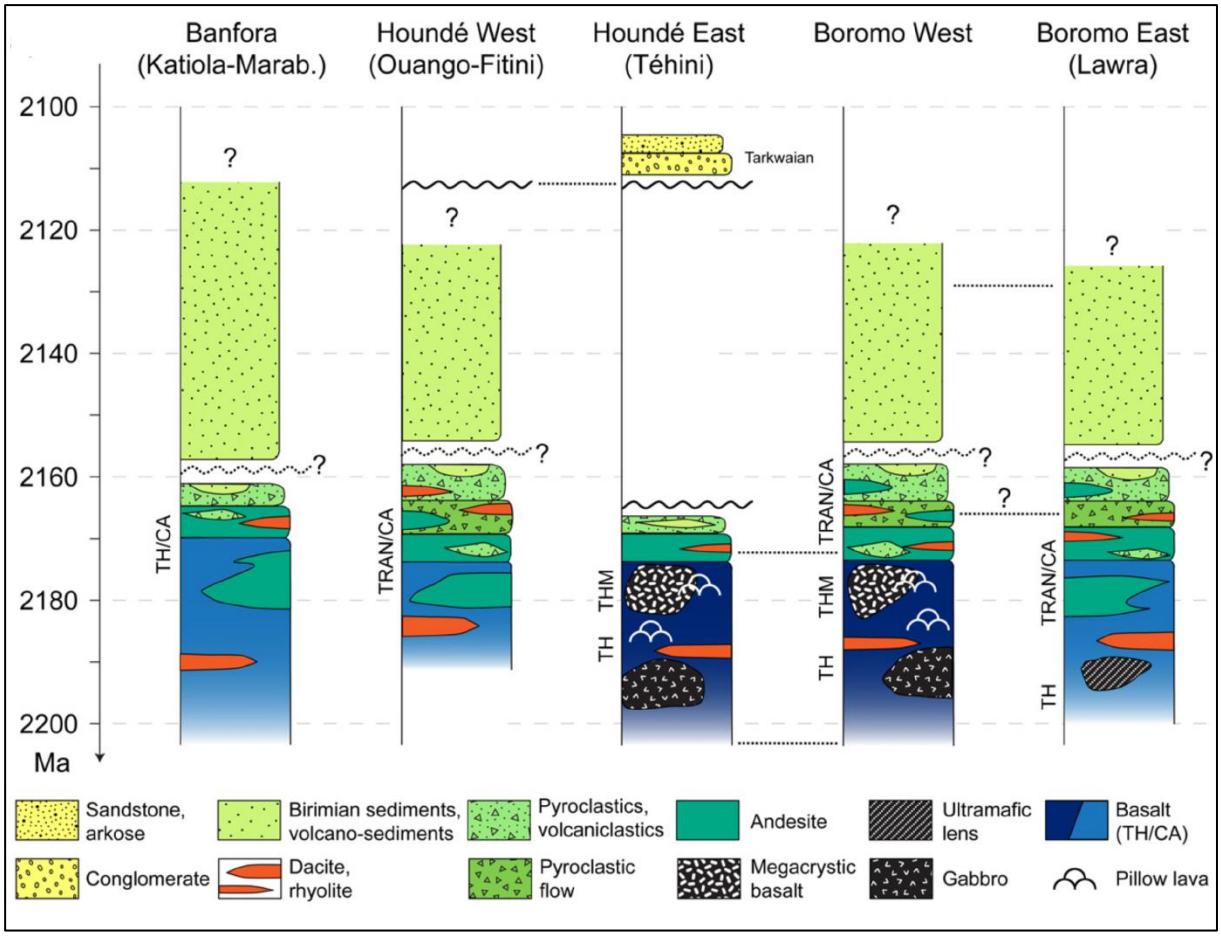

Figure 2.1*: The stratigraphy of the Palaeoproterozoic of Baoulé-Mossi domain in the eastern part of the study area, modified from Baratoux et al. (2011).*

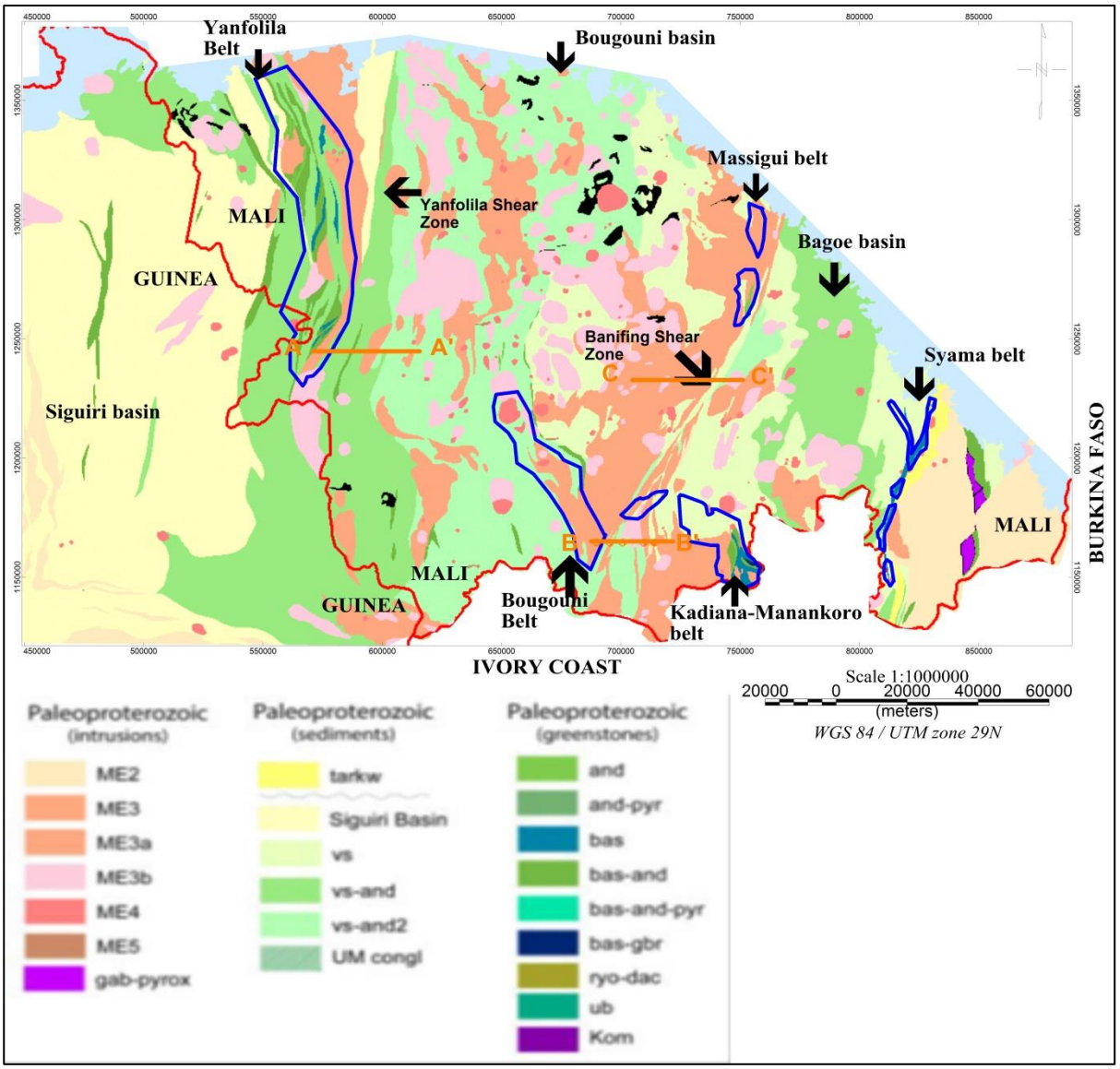

Figure 2.2*: The study area is divided into basins and volcano-sedimentary belts in overlay of the geological map modified from SIGAfrique (2000) and Miller et al. (2013). ME: magmatic event; VS: Volcano sediment; and: andesite; bas: basalt; pyr: pyroxene; and: andesite; ub: ultra-basic; ryo: rhyolite; kom: ,*

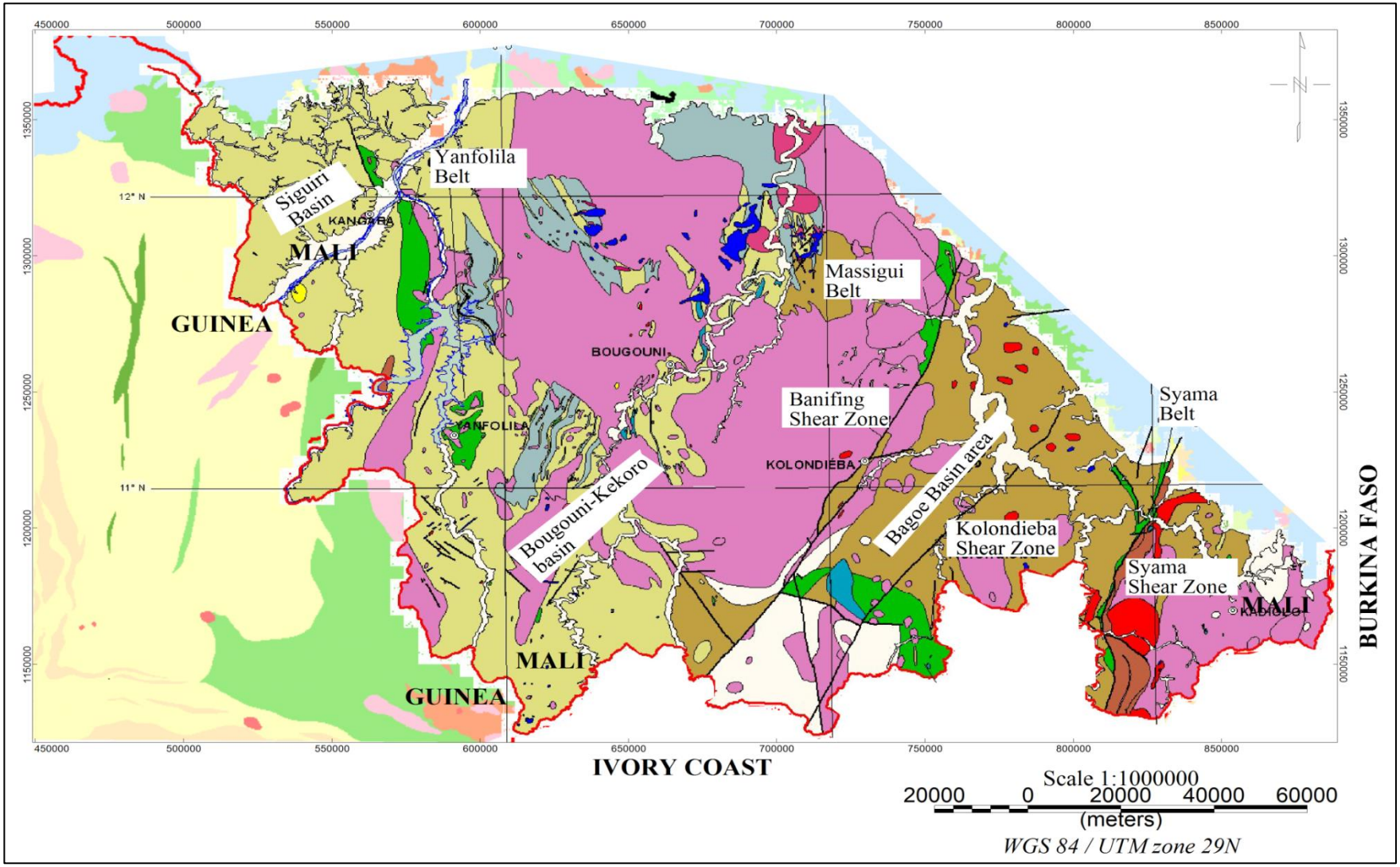

***Figure 2.3**: The Siguiri basin bordered by Yanfolila belt, and including the Bougouni-Kekorobasin, Banifing shear zone, Massigui belt, Bagoe basin, Kolondieba shear zone, Syama belat and Syama-(Bananaso)shear zone (modified after Girard et al., 1998 and Miller et al., 2013).*

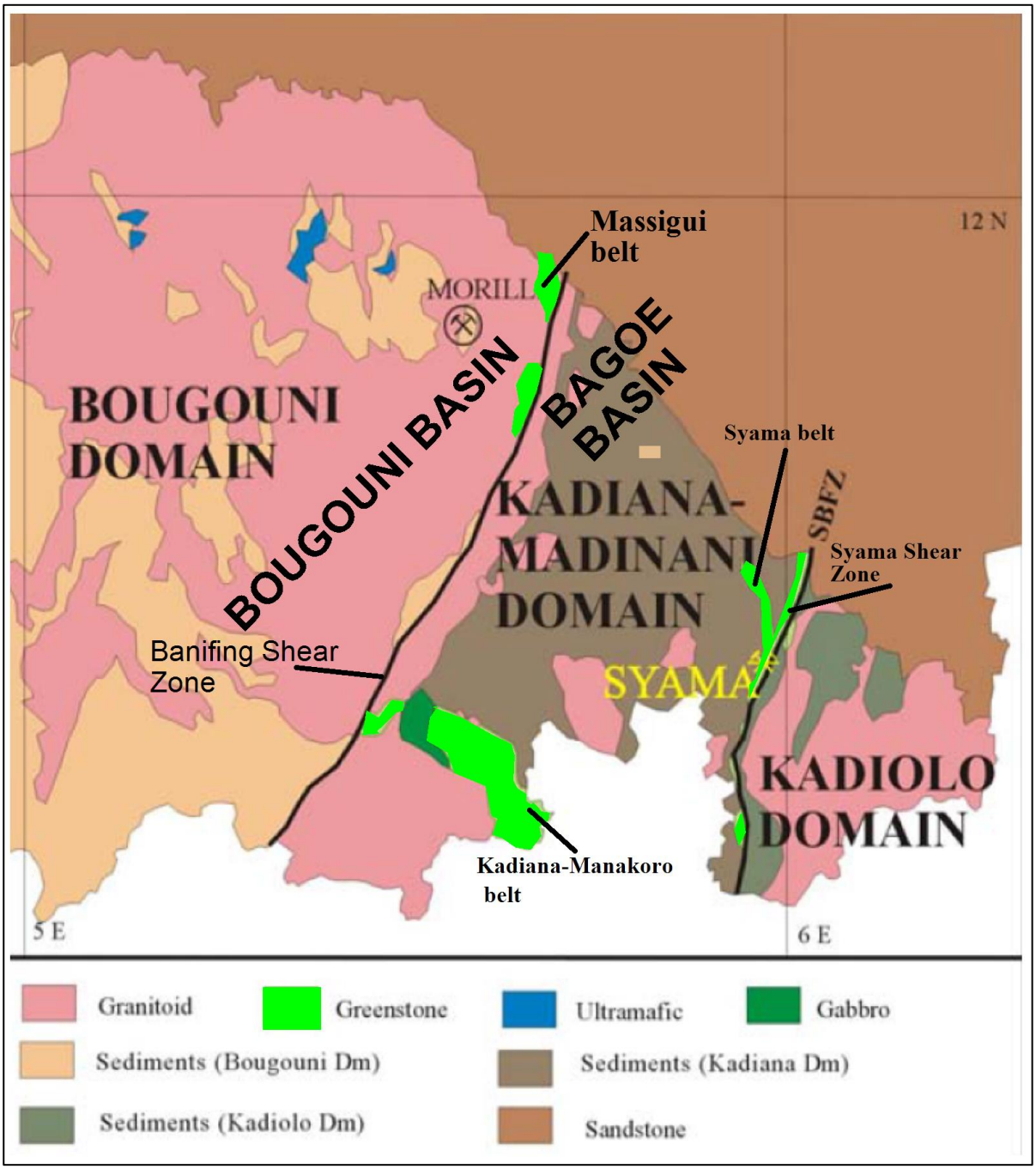

Figure 2.4*: The different domains and basins in the eastern part of the study area. The image show the Banifing shear zone which separates the Bougouni and Bagoe basins. It shows also the Syama-(Bananaso) fshear zone separating the Kadiana-Mandinani domain and Kadiolo domain. The Bagoe and Kadiana-Manakoro belts are also highlighted (modified after Girard et al., 1998; Bentley et al., 2000; Miller et al., 2013).*

3.0. METHODOLOGIES IN GEOPHYSICAL INVERSION MODELLING AND IMAGE PROCESSING TECHNIQUES

The combination of gravimetric and magnetic methods is a good way to interpret, identify and locate deep structures, lateral and vertical continuation of structures, and plutonic architectures. For example, a study of the Banifing shear zone by Féménais (2008) highlighted that basement lineaments are easily resolved in the magnetic and radiometric airborne geophysical datasets. However, a limitation to the interpretation of magnetic data in the study area is the fact that laterite-ferricrete covers a significant portion of the study area and major parts of the Baoulé-Mossi domain (Brown et al., 1994; Blot, 2004; Beauvais et al., 2008). The laterite-ferricrete can exceed 50m in thickness in parts, which complicates the presentation of magnetic data, but the effects of laterite-ferricrete can be minimised in the magnetic signature through filtering of the data.

Quantitative interpretation of geophysical data is critical; it involves making numerical estimates of the depth and dimensions of the sources of anomalies. Modelling is the stage used to achieve quantitative interpretation. It can determine stratigraphic units and contact zones covered by a conductive weathering layer deeper than 100m and/or covered by laterite-ferricrete.

3.1. Introduction

Geophysical modelling has historically been the method by which applied geophysicists interpret geophysical data. Modelling is performed as forward and inversion modelling. Inversion modelling allows construction of a model using data collected in the field.

Inversion modelling suffers from the non-uniqueness of solution, as indicated by Tikhonov and Arsenin (1977). The non-uniqueness of solution is determined as the fact that several geophysical models can fit the same geophysical data. The problem of non-uniqueness of inversion solution was studied by Tarantola and Valette (1982), Li and Oldenburg (1996; 1998; 2000), Lelievre (2009) and Williams et al. (2009). They concluded that constraints in modelling were necessary as the only solution to non-uniqueness.

In this study, the processing of combined gravity, magnetic, radiometric and limited electromagnetic datasets was undertaken to create a 3D geophysical model. A work flow diagram is presented in Figure 3.1 and outlines the fundamental steps taken in the development of the 3D geophysical model. (The theory of gravity and magnetic methods is presented respectively in Appendices A and B.)

The gravity and magnetic data were accessed as raw data corrected for non-geological effects. The non-geological effects are attributes to the diurnal effect, line effect, topographic effect for

magnetic data, altitude, plateau and latitude, topography, the position of the Sun and Moon effects, and instrumental drift for gravity data. Specific datasets used included:

1. Public domain gravity data provided by M. Jessell of the University of Western Australia. The data were surveyed by ORSTOM (*Office de la Recherché Scientifique et Technique Outre-Mer*) in collaboration with DMA (Defence Mapping Agency) and IGN (*Institut Geographique National*). The gravity data were divided into two surveys (Albouy et al., 1992) with 4 km spacing between station points in Guinea, and 3 km spacing between station points in Mali (Appendix C). The Bouguer anomaly was calculated with the POTSDAM 1930 system for 2.67g/cm^3 densities.

2. Magnetic, radiometric and topography data were sourced by SAGAX Afrique specifically for this project. In Guinea, the data were collected by High-Sense Geophysics Ltd for the *Ministerie des Mines Geologie et de l'Environnement de Guinee* between 1997 and 1998. In Mali, the data were collected by Kevron Pty Ltd for the *Ministere de Mines de l'Energie et de l'Eau* between 2000 and 2001. The line spacing for both surveys was 400m. The survey lines were oriented 135 degree north and 315 degree north, with 80m for the average flight altitude. Tie lines were spaced at 3000m. Radiometric data were also collected at the same time as the magnetic data. Magnetic and radiometric data corrections were completed by FUGRO Airborne Survey Pty Ltd.

3. Geological data obtained from public domain company technical reports, research work, and the SYSMIN project. In Guinea, geological data included geological maps of the Siguiri (Egal et al., 1999a), Sirakoro (Egal et al., 1999b; Costea et al., 1999), Kankan (Feybesse et al., 1999), Falama (Lahondère et al., 1999a; Iliescu et al., 1999) and Faraba 1:200 000 map sheets (Lahondère et al., 1999b) (Figure 1.3). There are no geology technical reports available at the regional scale for Guinea. In Mali, maps included the Kadiolo and Nielle (Kušnir et al., 1986), Massigui (Claessens et al., 1988), and Kadiana and Tingrela 1:200 000 map sheets (Kušnir et al., 1989), and additionally, the Yanfolila, Tienko, Bougouni, Massigui, Tingrela, Nielle, Bamako East and Bamako West 1:200 000 map sheets of Feybesse et al. (2006a) (Figure 1.3). Reports include the geological map of Mali by Girard et al. (1998), geophysical data interpretations of southern Mali by Randgold (2007, 2008), a technical report by Parker and Wilkinson (2011) and a geological map produced by Miller et al. (2013) covering the entire study area (southern Mali and northeast of Guinea).

3.2. Data Constraints

The geological data available for the study area included fact map data such as strike and dip of bedding and cleavage, lineation, absolute geochronological age data, and physical property data. Interpreted data included polygon line data, the trend of structures and bedding, and interpretations of homogeneity within polygons. Interpreted data attributes for many published geological maps and reports were extracted from magnetic and radiometric data; it is thus difficult to use these data

attributes to constrain the inversion modelling. However, fact geological data were extracted to fact geology attribute files when fact data was recorded on maps, or raw fact map files were obtained. The geological data available can thereby be classified into three groups:

1. Qualitative data maps constructed from interpretation of magnetic and radiometric data (with limited fieldwork to constrain the interpretation) included the SIGAfrique map, Miller et al. (2013), and magnetic data interpretations completed by Randgold (2007, 2008). The geological maps by Girard et al. (1998), and Parker and Wilkinson (2011) do not report fact data points and are classified as qualitative because they are effectively interpreted geological maps.
2. Qualitative data based on quantitative field data included maps by Kušnir et al. (1986; 1989) and Claessens et al. (1988), which were based on GPS georeferenced field data sampling points. For example, the European SYSMIN project (i.e., a special European financing facility to development mining) created numerous maps of West Africa, but was based on extensive field data collection and validation. This fact geology data was extracted to fact geology attribute files for input into the inversion modelling. These maps include those by Feybesse et al. (2006a).
3. Quantitative data including physical property data (magnetic susceptibility and density) and lithological and structural datasets measured on the rocks at GPS georeferenced field data sampling points (Figure 3.3).

3.3. Geophysical data processing and attribute extraction

The images created from processed magnetic and gravity raw data points were combined with radiometric grid data from SYSMIN. The gravity data were merged to form one database and resampled. The gravity data included Bouguer anomaly values and free air anomaly values. They were gridded using 1000 m grid cells and 4000 m for blanking distance to fill the gaps. The minimum curvature algorithm in GEOSOFT 6.4® was used to grid the gravity data.

Magnetic data for Mali and Guinea were merged into a single magnetic database covering the entire study area. The geographical coordinates were calculated using GEOSOFT 6.4®, which helped to determine the inclination and declination of each point in the database. The magnetic data were gridded using a minimum curvature algorithm in GEOSOFT 6.4® with 200 m cell size.

Radiometric data for Mali and Guinea were merged into one grid. The potassium, thorium and uranium grids were created by FUGRO Airborne Survey Pty Ltd. They were compared with gravity and magnetic data to confirm similarities of attributes. The attributes correspond to the elements of data that could be identified, classified and qualify as interpreted geological features.

The combined dataset were processed using edge detection filters with WinDisp® version 5.06 and GEOSOFT® version 6.4. Geophysical attributes were extracted after processing to create an attribute map (Figure 4.13). The attributes present at the same time with the magnetic data and gravity data were compared to the radiometric data in order to rank them in different levels of confidence.

Attributes were ranked as high, medium or low confidence (Table 3.1). A high level of confidence was awarded to attributes that occurred on all geophysical datasets with comparison to radiometric data, while a low level of confidence was awarded to attributes that only occurred on one geophysical dataset. Key areas for inversion modelling (Chapter 6) were only selected from regions that presented high confidence level attributes.

***Table 3.1**: Confidence level of structures in the study area.*

Attributes	Magnetic	Gravity	Potassium	Thorium	Uranium	Confidence level
Yanfolila Fault	+		+	+		High
Mandiana- Yanfolila Fault	+		+		+	High
Madina Fault	+		+			Fair
Farako Fault	+		+			Fair
Menankoro Fault	+	+		+	+	High
Kadiolo-Fourou Fault	+			+		Fair
Koumanto- Morila Fault	**+or-**	+			+	Medium
Siguiri Shear Zone	+		**0**			Low
Yanfolia, Shear Zone	+	+	+		+	Very high
Banifing Shear Zone	+	+	+	+	+	Very high
Fatou Shear Zone	+	+	+			Fair
Syama Shear Zone	+	**+ or -**	+	+	**+ or -**	Very high
Kadiolo Shear Zone	+		**0**			Low
Kalana-Kodieran Fold	+	+	+	+	+	Very high
Ouelessebougou Fold	+		+		+	High
Fatou Fold	+		+			Medium
Dykes 1,2,3,4	+					Low
Dykes 5, 6, 7	+					Low
Dykes 8, 9, 10	+					Low
Yanfolila Belt	+	**+ or -**	+			High
Bougouni Belt	+	**+ or -**				Fair
Kolondieba Belt	+					Low

3.4. Extraction of fact geology data

Fact geology data (quantitative data) were extracted from georeferenced geological (raster) maps into attribute layers (Chapter 4). Geological maps were compiled in Maplnfo® 11.0 or ArcGIS® 10.3. Images from reports were imported into GEOSOFT® v 6.4 and georeferenced. All maps and images were georeferenced using WGS84 projection UTM Zone 29N. Extracted fact geological data was imported into GEOSOFT® v 6.4 and is presented in summary in Figure 4.18. The extraction and integration are considered GIS work and are presented in Chapter 4. However, the key areas defined from geophysical attributes extraction constrained the fact geology and were used in inversion

modelling. Thus, high confidence level geophysical attributes were combined with fact geology (and physical property data) for key areas as an input into the inversion modelling.

3.5. Geophysical modelling

Modelling is defined in the broad sense as the model conception. It corresponds with the spatial distribution of main physical properties such as density, magnetic susceptibility and resistivity. This type of modelling depends on the objective and the method used. Modelling can be geometrical, mechanical and kinematic. It proceeds generally by using the available field parameters (fact geology and physical property data) as the constraint.

The modelling is characterized by direct or inverse modelling:-

1. *Direct modelling (forward modelling)* in geophysics involves the calculation of datasets that would occur if the survey were gathered over a known model. It is performed by manually fitting the physical properties until a good fit is found and may include errors. To reduce these errors, a beginning model must be fixed according to the available physical properties. Forward modelling is controlled by the interpreter and supported by geological information that reduces the errors considerably. In this study, the magnetic field in nT (nano Tesla) was computed using the magnetic susceptibility; the gravity response in milligal was computed from the density values. In WinDisp® it is possible to simultaneously compute gravity and magnetic fields from the drawn polygon. All distances were reported in meters, density in g/cm^3 and magnetic susceptibility in $SI.10^6$.
2. *Inverse modelling* is the process of inverse calculation from a set of causal factors that produced the data result. It attempts to determine a model that could give rise to observed effects (Scales et al., 2001). It is also called inversion (Sheriff, 2001). Inversion is effectively a mathematical problem that involves the creation of an algorithm. It includes the misfit function and objective function. The result is calculated through a process of iteration.

The algorithm requires the introduction of the field parameters (fact geology and physical property data) that control the accuracy of the result. The main problem with this type of modelling is that it depends on the input, i.e., quantitative field data, or quantitative data. In this study, quantitative field parameters were used as the input because quantitative field data is limited for the study area, as stated previously. The schematic in Figure 3.3 outlines the framework of interaction between forward and inverse modelling.

The forward modelling was performed in key areas (Section 5.2). Geological data were used to construct the model and calculate the geophysical responses of the model. Physical properties used were taken from the handbook by Telford et al. (1990) and Kearey et al. (2009) as presented in Table 3.2, taking into account the geology of the study area (Table 3.3) from WAXI (2013). However, it must be noted that geophysical modelling is limited by factors such as data quality, the

integration of parameters into the modelling, and the use of simple geological features in the modelling process.

Table 3.2: *The densities and magnetic susceptibility of certain rocks and minerals modified after Telford et al. (1990) and Kearey et al. (2009).*

Lithology	**Magnetic susceptibility**				**Density**		
	cgs	**microcgs**	**SI**		**cgs**	**microcgs**	**SI**
Basic igneous	0.002596	2.596	0.0326		2.79	2790	2790
Acid Igneous	0.000647	0.647	0.00813		2.74	2740	2740
Peridotite	0.01194479	11.9447853	0.15		3.15		
Pyroxenite	0.00994772	9.94772448	0.125				
Gabbro	0.00557423	5.57423313	0.07		3.03		
Basalt	0.00557073	5.57072571	0.07		2.99		
Diabase	0.00437975	4.3797546	0.055		2.9		
Diorite	0.00676871	6.76871166	0.085		2.85		
Quartz diorite					2.79		
Porphyry	0.00477791	4.77791411	0.06		2.74		
Granodiorite					2.73		
Granite	0.00019908	0.19907975	0.0025		2.64		
Andesite	0.0127411	12.7411043	0.16		2.61		
Dolerite			0.014		2.9		
Rhyolite			0.0002-0.03				
Syenite					2.7		
Metamorphic	0.000349	0.349	0.00439		2.74	2740	2740
Eclogite					3.37		
Amphibolite			0.0007		2.96		
Gneiss			0.02		2.8		
Graywacke					2.65		
Schists			0.0014		2.64		
Phyllite			0.0015				
Quartzite			0.004		2.6		
Dolomite	0.000008	0.008	0.0001		2.32	2320	2320
Limestone	0.000023	0.023	0.00028		2.42	2420	2420
Shale	0.000052	0.052	0.00065		2.61	2610	2610
Sandstone	0.000032	0.032	0.0004		2.54	2520	2520
Limonite			0.0025		3.78		
Ilmenite			1.8		4.67		
Pyrolusite					4.82		
Magnetite			6		5.12		
Hematite			0.0065		5.18		
Chalcopyrite			0.0004		4.2		
Pyrite			0.0015		5		
Arsenopyrite			0.003		6.1		
Non-metallic minerals							
Orthoclase					2.55		
Quartz			-0.00001		2.65		
Calcite					2.65		

Table 3.3: *The georeferenced coordinate of petrophysical data point measured in the study area rocks (Modified after WAXI, 2013).*

Location	y_proj	x_proj	Rock Description	Susceptibility (10^{-3} SI)	Density (g/cc)
SW Mali	1241896	591492	Sediment - coarse grained.	0.354	
SW Mali	1239500	589599	Sediment	0.161	
SW Mali	1232964	593764	Sediment. Interbedded. Bedding cut my later fabric. Large biotite clots observed to cut fabric and trend 020. Orientated sample.	0.206	
SW Mali	1232840	593817	Coarse sand/gravel bed. Sediment. Way up structures in sediments (erosional base, grading) indicate younging to east.	0.215	
SW Mali	1232618	593861	Folded sediment - sand - shale interbeds	0.604	
SW Mali	1232738	593905	Pillow Basalt. Pillows indicate younging to the east. remains true.	0.692	
SW Mali	1234714	571042	Coarse Qtz-Plag-Musc Granite	0.02	
SW Mali	1240387	573296	Granite	0.06	
SW Mali	1246110	574131	Diallo Granite	0.07	2.636
SW Mali	1246498	574904	Money Granite	0.03	2.634
SW Mali	1247095	615219	Granite. Plag-qtz-bt. Equigranular.	0.046	2.629
SW Mali	1245815	621681	Granite. Fairly weathered.	0.255	
SW Mali	1237520	633983	Granodiorite. Plag-Bt-amph. Xenoliths of mafic. Magmatic texture. Magma mixing. Some Sed xenoliths.	0.157	2.702
SW Mali	1261682	562320	Dacite?		2.71
SW Mali	1261818	562425	Fine grained intermediate intrusive		2.67
SW Mali	1262743	563828	Dacite?	0.219	2.764
SW Mali	1263363	567988	Feldspathic Sand	0.21	2.732
SW Mali	1259651	568660	Ryolite?		2.739
SW Mali	1262668	569318	Polymictic Conglomerate		2.696
SW Mali	1263388	569336	Polymictic Conglomerate	11.61	2.57
SW Mali	1263395	569393	Polymictic Conglomerate	14.32	2.812
SW Mali	1263286	570820	Diorite	0.25	2.731
SW Mali	1163629	708357	Orthogranite. Sediment and mafic xenoliths. 2-10mm plag phenos. Ghost clasts. Slightly banded in places. Alignment of clasts.	0.072	2.686
SW Mali	1158585	712621	Orthogneiss. Very deformed. With xenoliths. Folded pegmatite and qtz veins.	1.326	
SW Mali	1158152	713753		3.35	2.613
SW Mali	1230904	735601	Pegmatite. Massive fspar. Lithium bearing? 5m wide. Have 040 fabrics 080 strike.	0.443	2.628
SW Mali	1230990	735840	Feldspathic sand. 1-3mm g.s. Relatively undeformed.	0.149	
SW Mali	1230529	737436	Equigranular Int	0.09	
SW Mali	1230529	737436	Equigranular Int	0.09	
SW Mali	1230529	737436	Equigranular Int	0.014	
SW Mali	1230529	737436	Gneiss	0.139	
SW Mali	1230529	737436	Equigranular Int	0.094	2.675
SW Mali	1230529	737436	Gneiss	0.165	2.693
SW Mali	1228908	738783	Gneiss-granitoid	0.075	2.639
SW Mali	1241487	740272	Gneissic granitoid	0.149	2.697
SW Mali	1241487	740272	Gneissic granitoid	0.145	2.697
SW Mali	1253142	747696	Diorite-granodiorite	0.874	2.729
SW Mali	1251367	748898	Granodiorite	0.009	2.624
SW Mali	1263719	754193	Andesite. Strong fabric. Strung out texture. Bt growths within fabric.	18.694	
SW Mali	1266814	764430	Gastro River - Very large outcrop in the river. Highly metamorphosed sediment. Bt-Musc. Steep folds. Sheath folds (cm scale). Very strong fabric.	0.185	

3.6. Geophysical inversion

Geophysical inversion is an iterative mathematical procedure that can take several forms. The inversion can be carried out using field parameters (fact geology and physical property data), and inversion algorithms that represent the basic tools for inversion (Telford et al., 1990). The outcome is the model. In this study, the inversion algorithm used is the code developed by UBC-GIF (Appendix D) with the MGinv3D as utility in the WinDisp® software. However, the model is limited by the inherent problem of non-uniqueness of solution. According to Gauss's law, two factors can explain the non-uniqueness of a model: -

1. A surface for which the potential field values are known (in this case gravity and magnetic) are not unique because there can be other bodies inside of this surface that have the same response of the potential field corresponding to those of the surface as a whole, e.g., two rock types that give the same potential field response.
2. Potentials field data are finite values that are not unique to the surface physical properties.

To minimize the non-uniqueness of inversion, algorithms must use the input of physical properties measured directly from the field samples if possible or other information know for the area of study.

The area of inversion can be divided into a number of cells of defined size and physical property in the case of UBC-GIF (Li and Oldenburg, 1996). However inversion algorithms must always address three fundamental questions as stated by Scales et al. (2001):

1. What is the degree of accuracy of the input data?
2. How accurately can we model the response of the system?
3. What are the known parameters of the system independent of measured input data?

In this study the steps that have been followed for inversion include:

1. Determination of the inversion area for first-order geophysical attributes, in particular key zones where constraints are applied because more details on geophysical attributes should be completed to explain the architecture of the study area.
2. Smoothing of gravity and magnetic data using the mean filter of GEOSOFT® with five points in the window for magnetic data, and two points in the window for gravity data.
3. Preparation of the input file for the inversion using WinDisp® with inversion cell size X=150 m, Y=200 m and Z = 50 m on 5 km down for maximum depth. These dimensions were selected for definition according to the survey point spacing because they allow a good resolution in 3 dimensions (X, Y and Z).
4. Execution of an inversion process using default parameters with MGinv3D (3 dimensions magnetic/gravity) utility of WinDisp®.

5. The solution space was constrained using the field parameters (fact geology and physical property data) through the reference model for fact geological data and bound models for petrophysical data (Appendix E gives a comparison between unconstraint inversion and constraint inversion with the bound model for the study area). The reference model function is incorporated to the inversion through the objective function taking into account the depth weighting function, which is equal to 1 for these inversions. The bound model is calculated by using Fuzzy C means objective function for k=4 rock types.
6. Presentation of the results of the inversion model and commentary about the accuracy within the solution space.

3.7. Data and image processing techniques

Data and image processing techniques are used in potential field studies to enhance the detection of subtle features that cannot be identified on gravity and magnetic maps. They allow the extraction of the maximum information from geophysical data by transforming values into profiles, contours and grids (Milligan and Gunn, 1997). Image processing techniques are derived from mathematical and physical principles for geophysical data and are used to highlight geophysical features or remove the unwanted information (noise) in the data to improve the signal-to-noise ratio (SNR). Prior to the application of the image processing techniques, the geophysical data are conditioned or smoothed through gridding and the SNR is consequently increased by applying different filtering methods (Milligan and Gunn, 1997). A gridding method is itself usually a smoothing filter; it uses different mathematical algorithms (e.g., curvature, inverse distance, and more) to transform the data into seamless and continuous images. Image processing techniques are applied in order to produce more explicit information from gridded potential field anomaly maps (Mickus, 2008).

Image processing filters commonly used in potential field data can be categorized into two groups of operators according to Milligan and Gunn (1997), namely:

1. *Linear filters,* which are defined as the weighted average calculation of the neighbouring data points. These filters obey the principle of superposition and homogenization. The filters general apply to grid and profile processing. The filters depend on the separation distance and the relation between the nearest data points.
2. *Non-linear filters;* Non-linear filters compute the average of the amplitudes of the potential field at the sample positions within a specific window and remove high frequency background noise. In contrast to linear filters, they do not meet the principles of superposition and homogeneity. They are applied in both one and two dimensional studies.

The objective of using image processing filters in this study was to suppress any fluctuation, coherent or incoherent noise that is present in conventional maps such as total magnetic field and gravimetric

data, or to remove noise introduced during field acquisition and initial field processing workflow. These were computed to enhance detection of signals that correspond to specific gravity and magnetic anomalies. The data processing filters implemented in this study were the upward continuation, vertical derivative (vertical gradient), analytic signal, reduction to the pole, tilt angle, Hanning filter, mean filter and automatic gain control (AGC). Colour shading was used to display certain grids in order to strongly highlight geological features on these images.

It is evident that using the filters on the whole image is sometimes not desirable in terms of computer capacity and image width. Consequently it is better to apply filters to a small zone before applying to the whole image. Hence, fives (5) zones were selected across the study area to apply filters before using them on the whole study area grid.

3.7.1. Vertical continuation

The vertical continuation is used to calculate the potential field at some altitude or depth from the plane on which the gravity or magnetic anomaly is measured. It eliminates or enhances a range of wavelengths. The distance of vertical continuation depends on the range of wavelengths to be removed or enhanced. Vertical continuation includes:

1. The upward-continuation defined by Gilbert and Galdeano (1985) as a low pass filter. It enhances low frequency components of the data at the expense of high frequency attenuation. Upward continuation is used to smooth out near surface effects and to tie aeromagnetic surveys flown at different heights (Sheriff, 2001).
   Mathematically, the filter can be described as shown by Gilbert and Galdeano (1985) and Telford et al. (1990) in Equation 3.1.

$$A_z(u,v) = A_0(u,v)e^{-kz} \qquad (Equation\ 3.1)$$

   where **k** is the wavenumber, **z** is the continuation height, u, v are the wavenumber coordinates. $A_z(u,v)$ corresponds to the upward continuation (or downward continuation) of the magnetic field. $A_0(u,v)$ corresponds to the magnetic field to be transformed in wavenumber coordinate.

   The effect of upward-continuation is shown in Figure 3.4. Short wavelengths mostly correspond to shallow sources, while long wavelengths usually result from deeply buried sources as shown in the gravity map presented in Figure 3.5. The upward-continuation filter was therefore used to remove shallow or near surface effects such as ferricrete, which can exceed 50m in thickness, thereby enhancing deeper features (Figure 3.4).

2. The downward continuation filter increases the spatial resolution of the potential field data through computation of the magnetic and gravitational fields, with the measurements taken closer to the anomalous source. It enhances detection of shallow structures. This filter should be applied with caution because it is not only the anomalies that are enhanced, but the high frequency noise as well; it is highly dependent on the data quality and sample spacing (Milligan and Gunn, 1997). The mathematical formula for downward continuation is given by Gilbert and Galdeano (1985);

$$A_z(u,v) = A_0(u,v)e^{kz} \qquad (Equation\ 3.2)$$

where **k** is the wavenumber, **z** is the continuation height; u, v correspond to the wavenumber coordinate.

3.7.2. Vertical derivative

Vertical derivative filters are defined as the vertical rate of change in the potential field data. The vertical derivative formula is expressed in the space domain using gravity data by Equation 3.3 (Telford et al., 1990).

$$\frac{\partial g_z}{\partial z} = -\gamma\rho \iiint_{zyx} \left(\frac{1}{r^3} - 3\frac{z^2}{r^5}\right) dxdydz \qquad (Equation\ 3.3)$$

where γ is the universal gravitational constant; ρ is the density, r is the distance to source, z is the value of the vertical axis.

These derivatives are often used in potential field studies to enhance shallow geological features and sharpen edges. This filter is useful for delineating linear and elongated features. The vertical derivative maps, shown in Figure 3.6, clearly show smaller and sharper anomalies than those shown in the total field intensity maps. This is due to its responsiveness to local influences compared to regional effects. The inverse of the vertical derivative is simply the vertical integration of the field. However, the derivative filter becomes very sensitive to noise especially the line-levelling errors (Figure 3.7). In simple terms, the higher the derivative order, the more details are enhanced. Therefore, care must be taken when these filters are applied to the data.

3.7.3. Analytic Signal Amplitude

The amplitude of the analytic signal is defined as the total gradient. It is independent of the direction of magnetization, and represents the envelope of amplitude of both the vertical and horizontal derivatives. This implies that the amplitude of the analytic signal computed for the total

magnetic field provides maxima over magnetic contacts regardless of the magnetisation direction. When computed for the vertical integral of the magnetic field, it becomes similar to the strength of the magnetization. In the case of three dimensions, the amplitude of the analytic signal has been defined by Macleod et al. (1993) as follows;

$$|A(x,y)| = \sqrt{\left(\frac{DM}{dx}\right)^2 + \left(\frac{DM}{dy}\right)^2 + \left(\frac{DM}{dx}\right)^2} \qquad (Equation\ 3.4)$$

where A is the analytical signal amplitude, M the magnetic intensity.

Equation 3.4 explains the absolute positivity of A that is not affected by the direction of the magnetic field inclination and declination. This filter can delineate circular features such as intrusions (Figure 3.8). Its effectiveness involves the location of all bodies of the same geometry with the analytic signal map (Milligan and Gunn, 1997).

3.7.4. The vertical integral applied on the analytic signal

Vertical integration can be applied to the analytic signal to generate a transformed grid with the same units as the total magnetic field, but the effects of induced and remnant magnetization are almost the same (WinDisp®, 2012). The equation of the vertical integral is presented in Equation 3.5 (WinDisp®, 2012).

$$f(r,s) = \frac{1}{2\pi\sqrt{r^2 + s^2}} \qquad (Equation\ 3.5)$$

The letter r and s correspond to the coordinate frequencies; $f(r,s)$ is the output.

The application of the vertical integral of the analytic signal enhances detection of circular features. This smoothing operator also optimizes delineation of lithological boundaries, volcanic belts, shear zones and faults when compared to the total magnetic field and analytic signal (Figures 3.9, 3.10). The resulting image is characterised by high signal-to-noise compared to the amplitude of the analytical signal (Figure 3.10). It is, however, important to always use the filters in combination to achieve a better resolution of the analytic signal.

This filter was applied only on the magnetic data to enhance the detection of the main features and the relationship between the main features. The resulting map also shows dykes and other geological features such as shear zones and faults, which can help to understand and constrain the structural history of the area.

3.7.5. Tilt Angle Filter

Tilt Angle is a phase based filter that measures the local phase (correspondence between causative body and anomaly at a specific point) of the potential field data over images. It is mathematically defined as a ratio of the vertical derivative to absolute amplitude of the total horizontal derivative. This filter produces positive phase values when computed over the causative body, zero near body edges and negative outside the body. This filter has advantages over the vertical derivative (Figure 3.11) because of its simple interpretative properties. It shows the positive potential field upon the anomaly source and negative potential field elsewhere (Cooper, 2007). It is expressed by Equation 3.6 of Miller and Singh (2005):

$$T = \tan^{-1}\left(\frac{\frac{\partial f}{\partial z}}{\sqrt{\left(\frac{\partial f}{\partial x}\right)^2 + \left(\frac{\partial f}{\partial y}\right)^2}}\right) \qquad (Equation\ 3.6)$$

with f considered as the potential field response.

In this study, the tilt angle was used for magnetic (Figure 3.12) and gravity data to highlight linear structures. When comparing this filter to the first derivative map, it is superior because it produces detailed information for both deep and shallow structures. It appears sharper for gravity data than magnetic data due to the level of noise in the magnetic data. The tilt angle map for the gravity data highlights linear features that are not well detected by first derivative filters computed for the same data (Figure 3.13).

3.7.6. Automatic gain control

The automatic gain control filter is used to enhance the amplitude of low amplitude anomalies without diminishing the high amplitude anomalies (Rajagopalan and Milligan, 1995). The automatic gain control enables transformation of the input waveform (multiple amplitudes) into constant (semi constant) amplitudes. It balances the grid amplitudes. The choice of the window size (number of points) plays a role in the quality of the final images (Cooper, 2007).

This filter was used on the gravity and magnetic data to highlight particular linear and circular features (Figure 3.14) and confirm their continuity. Directional continuities of certain features were not clear using the automatic gain control. The automatic gain control is defined by Rajagopalan and Milligan (1995) as;

$$A_{xy} = (Gain_{xy})(f_{xy}) \qquad (Equation\ 3.7)$$

$$Gain_{xy} = \frac{1}{(2v+1)(2w+1)}\left[\sum_{i=x-v}^{i=y+v} \sum_{i=x-w}^{i=x+w} F_{ij}^{P}\right]^{r}$$

where A_{xy} is the data after the automatic gain control operation; f_{xy} corresponds to the data to be analysed by automatic gain control. P is the power and r is the root. The term $\frac{1}{(2v+1)(2w+1)}$ is equal to the size of window.

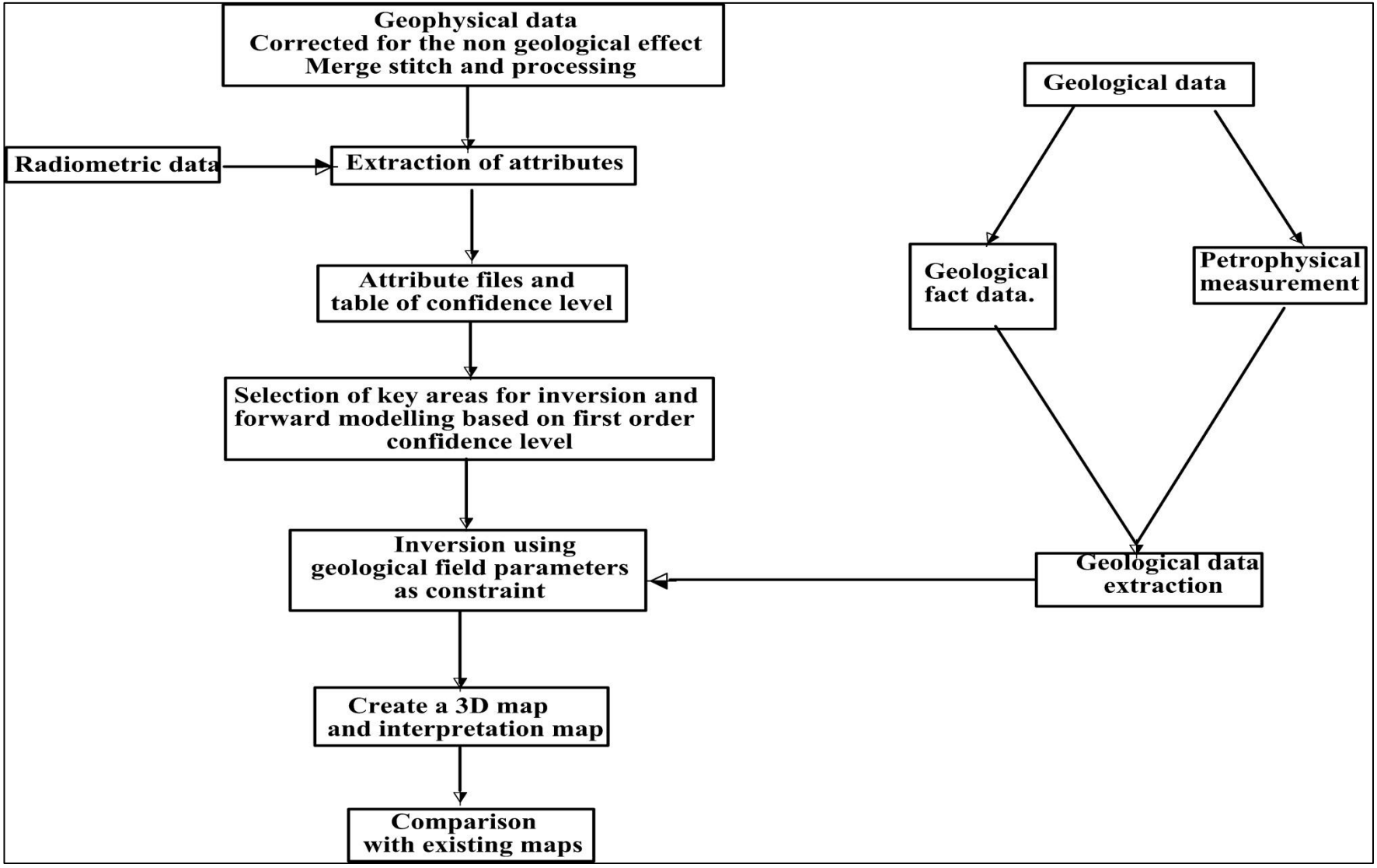

***Figure 3.1**: The methodology workflow diagram outlining the fundamental steps taken in the development of the 3D geophysical modelling in this study.*

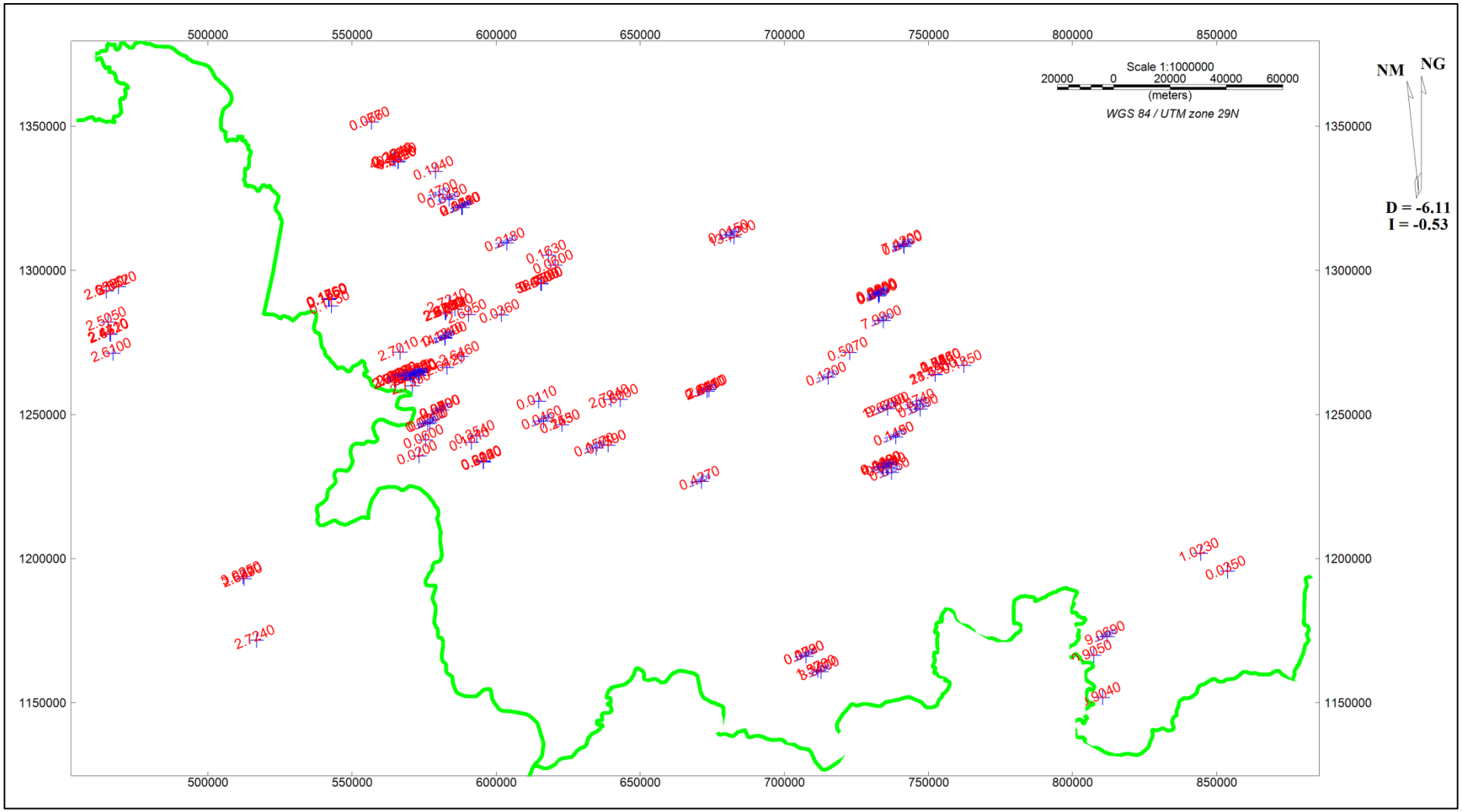

***Figure 3.2**: The georeferenced coordinates of petrophysical data; red for magnetic susceptibility and blue for density. The green line marks the international borders between Mali, Guinea to the west, and the Ivory Coast to the south.*

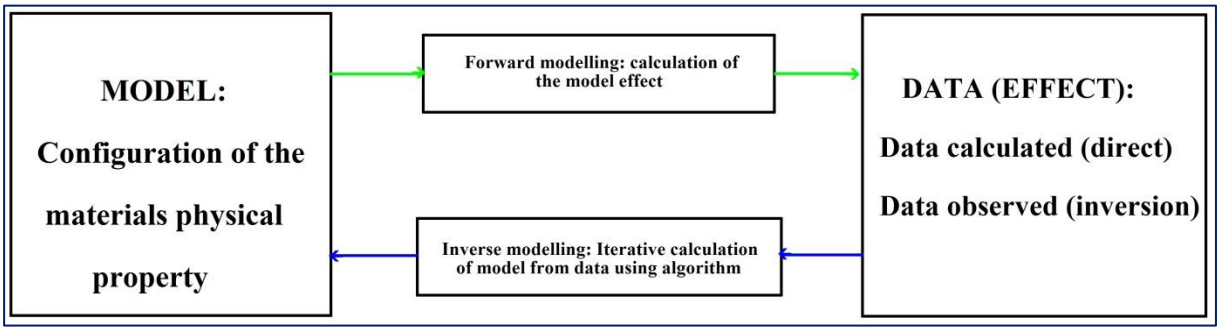

Figure 3.3: *The framework schema outlining the interaction between forward and inverse modelling.*

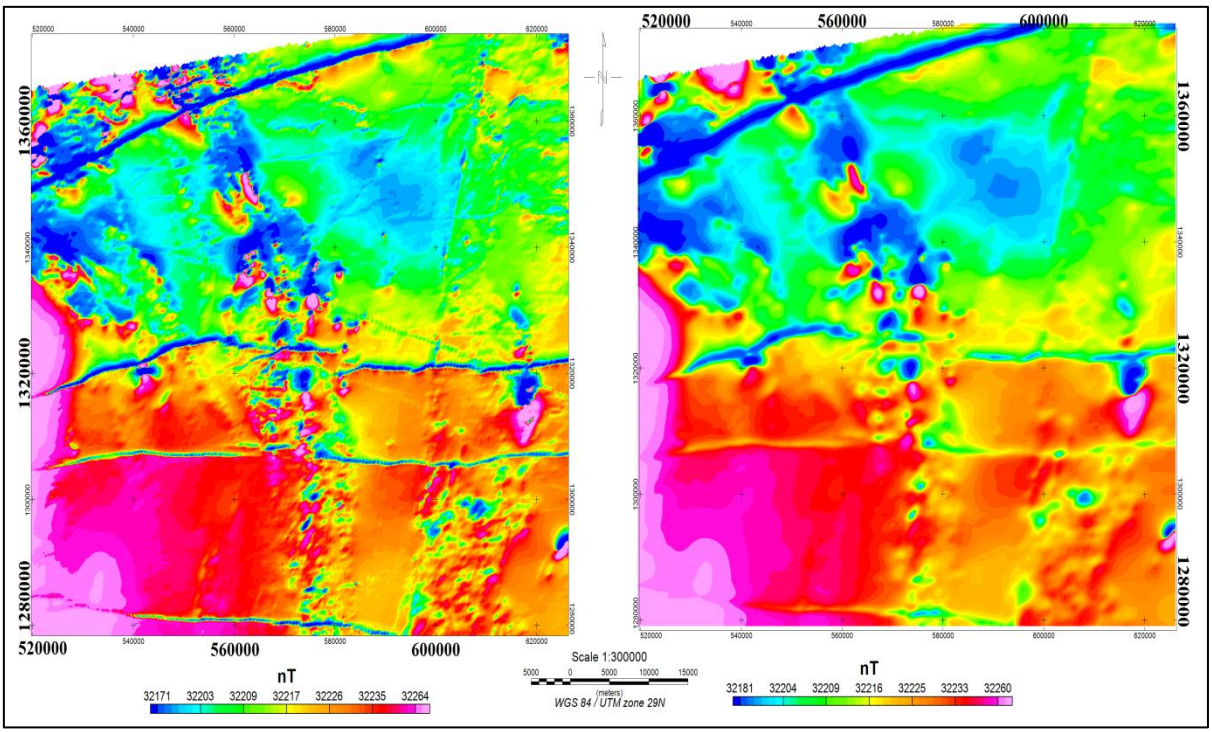

***Figure 3.4**: The total magnetic field map (left) compared to the upward continuation at 500m (right). Certain wavelengths of the total magnetic field are eliminated as shown with the upward continuation.*

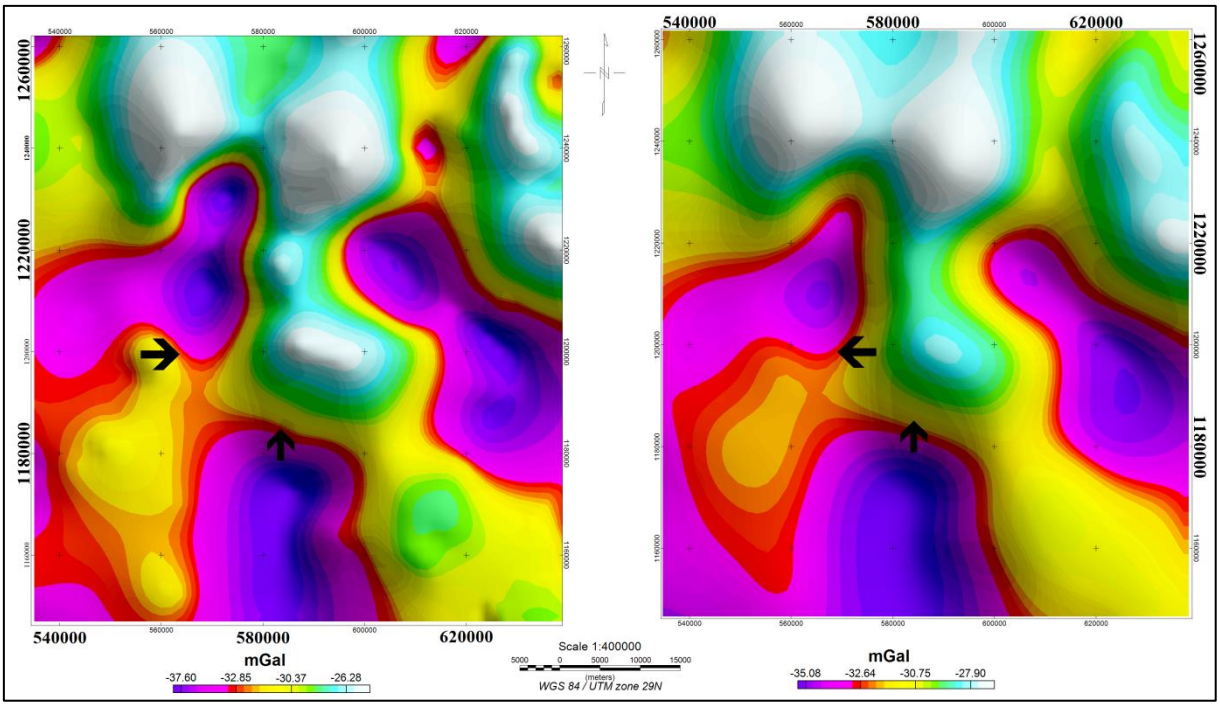

***Figure 3.5**: The Bouguer anomaly map (left) compared with the upward continuation at 1000m (right).*

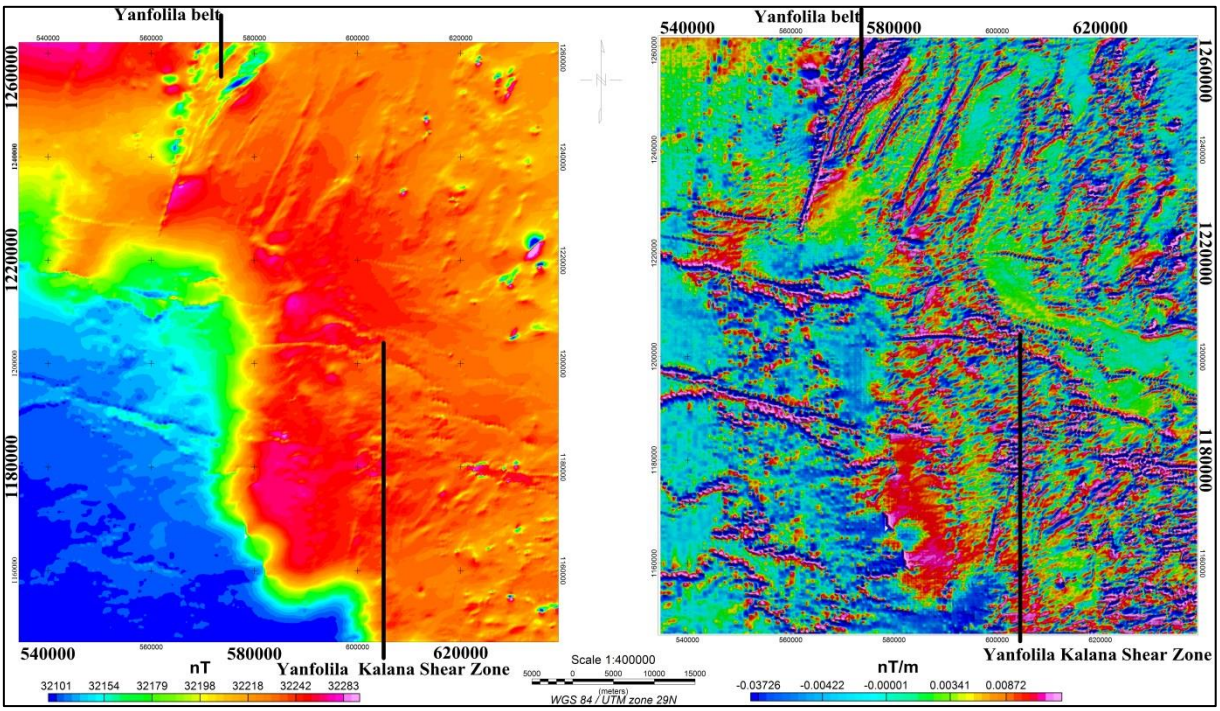

***Figure 3.6**: The total magnetic field (left) compared to the first derivative map (right). The Yanfolila-Kalana shear zone is clearly evident in the first derivative map but invisible in the total magnetic field map.*

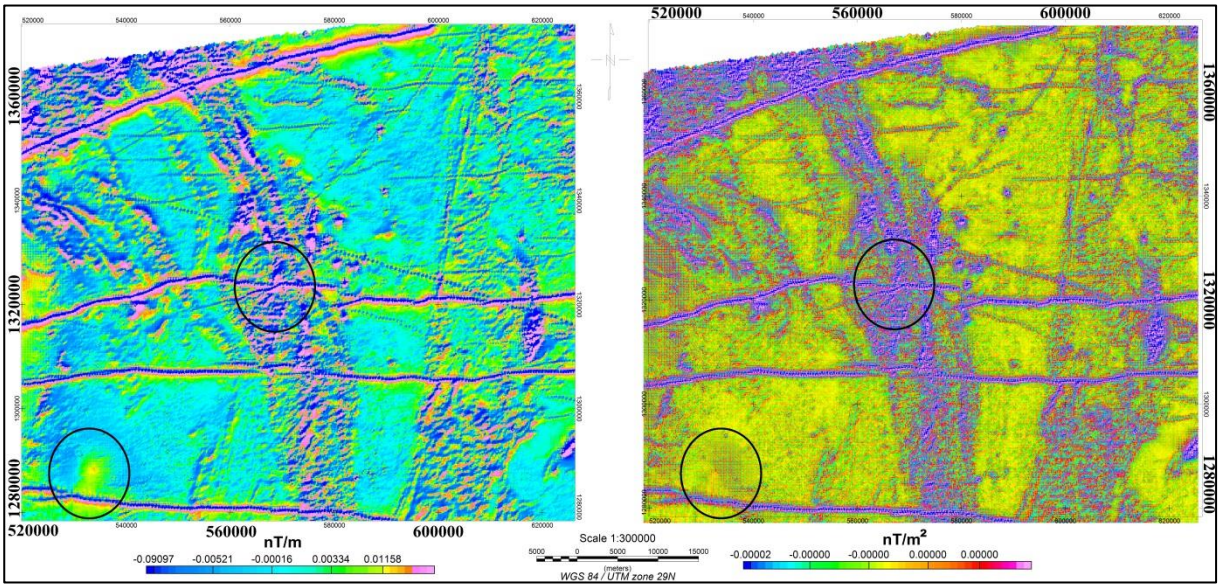

***Figure 3.7**: The first derivative map (left) compared with the second derivative map (right). The black circles highlight that the more the derivative is applied, the more noise increases.*

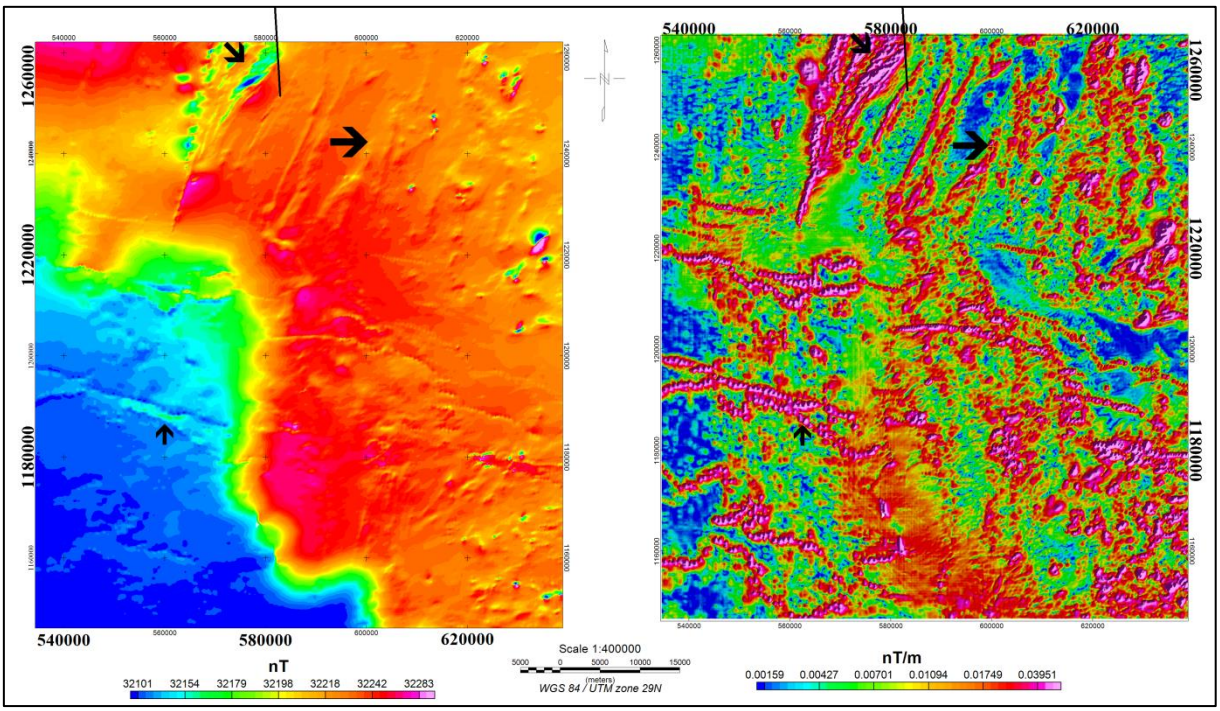

***Figure 3.8**: Analytic signal map to the right, and the total magnetic field to the left. The Yanfolila belt, folds and dykes present well in the analytic signal relative to the total magnetic field.*

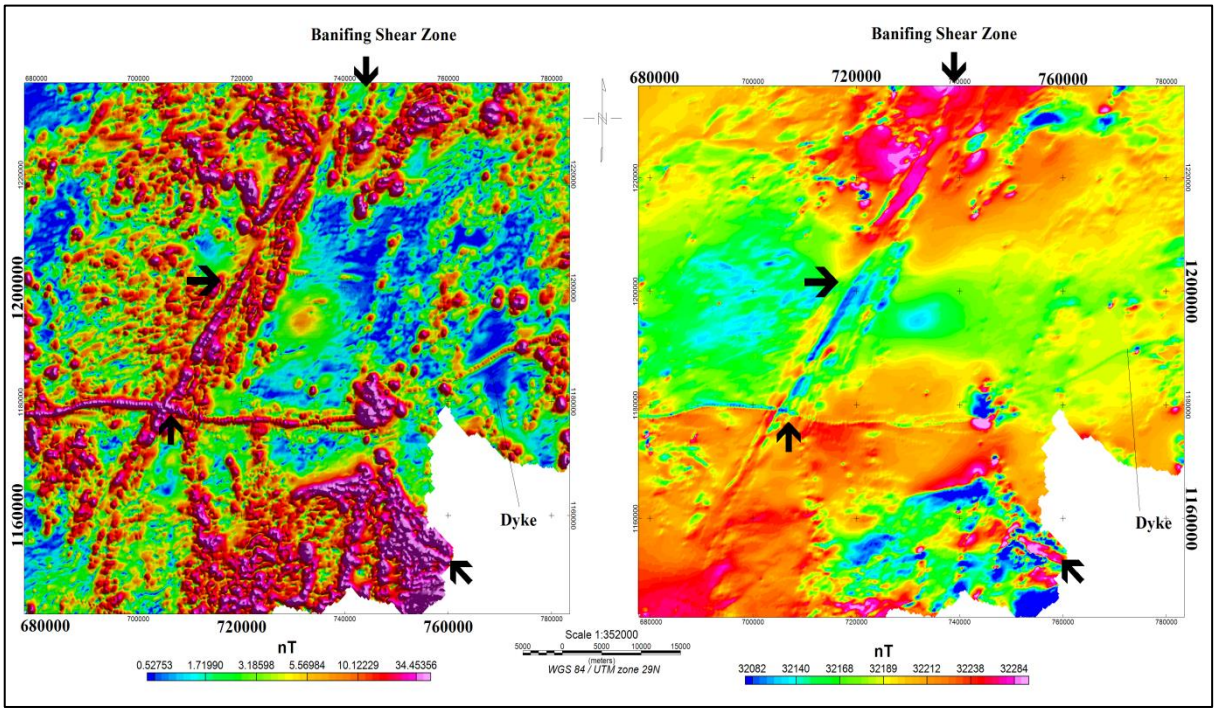

***Figure 3.9**: The vertical integral of the analytic signal map of the Banifing shear zone to the left compared to the total magnetic field to the right. The arrows mark points of comparison.*

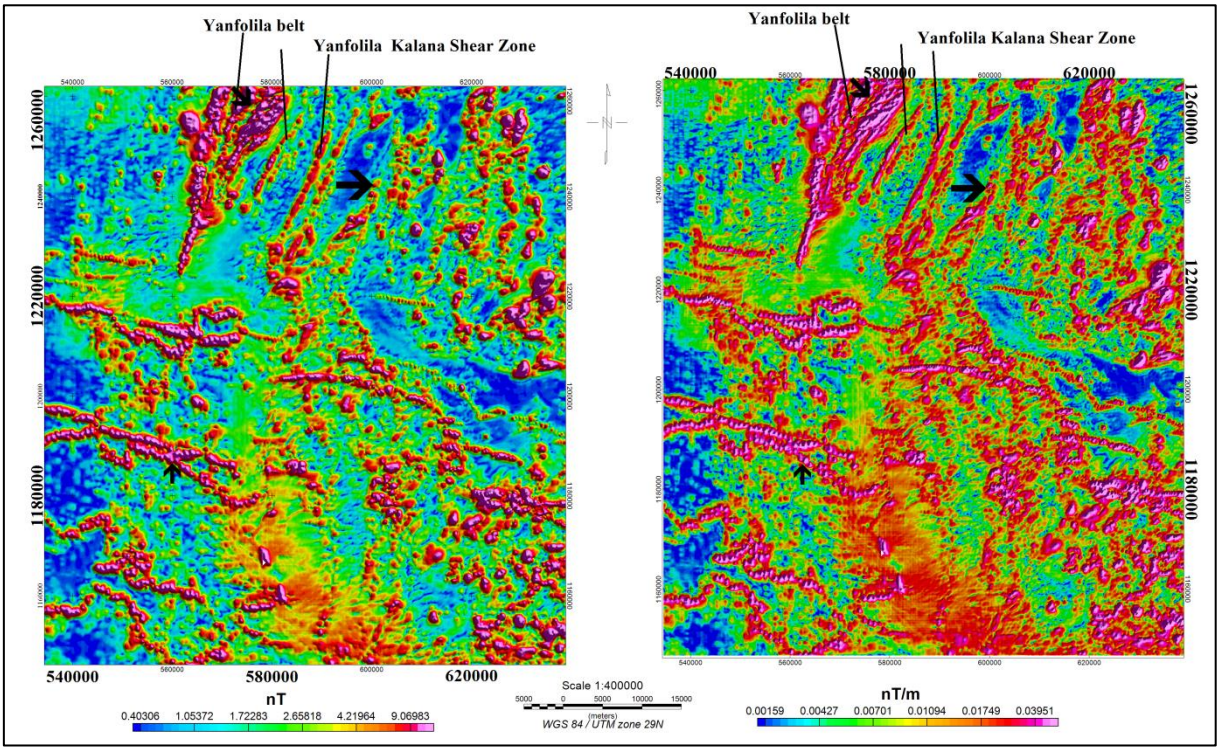

Figure 3.10*: A map of the vertical integral applied of the analytic signal to the left for the Yanfolia region, compared to the analytic signal to the right. The Yanfolila belt and Yanfolila shear zone are compared in the two images.*

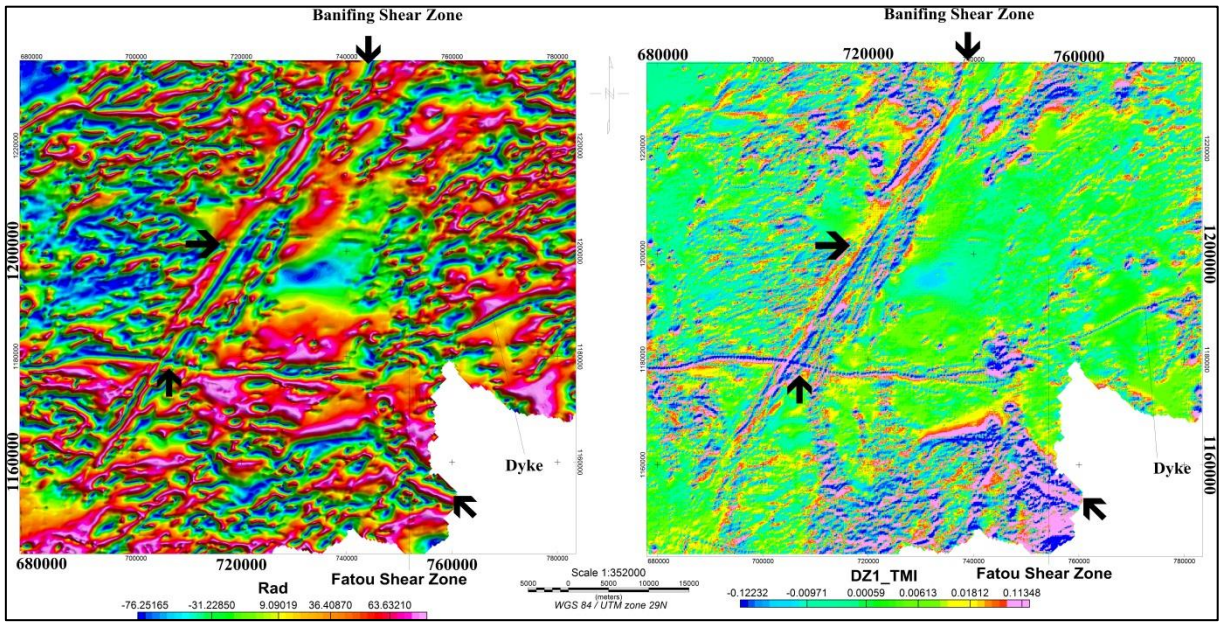

Figure 3.11*: The tilt angle of the total magnetic field of the Banifing shear zone to the left compared to the first derivative of the total magnetic field image to the right. The arcuate Fatou Shear Zone in the southeast is easy to resolve on the tilt angle image than with first derivative image.*

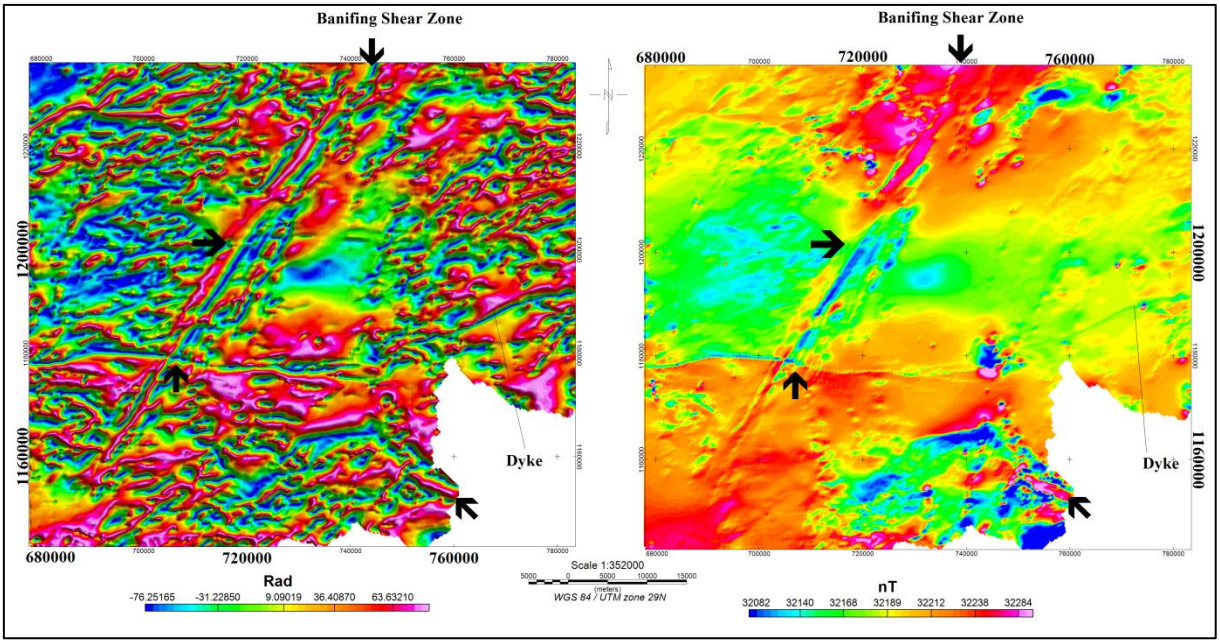

***Figure 3.12**: The tilt angle of the total magnetic field of the Banifing shear zone to the left compared to total magnetic field image to the right. The portion of Banifing Shear Zone is well defined in the tilt angle map. Also the crosscutting relationship between east-west trending dykes and the Banifing Shear Zone become easy to resolve with tilt angle filter.*

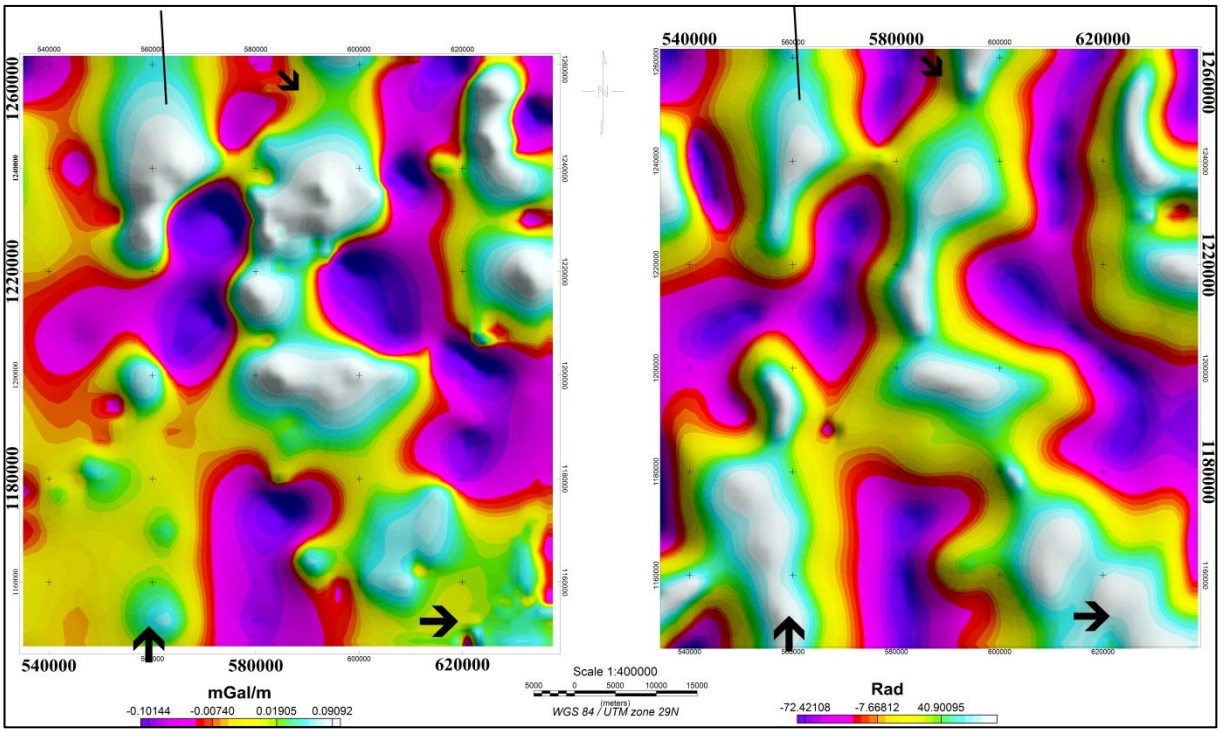

***Figure 3.13**: The first derivative of Bouguer anomaly image to the left compared to the tilt angle of the Bouguer anomaly to the right. The black arrows of the figures show the different comparison point and the usefulness of the tilt angle against first derivative with gravity data.*

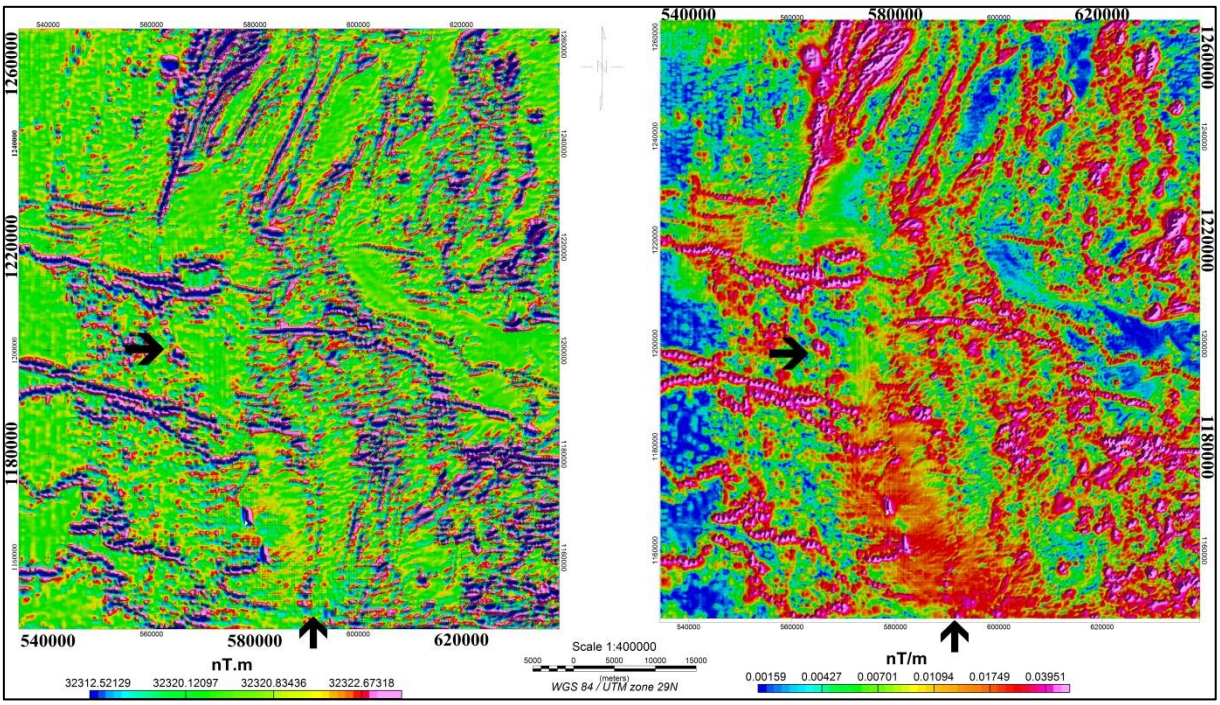

Figure 3.14*: The Automatic Gain Control map of the total magnetic field for the Yanfolila-Kalana region to the left, compared to the analytic signal of total magnetic field to the right. The horizontal arrow shows the continuity of a lineament at the bottom of Yanfolila belt which is not clear with analytical signal. The vertical arrow highlights the intersection between Yanfolila Kalana Shear Zone and an east-west trending dykes. This intersection was enhanced by using the AGC.*

4.0. GEOPHYSICAL ATTRIBUTES AND GEOLOGICAL FACT DATA EXTRACTION

Attributes were extracted from each geophysical image used including (1) upward continuation, (2) first vertical derivative, (3) analytic signal, (4) vertical integral applied on analytic signal, (5) tilt angle and automatic gain control applied on the magnetic field (Figure 4.1) and (6) Bouguer anomaly (Figure 4.2). The objective of this chapter is to validate the presence of certain structures, to identify and localise new attributes (if they exist) using magnetic and gravity data, and constrain these attributes using fact geological data. The need to validate attributes geophyscially is because there are few published geological articles for the study area. The attributes identified in these images were combined to establish a confidence level table (Table 3.1). Fact information was also extracted from geological interpretation and fact maps of Claessens et al. (1998) and Feybesse et al. (2006a). Key areas were selected using the confidence level, and petrophysical data, as discussed in Chapter 3.

4.1. Attribute extraction from geophysical maps

Using the qualitative interpretation principles of Parasnis (1996), and also the pre-existing maps of the study area, attributes can be extracted from geophysical data. Thus, the principle of qualitative interpretation can be applied to attribute extraction methodologies.

In accordance with Parasnis (1996), the first attributes that can be readily extracted from geophysical maps using the shape of anomalies includes:

- Circular attributes or attributes with similar geometries. These types of attributes are generally interpreted as a granitic or basic intrusions, and domes.
- Long narrow attributes or lineaments are generally interpreted as dykes, shear zones, and/or the axial trace of folds.
- Offset of attributes, where a displacement can be observed along the trend of the geophysical anomaly. These types of attributes are generally interpreted as faults or shears.
- Extensive anomalies with no regular pattern, but where the attributes can be delimited. These attributes can be interpreted as basaltic flows, large gabbro intrusive bodies and/or volcanic rocks, or volcano-sedimentary belts.
- Geophysical 'transparent' values with little relief and without distinctive shape(s). These types of attributes are often interpreted as quartzite rock formations, felsic intrusions and/or limestone.

In addition, previous geological interpretations based on field data can be used to classify and name geophysical attributes. The study area is located at a low magnetic latitude, which makes the interpretation of magnetic data difficult due to the inclination of the field. The application of the

reduction to the pole filter can create distortion of the anomalies, which becomes harsh at the inclination less than 20° (Wijns et al., 1997).

According to the inclination and declination of the study area, all the magnetic maps presented are interpreted as; (1) high magnetic intensity indicating the presence of low magnetic mineral content, and (2) low magnetic intensity corresponding to a high magnetic mineral content. This excludes the analytic signal map and vertical integral of analytic signal map.

4.1.1. Upward continuation

The map of the upward continuation of total magnetic intensity (TMI) allowed for the effective removal of the ferricrete layer (which unconformably overlies the Baoulé-Mossi domain) because the ferricrete has a moderate to high magnetic response and can be more than 50m in thickness. The effectiveness of the upward continuation filter (Section 3.7.1) was tested on the potential field data to smooth the grid. The results were compared to the original gridded data for both magnetic at 500 m (Figure 4.1) and gravity maps continuation level (500, 1000 and 3000m) maps (Figure 4.2). Generally, in all zones, the upward continuation algorithm tends to suppress subtle features at the expense of longer wavelength anomalies. Furthermore, the results illustrate that upward continuation up to 500m is more superior to conventional gridding methods in terms of highlighting deep magnetic and gravity anomalies.

The effective removal of the ferricrete allowed the identification of northeast to north-northeast trending lineaments that are approximately 155 km long, and east-west trending first-order scale lineaments that are approximately 270 km long (Figure 4.3). Northeast to north-northeast trending first-order scale lineaments in the west and east of the study area were interpreted as the Yanfolila-Kalana Shear Zone and Banifing Shear Zone, respectively, and are coincident with shear zones mapped at surface. East-west trending lineaments were interpreted as mafic dykes. The identification of these lineaments on the upward continuation map indicates that the structures extend at depth.

A homogenous zone of low magnetic intensity in Figure 4.3 occurs in the southwest of the study area. The area of low magnetic intensity indicates the presence of highly magnetic minerals. A homogenous zone of moderate magnetic intensity in green is located to the northeast and east of the study area. A heterogeneous zone of high magnetic intensity is located between these zones and indicates a region of low and variable magnetic mineral content. A homogenous zone of high magnetic intensity (low magnetic mineral content) is located to the northwest of the study area (Figure 4.3). The study area is thus characterised by a heterogeneous distribution in magnetic minerals.

The Bouguer anomaly upward continuation map (Figure 4.4) enabled the identification of two zones of low densities. They are located in the southwest, and south-southeast of the study area. The

low gravity intensity zone located in southwest of the study area (Figure 4.4) is coincident with low intensity magnetic (or high magnetic mineral content) on TMI map, and was mapped by Feybesse et al. (1999) and Lahondère et al (1999a) as rocks they assigned to the Archaean Kenema-Man domain, which is dominated by TTG suite granitoids. The low density zone in the south-southeast of Figure 4.4 was assigned to the Bougouni and Bagoe basin by Kušnir et al. (1989) and Girard et al. (1998), and is dominated by shale, sandstone and greywacke, and intercalated volcano-sedimentary rocks, and/or numerous TTG suite granitoids.

Moderate density zones in Figure 4.4 are located (1) in the far-east of the study area that coincide with a moderate susceptibility zones, and (2) between low densities zones that coincide with high susceptibility zones. The latter was mapped by Miller et al. (2013) as a zone of volcano-sedimentary rocks with granitoid intrusions.

A high density zone is located in the northwest of the study area and coincides with a low magnetic susceptibility zone (Figure 4.4). Egal et al. (1999a, 1999b) assigned this region to the Siguiri Basin that is composed of siltstone, mudstone and subordinate arkoses, with pelitic schists.

4.1.2. Magnetic First Vertical Derivative

The magnetic first vertical derivative map presented in Figure 4.5 was used to identify lineaments, circular to ovoid features, laterally extensive attributes and offsets. Lineaments were interpreted as (1) dykes that trend dominantly east-west, and (2) shear zones that generally trend northwest, northeast and north. A series of northwest trending lineaments correspond with faults as mapped by Egal et al. (1999a, 1999b) and Feybesse et al. (2006a). North and northeast trending lineaments correspond to shear zones identified by Kušnir et al. (1989), Girard et al. (1998), Egal et al. (1999a, 1999b) and Lahondère et al (1999b), and include (from west to east across the study area):

- The Siguiri Shear Zone, which is approximately 81 km long and 5 km wide and is north trending. The Siguiri Shear Zone has a western branch that trend northwest.
- The Yanfolila-Kalana Shear Zone, which is north-northeast trending. This shear zone is approximately 235 km in length and is 17 km wide.
- The Banifing Shear Zone (BSZ), which trends northeast and is approximately 168 km in length and 11 km wide.
- The arcuate Fatou Shear Zone, which trends northeast (overall), and is approximately 131 km long and 6 km wide.
- The Syama Shear Zone which trend northeast. This shear zone is approximately 64 km long and 4 km wide. It has also a western branch that trend to the north.

Circular and ovoid features were also identified, and according to Parasnis (1996), can be (tentatively) interpreted as mafic and granitic intrusions for qualitative interpretation. This

corresponds well with circular to ovoid granitic intrusions mapped by Egal et al. (1999a, 1999b) in the Siguiri basin.

A number of laterally extensive anomalies with no regular pattern were identified (Figure 4.5) and are (tentatively) interpreted as volcano-sedimentary belts. These anomalies correspond with volcano-sedimentary belts mapped by Girard et al. (1998) and Randgold (2007). The laterally extensive anomalies trend north-northwest and northwest (Figure 4.5) and correspond with:

- The Yanfolila volcano-sedimentary belt that trends north-northwest and is located west of Yanfolila-Kalana Shear Zone (Girard et al., 1998).
- The Bougouni volcano-sedimentary belt that trends northwest and is located to the southwest of the Bougouni basin (Randgold, 2007).
- The Kolondieba volcano-sedimentary belt, which is located in the Bagoe basin, and trends northwest. The belt was identified by Randgold (2007) who described its volcano-sedimentary character.

A number of curvilinear attributes in the study area can be (tentatively) interpreted as folds (Figure 4.5) and correspond with those interpreted by Feybesse et al. (2006a). These curvilinear attributes are located:

- Southeast of the Yanfolila belt and correspond to the Kalana-Kodieran fold.
- Northeast of the Yanfolila-Kalana Shear Zone and corresponds with the Ouelessebougou fold.
- Northwest of the Fatou Shear Zone and is hereafter termed the Farako fold (Figure 4.5).

From this data, the combined magnetic and gravity upward continuation maps developed for the study area (Figures 4.3 and 4.4) resolve four geophysical domains. According to the combination, the deep geological units can be located with the upward continuation map. They include:

- Domain 1 - A south-western domain that is characterized by low intensity magnetic (high magnetic mineral) and a low intensity of gravity signature. East-west trending dykes crosscut and dominate the domain. The interpreted high magnetic mineral content of this zone could be the due to the presence of dolerite dykes, and/or migmatite and granitoid of Archaean age that were described by Egal et al. (1999a) and Feybesse et al. (1999) for this domain.
- Domain 2 - A northeast to east domain that is characterized by a moderate magnetic mineral content and moderate to high density minerals. It also resolves the northeast trending Banifing, Fatou and Syama shear zones, and east-west trending dykes (Figure 4.5).
- Domain 3 is characterized by moderate magnetic mineral content and moderate intensity gravity signatures. The first vertical derivative of TMI resolved the Yanfolila-Kalana shear

zone, Yanfolila belt and Kalana-Kodieran fold (Figure 4.5).

- Domain 4 - A northwest domain that is characterized by low magnetic mineral content and high intensity gravity zone. This domain includes the Yanfolila fault and Siguiri Shear Zone (Figure 4.5).

4.1.3. Bouguer anomaly First Vertical Derivative

The Bouguer anomaly first vertical derivative of the study area (Figure 4.6) shows interpreted lineaments that coincide with attributes extracted from the magnetic first vertical derivative image (Figure 4.5). These features include: (1) in Domain 3, the Yanfolila-Kalana Shear Zone and Kalana-Kodieran fold; (2) in Domain 2, the Banifing and Syama Shear Zone. Additionally, the Bouguer anomaly first vertical derivative map interprets a series of northwest trending lineaments that are not evident in the Magnetic First Vertical Derivative map (Figure 4.5). These northwest trends are interpreted as faults and are herein referred to as the Manakoro fault and Koumantou-Morila fault (Figure 4.13).

4.1.4. Analytic signal

The analytic signal was applied on the regional magnetic data (Figure 4.7). The amplitude of the analytical signal was calculated for the total magnetic field to enhance the detection of linear, circular and elongated features. For example, shear zones, volcanic belts, lineaments and regional dykes manifest as clear positive magnetic anomalies in the analytical signal map. As one would expect, the analytical signal further showed magnetic highs over lineaments that coincide with large-scale folds (Figure 3.5). This filter is less sensitive to noise when compared to the derivative filters. Summarily, comparison of the amplitude of the analytical signal with the vertical derivative across all the zones of interest showed an increase in the numbers of structures delineated (Figure 3.6).

The attributes extracted from the regional magnetic data (Figure 4.7) coincide with those extracted from the Magnetic First Vertical Derivative (Figure 4.5) but are enhanced. The analytical signal applied on magnetic data enabled the identification of lineaments that included; (1) the Yanfolila volcano-sedimentary belt, (2) Yanfolila-Kalana and Banifing Shear Zone, (3) the Kalana-Kodienran fold as a complex fold with multiple fold axes, and (4) a NW trending lineament that separates the Kalana-Kodieran and Ouelessebougou folds. The lineament is interpreted as a fault or thrust.

In terms of magnetic and gravity domains, Domain 1 can be divided into three subdomains including from north to south;

- Domain 1a is characterized by moderate to high magnetic mineral content. This high magnetic mineral content may possibly be explained by the presence of numerous dolerite dykes.

- Domain 1b is characterised by low magnetic mineral content. Domain 1b includes circular features interpreted as granitoids (Feybesse et al., 1999).
- Domain 1c corresponds to high magnetic intensity zone, that according to Feybesse et al. (1999) is composed of multiple rock types including Archaean granites, undifferentiated granites, granites with biotite and amphibole, diorites, mica-schists, paragneiss and basic to ultra-basic rocks.

4.1.5. Vertical integral of the analytic signal

Figure 4.8 presents an image of the application of vertical integral on the analytical signal. The attributes extracted from Figure 4.8 coincide with those extracted from the analytical signal map in Figure 4.7 but are enhanced, including;

- Northeast, north and NNW trending lineaments that make up the Yanfolila belt. These lineaments correspond with the trend of lithologies in the Yanfolila belt.
- The NW trending Bougouni belt; it is surrounded by intrusions.
- The Kolondieba belt (Randgold, 2007).
- Linear trends that coincide with the Yanfolila-Kalana, Banifing and Fatou shear zones.
- Individualization of attributes that were interpreted as folds including the Kalana-Kodieran, Farako and Ouelessebougou folds.

Additionally a series of regional scale faults/discontinuities can be extracted including;

- The NW trending Yanfolila fault.
- The NNE trending Mandiana-Yanfolila fault. It crosscuts the Yanfolila-Kalana shear zone and separates the Ouelessebougou and Kalana-Kodieran folds.
- The Madina fault trends northeast. It crosscuts the Kalana-Kodieran fold, Bougouni and Kolondieba belt and Banifing Shear Zone.
- The NW trending Menankoro fault that crosscuts the Banifing and Yanfolila-Kalana Shear Zone, the Bougouni belt, Mandiana-Yanfolila and Madina fault.
- The NW trending Kadiolo-Fourou fault that crosscuts the Kadiolo, Syama and Fatou Shear Zone.
- The Koumatou-Morila fault that trends northwest and crosscuts the Banifing and Fatou shear zones.
- Farako fault that trends northeast and crosscuts the Banifing and Fatou shear zones, and Bougouni belt.

A northwest trend that was highlighted on the first derivative map of Bouguer anomalies is confirmed by the Menankoro fault (Figure 4.6).

Furthermore, Figure 4.8 enabled enhancement of a series of east-west trending lineaments that were extracted from the upward continuation of the TMI (Figure 4.3), Magnetic First Vertical

Derivative (Figure 4.5) and Analytical Signal (Figure 4.7); they are reasonably interpreted as dykes. The relative age of the dykes resolved two groups. Dyke group 1 is composed of four discrete dykes (dykes 1-4) and located in the northern of the study area (Figure 4.8). Dyke group 2 in the southern region of the study area is composed of six dykes (dykes 5-10) (Figure 4.8). Dyke groups 1 and 2 crosscut faults, folds and shear zones in the southwest and northwest of the study area and are thus younger that these attributes.

4.1.6. Tilt angle

The tilt angle of the total magnetic field (Figure 4.9) enhanced the boundaries of dykes, as well as the Yanfolila-Kalana and Banifing shear zones, at the expense of faults and folds in the study area because these attributes have high magnetic mineral content than other attributes in the area. The tilt angle filter confirmed the relative young age of dykes (Figure 4.8).

The tilt angle of Bouguer anomaly is presented in Figure 4.10 and confirmed the existence of the Menankoro and Koumanto-Morila faults and a distinct NE-trending lineament that crosscuts the Yanfolila belt and Yanfolila fault. The Menankoro and the Koumanto-Morila faults are interpreted as deeply penetrating according to their signature (Figure 4.10). The trend of basic rocks was also resolved (red line in Figure 4.10)

4.1.7. The automatic gain control (AGC)

The automatic gain control of the total magnetic field is presented in Figure 4.11 and enhances volcano-sedimentary belts resolved previously (Figures 4.5, 4.7 and 4.8). However, Figure 4.11 clearly resolves a connection between Bougouni and Kolondieba belts suggesting they are one belt. Figure 4.11 again confirms the presence of the Yanfolila and Madina faults, the Yanfolila-Kalana and Banifing shear zones, and the crosscutting relationship between dykes and others features. Importantly the Yanfolila fault crosscuts Dyke group 2 in the south, but is crosscut by Dyke group 1 in the north confirming two ages of dyke formation.

The AGC of Bouguer anomaly is presented in Figure 4.12, which resolved many of the same features presented in the first vertical derivative of Bouguer anomalies (Figure 4.6). The northwest trending Menankoro fault (Figure 4.12) crosscuts the Yanfolila-Kalana and Banifing shear zones and is thus younger in relative age.

4.1.8. The attribute map from geophysical data

The attributes extracted from the geophysical maps are presented in Figure 4.13 as an attribute map and includes first and second-order structures that were characterized by their length, width and probable depth. First-order attributes included shear zones (Yanfolila-Kalana and Banifing) and faults (Yanfolila, Mandiana-Yanfolila and Farako). Second-order structures included folds (Kalana-

Kodieran and Ouelessebougou), faults (Menankoro, Madina, Koumantou and Kadiolo) and shear zones (Siguiri, Fatou, Syama and Kadiolo). Group 1 dykes were interpreted as first-order structures (because they crosscut the entire study area), while Group 2 dykes were interpreted as second-order structures because of their limited spatial distribution. The Yanfolila, Bougouni and Kolondieba volcano-sedimentary belts are also evident.

Importantly, these attributes coincide with some geological structures presented in previous studies that were generally based on interpretation magnetic and radiometric data (with some fact data combination). However, the attribute analyses in this study resolve more structures indicating that a combined geological-geophysical approach is the best approach.

4.1.9. The potassium map

The Figure 4.14 presents the potassium map of the study area. This image was used for comparison with attributes extracted from geophysical maps (Figure 4.13) to establish the confidence level of the study area. According to the similarity between Figures 4.13 and 4.14 the attributes that can be highlighted include:

- The Yanfolila, Mandiana-Yanfolila, Madina and Farako faults (Figure 4.13)
- The Yanfolila volcano-sedimentary belt is the only belt that can be confirmed from Figure 4.14.
- The folds were all confirmed in the potassium map (Figure 4.14).
- The shear zones were all confirmed apart from Siguiri and Kadiolo shear zones.

4.1.10. The thorium map

The thorium map is presented in Figure 4.15. This image enabled the confirmation of several attributes presented in Figure 4.13. These include:

- Kalana-Kondiaran and Fatou folds.
- Banifing and Syama shear zones
- Yanfolila, Menankoro, and Kadiolo-Fourou faults.

4.1.11. The uranium map

Figure 4.16 presents the uranium maps of the study area. The image enables the confirmation of certain attributes presented in Figure 4.13. The similarity that can establish between Figure 4.13 and Figure 4.15 include:

- Yanfolila and Banifing shear zones in Figure 4.16. The Syama Shear Zone can be also resolved in Figure 4.16.
- Mandiana-Yanfolila, Menankoro and Koumantou-Morila faults present similarities with Figure 4.16.

- Kalana-Kodieran and Ouelessebougou folds are similar on the uranium map (Figure 4.16).

4.2. Confidence levels of the study area

As discussed in Section 3.3 a table of confidence levels of attributes was established (Table 3.1) by comparing Figures 4.13 and 4.17. Regions for forward and inversion modelling were subsequently selected according to the high and moderate level of confidence. Dykes and volcano-sedimentary belts were assigned a high level of confidence even though they appeared only on magnetic data because they exist as field mapped entities. The Yanfolila and Banifing shear zones were assigned a high confidence level because they are resolved from all geophysical datasets. The key areas for detailed study were selected across these attributes and reported in Chapter 6.

4.3. Geological fact data extraction

The geological fact data was extracted for forward and inverse modelling. Additionally for the key areas, geological data was extracted in addition to the petrophysical data. Figure 4.18 presents the fact data extracted for geophysical modelling and key areas.

4.4. Geophysical and structural architecture

4.4.1. Geophysical map of the study area

The different rocks types of the study area are presented in Figure 4.14 and correspond to the combination of density values and susceptibility for the study area. Nine (9) combinations are resolved according to magnetic susceptibility and density values (Table 3.2; Section 3.5), and also their coincidence with the physical property data (Table 3.1; Section 3.3). The low, moderate and high susceptibility and density are indicated in Figure 4.14. The nine combinations include:

1. High susceptibility values with low density corresponding to acid igneous rocks. In certain parts of the study area the combination corresponds to rocks composed of quartz with feldspar and biotite.
2. High susceptibility values with moderate density values are related to gneiss or certain types of metamorphic rocks.
3. High susceptibility values with high density values correspond to basic to ultrabasic igneous rocks such as basalt, pyroxenites, peridotite, kimberlitic (Bougouni area) or komatiite.
4. Moderate susceptibility values with low density values correspond to granitoids. The low density values are due to the lack of compaction and/or the presence of silicate in these areas.

5. Moderated susceptibility values with high density values correspond generally to the decrease of quartz in these rocks.
6. Low susceptibility values with low density values correspond to sedimentary rocks without compaction.
7. Low susceptibility values with moderate density values correspond to sedimentary rocks derived from acid igneous rock.
8. Low susceptibility values with high density values are related to sediment with high compaction and the presence of dolomite, and the presence of dacite in the Siguiri and Yanfolila areas.

4.4.2. Structural map of the study area

The structural setting of the study area is presented in Figure 4.13 including shear zones, faults, dykes and folds, and include:-

1. The Siguiri shear zone, which trends north. It crosscuts the Siguiri basin sedimentary rocks and is branched in the north. The Siguiri basin is crosscut by dykes. The Siguiri shear zone is interpreted as a second-order structure and exhibits approximately 8 km of apparent lateral displacement (c.f., Kim and Sanderson, 2005; Bergen and Shaw, 2010).
2. The arcuate Yanfolila fault is interpreted as a second-order structure. It is north to northwest trending along its length. The Yanfolila fault crosscuts dykes in the south, but is itself crosscut by dykes in the north constraining the ages of formation of these attributes, as stated previously, i.e. Dyke group 2 was crosscut by the Yanfolila fault and crosscut but east-west trending Dyke group 1 as the youngest attribute set.
3. The Yanfolila shear zone (YSZ) is a first-order crustal structures (steeply dipping) and hosts gold mineralisation in the study area (at Komana, Kalana, Kodieran). It is characterised by apparent dextral strike-slip in the south and sinistral strike-slip shear in the north. Secondary splay shears are characterised by sinistral displacement. The maximum (apparent) displacement of Yanfolila shear zone can be estimated at 23km according to the total length of the YSZ which is 223 km in the study area. The displacement is calculated by the principle of Kim and Sanderson (2005), which expresses the maximum displacement of fault against the fault length.
4. The Menankoro and Mandianan-Yanfolila faults are classified as a third order structure in the study area.
5. The Banifing shear zone (BSZ) is a first-order crustal structure and is important for gold mineralisation at Fatou in the south and Morila in the north. The BSZ resolves and apparent dextral strike-slip displacement in the southern part, which could change to sinistral in the centre and the northern part. Secondary splay shears are apparently characterized by sinistral strike-slip shear. According to the relation between displacement and strike-slip fault length (Kim and

Sanderson, 2005); the total length of displacement of BSZ strike slip shear is estimated at approximately 16km.

6. The Fatou shear zone (FSZ) is classified as a third order structure. The FSZ is only resolved with first derivative, vertical integral of the analytical signal and automatic gain control of magnetic, which are magnetic images. The southern part of FSZ is connected to the BSZ.
7. The Syama-(Bananso) shear zone is classified a second-order structures showing a tip damage shape. The analyses of the tip damage resolves and apparent sinistral strike-slip shear architecture for Syama-(Bananso) shear zone, which accords with Sigafrique (2000), and Ballo et al. (2016). The western arm of Syama-(Bananso) shear zone corresponds to the tip damage zone. The western arm of structure could be an important place for gold mineralisation if the rocks of that area correspond to low metamorphism grade.

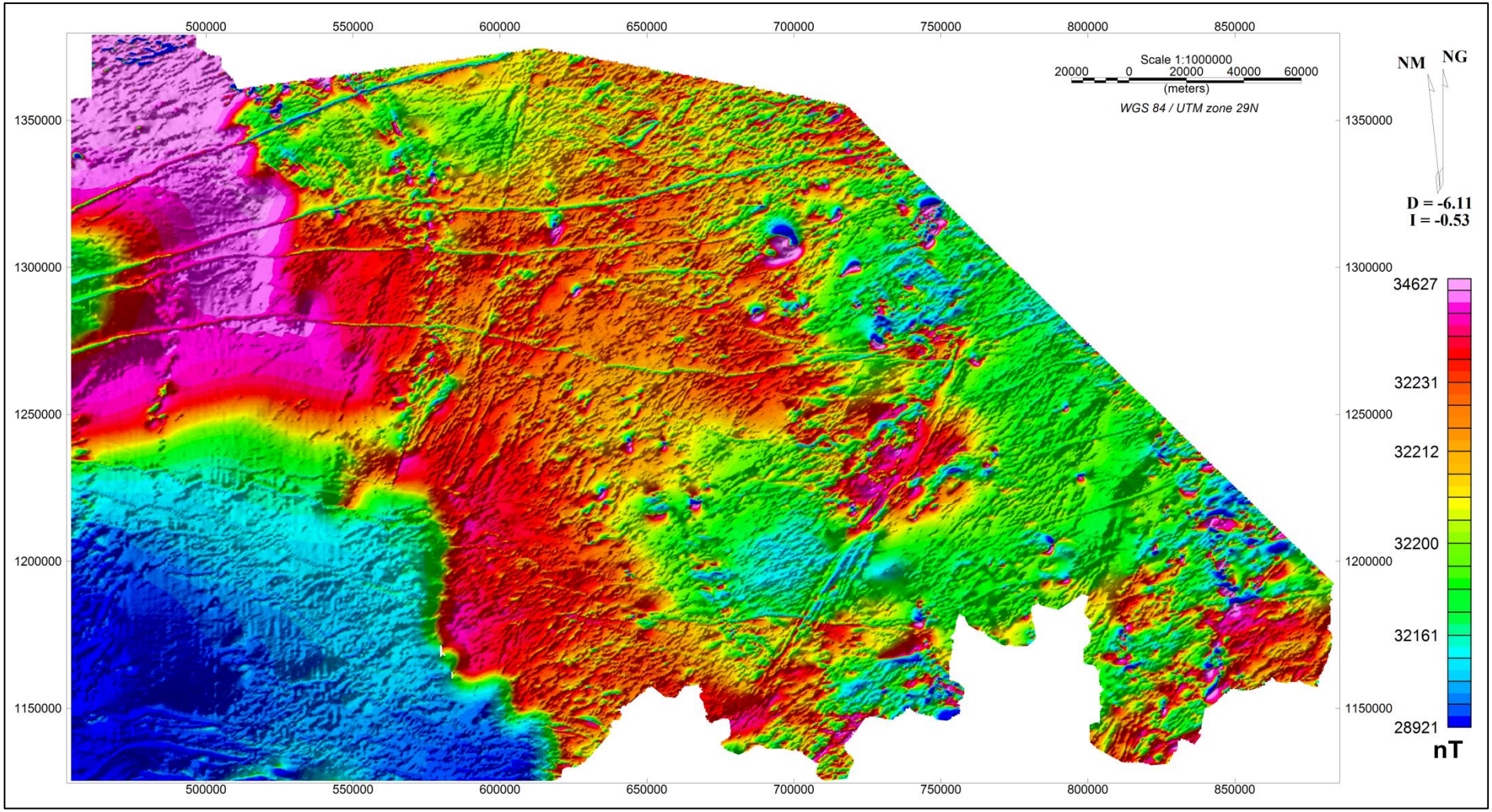

Figure 4.1: *Image of the total magnetic intensity map of the study area. The inclination of the zone is ≈-0.528, the declination ≈-6.107.*

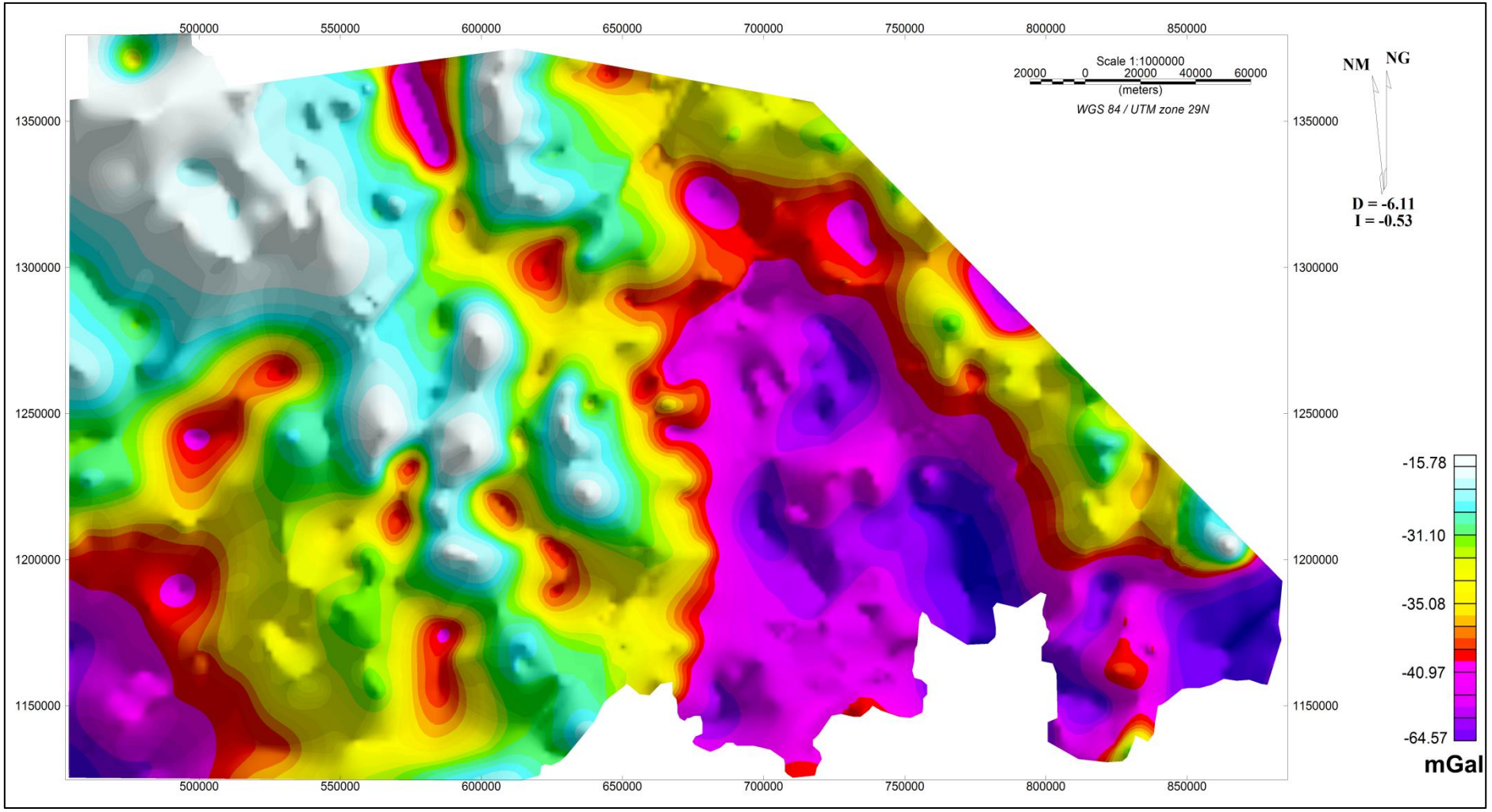

Figure 4.2 *Image of the Bouguer anomaly map of the study area using colour shaded with the sun inclination = 25; Declination = 125; vertical scale = 10 000.*

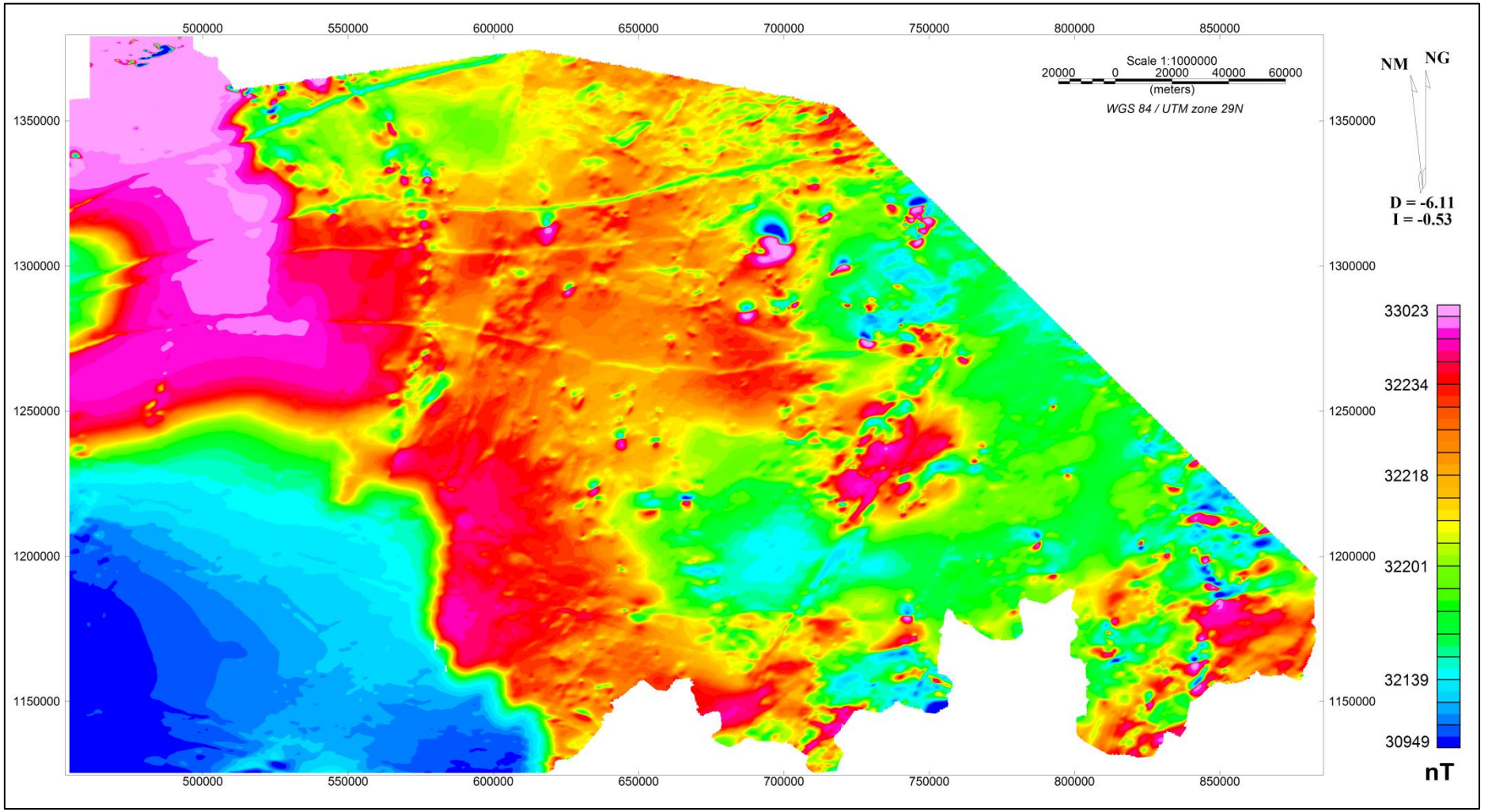

Figure 4.3: *Image of the upward continuation of the TMI presenting weakly defined NE trending lineaments. The image resolves the different magnetic zones, and a series of east-west trending lineaments that are interpreted as dolerite dykes that are greater than 270 km long. Northeast to north-northeast trending first-order scale lineaments in the west and east of the study area were interpreted as the Yanfolila-Kalana Shear Zone and Banifing Shear Zone, respectively, and are coincident with shear zones mapped at surface.. The identification of these lineaments on the upward continuation map indicates that the structures extend at depth. The study area is thus characterised by a heterogeneous distribution in magnetic minerals.*

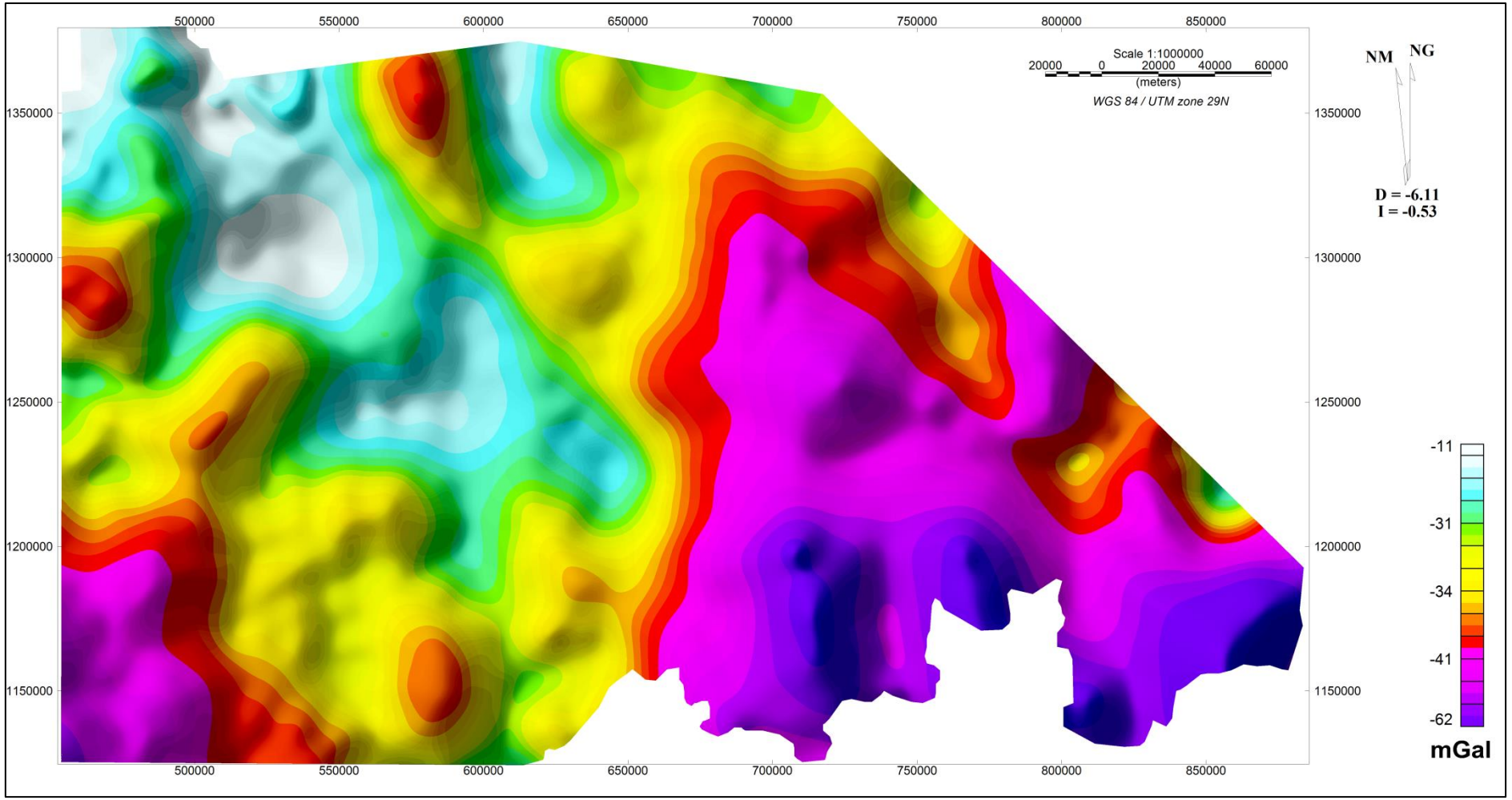

Figure 4.4: *Image of the upward continuation of the Bouguer anomaly \ using colour shaded with inclination = 25, declination = 125 and vertical scale = 10 000. The image presents the different gravity zones. The low gravity intensity zone located in southwest of the study area is coincident with low intensity magnetic (or high magnetic mineral content) on TMI map. They region was assigned to the TTG suite granitoids Archaean Kenema-Man domain by Feybesse et al. (1999) and Lahondère et al (1999a). The low density zone in the south-southeast was assigned to the Bougouni and Bagoe basin by Kušnir et al. (1989) and Girard et al. (1998), and is dominated by shale, sandstone and greywacke, and intercalated volcano-sedimentary rocks, and/or numerous TTG suite granitoids. The A high density zone in the northwest coincides with a low magnetic susceptibility zone and is assigned to the Siguiri Basin that is composed of siltstone, mudstone and subordinate arkoses, with pelitic schists.*

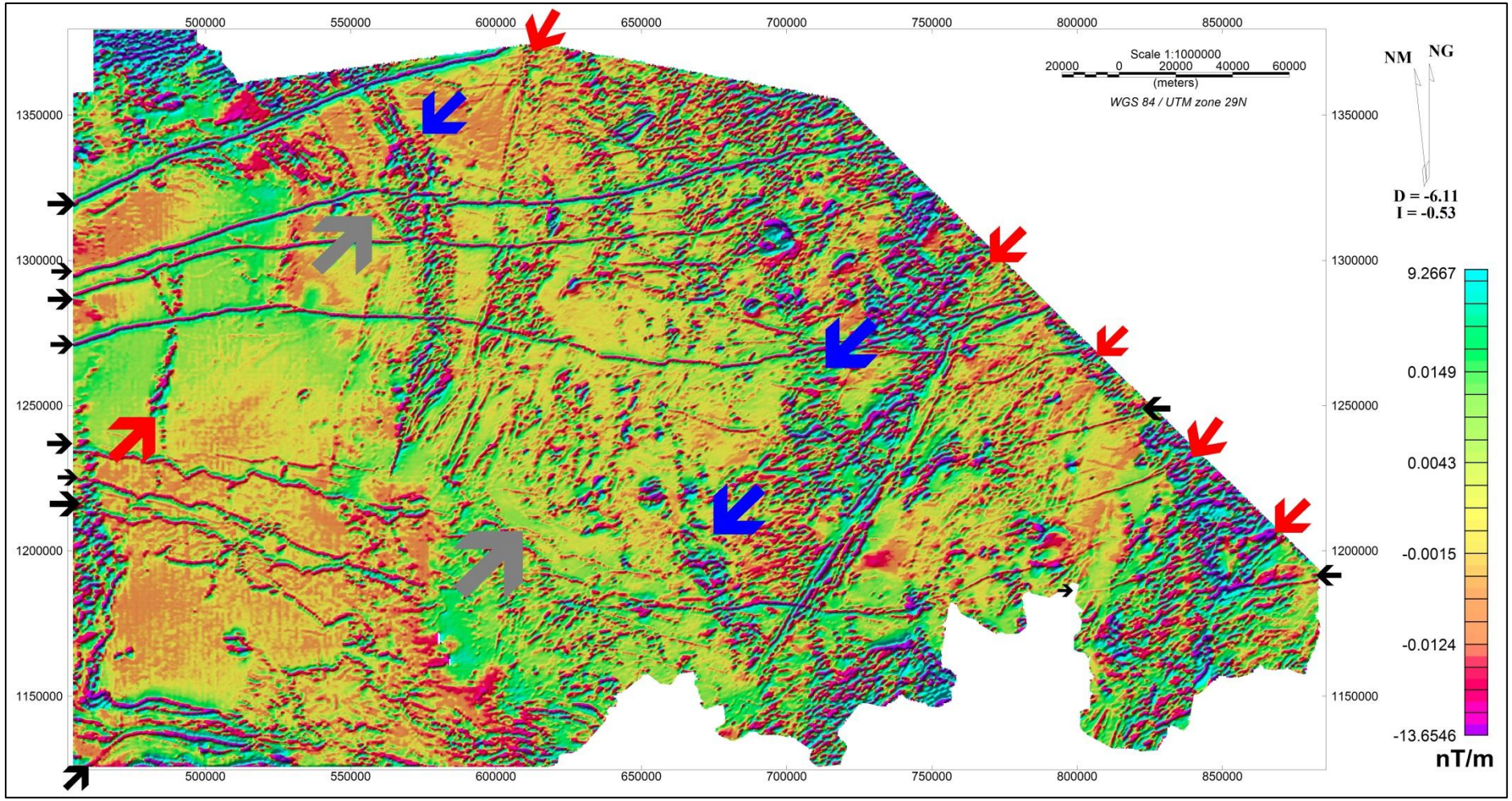

Figure 4.5: *Image of the first derivative map of the TMI. The red arrows correspond to a series of NNE to NE lineaments. The blue arrows are interpreted as sites of folds; the grey corresponds to the NS lineament. Black arrows mark the location of a series of east-west trending dolerite dykes.*

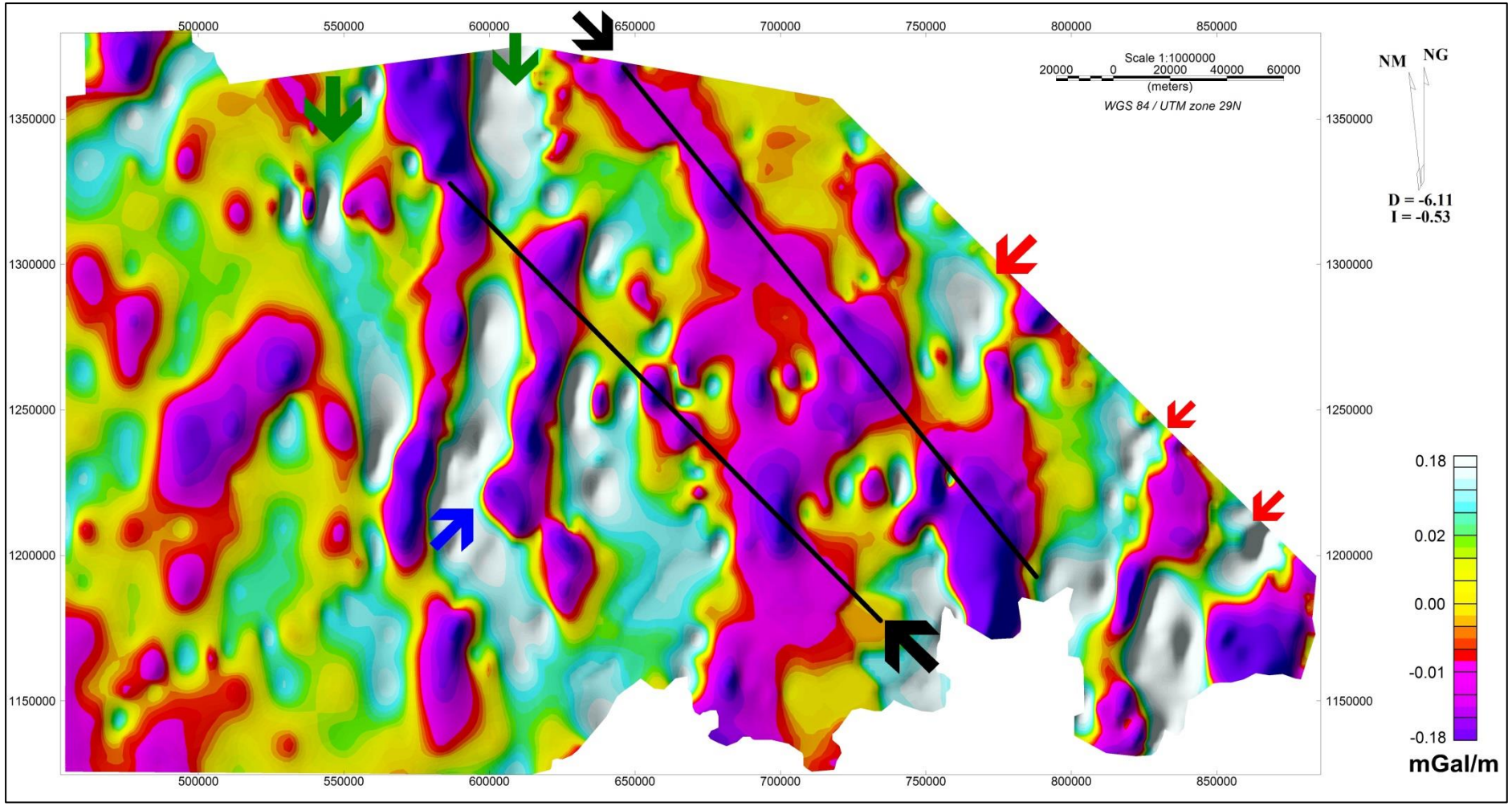

Figure 4.6: *Image of the first vertical derivative map of the Bouguer anomaly, resolves NE to NNE trends in the data set (red arrows); black arrows and black lines indicate NW trending lineaments; the green arrow marks the trace of north-south trending lineaments in the data; the blue arrow is interpreted as a fold.*

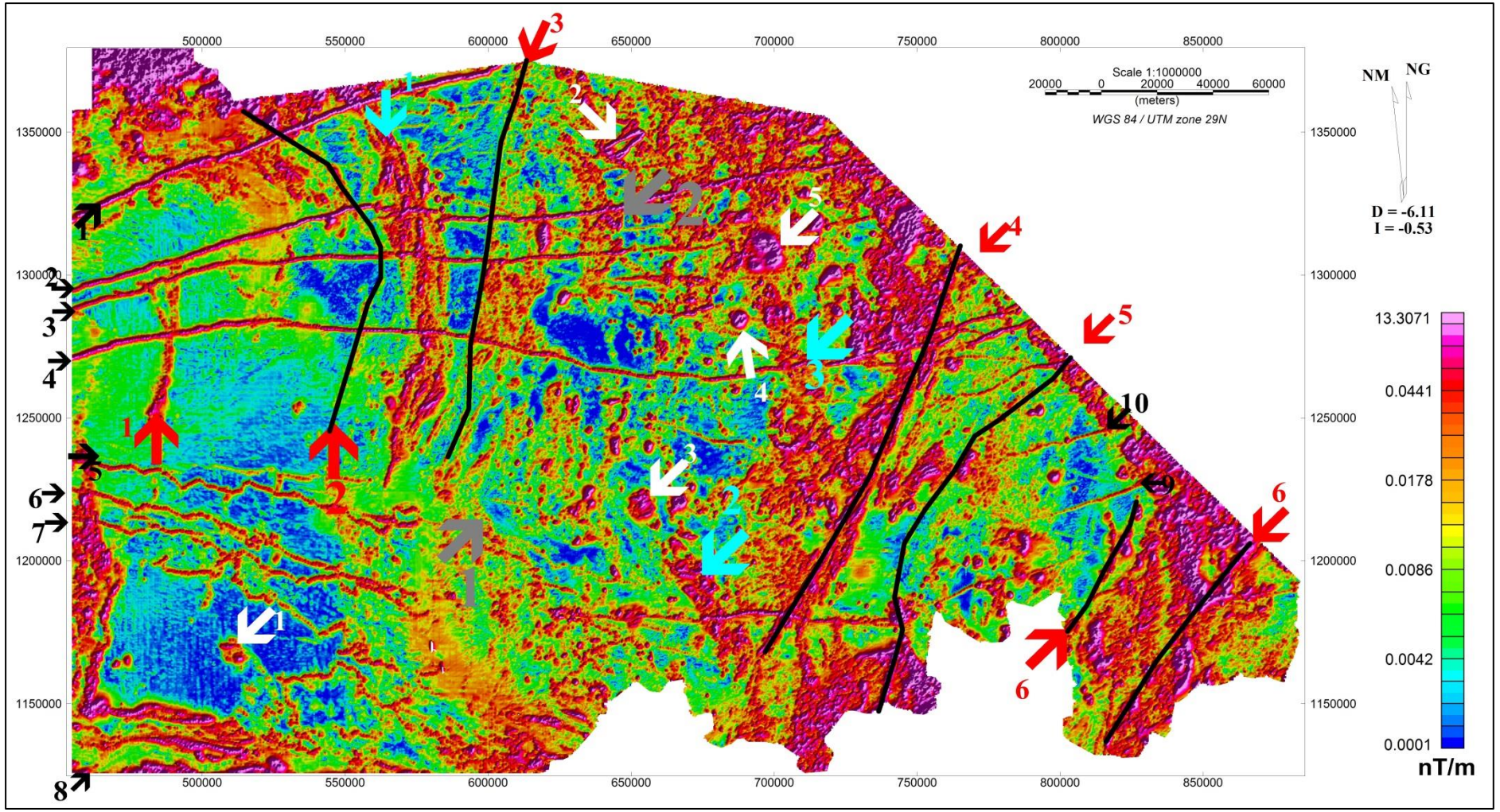

Figure 4.7: *Image of the analytic signal map showing N to NE trending lineaments (red arrow and black lines); the white arrows show circular features interpreted as plutons; the grey arrows marks the position of folds. The black arrows indicate the position of east-west trending dykes*

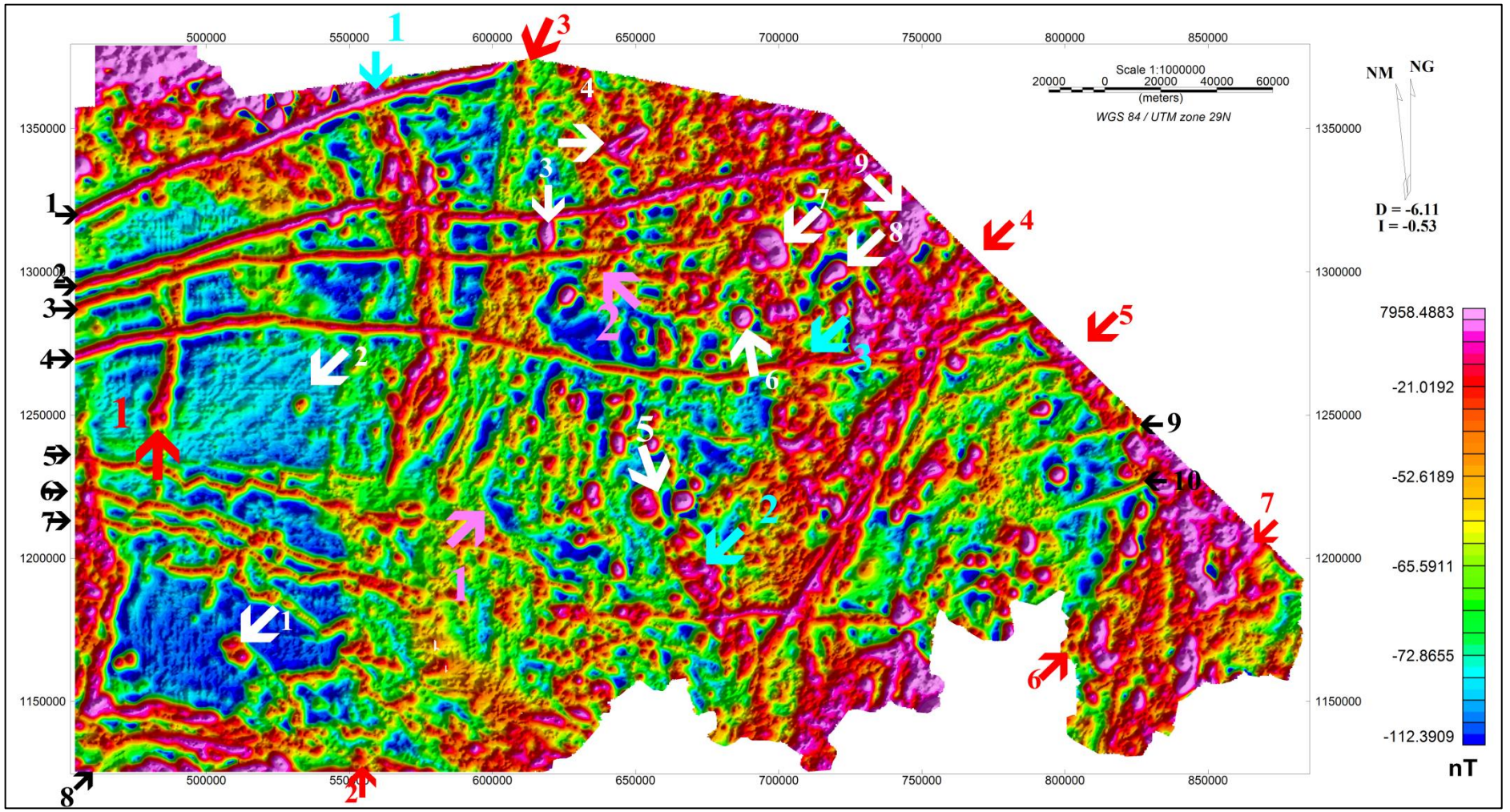

Figure 4.8: *Image of the application of the vertical integral on the analytic signal. The N to NE trending lineaments are presented by red arrows. The blue arrows correspond to the folded greenstone belts. The white arrows mark the position of circular features that are interpreted as intrusions. The black arrows once again mark east-west trending lineaments and are interpreted as dykes.*

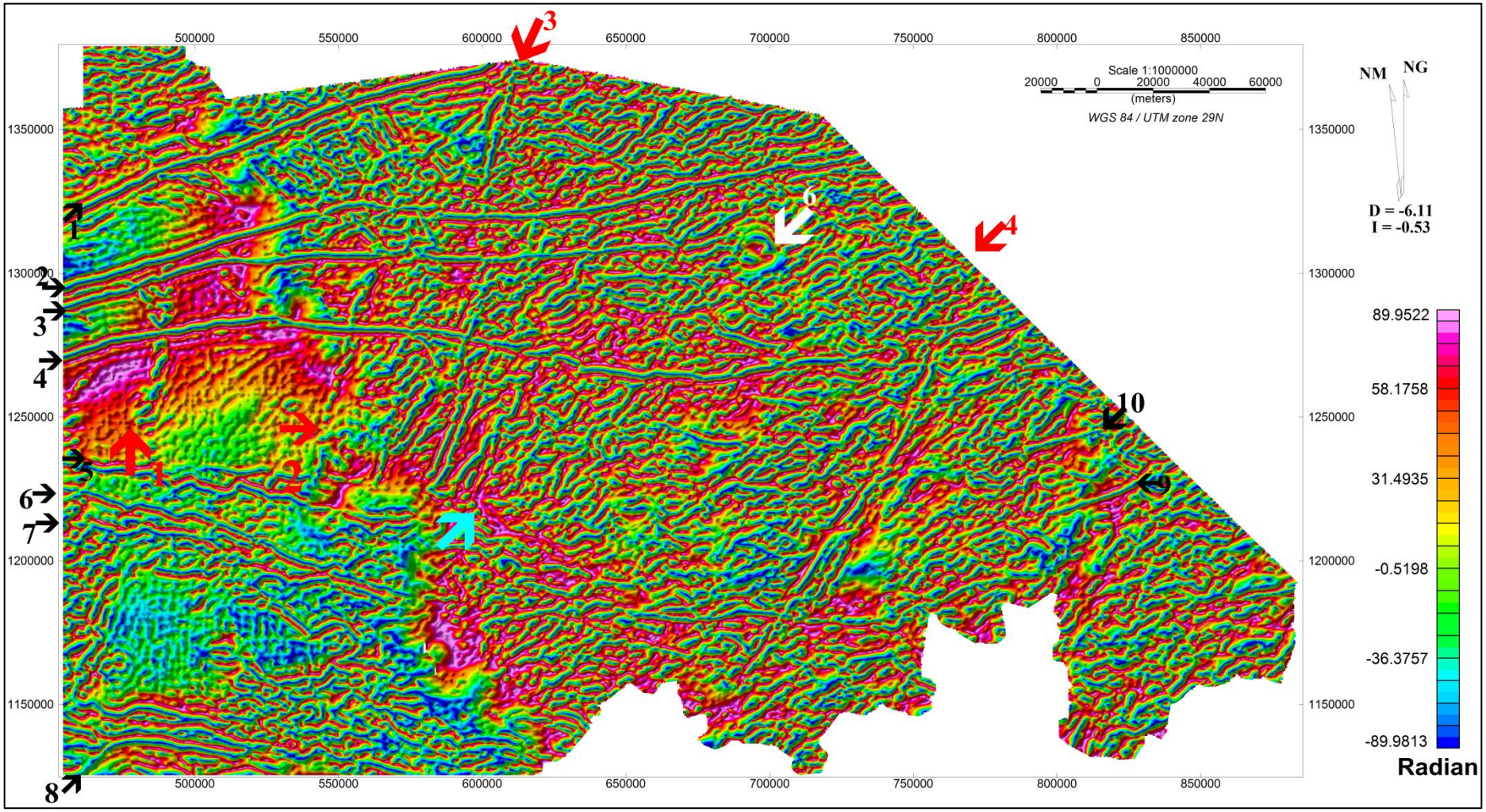

Figure 4.9: *Image of the tilt angle of the magnetic total field map. Dykes are marked by black arrows; main shear zones are marked by red arrows; significant intrusions in white; blue is interpreted as a fold.*

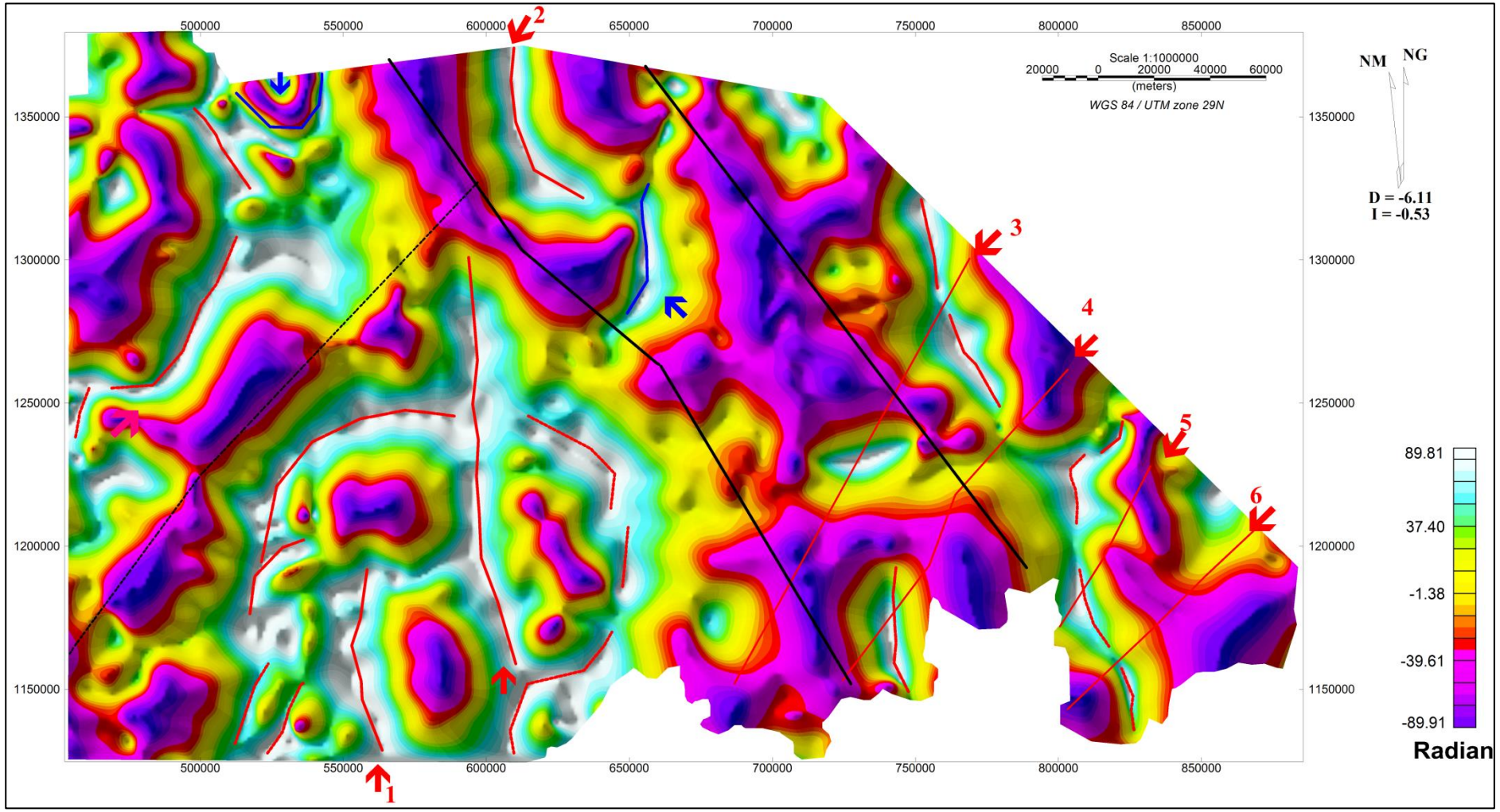

Figure 4.10: *Image of the tilt angle of the Bouguer anomaly map presents many of the same features as seen in Figure 4.9, including NW trending faults (black), NE trending fault (red).*

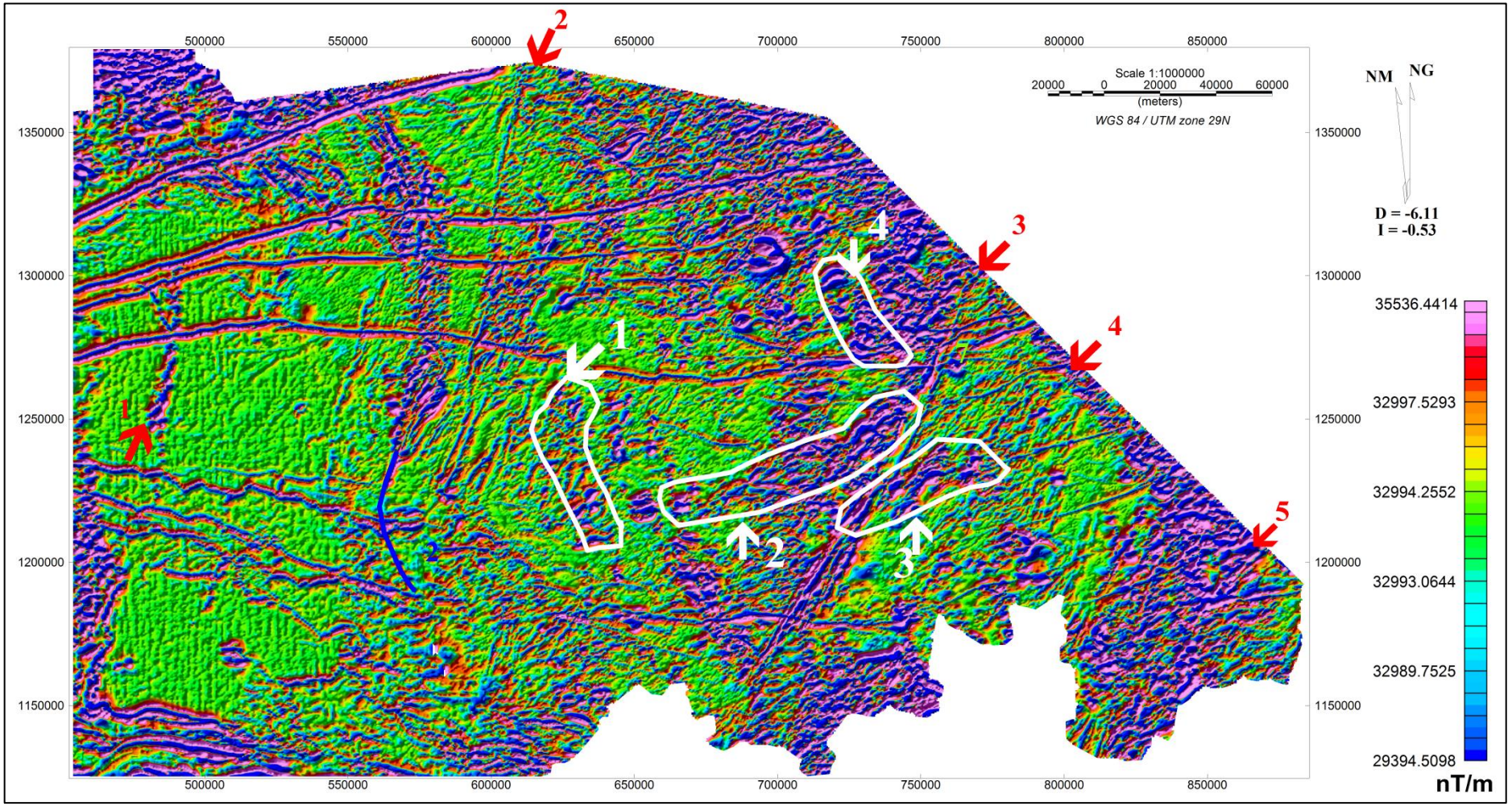

Figure 4.11: *Image of the automatic gain control of the total magnetic field indicating first-order scale structures (red arrows), and possible outliers of greenstone belts and their relationship to other attributes (white).*

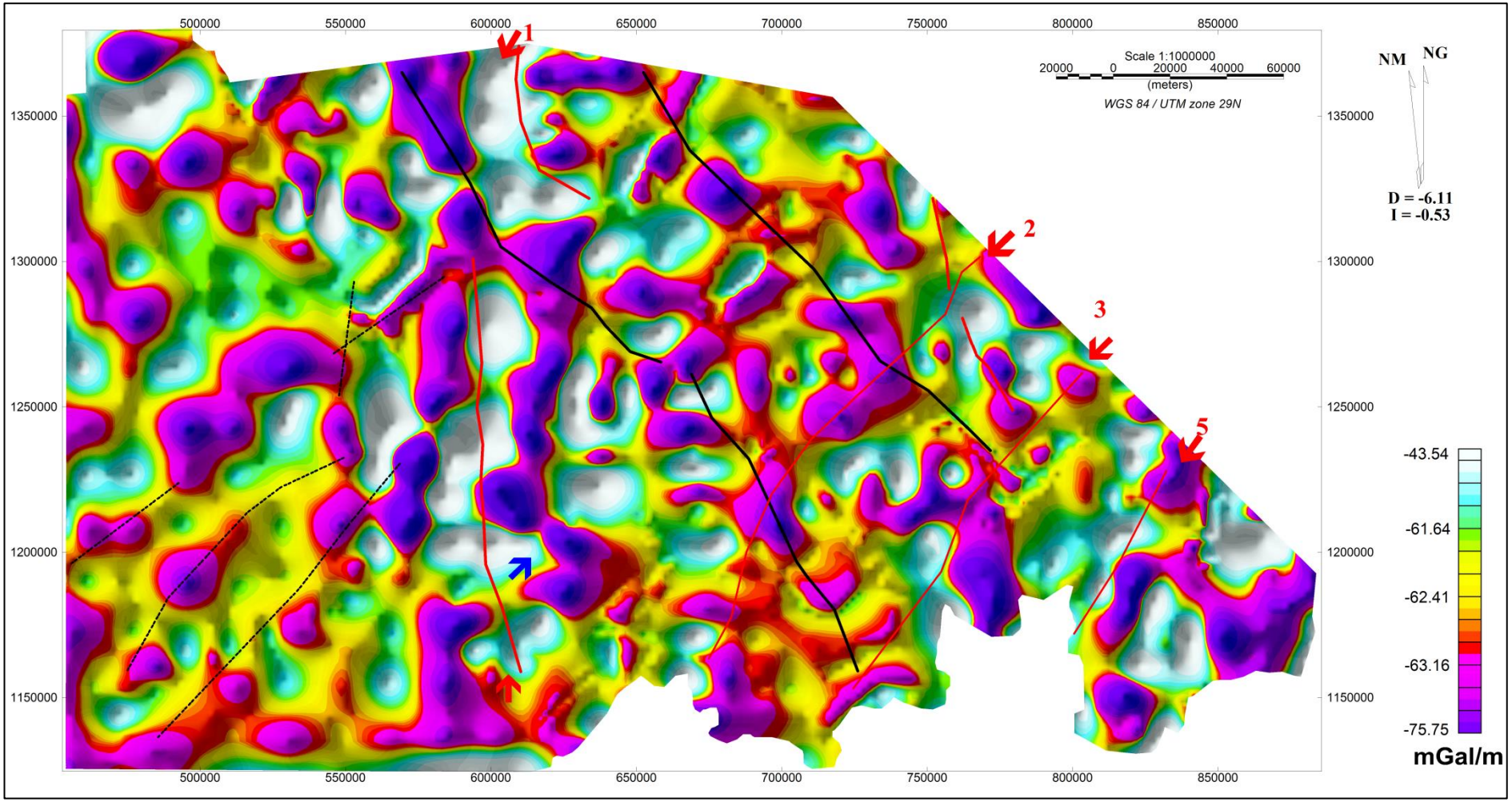

Figure 4.12: *Image of the automatic gain control of the Bouguer anomaly. Red arrows indicate the main interpreted shear zones as indicated previously. NW trending faults are marked in black. NE faults are shown as dotted black lines. The blue arrow marks the position of a fold, as marked on other images.*

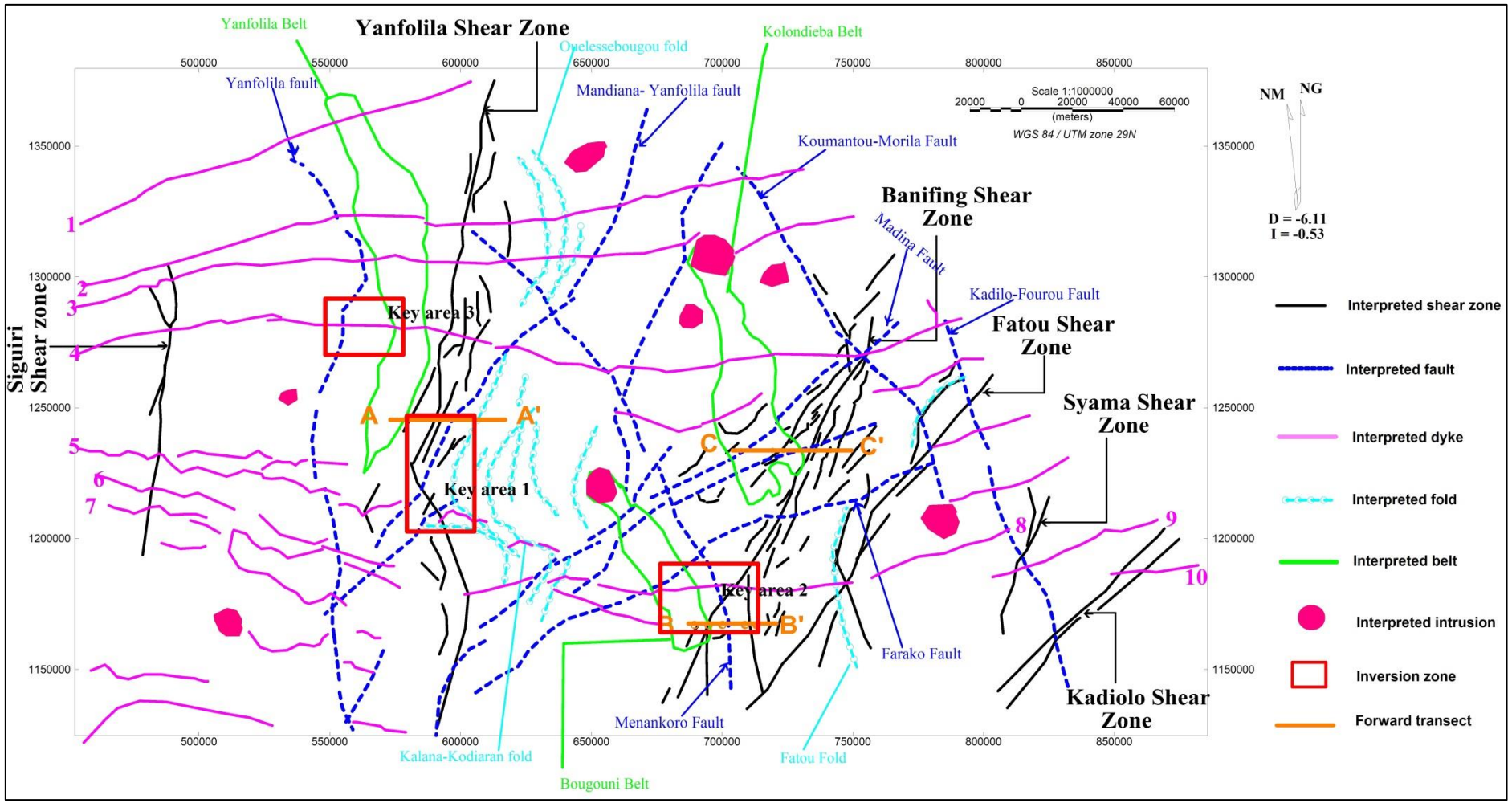

Figure 4.13: *Geophysical attributes showing interpreted attributes of first and order structures in the study area, with key areas 1-3 and profiles A-A', B-B' and C-C' indicated.*

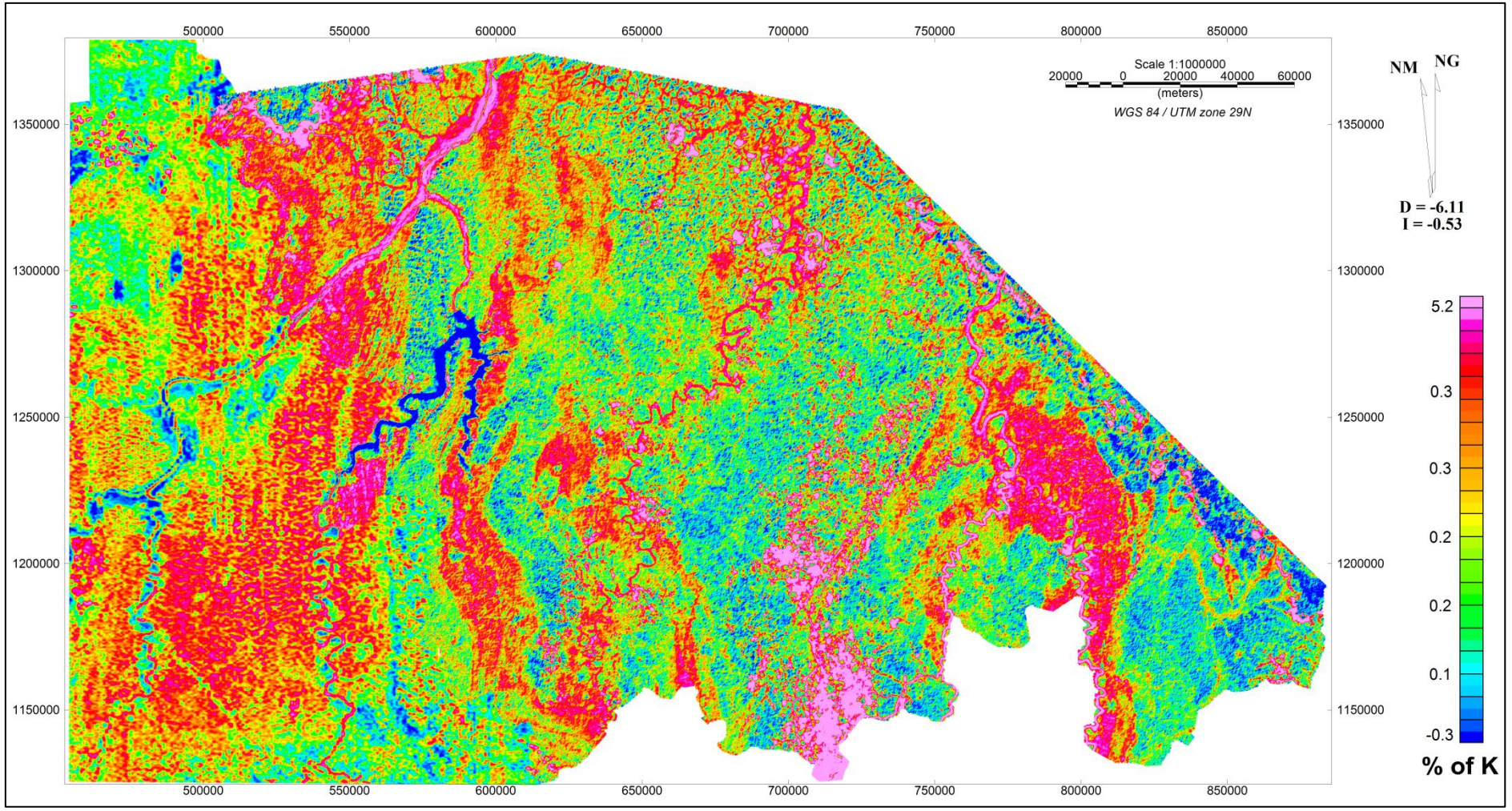

Figure 4.14: *The potassium map of the study area from radiometric data. The red correspond to the high levels of potassium, and the blue to the low level or drainage systems.*

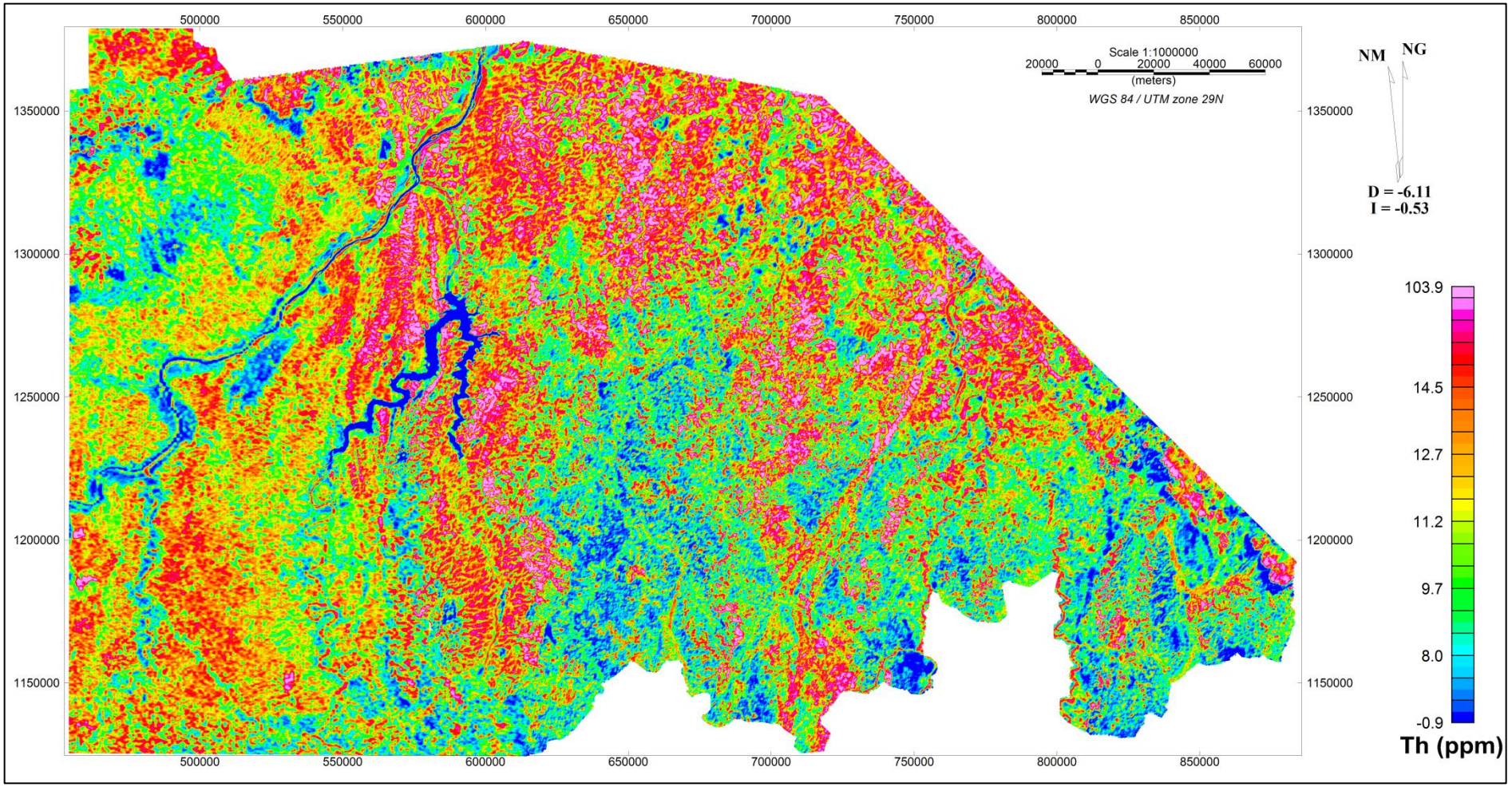

Figure 4.15: *The thorium map of the study derived from radiometric data. The red colours of this image correspond to the high zone of thorium, the blue zone to the low thorium zones.*

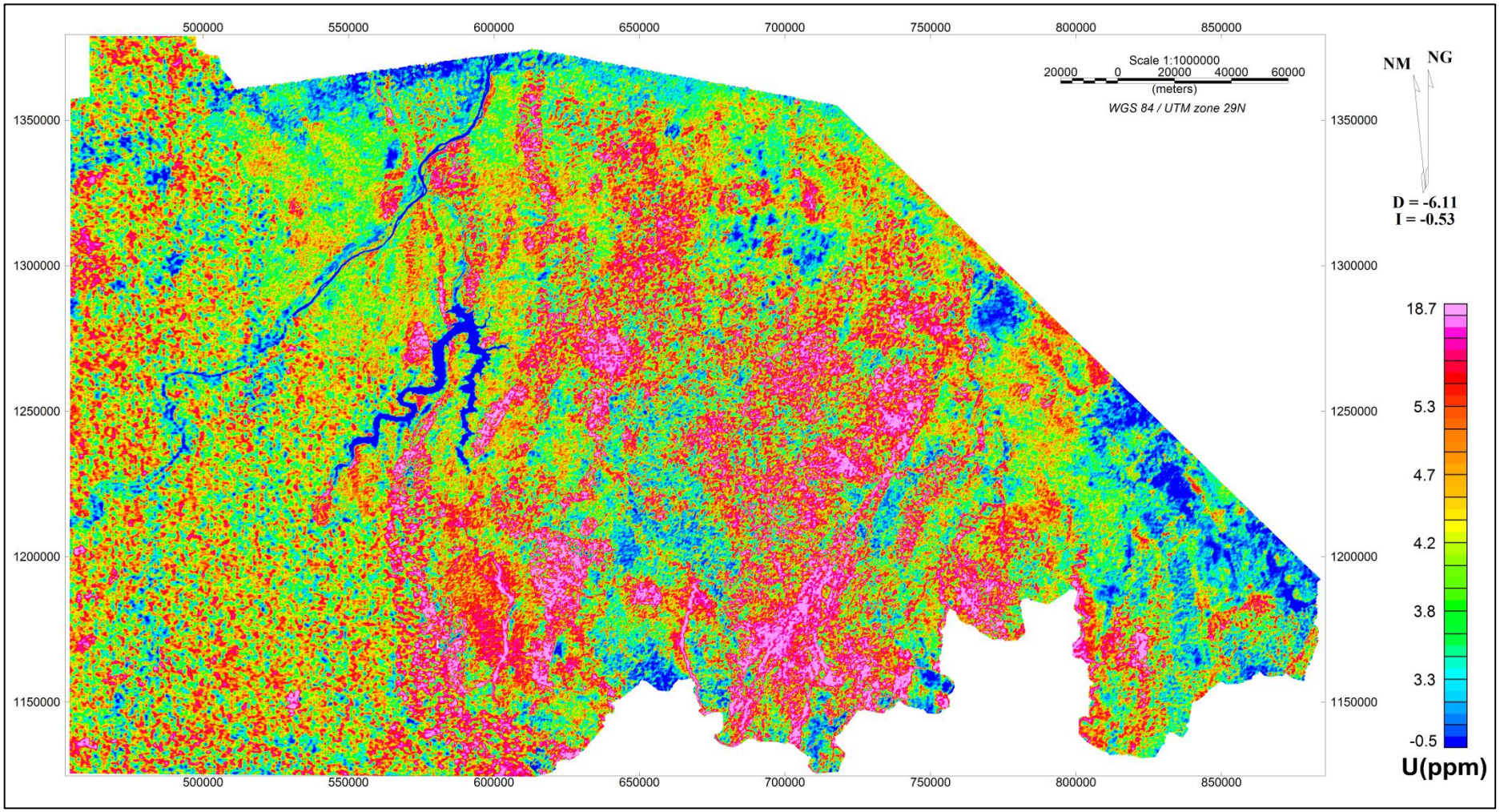

Figure 4.16: *The uranium map of the study area from radiometric data. For this image, the red are high level of uranium and blue the low.*

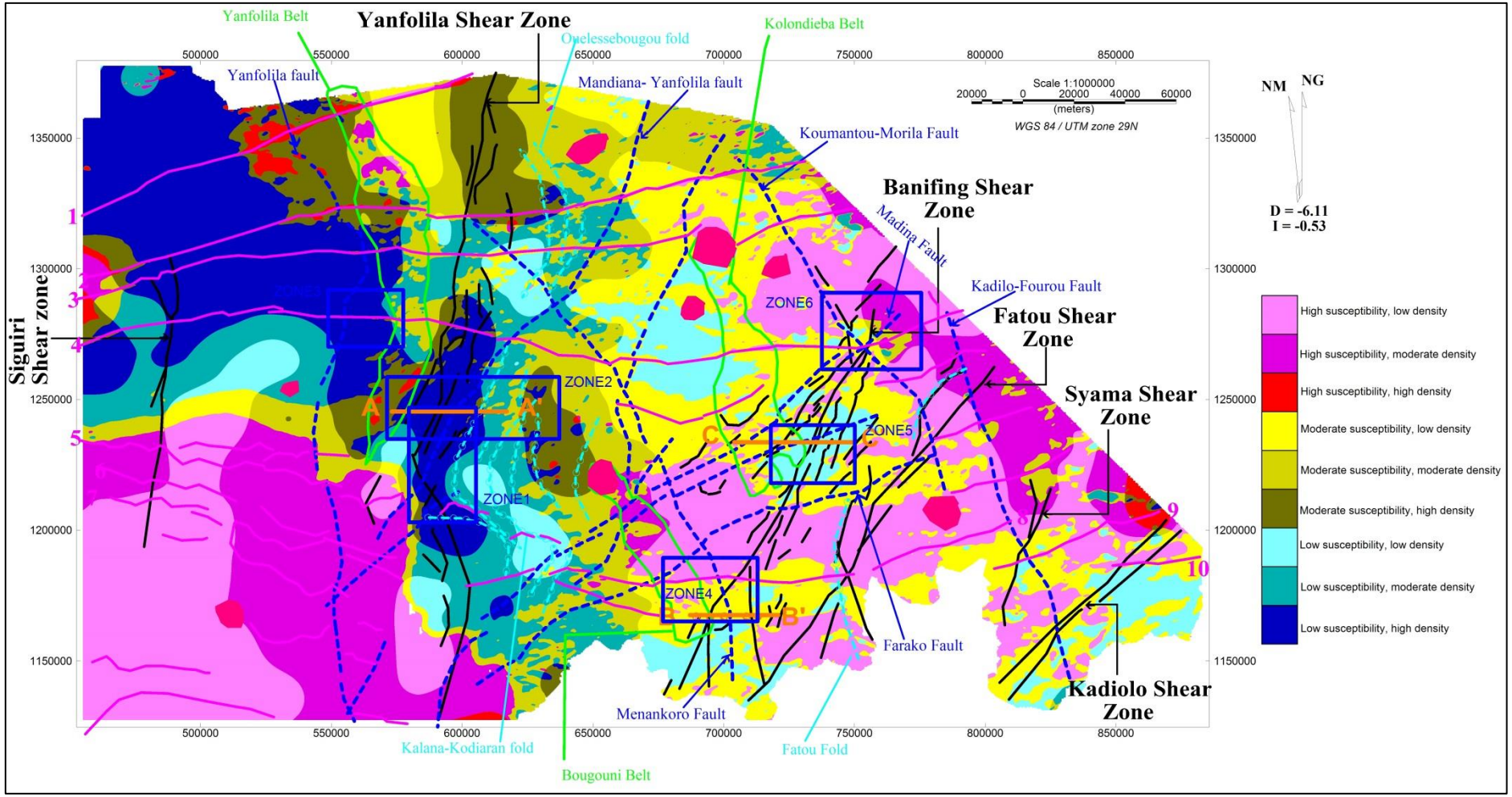

Figure 4.17: *A schematic pseudo lithology map showing lithological attributes extracted from the combination of magnetic susceptibility and density datasets. The figure interprets rock type according to their susceptibility and density mineral content. The key inversion zones described in the following chapters are indicated in blue. The figure shows the AA', BB' and CC' profiles in orange.*

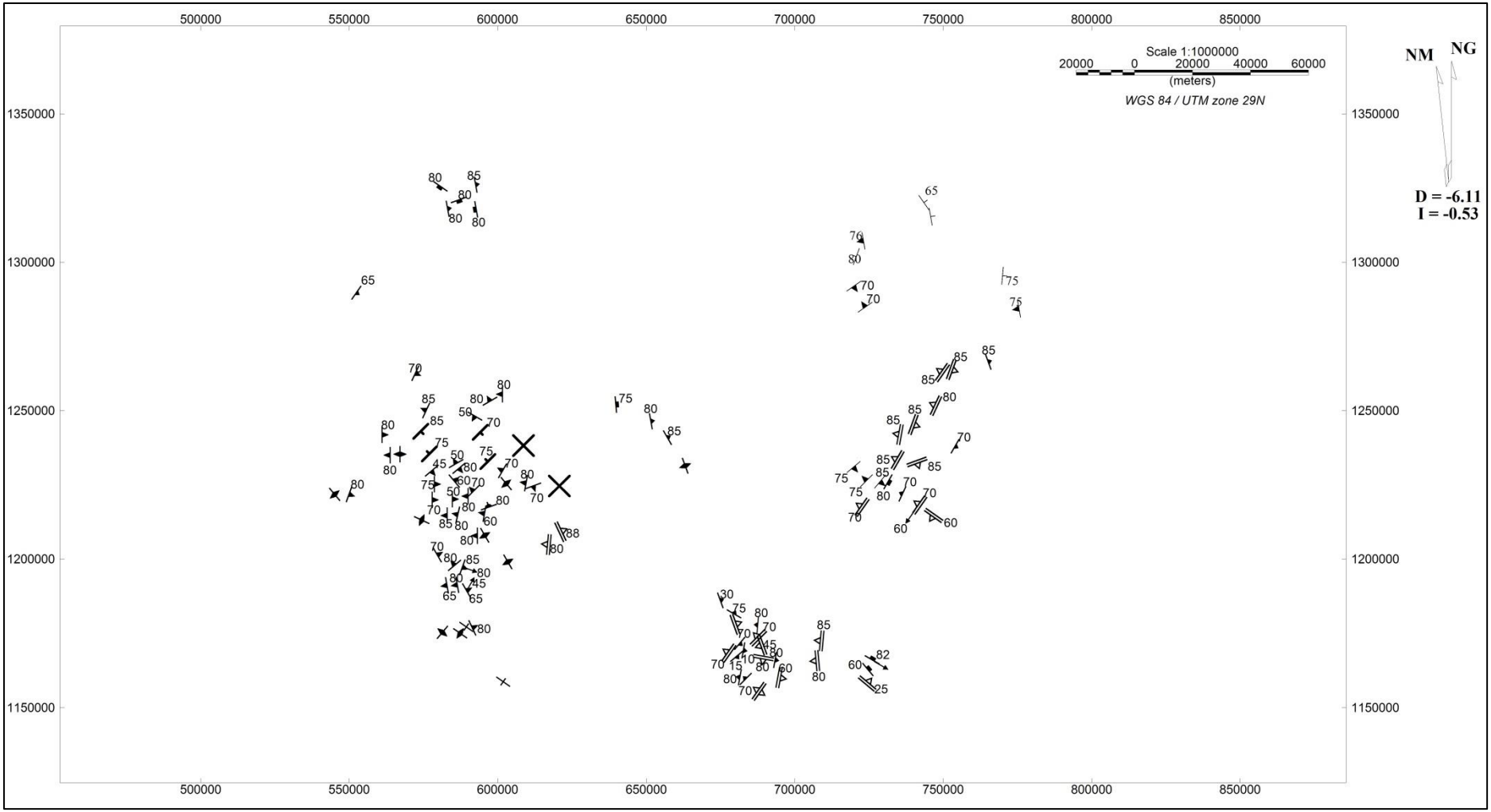

Figure 4.18: *The georeferenced fact geological data extracted from Claessens et al. (1988) and Feybesse et al. (2006a). The image shows the structures elements and their dip values (in degree).The fact data are located in the inversion zones 1 to 6 in Chapter 5. There is a general lack of fact geology data for the study area, and structural notation is not consistent across the mapped regions.*

5. GEOPHYSICAL MODELLING

5.1. Introduction

This chapter presents the results of geophysical modelling; it includes 2D forward modelling and 2D/3D inversion modelling. The models present the characteristics, depth, geometries of attributes extracted from the geophysical images presented in Chapter 4. The geophysical transect lines and inversion zones used in forward and inverse modelling were selected according to the confidence level table, i.e. Table 3.1.

5.2. Forward modelling

The experimental forward models were constructed to evaluate the effectiveness of the forward modelling in the study area. These models are presented in Figures 5.1 and 5.2. The models are based on the magnetic susceptibility and density values from the petrophysical data measured and published data. The benefit of forward modelling in the study area is to support the map plan view interpretation and confirm the geometric description at depth.

The forward modelling was performed on three transects with a 2.55g/cm^3 density and 8000 SI.10^6 as background values. The east-west transects included AA' across the Yanfolila belt (Inversion Zone 2 in Section 5.3.2), BB' at the southern end of the Banifing shear zone (in Inversion Zone 4 in Section 5.3.4), and CC" in the central region of the Banifing shear zone (Inversion Zone 5 in Section 5.3.5) (Figures 4.13, 4.17).

Forward models were constructed using available geological fact and physical property data. The correspondence between observed and calculated data was performed. The forward modelling aided in the creation of conceptual models of the subsurface. Anomalies were calculated and compared with observed data. Transect lines include:

- Transect AA' that extends from GPS coordinates 570950E 1245150N to 616000E 1245150N. It is approximately 45 km in length and traverses the Yanfolila belt, Yanfolila shear zone, Madiana-Yanfolila fault, and the Kalana-Kodieran fold (Figures 4.13, 4.17).
- Transect BB' that extends from GPS coordinates 687510E 1164475N to 721944E 1164475N, and is approximately 34km in length. It transects the Bougouni belt, Banifing shear zone and Menankoro fault (Figures 4.13, 4.17).
- Transect CC' that extends from GPS coordinates 704880E 1232696N to 751630E 1232696N, and is approximately 47km in length. It transects the Kolondieba belt, Madina fault, and Banifing shear zone in the east-central region of the study area (Figures 4.13, 4.17).

The upward continuation of magnetic data was calculated for each transect to produce three profiles (Profile AA', BB' and CC'). The upward continuations of total magnetic field for the profiles were 500m in order to locate deep anomalies. The magnetic susceptibility data used to calculate the magnetic field was obtained from the physical property data by WAXI (2013) taking into account the petrophysical data from literature (Table 3.3). The depths of structures were affected by the upward continuation that showed up to 1000m for depth-to-the-top of certain structures. For this reason the depth-to-the-top of structures indicates the relative depth of the source to anomalies only. Also, low susceptibility is not exclusively related to sedimentary rocks.

As stated previously, care was taken when interpreting the magnetic field in low magnetic latitude zone, as is the case for the study area. For the study area, high magnetic field generally corresponds with low magnetic mineral content and vice versa. The profiles presented in the following sections are the best fit that can be achieved between observed data and calculated data.

5.2.1. Profile AA'

Profile AA' is located in a low magnetic susceptibility and high density zone (Figures 4.14. 4.17) and corresponds with Transect AA' (in Inversion Zone 2, Section 5.3.2). The physical property data from WAXI (2013) reported that the geology along the Transect AA' is composed of granite, coarse-grained metasedimentary rocks, pegmatite veins, and biotite granite.

The interpreted model for Profile AA' presents six bodies (Figure 5.3). The parameters of the six bodies are presented in Table 5.1. According to the parameters, the top-depth of the bodies is located at approximately 1000m depth.

Table 5.1: *Profile AA' parameters*

				Profile AA'					
Body	**East (m)**	**North (m)**	**Depth (m)**	**Width (m)**	**Strike (Degree)**	**Dip (degree)**	**Suscp ($SI.10^6$)**	**Dens (g/cm^3)**	**Depth Extent (m)**
1	573063.4	1245189	-1500	110.34	225	65	27000	2.71	8000
2	579219.9	1245125	-800	57.74	60	60	50000	2.63	800
3	587954.1	1245121	-850	75	50	90	65000	2.67	500
4	591114.5	1245129	-800	50.77	55	80	60000	2.62	2000
5	605875.1	1245201	-800	159.63	220	105	15000	2.62	5000
6	611220.1	1245165	-1500	75	225	65	35000	2.62	8000

Bodies 1, 5 and 6 show different values of magnetic susceptibility and density values and reflect different rocks types in the Yanfolila belt. Bodies 2, 3 and 4 exhibit high susceptibility values that correspond to a low magnetic field. Bodies 1, 5 and 6 exhibit low susceptibility values.

The profile shows similarities between bodies 1 and 6 in terms of parameters (dip, top depth and depth projection) (Table 5.1). Bodies 2, 3, 4 and 5, with approximately the same parameters (Table 5.1), are situated between bodies 1 and 6 and correspond with the position of the Yanfolila shear zone,

which crosscuts the region. Body 5 is slightly different relative to bodies 2, 3 and 4 and corresponds with the position of the Kalana-Kodieran fold. Bodies 1 and 6 are respectively located to the west and east of the fold (Figure 5.3).

5.2.2. Profile BB'

Profile BB' (in Inversion Zone 4, Section 5.3.4) transects the central Bougouni belt, and is located in a moderate to high magnetic susceptibility and low density zone (Figure 4.14). The physical property data from WAXI (2013) reported that the geology along transect line B-B' is composed of orthogranite, sediments, pegmatite and quartz veins.

The interpreted model of profile BB' presents five bodies (Figure 5.4). The parameters of the five bodies are presented in Table 5.2. According to the parameters, the top-depth of the bodies is located at approximately 750 m depth and all bodies project at depth.

Table 5.2: *Profile BB' parameters*

				Profile BB'					
Body	**East (m)**	**North (m)**	**Depth (m)**	**Width (m)**	**Strike (Degree)**	**Dip (degree)**	**Susc (SI)**	**Dens (g/cm^3)**	**Depth Extent (m)**
1	689881	1164511	-1000	110	320	65	40000	2.67	5000
2	695358	1164426	-500	102	105	80	20000	2.69	3000
3	700729	1164528	-500	110	255	65	10000	2.67	3000
4	709526	1164500	-1000	76	320	80	35000	2.67	3000
5	714073	1164495	-800	55	225	65	25000	2.67	3000

According to the magnetic susceptibility and density data, bodies 2, 3 and 5 are different from bodies 1 and 4, reflecting different rock types. Bodies 2, 3 and 5 exhibit low susceptibility values corresponding to a high magnetic field. Bodies 1 and 4 show similarities in terms of parameters (dip, top depth and depth projection) (Table 5.2) and exhibit high magnetic susceptibility values. The bodies 2, 3 and 5 correspond with the Banifing shear zone and are possibly west-dipping splay shears. Consequently the Banifing shear zone is interpreted as a complex structure. The high susceptibility and low density of bodies 1 and 4 could indicate granitoid intrusions as these rocks were found during surface mapping.

5.2.3. Profile CC'

Profile CC' (in Inversion Zone 5, Section 5.3.5) transects the Kolondieba belt, and is located in a low to moderate susceptibility and low density zone (Figures 4.14, 4.17). The physical property data from WAXI (2013) reported that the geology along the transect line is composed of feldspathic sandstone, gneiss and gneissic granitoid.

The interpreted model of Profile CC' presents six bodies (Figure 5.5). The parameters of the six bodies are presented in Table 5.3. According to the parameters, the top-depth of the bodies is located at approximately 800m depth and all bodies project at depth.

Table 5.3: *Profile CC' parameters*

				Profile CC'					
Body	**East (m)**	**North (m)**	**Depth (m)**	**Width (m)**	**Strike (Degree)**	**Dip (degree)**	**Susc**	**Dens (g/cm^3)**	**Depth Extent (m)**
1	708178	1232696	-900	100	170	85	25000	2.63	3000
2	720450	1232696	-1000	110	225	65	20000	2.65	8000
3	724556	1232696	-749	110	25	85	50000	2.67	8000
4	731689	1232696	-800	100	220	65	20000	2.65	5000
5	737398	1232696	-800	50	25	85	40000	2.67	8000
6	743077	1232696	-700	50	25	85	40000	2.67	6000

According to the magnetic susceptibility and density, bodies 1, 2 and 4 are classified as different from bodies 3, 5 and 6, reflecting different rock types. Bodies 2 and 4 exhibit low susceptibility values and are interpreted as splay shears of the Banifing shear zone. Bodies 3, 5 and 6 exhibit high susceptibility values. The high susceptibility with high density corresponds with mafic rocks affected by the zone of shearing.

The profile resolves similarities between bodies 3, 5 and 6 in term of parameters (dip, top depth and depth projection) (Table 5.3). The bodies 2 and 4 are similar in parameters, and different from body 1. The low susceptibility (high magnetic field) observed with bodies 1, 2 and 4 indicate the low magnetic mineral content, or alteration of the magnetic minerals. In contrast, bodies 3, 5 and 6 show high susceptibility (low magnetic field), which indicates the presence of high magnetic minerals in these bodies and less alteration.

In any event, bodies 2, 3, 4, 5, 6 are located in the Banifing shear zone. Consequently, the Banifing shear zone can be considered a complex structure formed by a main shear and several secondary splay shears that resolve differences in dip and trend.

5.2.4. Synthesis of forward modelling

The forward modelling of profile AA', BB' and CC' showed that:

1. Transect AA' is situated across the Yanfolila shear zone and reveals its complexity. The trends are subvertical to east-dipping for body 3, and east-dipping for bodies 2 and 3; they are interpreted as splay shears to the main Yanfolila shear zone. The Yanfolila shear zone crosscuts the Yanfolila belt according to the similarity of bodies 1 and 6. The Kalana-Kodieran fold also is identified in Transect AA'.

2. Transect BB' and CC' traverse the Banifing shear zone, which is also a complex structure composed of several shear trends and secondary splay shears.

3. The use of upward continuation data for forward modelling places an important constraint on the top depth of bodies. The top depth presented by the three profiles cannot reflect the true top-depth of bodies, but the relative depth between the attributes.

4. The high susceptibility (low magnetic field) observed with the profiles explain the presence of magnetic mineral in the bodies that could be the ferromagnesian if they show a relative high density.

Additionally, the forward modelling of the profiles across the Yanfolila and Banifing shear zone facilitated the characterization and geometry of first-order structures, in terms of trend and dip. The depth of the anomalies is greater for the Yanfolila shear zone than the Banifing shear zone. The difference of source depth is due to the presence of sedimentary cover rocks (of undefined age) along Transect AA' to 1100 m, and 850 m for transects BB' and CC'.

Importantly the data show that the cover sequences postdate activity on the shear zones suggesting that the shear zones were truncated and unconformably overlain by younger sedimentary cover rocks; they may represent the sediments of the Taoudenni basin, which unconformably overlies the region to the north and east, or younger basinal sequences currently not mapped or studied. The low magnetic susceptibility and high density values along Transect AA' are therefore interpreted as related to the thickness of the sedimentary cover rocks. The higher density values may possibly be due to compaction effects. The rocks types are likely to be siltstone, shale and/or volcaniclastic sediments.

5.3. Inverse modelling

Inverse modelling was performed for the six (6) key zones (Inversion zones 1-6) according to high levels of confidence established in Table 3.1, and available fact and physical property data (Figure 4.18). The locations of inversion zones are presented in Figures 4.14 and 4.17. The inversion zones are situated on the first-order crustal scale Yanfolila and Banifing shear zones, and certain second-order structures and dykes (Figure 5.6). The selection of second-order structures was based on proximity to the first-order crustal scale structures. The inversions were performed using magnetic and gravity data with addition to fact data, petrophysical data and forward modelling of transects AA', BB' and CC' to produce a consistent model of the selected zone. The results of the inversions enabled the determination of the form, shape and geometries of rock volumes and structures. The trend, depth, dip, and the crosscutting relationship between rock volumes and structures were calculated to develop an architectural model for the key areas.

Additionally a reference model was produced using the surface fact data and the approximate dip information derived from forward modelling transects (Section 5.2). Bound models improved the quality of the inversion (Appendix F).

5.3.1. Inversion zone 1

The inversion model of Zone 1 is presented in Figures 5.6-5.8. Zone 1 is located approximately in the centre of the study area (Figures 4.13 and 4.14). The inversion model of Zone 1 included the Yanfolila shear zone, Kalana-Kodieran fold, Mandiana-Yanfolila fault, and dykes. According to the combination of susceptibility and density maps (Figure 4.14), the area is located in a low susceptibility, and low to high density zone of the region.

The inversion of magnetic and gravity data (Figure 5.6) resolves the Yanfolila shear zone and specific rock volumes that trend north and north-northeast. These can be divided into two susceptibility groups, namely (1) high susceptibility rock volumes, and (2) moderate to low susceptibility north-northeast trending rock volumes.

A low density rock volume in the southeastern corner of the inversion could be due to granitoids in that region. North-northeast trending rock volumes in the magnetic data exhibit high density values in the north and south of the inversion (Figure 5.6) that probably correspond to basalt-andesite rocks according to the plan map interpretation and preview study (c.f., Girard et al., 1998; Feybesse et al., 2006a; Miller et al., 2013). The Yanfolila shear zone is characterised by two parallel trends and the presence of a close upright symmetric fold in the south on the inversion (Figure 5.6). A number of southeast trending splay shears are also evident.

Geometric elements such as dip, depth of structures and rock volumes were determined for the magnetic and gravity inversion sections of Zone 1 (Figures 5.7-5.8). The geometry of Yanfolila shear zone can be described using the volume of rocks along the shear zone. The shears dip steeply west in the south, and steeply east in the centre and north of the inversion model. Secondary southwest trending splay shears dip subvertically to steeply west. The shears bound high susceptibility rock volumes, and in the centre of the inversion, form a left-handed (anticlockwise) sigmoid volume that is consistent with sinistral displacement in the plane of the Yanfolila shear zone (Figure 5.6).

5.3.2 Inversion Zone 2

The inverse models of Zone 2 are presented in Figures 5.9-5.11. Zone 2 includes the Yanfolila shear zone, Kalana-Kodieran fold and Madiana-Yanfolila fault. According to the physical property data, Zone 2 is composed of granite, sedimentary rocks, pegmatite and weathered granite. Zone 2 is characterised by low magnetic susceptibility according to Figure 4.14.

The inversion of magnetic and gravity data maps rock volumes and structures that trend north-northeast (Figure 5.9). According to the gravity model, high density rock volumes are located in the western region of the inversion adjacent to the Mandina-Yanfolila fault. The model also confirms the presence of this zone at depth. High susceptibility rock volumes generally trend north-northeast in Zone 2 and are bounded by shears.

Geometric elements such as dip, depth of structures and width were determined for the magnetic and gravity inversion sections of Zone 2 (Figures 5.10-5.11). The majority of high susceptibility rocks dip steeply east, as do their bounding shear zones. The inversion section of gravity data presented in Figure 5.11 shows high density rock volumes at depth in the region of the Yanfolila shear zone, but these are (apparently) not crosscut by the shears. The high density rocks could associate to an intrusion at depth that is younger than the Yanfolila shear zone. Low density rocks occur in the extreme west of Zone 2, and to the east of the Yanfolila shear zone (Figure 5.11). These low density rocks are interpreted as unconsolidated sediment and/or deeply weathered granite.

5.3.3. Inversion Zone 3

The inversion model of Zone 3 is presented in Figures 5.12-5.15. Zone 3 is located to the northwest of the Inversion Zone 1 toward the western centre of the study area (Figure 4.14). It includes the Yanfolila fault and part of the Yanfolila belt. The area is characterised by low magnetic susceptibility and high density rocks. According to published geological data, a felsic intrusion can be observed in the inversion area. The high density can be due to the degree of compaction in this inversion zone, or the presence of intrusions of the Central Atlantic Mafic complex which are mapped in the region.

The inversion model of magnetic and gravity data resolves generally north to north-northeast rock volumes. The north trending rock volume in the east of Zone 3 corresponds with the position of the Yanfolila belt. The north-northeast trending rock volume in the west of Zone 3 corresponds with the position of the Yanfolila fault. The Yanfolila fault is arcuate and is north trending in the south of Zone 3 and north-northeast trending in the north of Zone 3. An east-west trending dolerite dyke is clearly evident in the inversion model and corresponds with dyke 1 marked in Figure 4.13; the dyke crosscuts the Yanfolila fault and Yanfolila belt. East-west trending linear intrusions have been mapped as dolerite dykes across the study area (Feybesse et al., 2006a).

According to the gravity data inversion, high density rocks are located in the northwest of Zone 3 (Figure 5.14). The high density values coincide with a north-northeast trending susceptibility volume owing to the presence of basaltic rocks.

Geometric elements such as dip, depth of structures and rocks volumes were determined for the magnetic and gravity inversion sections of Zone 3 (Figures 5.13-5.14). The Yanfolila fault dips steeply west.

The geometry of the dyke that crosscuts the Yanfolila fault and Yanfolila belt and the high density (basaltic) rocks in the northwest of Zone 3 is presented in Figure 5.15 as viewed from the east. The dyke dips steeply to the south in the east of Zone 3, but rolls-over to dip steeply north in the west of Zone 3. High susceptibility values are located at approximately 300m depth for the dyke and 600 m depth for the basalt. The metamorphosed sediment, volcano-sedimentary rocks and thick

sedimentary cover above the dyke and basalt are attributed to low susceptibility values with the model. The model shows that the dyke and basalt are not affected by alteration at 300m and 600m.

5.3.4. Inversion Zone 4

The inversion of Zone 4 is presented in Figures 5.16-5.19. Zone 4 is located in the southeast of the study area and includes the Banifing shear zone (Figures 4.13, 4.17), the Bougouni volcanic belt, Menankoro fault, and dykes. Zone 4 is composed of low to high magnetic susceptibility, and low density rocks. According to physical property measurements of surface rocks, orthogranite, sediment, orthogniess and pegmatite are reported in zone 4 (WAXI, 2013).

The inversion of magnetic data of Zone 4 is presented in Figure 5.16. In the west of the inversion, zone 4 is characterised by northwest to north trending rock volumes, and northeast trending rock volumes in the east of the inversion. An east-west trending dyke is evident and corresponds with dolerite dyke mentioned and marked in Figure 4.13. These dykes coincide with the dolerite dykes of Feybesse et al. (2006a).

The northwest to north trending rock volumes correspond with the Bougouni volcano-sedimentary belt. Segments of the northwest trending Menankoro fault crosscut this belt. The northeast trending rock volumes in the east of the inversion are located adjacent to the Banifing shear zone and could be granitoid as the susceptibility is high and density low, perhaps as a result of a high content of silica. Additionally, a high density high susceptibility zone is located in the northwest corner of the inversion model, which could be related to gneissic rocks in the Bougouni belt.

Inversion sections from magnetic and gravity data of Zone 4 are presented in Figures 5.17-5.18. In Figure 5.17, northwest trending rock volumes in the Bougouni belt dip sub-vertically to steeply west, while north trending rock volumes dip steeply east.

In contrast, northeast trending rock volumes in the region of the Banifing shear zone dip steeply east; they are bound by the shear zone and north to north-northeast secondary splay shears. According to the inversion sections, the Banifing shear zone is characterised by low density and low susceptibility.

The parameters of the east-west trending dyke that crosscuts Zone 4 are presented in Figure 5.19 with sections, as viewed from the east. From this data the dyke dips steeply north to vertical. The thick sedimentary cover above the dyke is attributed to low susceptibility values at surface.

5.3.5. Inversion Zone 5

The inversion of Zone 5 is presented in Figures 5.20-5.22. Zone 5 is located in the central east of the study area on the widest part of the Banifing shear zone and includes the Madina fault and the southern extension of the Kolondieba belt (Figure 4.13). According to the physical property measurements of surface rocks, zone 5 includes granitoid gneiss, various metasedimentary rocks,

feldspathic sand, and pegmatite veins (WAXI, 2013). The low susceptibility of the Zone 5 model is related to a generally thick sedimentary cover.

The Zone 5 is composed of low to high susceptibility values and the low density volumes, that trend north to northeast. Some rock volumes are arcuate in shape (Figure 5.20).

Northeasterly and north-northeasterly trending rock volumes dominate the centre and east of the inversion model and correspond to high magnetic susceptibility values in and adjacent to the Banifing shear zone (Figure 5.20). The overall shear trend can be defined as northeasterly, but internal north-northeast trending rock volumes form right-handed (clockwise) sigmoids that are consistent with dextral displacement in the plane of the Banifing shear zone.

Northerly trending rocks volumes occur in the Kolondieba belt in the west of Zone 5, and in the east, and are arcuate in form. This may relate to folding of the rock units they represent.

Two areas of high density values are resolved in the Zone 5 inversion model (Figure 5.20). Area 1 is located in the Kolondieba belt, where the high density coincides to the high susceptibility. The coincidence of high susceptibility and high density corresponds to gneissic rocks identified from surface rock petrophysics measurements. Area 2 is located in the Banifing shear zone and is also interpreted as a gneissic rock volume.

The magnetic and gravity inversion sections of model 5 are presented in Figures 5.21-5.22. The inversion sections demonstrate that the Banifing shear zone is steeply dipping overall, with segments that dip west or east. According to the magnetic section, the rock volumes are located at approximately 500-700m depth.

According to gravity sections (Figure 5.22), high density rocks are located in the northern part of model 5 at depth; they are not crosscut by the Banifing shear zone and may represent younger intrusions. A high density region in the northwest of Zone 5 in the Kolondieba belt could be due to the basalt or gneiss.

5.3.6. Inversion Zone 6

Magnetic and gravity inversion of Zone 6 are presented in Figures 5.23 to 5.25. Zone 6 is located in the northern part of Banifing shear zone in the northeast of the study area. Zone 6 includes the Madina fault and Koumantou-Morila fault (Figure 4.13). The geology includes andesite and biotite-muscovite bearing metasedimentary rocks according to the surface physical property measurements. Zone 6 is characterized by low, moderate and high susceptibility (Figure 4.14). The density values of Zone 6 vary from low to moderate.

In the magnetic data inversion for Zone 6, north to north-northeast trending rock volumes are readily identified. They correspond to the high susceptibility values of the rocks. In the north of Zone 6, high susceptibility values coincide with high density values and could indicate the presence of andesite in that region.

The magnetic and gravity inversion sections of model 6 are presented in Figures 5.24-5.25. The inversion sections demonstrate that north trending rock volumes dip steeply east, while north-northeast trending rock volumes dip steeply west.

5.3.7. Geological synthesis of inverse modelling

As described by Williams et al. (2009), surface mapping (fact data geology and structural data) can be used to constrain inversion models. These data were used in the reference models and bound models to constrain the inversions. The results of inversion were compared to the available geological data, fact data and qualitative geophysical interpretation to evaluate best fitness. Unfortunately, the lack of an available geological model for the study area makes it difficult to control or constrain the quality of inversion. However, the comparison shows good fitness for inversion zones 1, 2, 4, 5 and 6. Inversion zone 3 present a limited fit with the surface geological data currently available.

The use of reference and bound models in the inversion presents some limit. They show that the inversions using the reference model, with structural fact data, is limited and cannot resolve any differences with unconstrained inversions. In contrast, the bound model using the petrophysical data reported by WAXI (2013) and dip information from the forward modelling locates the shape and the geometry of the geological volume space quite well.

Inverse modelling was performed on two first-order crustal-scale structures, namely, the Yanfolila and Banifing shear zones. The inversion modelling provided information about the geometry of the shear zones using the surface physical property and fact data available. The inversion showed:-

1. There is a difference in thicknesses of sedimentary cover between Yanfolila shear zone region and Banifing shear zone regions. The Banifing shear zone hosts more felsic intrusions, which explains the low densities values. On the other hand, the Yanfolila zone hosts more basalt particularly in the Yanfolila belt and volcano-sedimentary rocks are present in this area.
2. First-order scale shear zones dip steeply to the west or east and are complex structures, with numerous second-order splay shears.
3. The Yanfolila shear zone is characterised by parallel shears. A number of southwest trending second-order splay shears are also evident. The shears bound high susceptibility rock volumes that (internal to the Yanfolila shear zone) form left-handed (anticlockwise) sigmoids that are consistent with sinistral displacement in the plane of the shear zone. The high density rocks at depth could be intrusions that are younger than the Yanfolila shear zone.
4. The Yanfolila fault to the west of the Yanfolila belt is arcuate and dips steeply west.
5. The Banifing shear zone is also characterised by parallel shears. A number of southeast

trending splay shears are also evident. The shears bound high susceptibility rock volumes that internal to the Banifing shear zone form right handed (clockwise) sigmoids that are consistent with dextral displacement in the plane of the shear zone.

6. It is possible to resolve the geometry of dolerite dykes and establish their crosscutting relationship. Thick sedimentary cover above dykes is attributed to low susceptibility values at surface.
7. The inversions show the difference between the Siguiri basin and Bougouni basin. The Siguiri basin is characterised by volcano-sedimentary and sedimentary rocks with high densities values, and the Bougouni basin is dominated by granitoid intrusion and lower density values.
8. The petrophysical data collected from surface rocks or drill core can be used to constrain the inversions because all the inversion were run with the bound model and the results show differences with respect to the unconstrained inversions. But the result should be controlled as there is no fact geology data at depth in the study area.
9. The descriptions confirm that the presence of geology and structures as described in Chapter 4 extend at depth, as showed from the inversions.

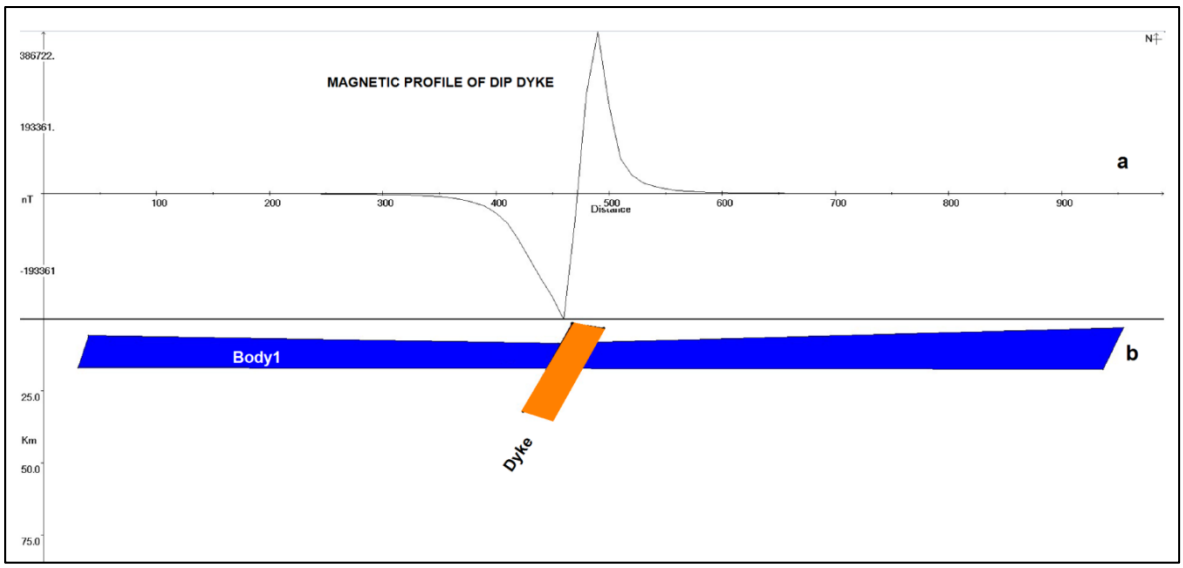

Figure 5.1*: Experimental model of dyke using magnetic data from published petrophysical data. Body 1 corresponds to the low magnetic susceptibility (sedimentary rocks or certain volcano sediment rocks). The profile is given by 'a', while 'b' corresponds to the model constructed.*

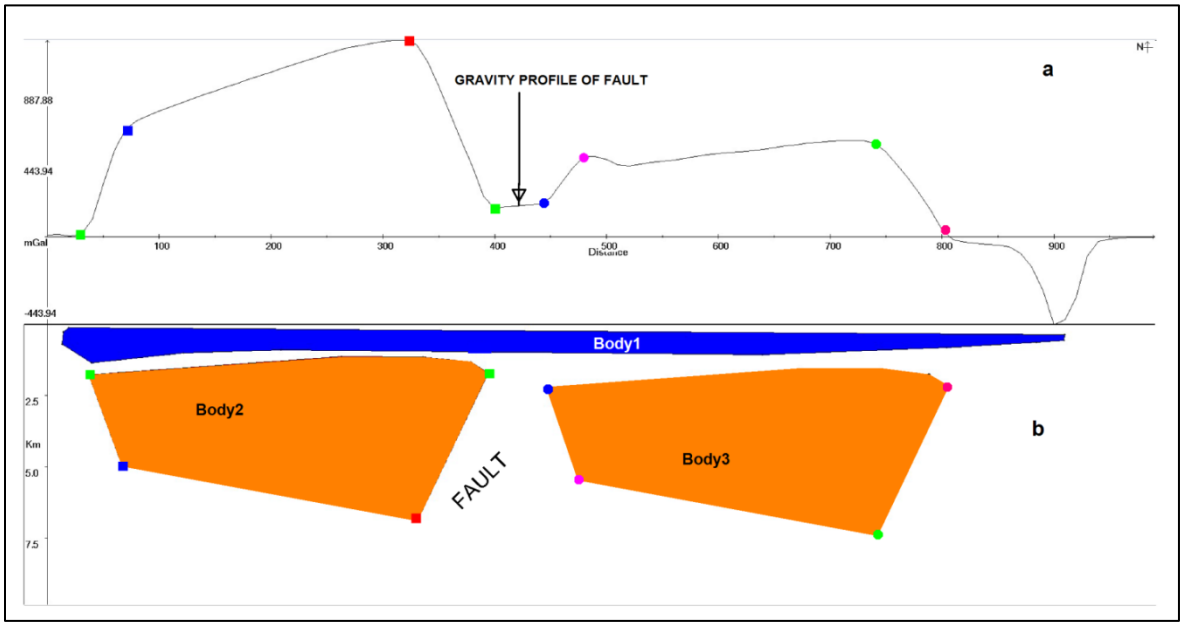

Figure 5.2: *Experimental model of a fault using gravity data from published petrophysical data. Body 1 corresponds to low density; bodies 2 and 3 correspond to the high densities; the fault is affected by erosion that reports as an irregularity in the profile between bodies 2 and 3. The letter a: represent the profile, b; correspond to the model constructed.*

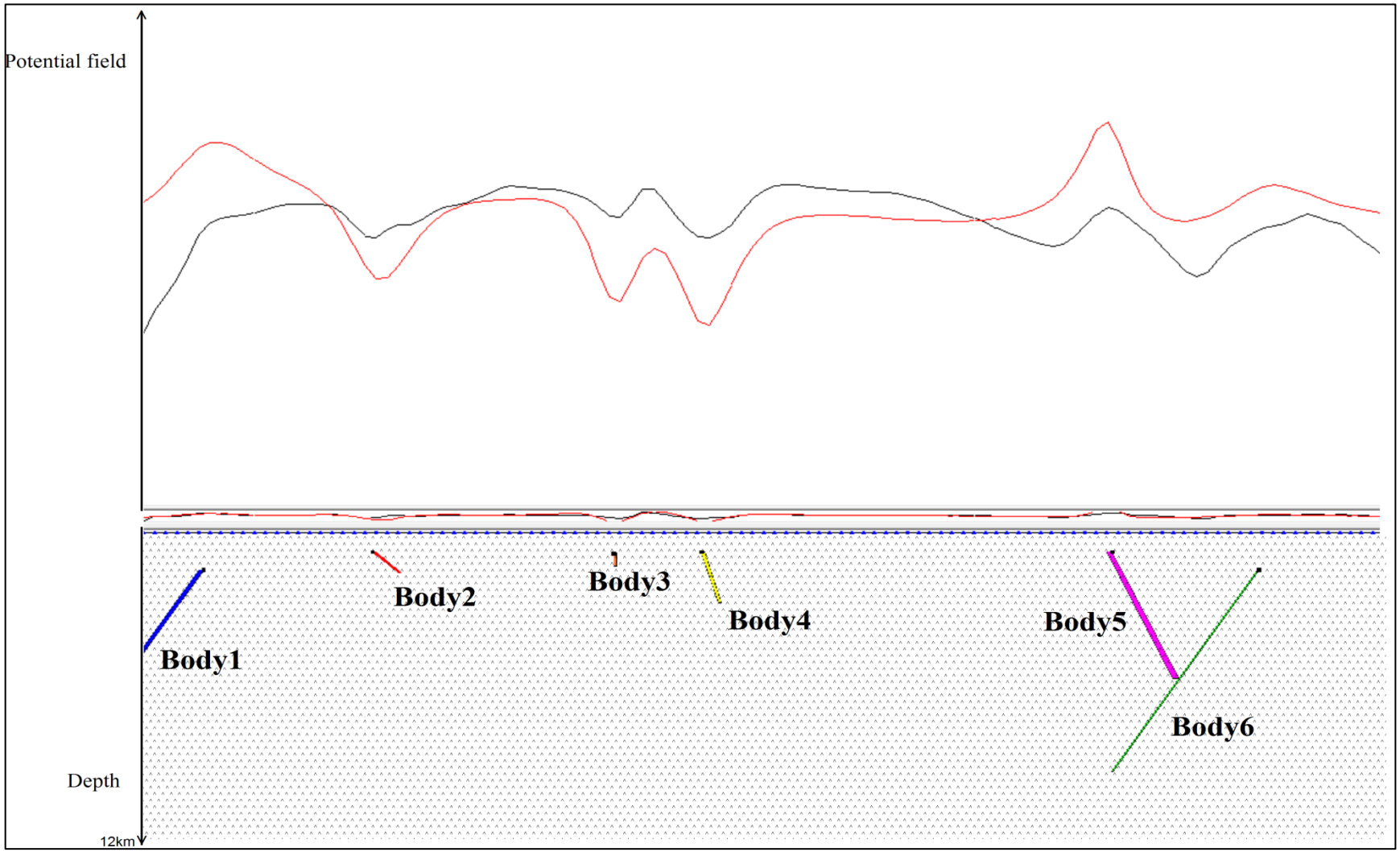

***Figure 5.3**: Forward model of the Transect AA' showing Profile AA'. The red curve is the calculated data and the black curve corresponds to the data measured. Bodies 1, 2, 3, 4, 5, 6 correspond to the different rocks type of the profile.*

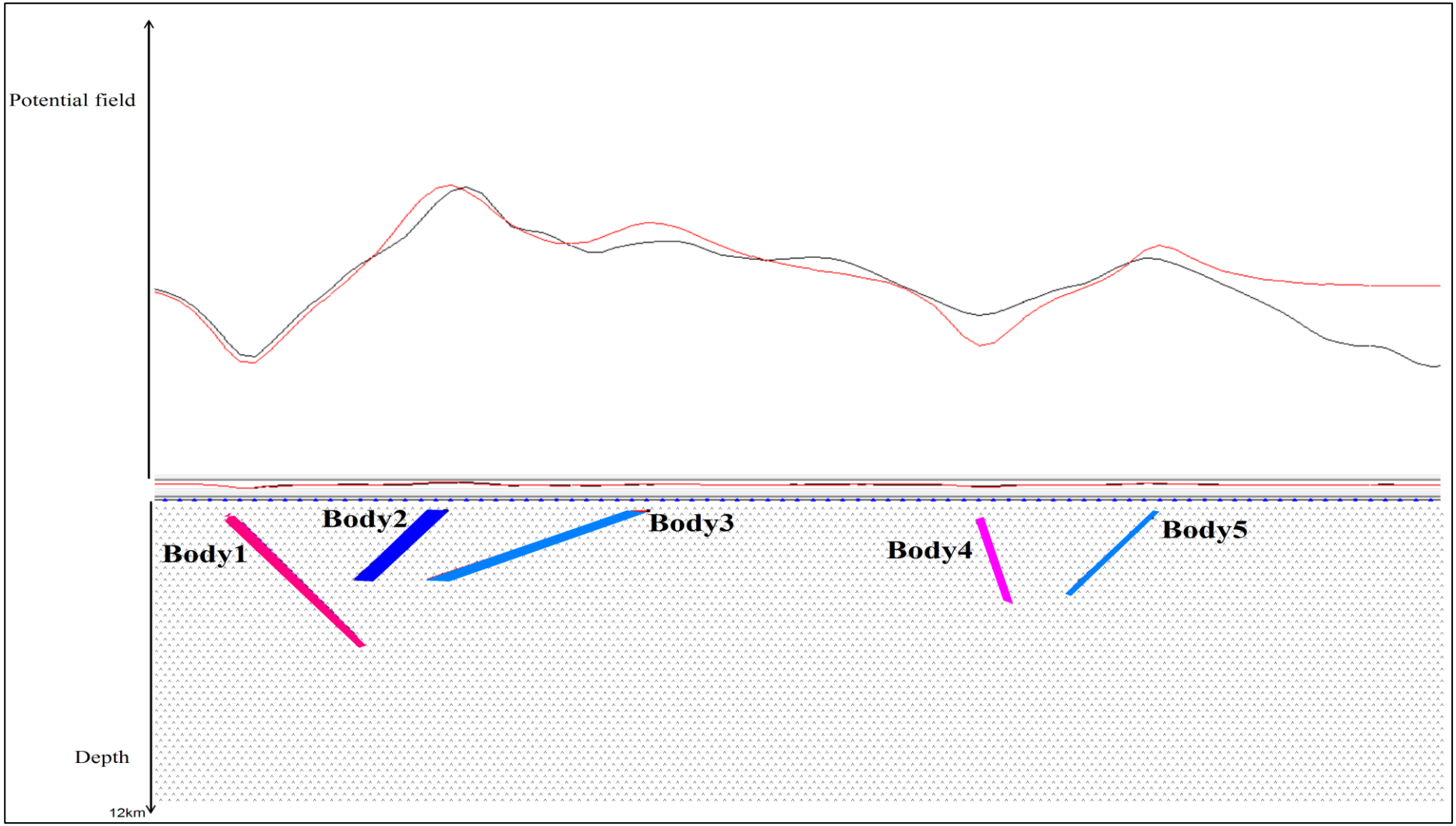

***Figure 5.4**: The forward model image of the Transect BB' showing the model for Profile BB'. The red curve is the calculated data and the black curve corresponds to the data measured. The bodies 1, 2, 3, 4, 5 correspond to the different rocks type of the profile.*

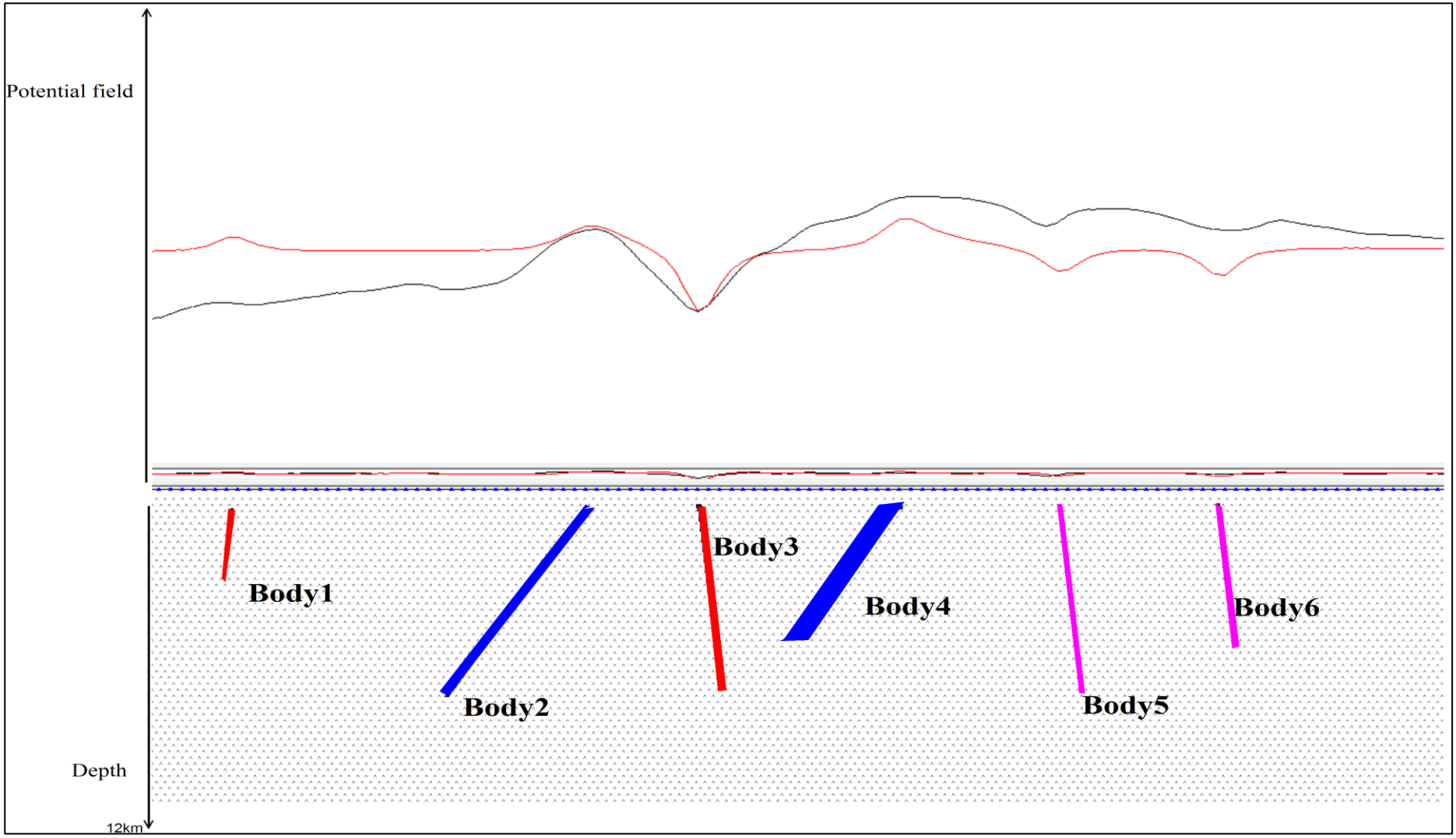

Figure 5.5: *The forward model of the Transect CC' showing the Profile CC' model. The red curve is the calculated data and the black curve corresponds to the data measured. The bodies 1, 2, 3, 4, 5, 6 correspond to the different rocks type of the profile.*

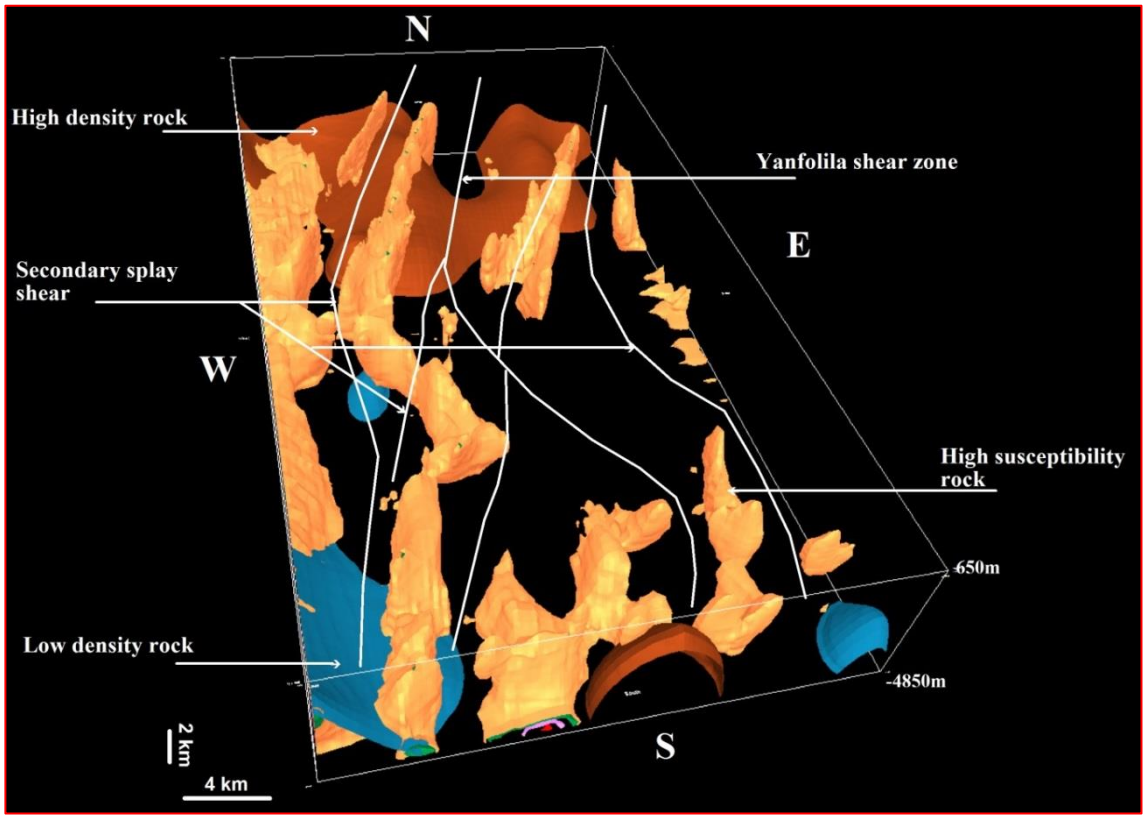

Figure 5.6: *The 3D inversion model of magnetic and gravity data for zone 1. The Yanfolila shear zone and the secondary splay shear are easily resolved. The shear zone is characterised by two parallel trends and the presence of a close upright symmetric fold (brown) in the south on the inversion. A number of southeast trending splay shears are also evident.*

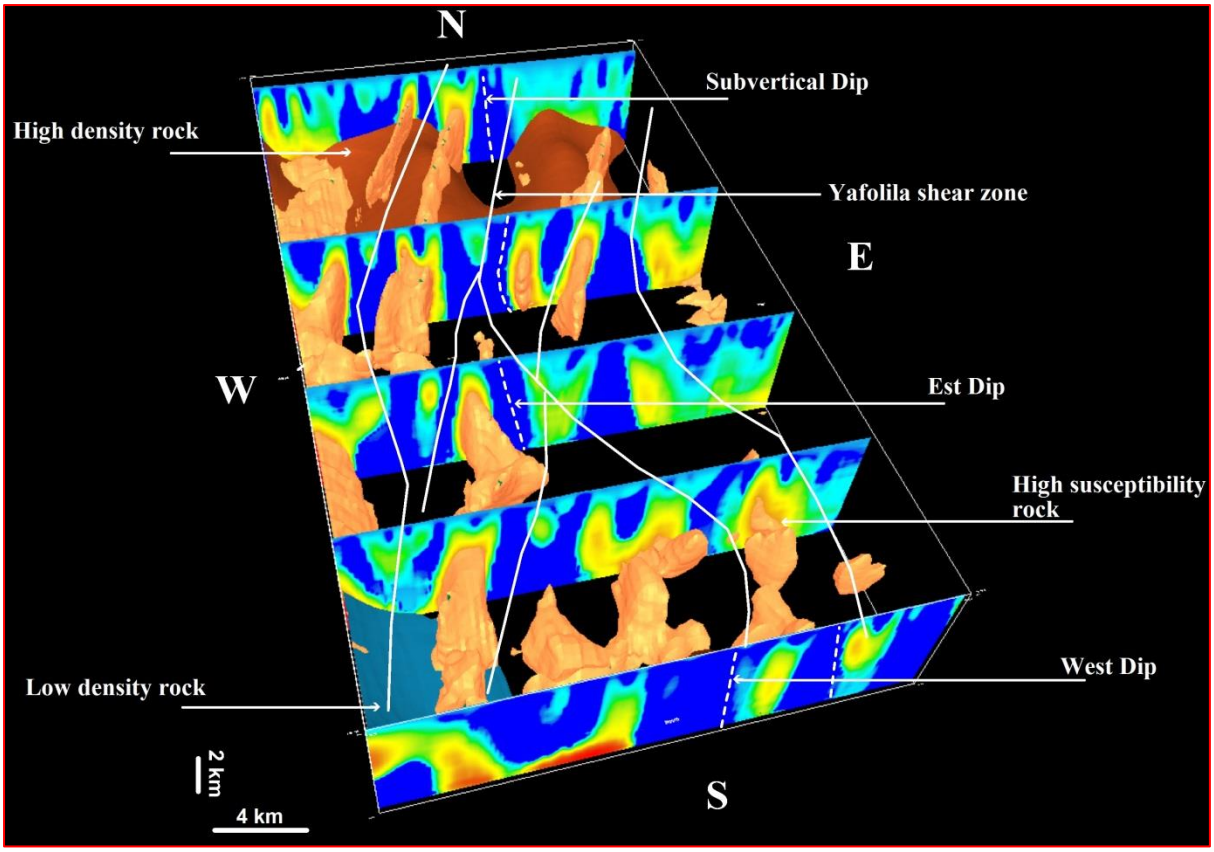

Figure 5.7*: Inversion section of magnetic data combined with magnetic and gravity isosurface of zone 1. The image describes the dip of Yanfolila shear zone with the section. The shear zone dip steeply west in the south, and steeply east in the centre and north of the inversion model. Secondary southwest trending splay shears dip subvertically to steeply west. The shears bound high susceptibility rock volumes, and in the centre of the inversion, form a left-handed (anticlockwise) sigmoid volume that is consistent with sinistral displacement in the plane of the Yanfolila shear zone.*

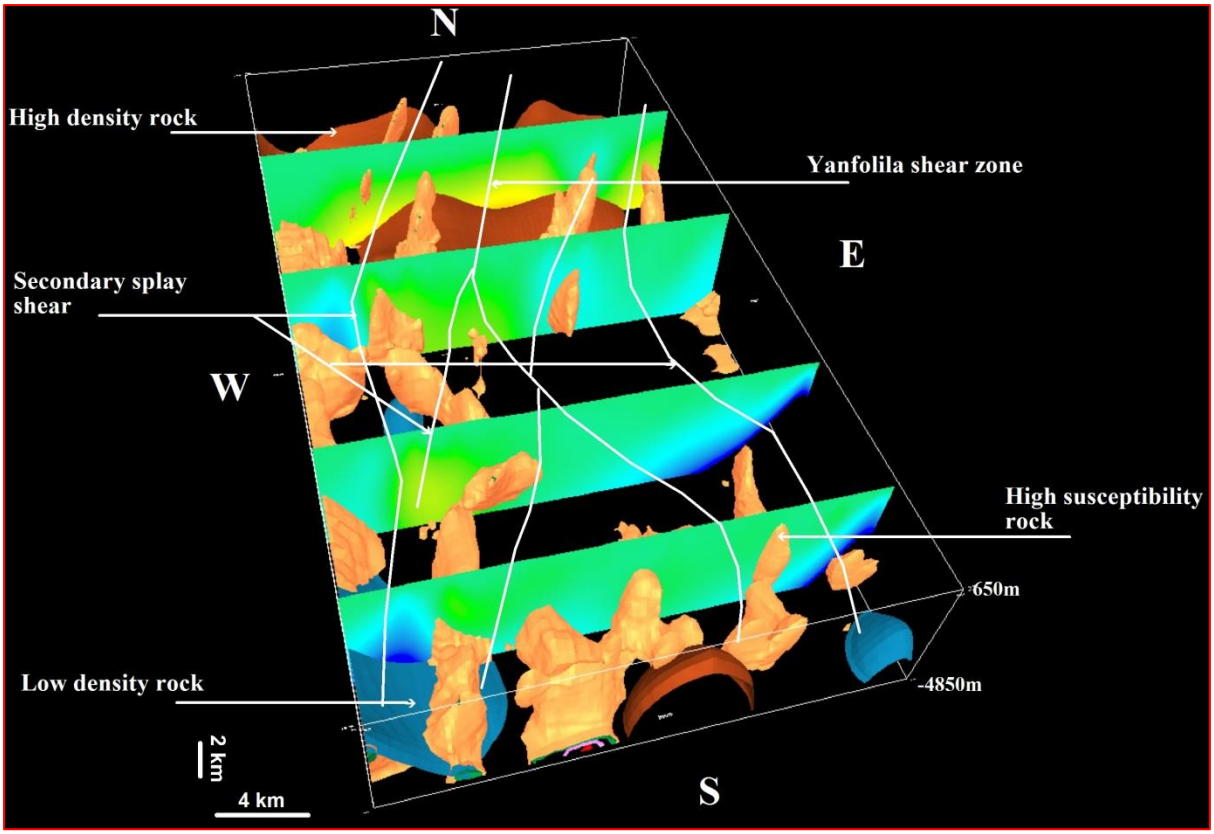

Figure 5.8: *Inversion section of gravity data combined with magnetic and gravity isosurface of susceptibility and density of zone 1.*

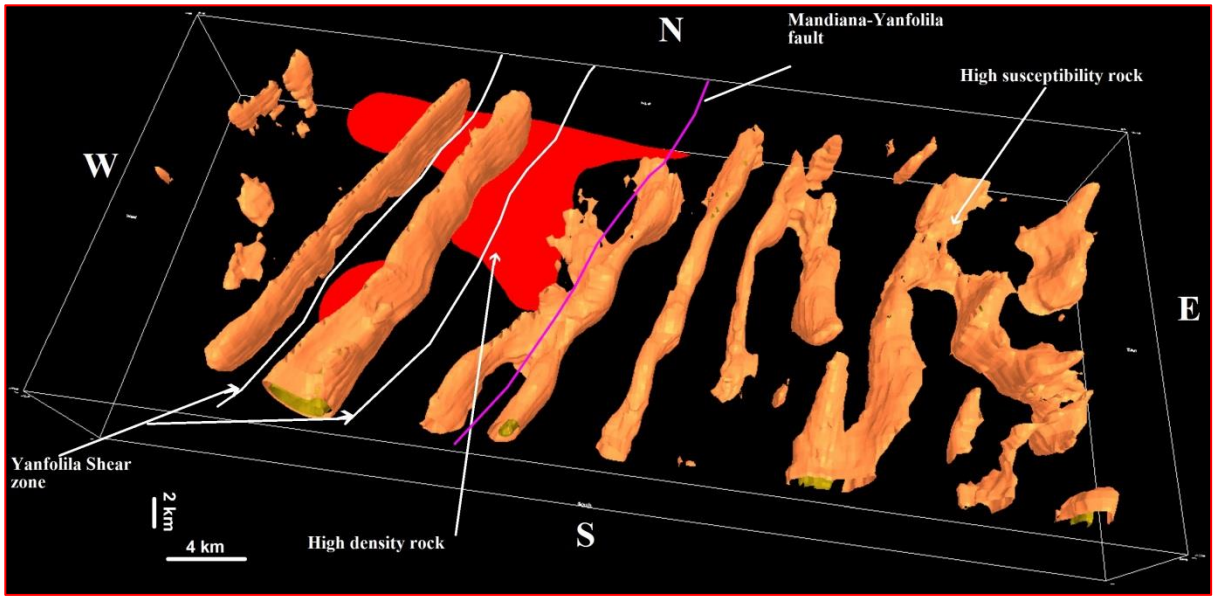

Figure 5.9: *The inversion image of magnetic and gravity data from zone 2. The image presents the trend of structures and rock volumes in 3D. High density rock volumes are located in the western region of the inversion adjacent to the Mandina-Yanfolila fault. The model also confirms the presence of this zone at depth. High susceptibility rock volumes generally trend north-northeast and are bounded by shears.*

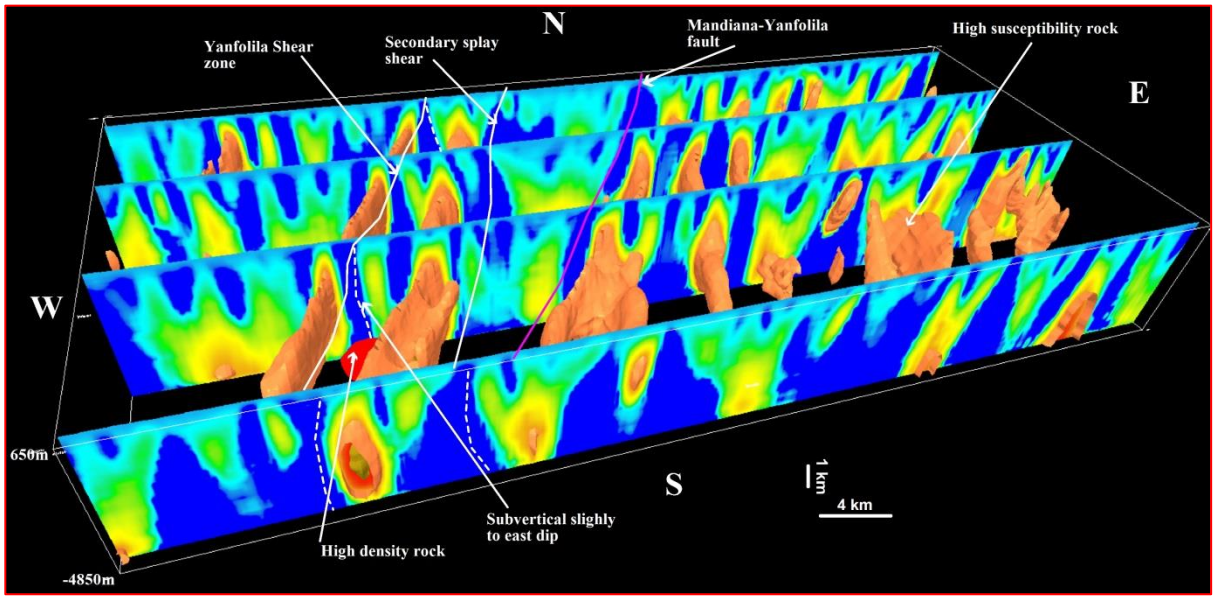

Figure 5.10: *Inversion section of magnetic data combined with magnetic and gravity isosurface of zone 2. The image describes the various dip orientations of Yanfolila Shear Zone in section. The majority of high susceptibility rocks dip steeply east, as do their bounding shear zones.*

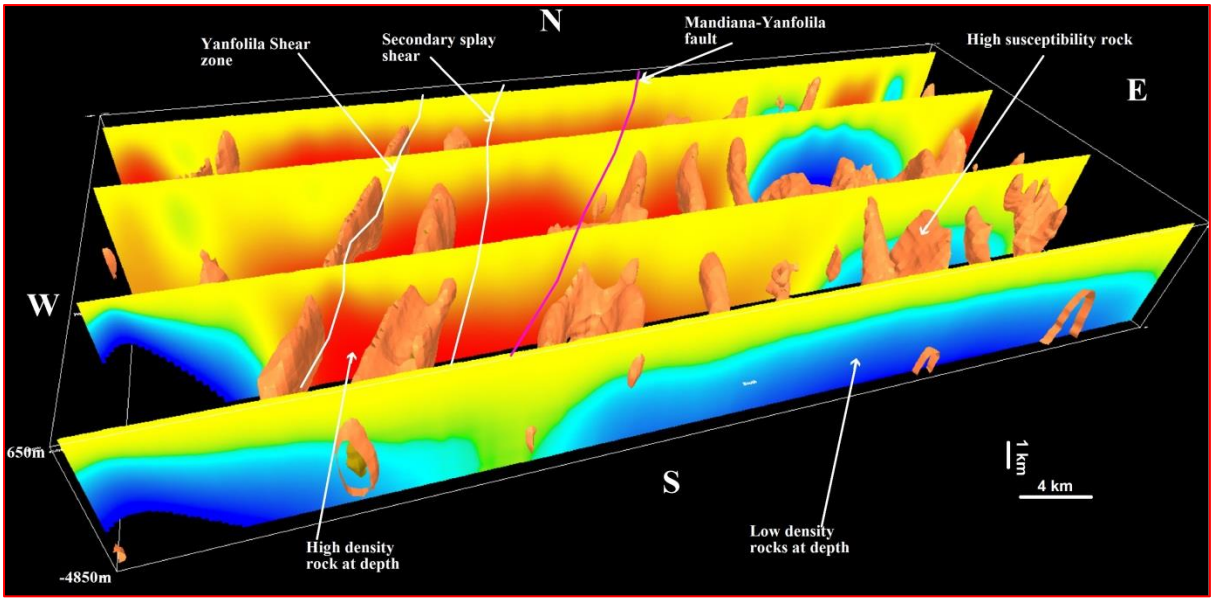

***Figure 5.11**: Inversion section of gravity data combined with magnetic isosurface of zone 2. The image shows the depth information of rock densities of zone 2. High density rock volumes occur at depth in the region of the Yanfolila shear zone, but these are (apparently) not crosscut by the shears.*

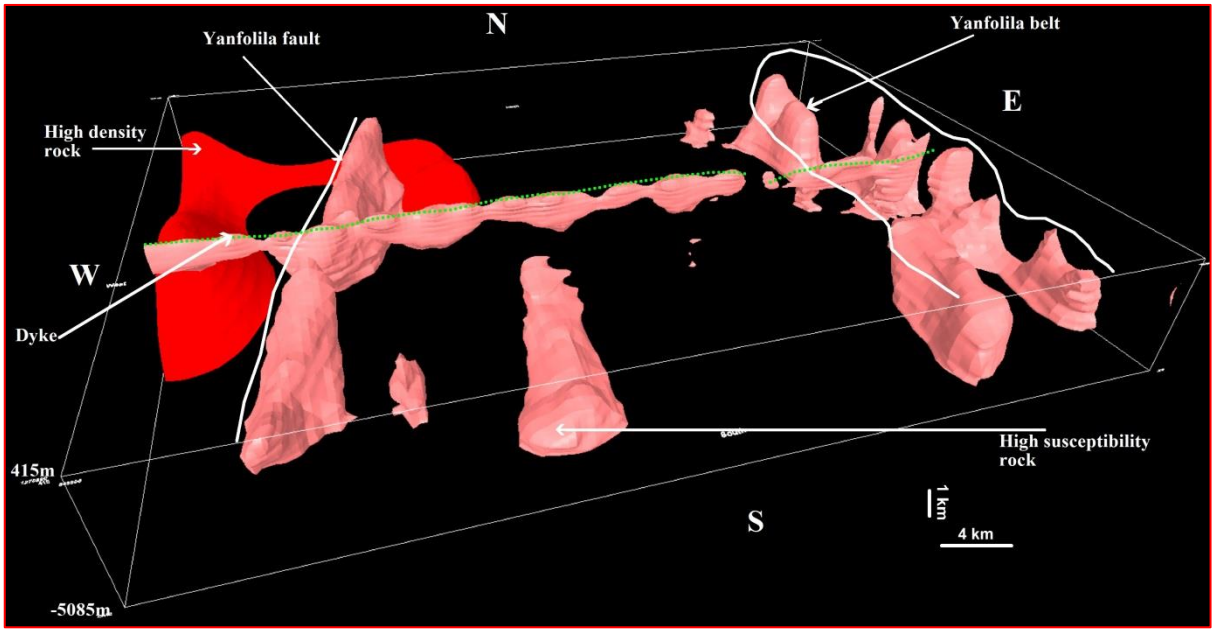

***Figure 5.12**: The inversion result image of magnetic and gravity data from zone 3. The image shows the trend of rock volumes in 3D including the Yanfolila Fault, Yanfolila, belt and east-west trending dyke. The model resolves generally north to north-northeast rock volumes. The north trending rock volume in the east corresponds with the position of the Yanfolila belt. The north-northeast trending rock volume in the west corresponds with the position of the Yanfolila fault. An east-west trending dolerite dyke is clearly evident in the inversion model and crosscuts the Yanfolila fault and Yanfolila belt.*

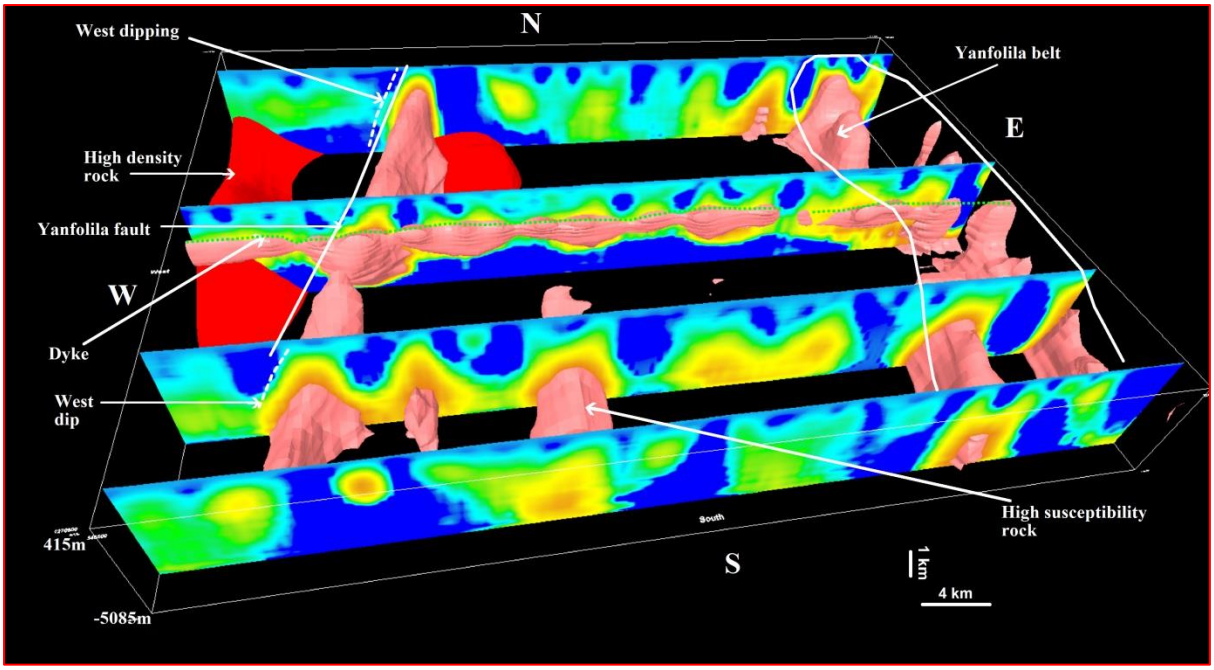

***Figure 5.13**: Inversion sections of magnetic data combined with magnetic and gravity isosurfaces of zone 3. The image describes the rocks geometry in section to give an overall 3D model of the region. The Yanfolila fault dips steeply west.*

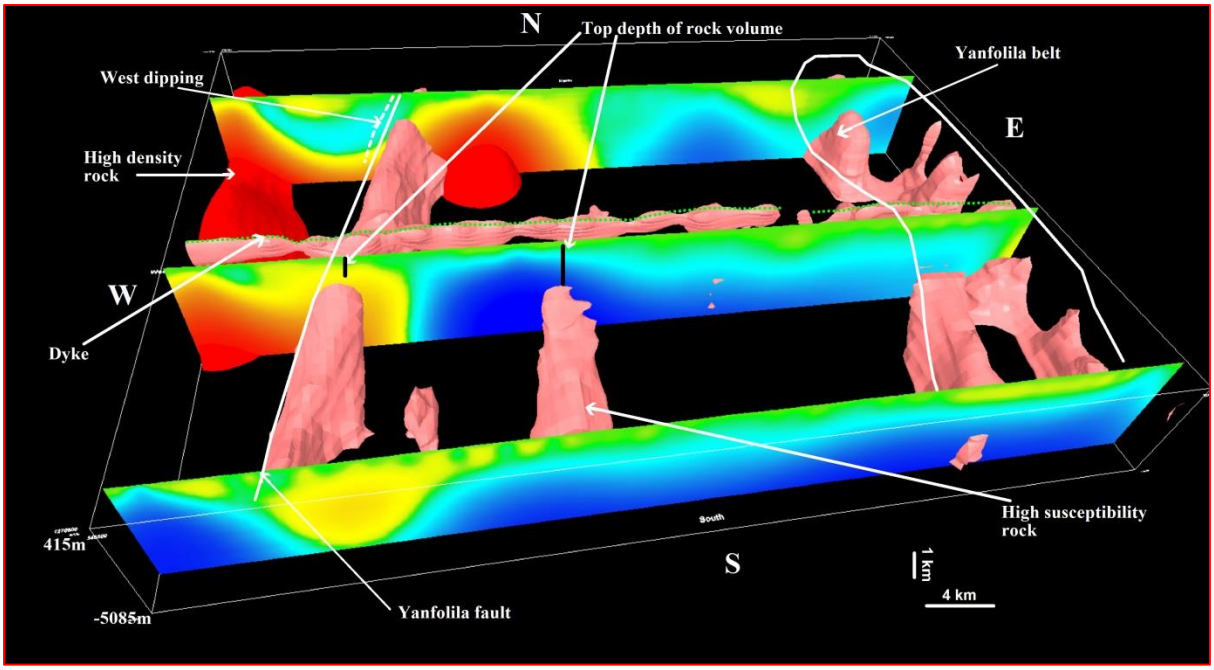

***Figure 5.14**: Inversion section of gravity data combined with magnetic and gravity isosurfaces of zone 3. The image shows depth information of rock densities, and high susceptibility rock volume top-depth as black lines.*

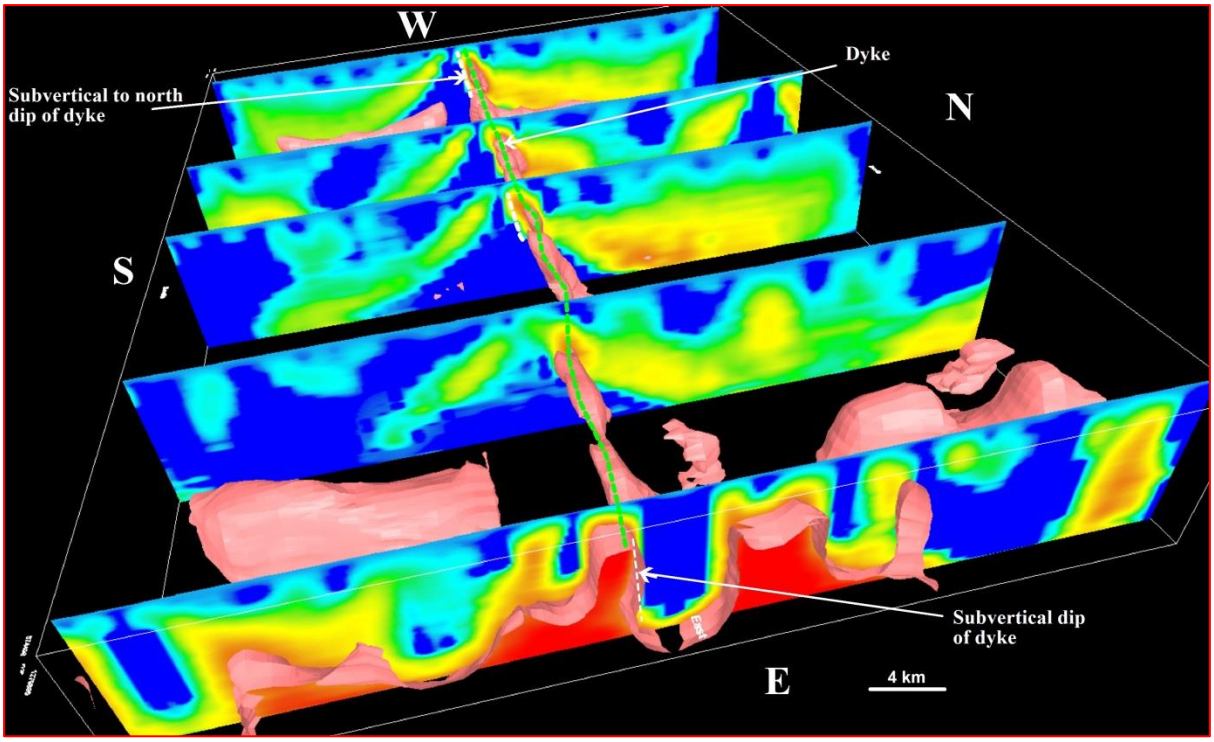

***Figure 5.15**: Inversion section of magnetic data combined with magnetic isosurface of zone 3 as viewed from the east. The image shows the dyke geometry with the magnetic sections. The dyke dips steeply to the south in the east, but rolls-over to dip steeply north in the west. High susceptibility values are located at approximately 300m depth for the dyke.*

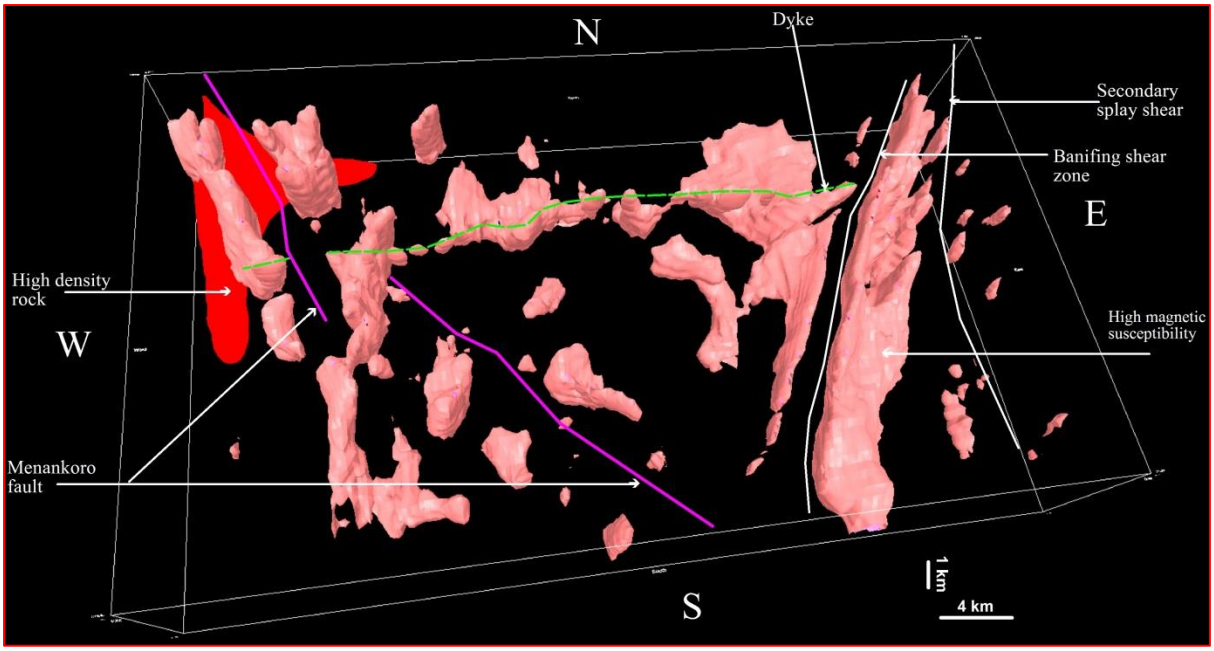

***Figure 5.16**: The inversion result of magnetic and gravity data for zone 4. The image shows the trend of rock structures and rock volumes with the magnetic and gravity isosurfaces. Structures include the Banifing shear zone and secondary splay shears, and the Menakoro fault, as well as an east-west trending dyke.*

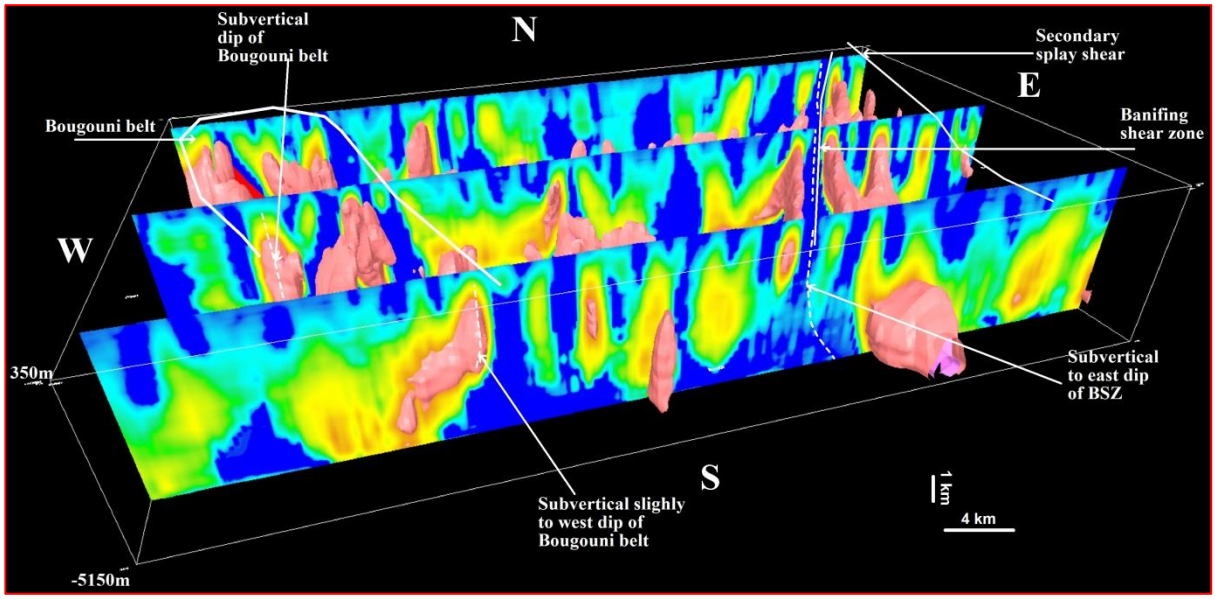

***Figure 5.17**: Inversion sections of magnetic data combined with magnetic and gravity isosurface of zone 4. The image describes the Banifing shear zone and rocks geometry in section as viewed from the south. Northwest trending rock volumes in the Bougouni belt dip sub-vertically to steeply west, while north trending rock volumes dip steeply east*

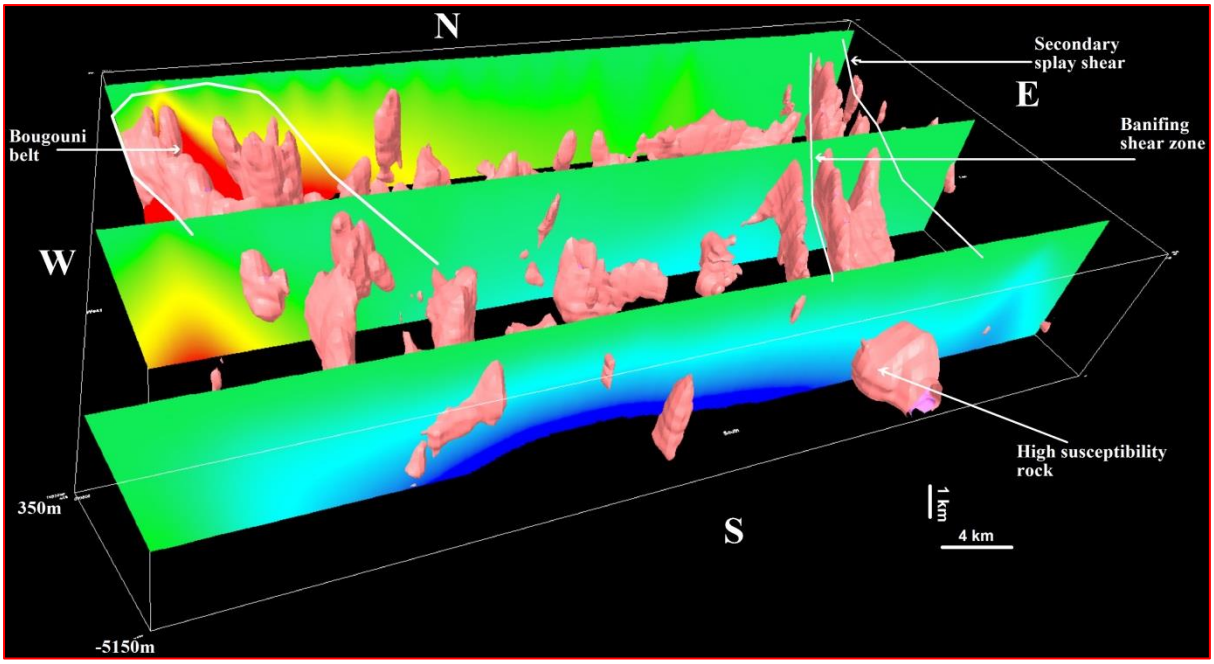

***Figure 5.18**: The inversion section of gravity data combined with magnetic isosurface of zone 4. The image shows the depth information of rock densities of zone 4. Also the density of Banifing shear zone can be determined from the gravity inversion sections.*

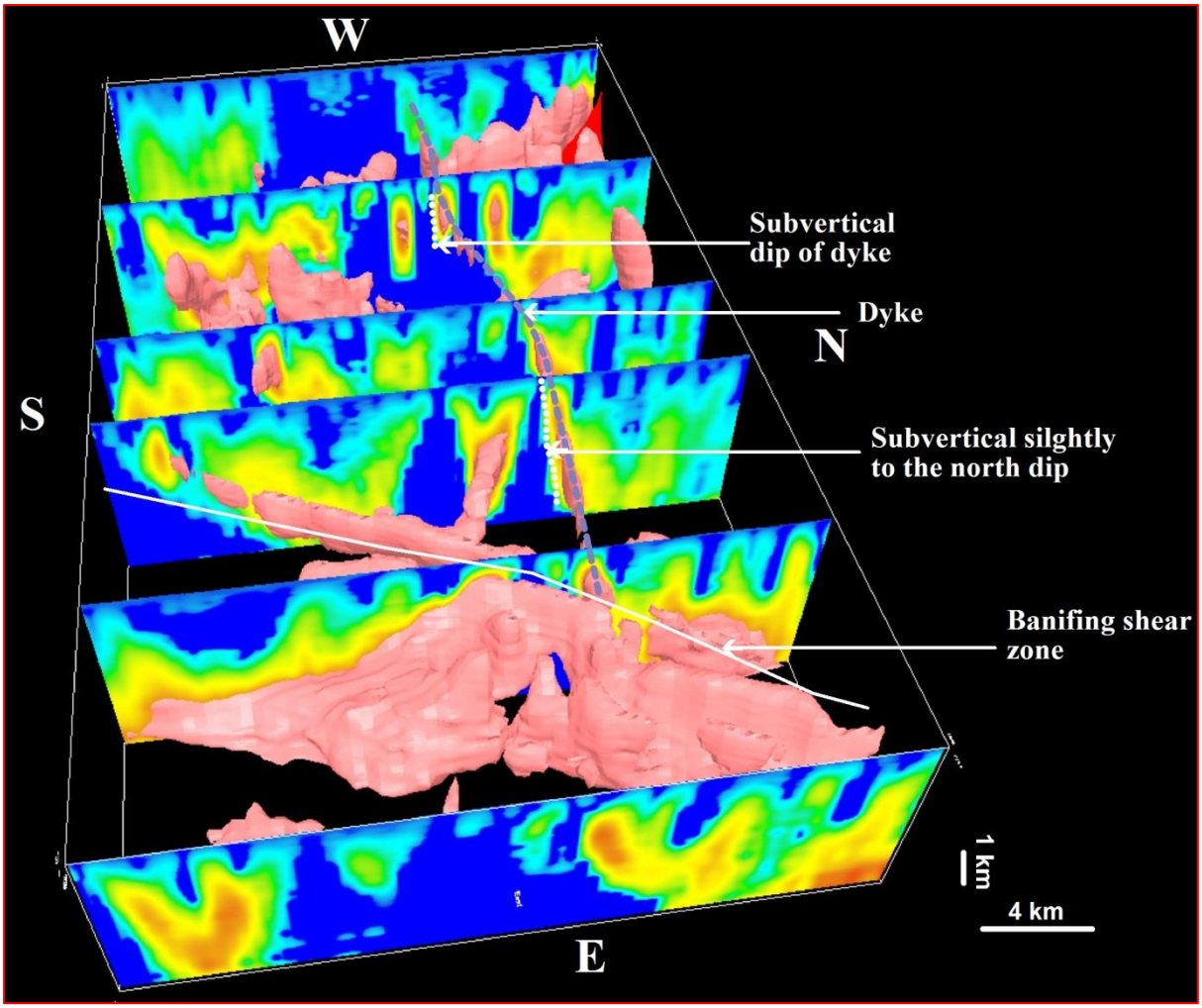

***Figure 5.19**: Inversion section of magnetic data combined with magnetic isosurface of zone 4 as viewed toward the west. The image shows the geometry of east-west trending dyke with a clear dip to the north to vertical. The thick sedimentary cover above the dyke is attributed to low susceptibility values at surface.*

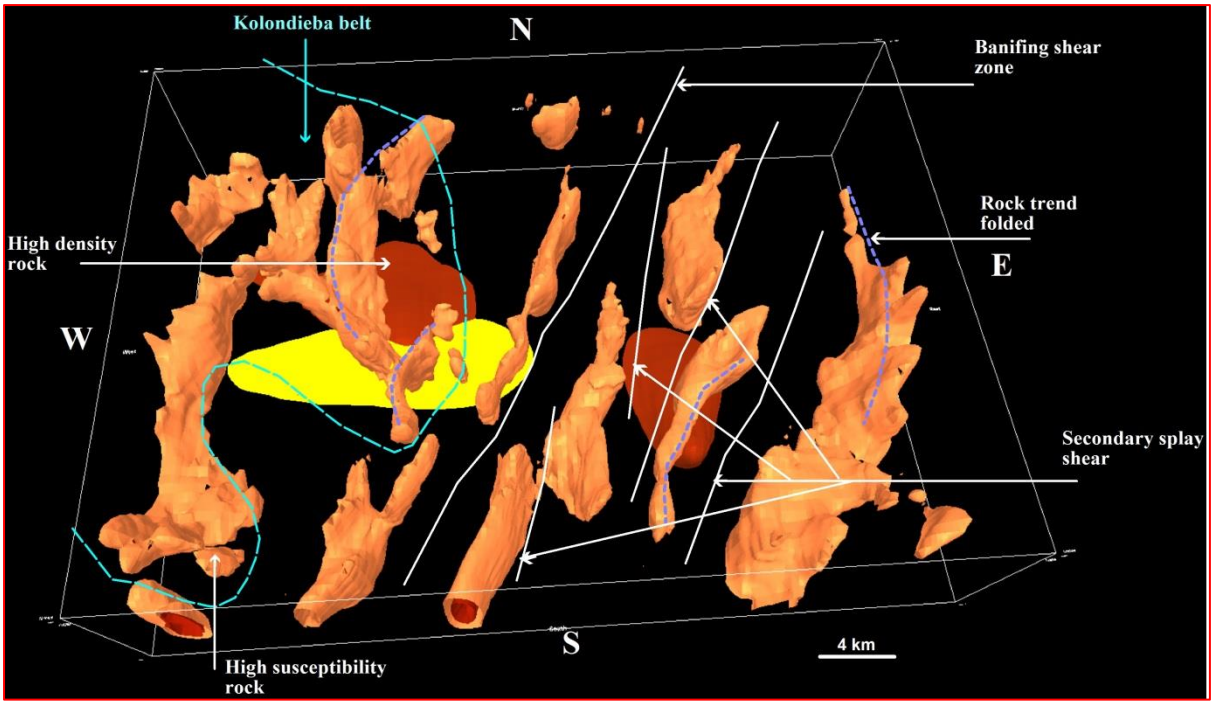

***Figure 5.20**: The inversion image of magnetic and gravity data from zone 5. The image shows the trend of magnetic and gravity isosurfaces and also structures and rock volumes. The structures include the Banifing shear zone and secondary splay shears. The overall shear trend can be defined as northeasterly, but internal north-northeast trending rock volumes form right-handed (clockwise) sigmoids that are consistent with dextral displacement in the plane of the Banifing shear zone. Two areas of high density values (brown) are resolved in the inversion model and correspond to gneissic rocks.*

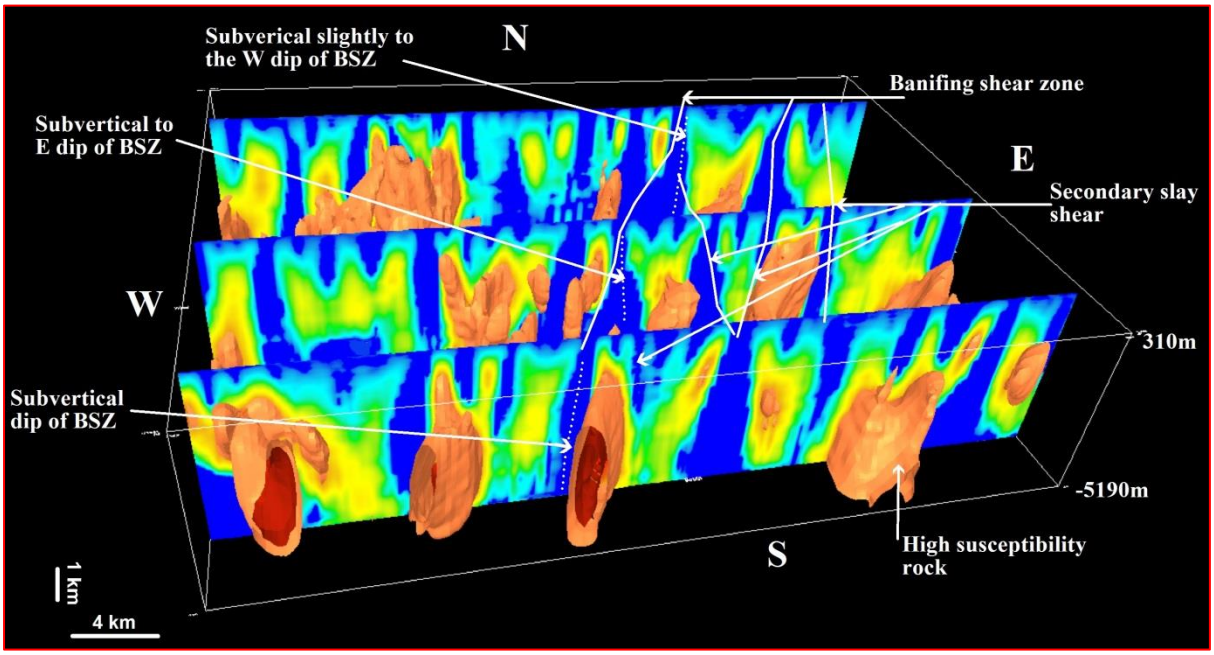

***Figure 5.21**: Inversion sections of magnetic data combined with magnetic isosurfaces for zone 5. The image describes the Banifing shear zone (BSZ) and rock geometries that are steeply dipping.*

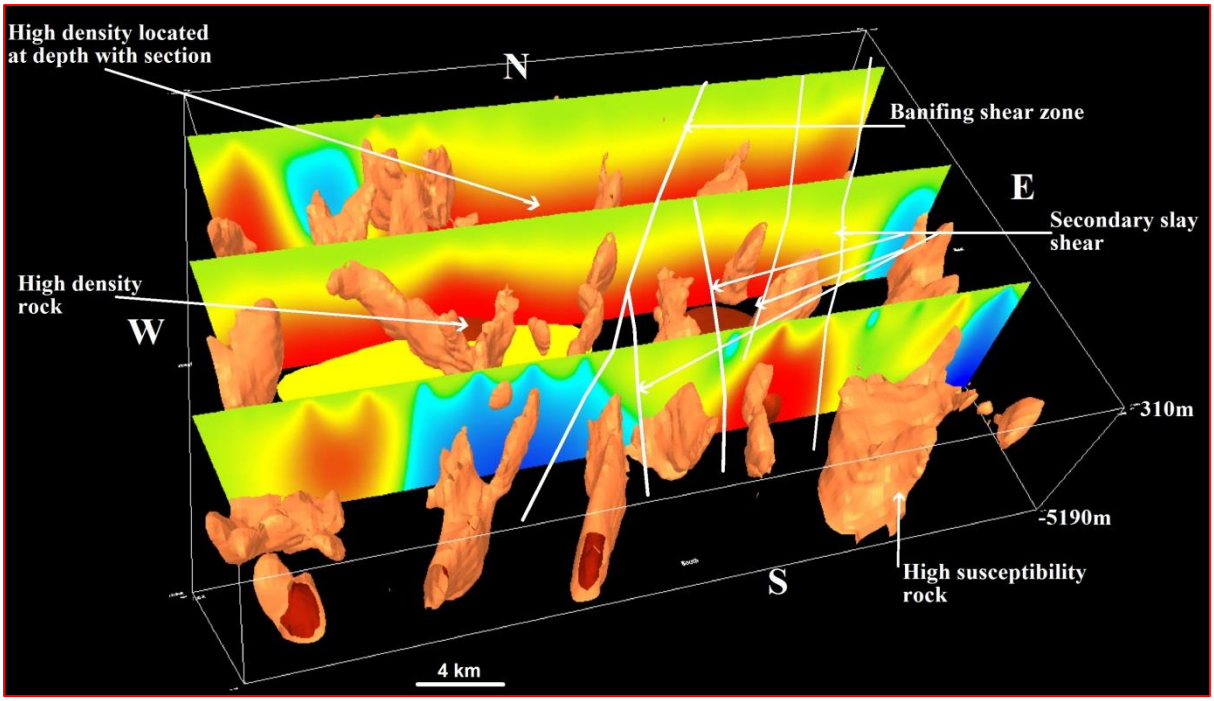

***Figure 5.22**: The inversion section of gravity data combined with magnetic and gravity isosurfaces for zone 5. The image shows the depth information of rock densities of zone 5. Also the density of Banifing shear zone and secondary splay shears can be determined in the gravity inversion sections.*

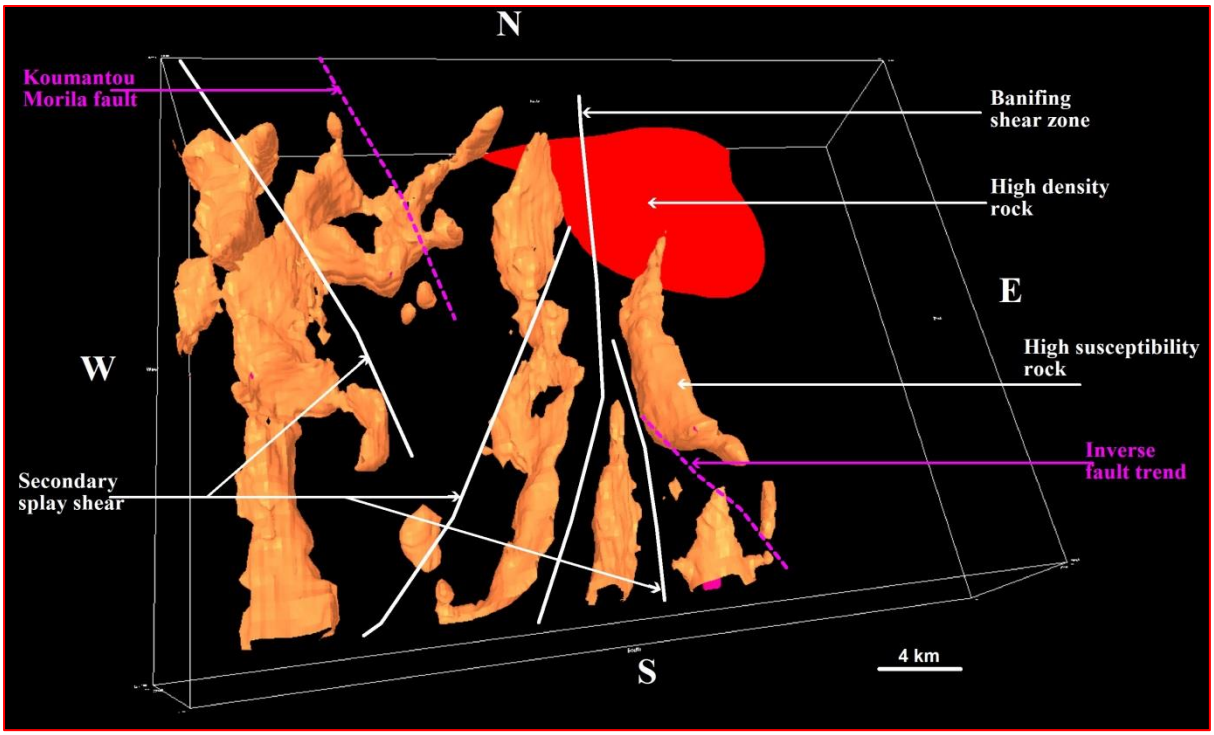

***Figure 5.23**: The inversion model of magnetic and gravity data from zone 6. The image shows the trend of structures and rock volumes in 3D, and the isosurface of magnetic and gravity data. The Koumantou-Morila fault is interpreted as are the Banifing shear zone and splay shears.*

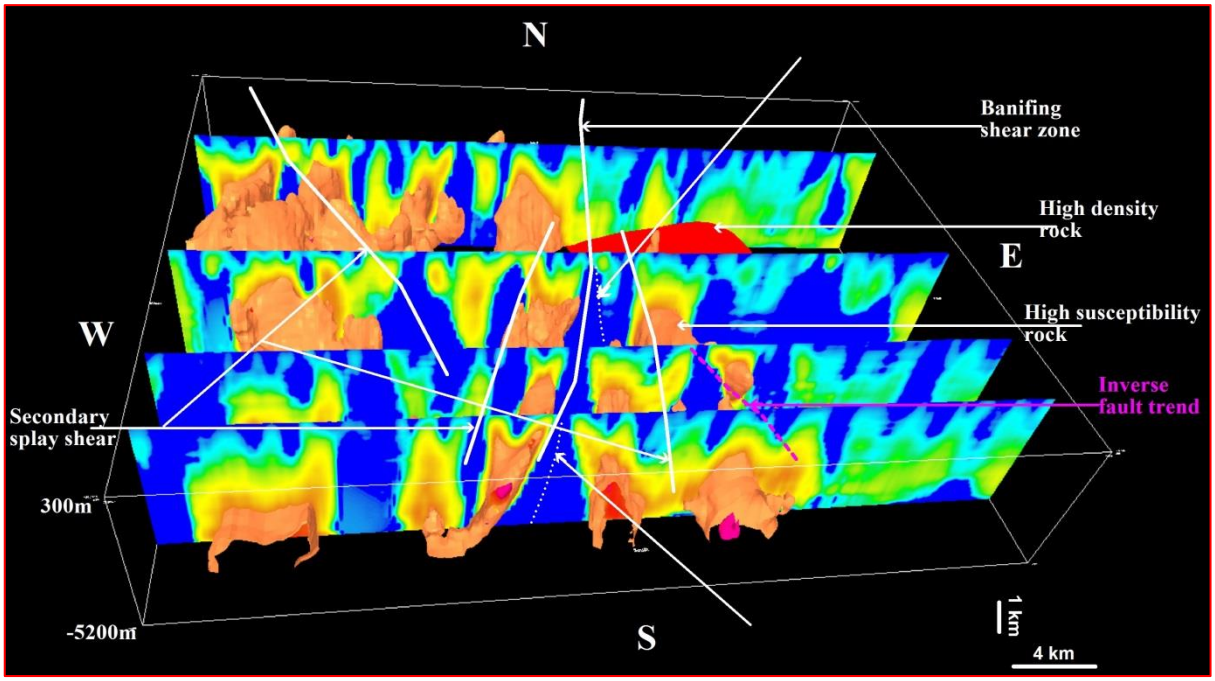

***Figure 5.24**: Inversion sections of magnetic data combined with magnetic and gravity isosurfaces of zone 3.*

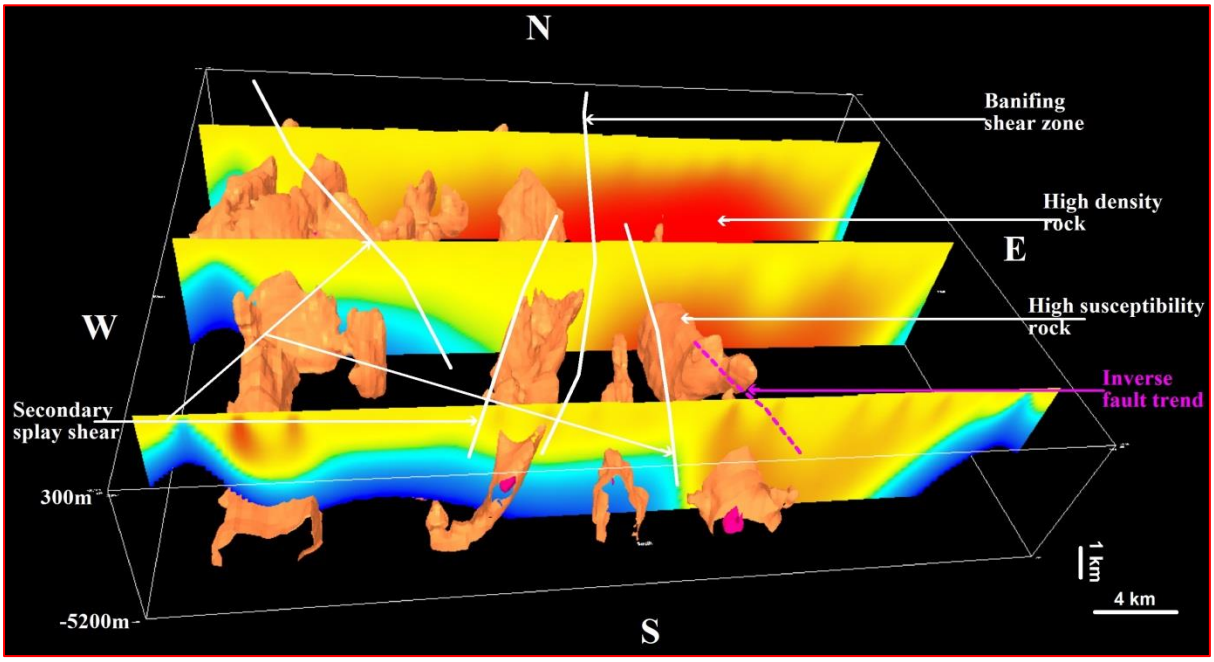

***Figure 5.25**: The inversion section of gravity data combined with magnetic isosurfaces of zone 6. The image shows the depth information for rock densities in Zone 6.*

6. KEY AREAS

6.1. Introduction

A critical aspect of inversion in geophysics is its limitation in terms of depth constraints and geological data for rock volumes beyond the level of drilling programs. In the absence of geological and structural model in the area of inversion it becomes hard to control the quality of the final model of inversion. However, the architecture, geometry and form of structures and dykes can be predicted to some extent using experimental analogue models as being a reasonable predictive tool for the behaviour of structures and dykes at depth. In this chapter, published experimental analogue models, such as those presented by McClay and Bonora (2001), Kim and Sanderson (2005), Bergen and Shaw (2010) and others, are used to control the quality of inversion (using surface petrophysical data) at depth for structures and dykes.

Geophysical data combine all geological phenomena into one dataset, from oldest to youngest for a given area. For the study area, the geological phenomena span at least 3.0Ga of Earth history. Consequenltey, care was taken in the quantitative interpretation by using the map from Whiteside et al. (2007) to locate young intrusions on the geophysical maps. It was important to have a good appreciation of the geological background of the region in order to facilitate the interpretation of geophysical data. For example, for a robust and plausible interpretation of the study area, young geological signatures such as high density, high magnetic mafic dykes, sills and intrusions of the Central Atlantic Magmatic Provinces (CAMP) were taken into account (Whiteside et al., 2007). These mafic dykes, sills and intrusions were emplaced at approximately 202 Ma which is considerably younger than the Palaeoproterozoic geology of the Baoulé-Mossi domain that dominates the study area.

Key areas in Figure 6.1 can be correlated with inversion zone and transect lines in Figures 4.17. They include:

(1) Key study area 1 is equal to Inversion Zone 1 (Section 5.3.1) and incorporates part of the Yanfolila shear zone. It covers transect and profile AA’ (Section 5.2.1).

(2) Key study area 2 is equal to the Inversion Zone 4 (Section 5.3.4) located in the southern part of Banifing shear zone. It covers transect and profile BB’ (Section 5.2.2)

(3) Key study area 3 inversion zone includes Inversion Zone 3 (Section 5.3.3).

6.2. Geophysical processing

The geophysical inversion workflow included the inversion algorithm developed by UBC-GIF incorporated into WinDisp® software. The executable program is named MGinv3d, which is used as

a utility in WinDisp®. 3D model construction was achieved using 3D MODELLER in WinDisp®. Magnetic and gravity data were used for inversion. The magnetic data was smoothed using the upward continuation to remove short wavelengths and minimize the effect of ferricrete on the data. In West Africa, ferricrete was formed during the Cretaceous and remobilised during the Miocene-Eocene (Brown et al., 1994; Blot, 2004; Beauvais et al., 2008). The topography was also used to determine the relative elevation of the area of inversion in order to estimate the relationship between topography with geology and structures.

6.3. Key study area 1- southern part of Yanfolila shear zone

This key study area 1 was selected as a case study to test the application of experimental analogue models of shear zones to constrain the inversion of the Yanfolila shear zone at depth. Key study area 1 is composed of sedimentary and volcanic rocks (WAXI 2013). The Yanfolila shear zone trends north-northeast, and measures approximately 235km in length and 18km in width.

The 3D model from the inversion is presented in Figures 6.2 and 6.3. They show four different isosurfaces for magnetic data, and three for gravity data according to the susceptibility and density values. The values of the susceptibility isosurfaces for magnetic data (in $SI.10^{6)}$ range from 10000 (in orange colour), 12000 (green), 18000 (pink) to 22000 (red). The density values in cgs are 89 (blue), 100 (orange) and 115 (red). Faults, shears and other geological discontinuities are easily resolved on the magnetic inversion isosurfaces (Figure 6.2).

Figures 6.4 and 6.5 respectively present magnetic susceptibility and density inversion sections combined with the magnetic isosurfaces. The sections show high magnetic susceptibility (red), intermediate (yellow) and low susceptibility values (blue) for magnetic and gravity inversions. The blue in the magnetic data sections corresponds to low magnetite content related to faults or shears. The red and yellow isosurfaces correspond to various undifferentiated rocks types with medium to high magnetite content.

The low susceptibility on magnetic sections coincides with the high density of gravity section, which could correspond to young sedimentary rocks with high compaction or meta-volcanic sedimentary rocks, i.e., the process of metamorphism could change low density mineral into dense mineral in the rocks.

The moderate susceptibility values that coincide with low density correspond to the granite according to the density and susceptibility of certain rocks and minerals (Telford et al., 1990; Parasnis, 1996; Kearey et al., 2009;) and also the petrophysical data and geological maps available (c.f., Girard et al., 1998; Feybesse et al., 2006a; Parker and Wilkinson, 2011; Miller et al., 2013; WAXI, 2013). The granite in key study area 1 is interpreted as Palaeoproterozoic in age because there are no granitic rocks associated to the intrusion of the CAMP (202Ma).

The high susceptibility values that coincide with high density values are interpreted as basalt-andesite. The basalts in key area 1 are not intruded by Palaeoproterozoic granitoids and may correspond to the CAMP stage, approximately 202 Ma (Whiteside et al., 2007).

Figure 6.6 is a combination of sections and isosurfaces. The trend of the isosurfaces exhibit high magnetic susceptibility that coincides with rocks of low density in the south, but high density in the north. The same rock volume presents high density in the northern part of key area 1. They could be granodiorite according to the density and susceptibility values (Telford et al., 1990; Kearey et al., 2009; Parasnis, 1996) and from maps of Girard et al. (1998); Feybesse et al. (2006a); Parker and Wilkinson (2011). The moderate density values with high susceptibility are related to andesite.

The discontinuities observed with the section and trend of isosurfaces are oriented north-northeast, northeast and northwest for key area 1. According to the inversion modelling of key area 1 (Section 5.3.1), the Yanfolila shear zone presents a complex structure with a series of secondary splay shear (Figure 6.4). The Yanfolila shear zone as a complex structure forms a series of discontinuity and breaks.

According to the Figures 6.4 and 6.5, the Yanfolila shear zone is made up of 3 parallel shears (rather than 2) with a splay that bifurcates to the southwest. This arrangement corresponds to the sinistral strike-slip and a clockwise rotation of the rocks volume in the inversion space, using analogue models of strike-slip restraining step-over faults from McClay and Bonora (2001), and the dual layer model of Dooley and Schreurs (2012). Sinistral strike-slip architectures can be confirmed for the Yanfolila shear zone with possible flower structure. Folds are observed where the Yanfolila shear zone changes dip.

6.4. Key study area 2 - southern Banifing shear zone

The southern part of the Banifing shear zone was selected as a key area to model dykes that crosscut the Bougouni belt, Menankoro fault and Banifing shear zone. This study area tests the inversion of dykes crosscutting shear zones, faults and a volcano-sedimentary belt, in comparison with the analogue models where dyke formation is explained.

The geology of key area 2 is the same as described in Inversion Zone 4 (Section 5.3.4). The main structure of the study area is the Banifing shear zone, which is a first-order crustal scale structure. The Banifing shear zone trends northeast, and is approximately 168 km long and 16 km wide. In addition to the Banifing shear zone, the Menankoro fault occurs as a second-order structure that trends northwest.

The 3D model from magnetic and gravity inversions are presented in Figure 6.7. The Figure 6.7 exhibits;

1. Three different isosurfaces according to the susceptibility values. The values of susceptibility

isosurfaces for magnetic data in SI.10^6 range from 20000 (low) orange, 30000 (moderate) in pink to 42000 (high) in red.

2. The density values for gravity isosurface in mGal are 88 low value (blue), 95 moderate value (orange) and 99.9 (high value) corresponding to the red. Discontinuities can be observed with the isosurface trends (Figure 6.8).

According to the combination of susceptibility and density isosurfaces, the geological rock types present in key area 2 can be established. Figures 6.8 and 6.9 show a coincidence of high susceptibility and high density values in the northwest of key area 2 that could correspond to basalt. The moderate density values in the gravity section combined with the susceptibility section and isosurface (Figure 6.9) show a dolerite dyke. The dyke crosscuts other geology (granite, gneiss, sediment with quartzite intercalation) indicating it is younger than those units.

Figure 6.8 presents rock volumes that trend northeast and which are bound by the Banifing shear zone. Figure 6.9 resolves moderate to high magnetic susceptibility values that coincide with low to moderate density, and high density can also be observed in the northwest. The coincidence of moderate to high susceptibility and low to moderate density is interpreted as granite. The moderate susceptibility and low density is interpreted as undifferentiated sediment with intercalation of quartzite. The northwest of the key area 2 shows a coincidence of high susceptibility and high density that corresponds to basalt-andesite in the Bougouni belt.

Gneissic rocks can also be identified in the Bougouni belt as derived from high susceptibility and moderate density. Although gneiss and granite are similar in terms of composition, the difference is that the susceptibility and density of gneiss is higher than that of granite (*sensu stricto*).

It is also possible to map the Menankoro fault in Figure 6.8, which is oriented northwest and crosscuts granite, and sedimentary rocks with quartzite intercalation. The trend of the Banifing shear zone is easily resolved in Figure 6.8, as are secondary splay shears that merge with the Banifing shear zone in the north of the study area.

Figure 6.9 is a combination of magnetic and gravity sections plus magnetic isosurfaces and resolves the Banifing shear zone and an east-west trending dyke. The magnetic inversion sections map: (1) a subvertical to north dip for the dyke where it crosscuts the Menankoro fault, (2) the dyke dips north in the Bougouni belt and (3) the dyke dips sub-vertically where it crosscuts the Banifing shear zone.

The magnetic sections combined with magnetic isosurfaces (Figure 6.10) resolve an east dip for Banifing shear zone in the south, to subvertical in the centre and the north. Secondary splay shears dip steeply to the west. The Menankoro fault dips subvertically to steeply east. The rock volumes bounded by the Banifing shear zone are interpreted as sedimentary rock with quartzite intercalation and granitoid.

The comparison of the analogue modelling (McClay and White, 1995) with the key study area 2 shows a system of faults. The western part of the key area 2 shows a series of faults that could be compared to transfer faults with an accommodation zone (Figure 6.8). The presence of transfer fault in this area may indicate extensional tectonics characterised by basin and normal faults geometries in the study area.

6.5. Key study area 3- southern part of Yanfolila belt

The choice of southern part of Yanfolila belt as a key study area 3 was because the Yanfolila belt and Yanfolila fault are crosscut by a dolerite dyke. Key area 3 is compared to key area 2 where the dyke crosscuts a volcano-sedimentary belt, a fault and a shear zone. The comparison of key area 3 with key area 2 was undertaken to evaluate the limitations in the results of inversion when using analogue models.

The geology of the key area 3 has been described by WAXI (2013) as composed of diorite, sandstone, conglomerate, felsic intrusive contains rich in xenoliths, porphyry intrusives, granodiorite-diorite, granite, and pegmatites with very large plagioclase phenocrysts. The main structure of the key area is the Yanfolila fault and trends northwest. The key area is also characterized by Yanfolila belt and dyke.

The 3D model from the inversion presented in Figure 6.11 shows four different isosurfaces for magnetic data, and three for density according to the susceptibility and density values. The isosurfaces for magnetic data in SI 10^6 range from 10000 in orange colour, 12000 green, 14000 for pink to 17000 (high) for red. The density values in CGS are 88 (low) corresponding to the blue colour, 94 (orange) and 99 (high value) corresponding to red.

Figure 6.12 is a magnetic isosurface describing the rock volume trend; three (3) rock volume trends can be identified and include north-northeast, north and east-west. A discontinuity marks the trace of the Yanfolila fault. The north trend in the eastern part of key area corresponds to the Yanfolila belt rock volume. The north-northeast and north trend in the centre and the western part of key area is related to the rock volumes that bound the Yanfolila fault. The east-west trend is related to a dolerite dyke. Non-consolidated sedimentary rocks are situated between the Yanfolila fault and Yanfolila belt and are characterized by low susceptibility values and low density values (Figure 6.12).

Figure 6.13 presents magnetic and gravity inversion sections. The sections exhibit high magnetic susceptibility in red and yellow, intermediate in green and low susceptibility values in blue and high density in red, moderate (yellow) and low (blue) for gravity inversion sections. The blue in magnetic data sections is related to less magnetite content in the host rocks. The red and yellow correspond to the different rocks types in the inversion zone. The blue in the gravity data could be related to a discontinuity and/or unconsolidated sediments.

According to the Figure 6.14, the east-west trending dyke that crosscuts the key area resolves two dip directions: (1) a north dip in the west and the centre of the section where the dyke crosscuts the Yanfolila fault and sedimentary rocks, (2) a subvertical dip where it crosscuts the Yanfolila belt in the eastern part of the key area.

The comparison of key area 3 with analogue models shows a limited use of analogue model in certain cases to control the quality of inversion for structural description of the key area 3. However, the Yanfolila can be described as a sinistral strike-slip fault.

6.6. Synthesis

The inversion model of the Yanfolila shear zone using analogue models in key area 1 shows that:

- The Yanfolila shear zone is a complex structure composed of a main shear zone with secondary splay shears that bifurcate to the southwest.
- Volumes of the sedimentary rock are enclosed by the Yanfolila shear zone and splay shears. There distribution and extend can be estimated at depth beneath sedimentary cover sequences. The rock volumes dip subvertical to west.
- In a limited way it is possible to establish a relative history of geological events, i.e., sedimentation and formation of the host rock types preceded formation of shear zones and splay shears.

The inversion model of a dyke crosscutting the Banifing shear zone and Menankoro fault using the analogue models in key area 2 shows that:

- The dip of the east-west trending dyke varies; subvertical to a slightly north dip in the west; north dip in the centre; subvertical in the east. The change in the dip of the dyke coincides with the position where it crosscuts the Menankoro fault and Bougouni belt.
- A volume of the rock is bounded by the Menankoro fault and Banifing shear zone. Secondary splay shears are evident in the eastern part of the key area.
- The Banifing shear zone is dextral strike-slip, while the Menankoro fault is sinistral strike-slip.
- In a limited way it is possible to establish a relative history of geological events, i.e., sedimentation and formation of the host rock types; formation of shear zone and splays shears; crosscut by dykes.

In key area 3, the inversion model when compared to analogue models of a dyke that crosscuts the Yanfolila belt and Yanfolila fault shows that:

- The dyke dips from north to subvertical.
- The dip changes where the dyke crosscuts sedimentary rocks in the Yanfolila belt.
- The rock volume corresponds to metamorphosed volcano-sedimentary rock and granite. The

rock volume dips subvertical to slightly west. The rock volume between the Yanfolila belt and Yanfolila fault dips slightly west.

- In a limited way it is possible to establish a relative history of geological events, i.e., deposition of volcano-sedimentary sequences; dyke emplacement; formation of the Yanfolila fault; second dyke emplacement event.

The use of analogues models is very helpful to control the quality of inversion at depth where there is a lack of geological data. The trend of rock volumes and structures are determined. The analogue model also helps to improve the confidence level of inversion results, but limitations remain.

The modelling performed in the key study areas shows details of the first-order structures and rock volumes at depth even with the lack of available data at depth. The main problem is the fact that there are no geological and structural models available in the study area at regional scale. Most of the models available are small-scale, or derived by correlation with the nearest countries.

The inversion modelling in the study area shows a limited use of constraint in the study area using the MGINV3D utility of WinDisp®. It appears that the bound model (using the petrophysical data) is more useful than reference model (using the surface mapping data).

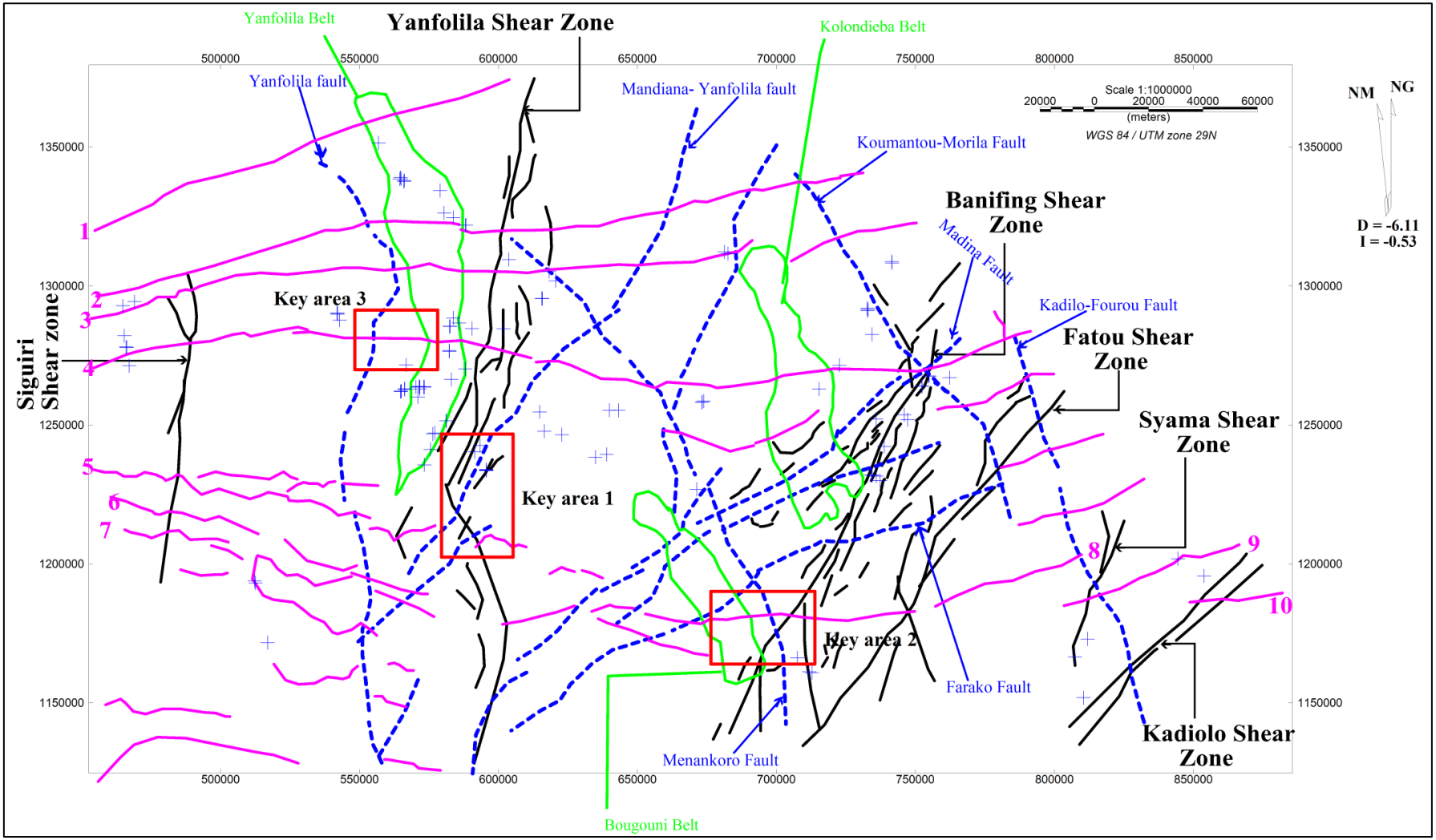

***Figure 6.1**: The geological and structural interpretation map of the study area showing the key areas as red rectangles. The volcano-sedimentary belts are indicated in green. Key structures and dyke are also indicated.*

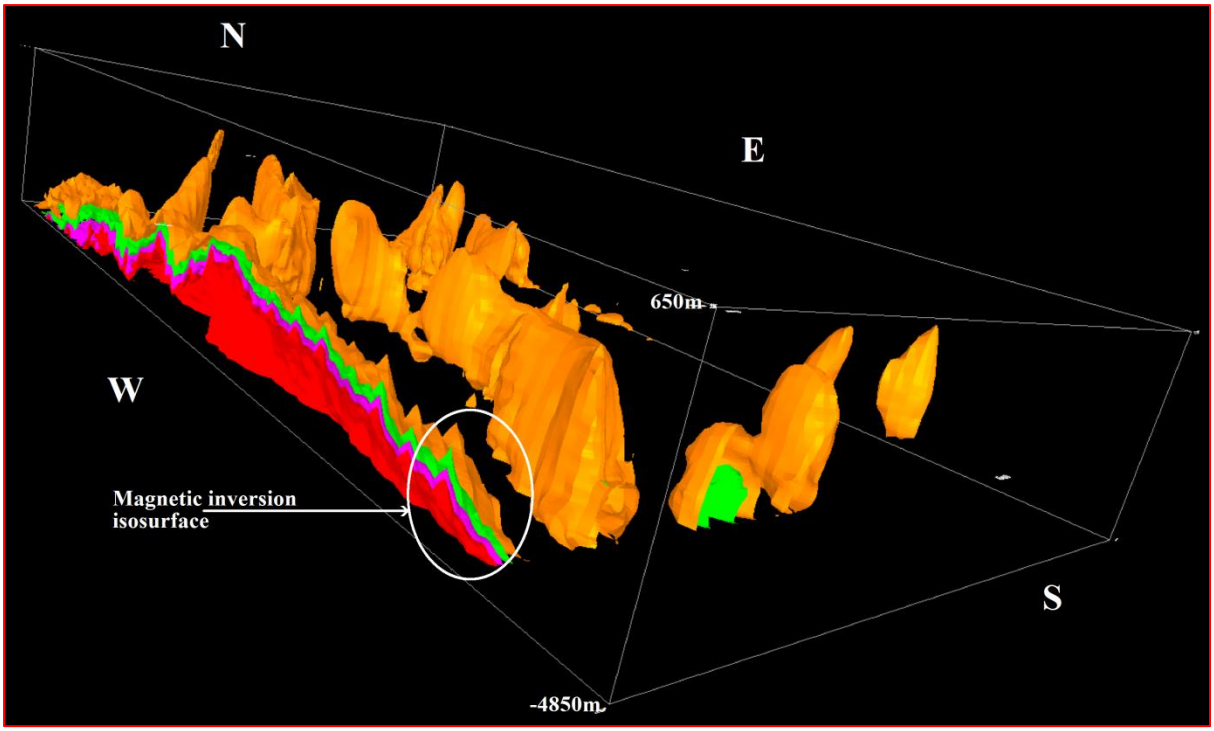

***Figures 6.2**: The magnetic inversion isosurface of key area 1. The image shows four isosurfaces (orange, green, pink and red).*

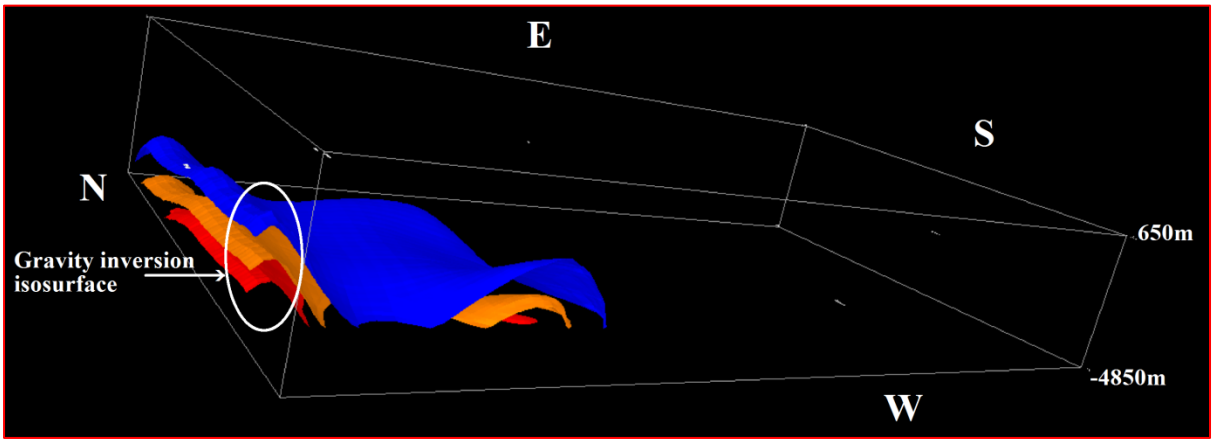

***Figures 6.3**: The gravity inversion isosurface of key area 1 showing three level of isosurface (blue, orange and red).*

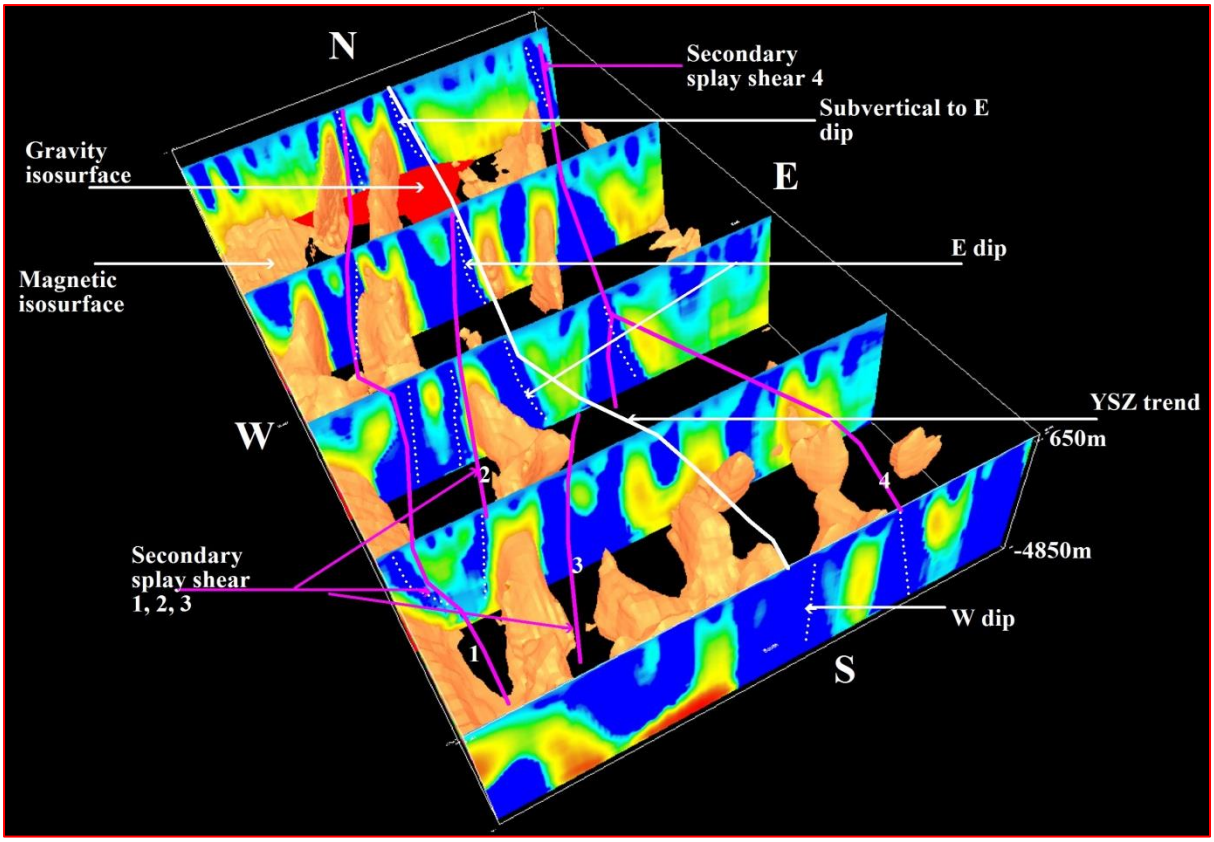

***Figure 6.4**: The magnetic susceptibility section combined to the isosurface of key zone 1 and is the same as Figure 5.7 for Inversion zone 1. The image shows the dips of the Yanfolila Shear Zone (YSZ) and the secondary splay shear. The structures and rocks volume trend is shown in the figure. The magnetic sections and depth of rocks volume and structures are displayed.*

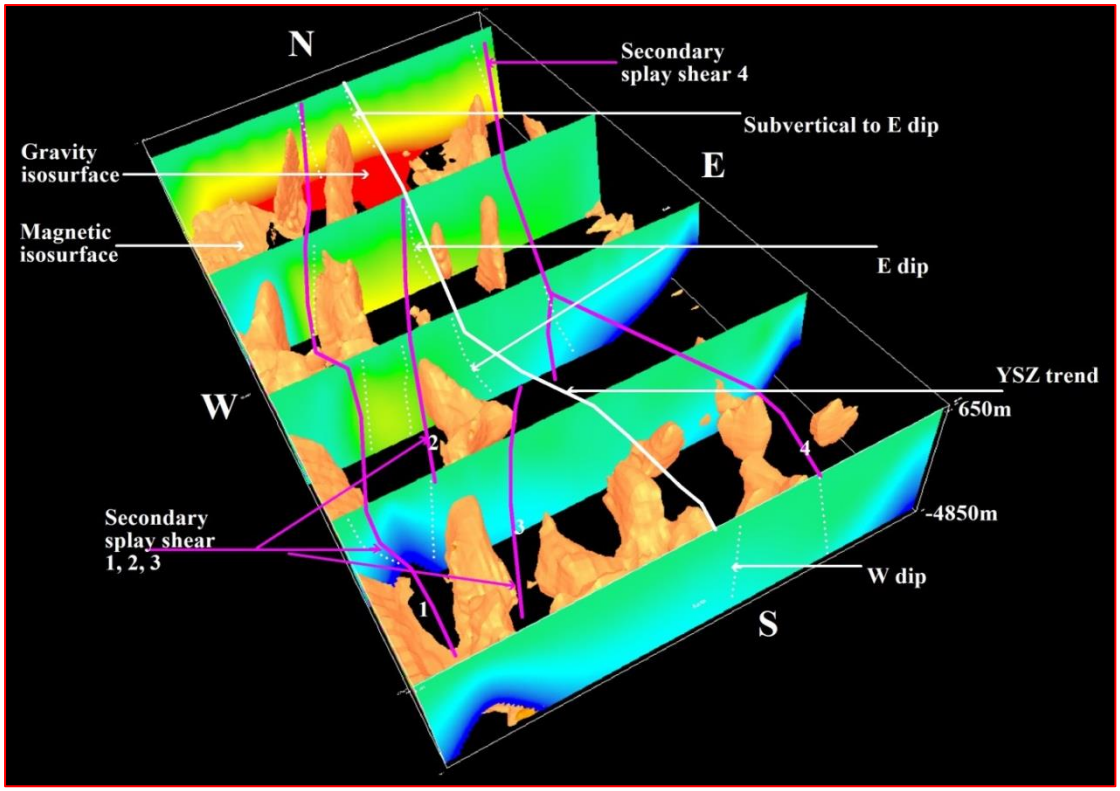

Figure 6.5*: The gravity inversion section combined with magnetic and gravity isosurfaces of key zone 1. The image shows the dip and trend of shear zones from magnetic sections. Compare with Figure 5.8 for Inversion Zone 1.*

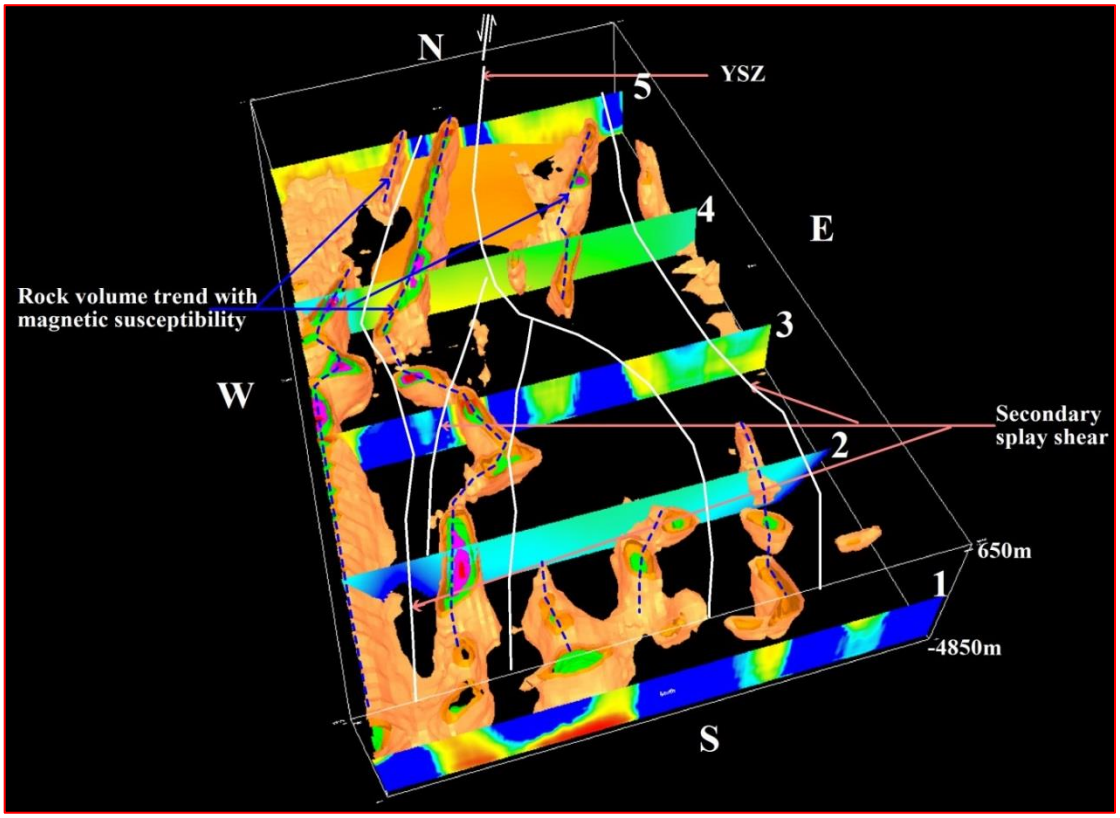

Figure 6.6: *The combination of magnetic and gravity sections with magnetic and gravity isosurfacesfor key zone 1 for Inversion Zone 1. The image shows the trend of structures and rock volumes. The number 1, 3 and 5 correspond to the magnetic section; 2 and 4 are the gravity inversion sections.*

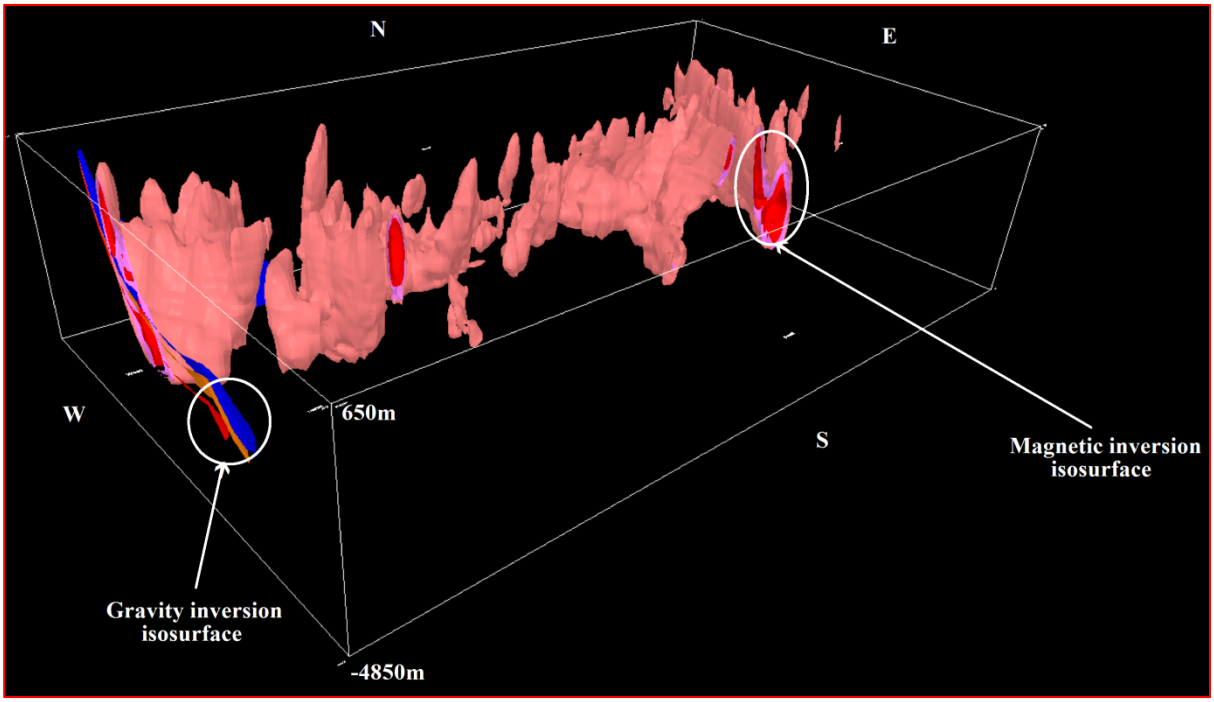

***Figures 6.7**: The magnetic and gravity inversion isosurface of key area 2 for Inversion zone 4. The image presents three density isosurface in blue, orange and red, and three magnetic susceptibility isosurface (orange, pink and red) .The images shows high susceptibility and high density values at depth.*

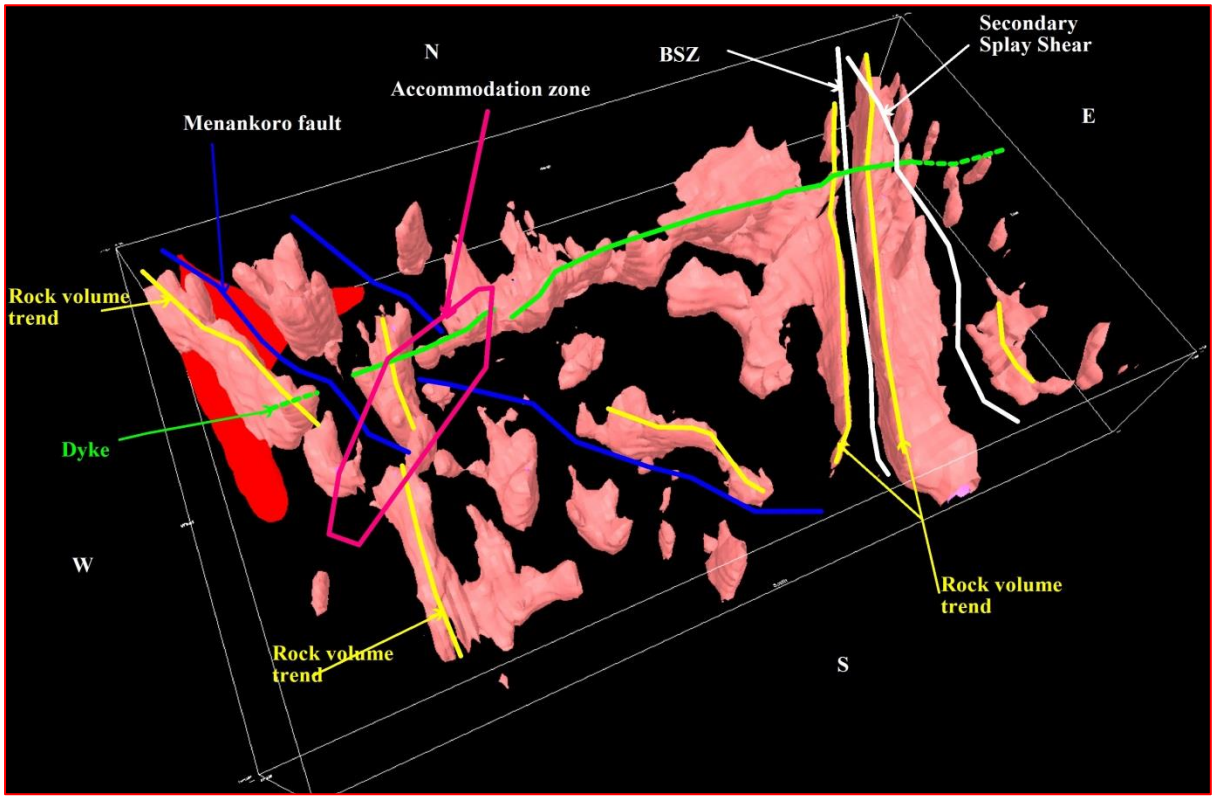

***Figure 6.8**: The isosurface showing the trend of different rock volumes and structures in the key area 2. Compare with Figure 5.16 for Inversion Zone 4**.** The secondary splay shear and Banifing shear zone can be identified with the figure. An interpreted accommodation zone (pink) and transfer faults (blue) can be identified.*

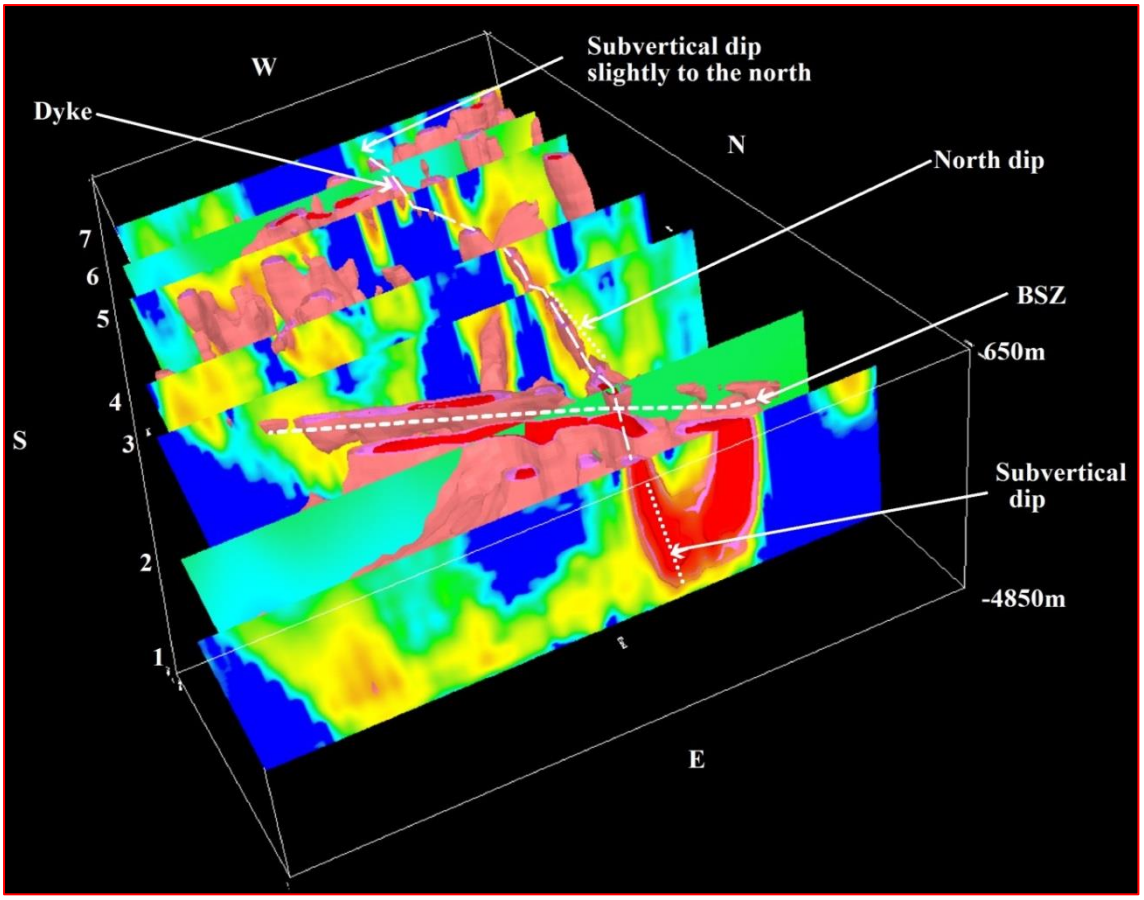

***Figure 6.9**: The section of inversion for gravity and magnetic data showing the dip of dyke viewed from east. The numbers 1, 3, 4, 5, 7 are related to the magnetic sections, the numbers 2 and 6 correspond to the gravity sections.*

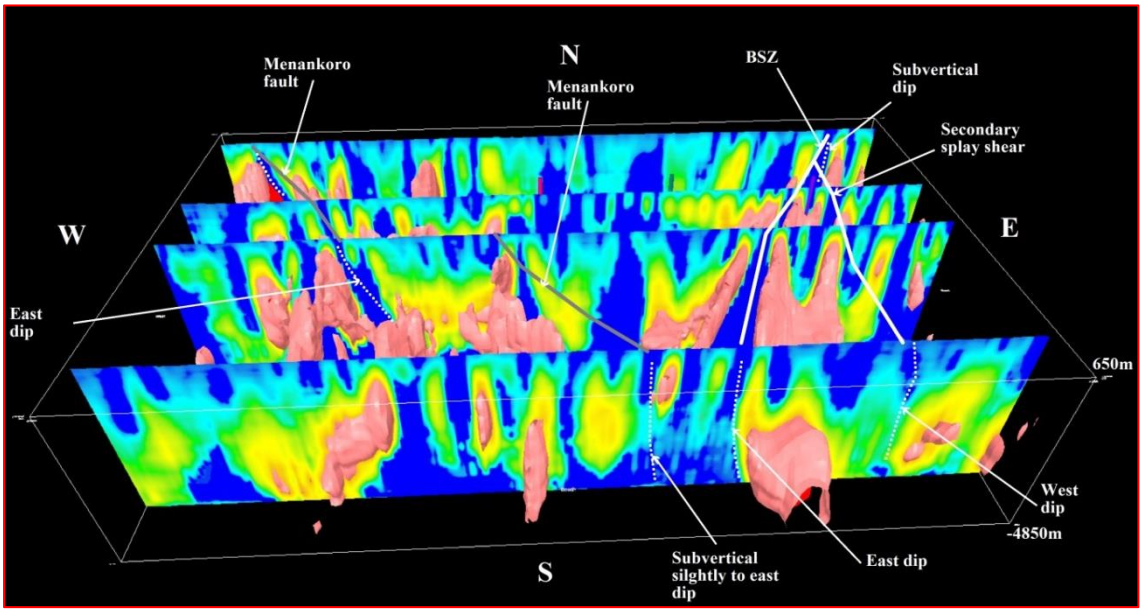

***Figure 6.10**: The magnetic isosurface combined with magnetic sections for key zone 2. The image shows the trend of the Banifing shear zone (BSZ) and secondary splay shears; also the trend of Menankoro fault is highlighted. The change of dip can be observed for the BSZ and Menankoro fault from south to north. The dip of secondary splay shear is defined. Also the merging point of secondary splay shear and BSZ is well highlighted.*

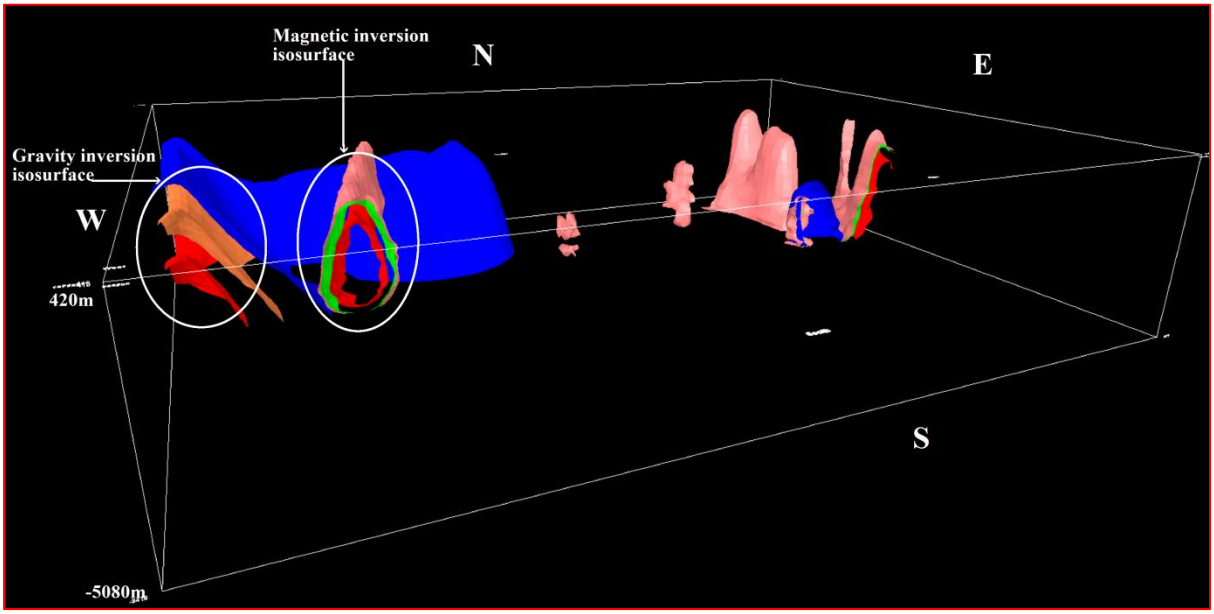

***Figure 6.11**: The magnetic and gravity inversion isosurfaces of key area 3. The gravity inversion isosurface present three of isosurface in blue, orange and red. The magnetic inversion present three level of isosurface (orange, pink and red). The coincidence of gravity inversion isosurface and magnetic isosurface can be identified at depth in term of rock volumes.*

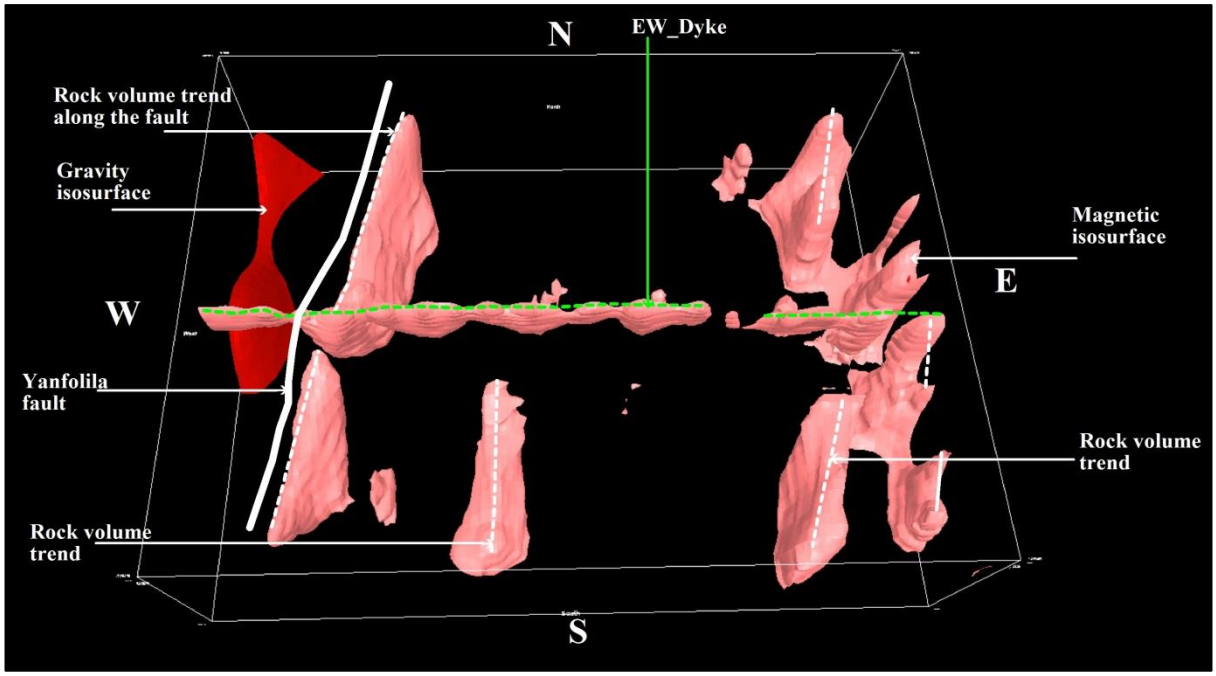

***Figure 6.12**: Magnetic and gravity isosurfaces showing the trend of rock volumes for key area 3 according to the rock densities and susceptibilities. An east-west trending dyke is highlighted in green.*

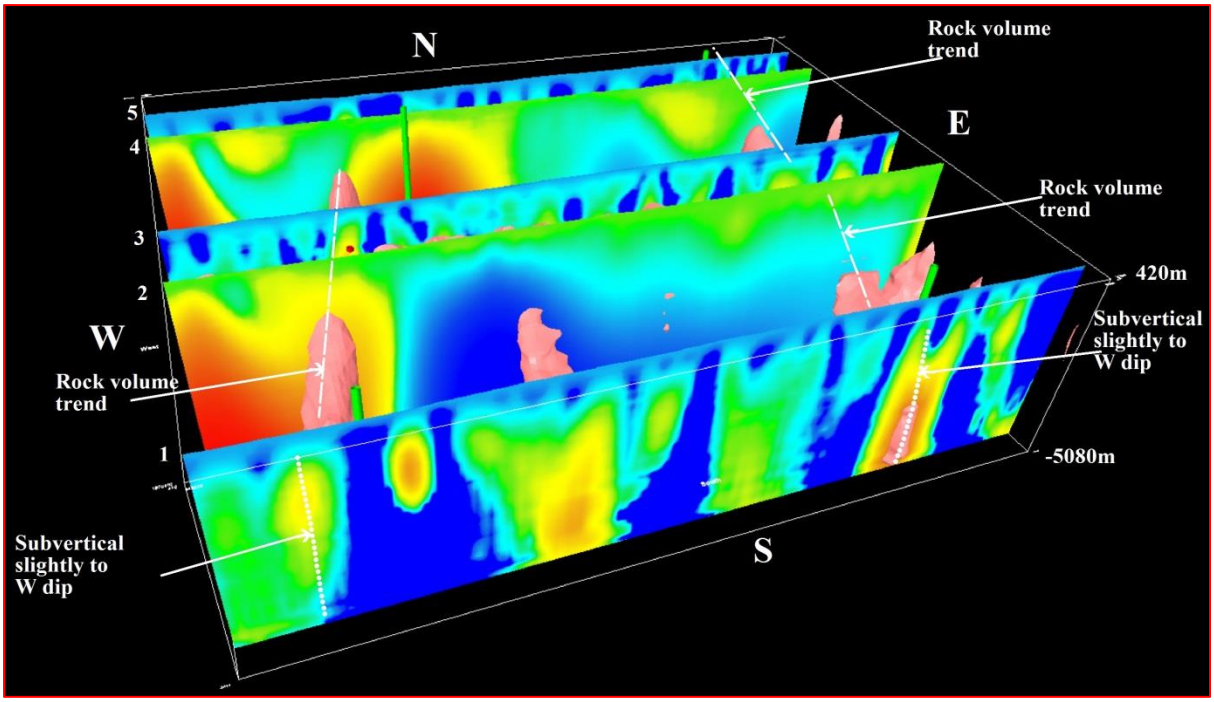

***Figure 6.13**: The section of inversion for gravity and magnetic data showing the dip of rock at depth. The numbers 1, 3, and 5 are related to the magnetic sections, and 2 and 4 correspond to the gravity sections.*

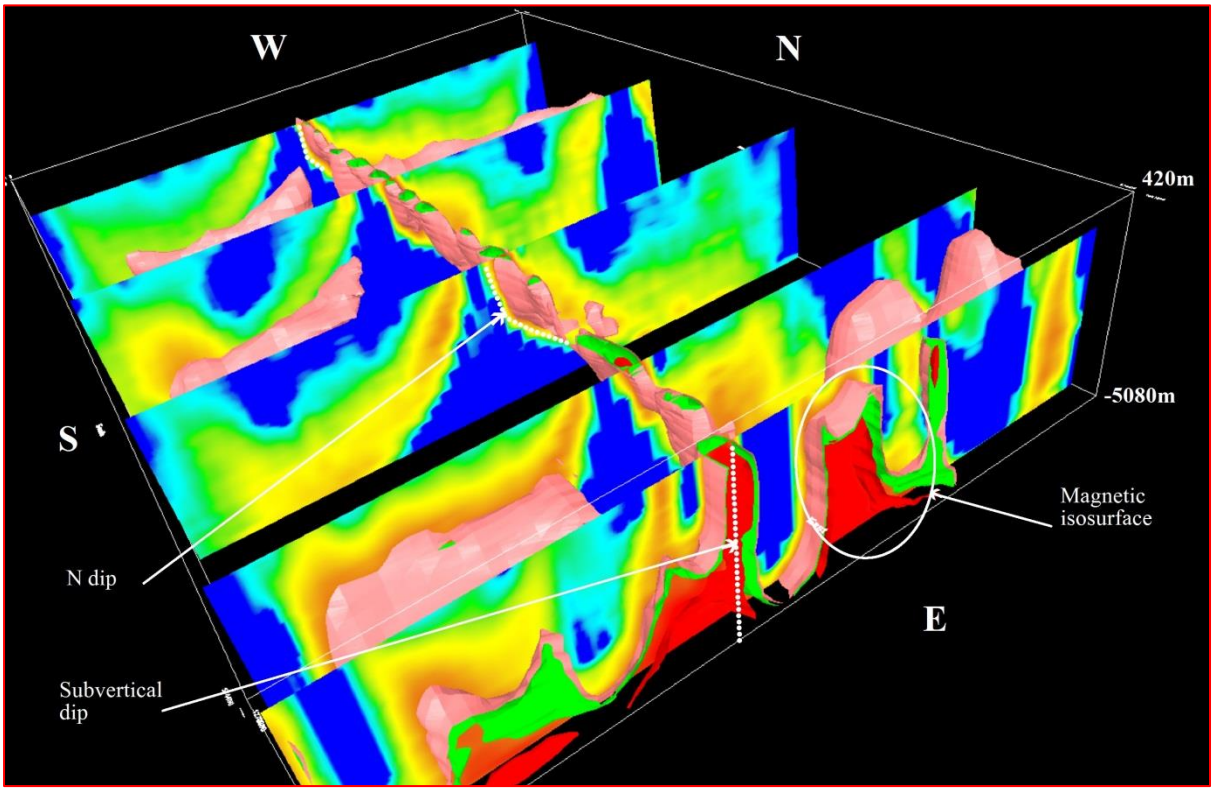

***Figure 6.14**: The magnetic inversion section combined with the magnetic isosurface showing the trend and dip of a dyke.*

7. DISCUSSION

7.1. Geophysical context

The geophysical data available were used to develop geological and structural interpretations of southern Mali and northeast Guinea (Figures 7.1, 7.2). Two main steps were performed, namely, geophysical image processing and geophysical modelling.

Geophysical data processing and interpretation resolved a coincidence of different physical properties using gravity and magnetic data. The coincidence of physical properties enabled the discrimination of structures and rock types. The combination of different geophysical methods divided the study area into discrete zones (Figure 4.14).

1. High magnetic susceptibility values and high density zones that correspond to basic igneous rocks.
2. High susceptibility values and moderate to high density zones that correspond to metamorphic rocks.
3. Moderate to high susceptibility and low to moderate density zones that correspond with acid igneous rocks.
4. Low susceptibility with low to moderate density zones that correspond with metasedimentary rocks.
5. Low susceptibility with high density zones that represent dolomitic rock.
6. Low susceptibility and low density zones that are attributed to the sandstone.
7. Low susceptibility and moderate density zones that correspond to greywacke.

The latter four zones generally occur in the 1) northwest of the study area and in the northern part of Siguiri basin, which agrees with field studies by Egal et al. (1999b) who recorded sedimentary sequences in those regions; and 2) in part of the Yanfolila belt where sedimentary rocks of the Siguiri basin were identified by Girard et al. (1998). The greywacke and sandstone rock types are also generally distributed across the study area.

Granitoid, dolerite and gneiss are localised in the southwest of the study area (Figure 4.14) and correspond to the southern part of Siguiri basin as described by Lahondère et al. (1999a) and Feybesse et al. (1999) who mapped metasedimentary rocks and TTG suite intrusions. However, metasedimentary rocks also occur along the eastern part of the Siguiri basin, which has not been identified prior to this study. High susceptibility with high density rocks interpreted as mafic volcanics (Figure 4.14) may be related to the Central Atlantic Mafic Complex of Whiteside et al. (2007) and are not (thereby) Palaeoproterozoic in age.

The lineaments resolved in this study area correspond to structures such as faults and shear zones, with a range of orientations. East-west trending lineaments are interpreted as dolerite dykes

according to the geological data available, and some are assigned to the dykes of the CAMP. Two generations of dykes were also determined in the study area. The first generation is located in the southern part of the study area where it is traversed by the Yanfolila shear zone, but crosscut by the Banifing shear zone. It is thus older than Yanfolila shear zone and younger than Banifing shear zone. The second generation located in the north of the study area postdates the CAMP magmatic event. The presence of multiple generations of dykes is known for West Africa and was reported by Baratoux et al. (2011) who described three generation of dykes in Burkina Faso.

Geophysical modelling was performed in order to predict the behaviour of structures at depth. The filtered maps showed complex structures for Yanfolila and Banifing shear zones. The inversions also confirm these complex structures at depth and determined their geometries. The Yanfolila and Banifing shear zones represent first-order structures (c.f., Claessens et al., 1988; Girard et al., 1998; Feybesse et al., 2006a and WAXI, 2013). Secondary splay shears merge and bifurcate from the main shear zones.

The combination of magnetic and gravity data inversion section and isosurface assists in the determination of the relative age of structures. The inversion performed across the Banifing shear zone confirmed the presence of tip damage structures when compared to data by Kim and Sanderson (2005) for tip damage zones.

7.2. Geological context and implications

The rocks of the study area can be classified into volcanic, subvolcanic and plutonic rocks, metamorphosed volcano-sedimentary and sedimentary rocks according to Girard et al. (1998); Egal et al. (1999a); Feybesse et al. (1999); Lahondère et al. (1999a); Feybesse et al. (2006a); Baratoux et al. (2011); Miller et al. (2013) from field studies. These rocks are generally Palaeoproterozoic in age, but Archaean and also post-Palaeoproterozoic age rocks are present. The identification of rocks of the CAMP adds important information to the geophysical interpretation because these rocks may be incorrectly mapped in field studies.

Three ages for basalt have been identified. (1) The first, which is the oldest, is located in the centre and the east of the study area. These basalts correspond to the lower basalt (lower Birimian Supergroup) described by WAXI (2013) and correspond to the oceanic island arc-backarc-ocean floor environments of emplacement. (2) The second age of basalt emplacement as located in the western and the southern part of the study area and corresponds to with calc-alkaline basalts from the upper Birimian Supergroup. They correspond with arc accretion and associate with diorite intrusions and calc-alkaline volcanoclastic rocks (WAXI, 2013). They can also be found in the south of the study with the presence of andesite lavas. (3) The third basalt which is the youngest corresponds to the position of CAMP basaltic flow or sills as reported by Whiteside et al. (2007).

A ubiquitous upper layer of sedimentary rocks that unconformably overlies most of the geology in the study is interpreted as younger basin sediments, and possibly part of the Taoudenni basin sediments. Mickus (2008) reported that the Taoudenni basin sediment layer extends to depths of up to 1.5km in the western part of Burkina Faso (on the eastern edge of the study area).

Additionally a regolith (weathering profile) layer could penetrate to 80m deep in certain zones of the study area. The combination of a deep regolith layer and upper (possibly Taoudenni) sedimentary package resolves a high amplitude that makes the determination of older geology at depth difficult.

The high amplitude gravimetric data corresponds to meta-volcanic rocks throughout the Baoulé-Mossi domain as described by Bonvalot et al. (1988) and Mickus (2008). Consequently, the high gravity amplitude with low susceptibility measured in southern Mali and eastern Guinea (as per the three transects of forward modelling) can reasonably be considering as corresponding to meta-volcanic belts.

In the study area, first-order structures are characterised by low density and low susceptibility, but the high density and high susceptibility domains are bounded by the shear zone. The combination of density and susceptibility determines the type of rock that postdates the formation of the shear zones, but also the geology crosscut by the shear zones as described by the inversion modelling.

The forward modelling and inversion modelling were combined to evaluate the depth and depth-extension of structures. The parameters are more accurate with the forward modelling than 3D inversion modelling.

7.3. Understanding the geology using inversion modelling

The structural architecture of the Baoulé-Mossi domain as presented by Lompo (2010) can be identified in the study area as dome and basin geometry related to vertical magmato-tectonic and horizontal transcurrent tectonics in the broad sense. The domes are located along the shear zones while the basins are located between the shear zones.

The thickness of the upper sedimentary and regolith layer in the study area is not constant. At the position of the Yanfolila shear zone (in the west of the study area) it attains a depth of 1100m, but is shallower at the position of the Banifing shear zone (in the east of the study area) where it attains a depth of 850m. The Taoudenni basin on the eastern margin of the study area attains a depth of 1.5km (c.f., Mickus, 2008), suggesting that a broad basement arch occurs in the Taoudenni basin that os focussed on the position of the Banifing shear zone. The sedimentary package near the Yanfolila shear zone is proximal to the Siguiri basin sediments in eastern Guinea (Figure 4.14).

Additionally, a difference between Yanfolila region and the northern Siguiri basin may simply be due to the presence of intrusions in the Yanfolila region, which limited deposition in the Siguiri basin towards the east (Girard et al., 1998).

Mafic rocks are present in key area 1 (near the Yanfolila shear zone) and key area 2 (near the Banifing shear zone). The old mafic rocks identified in the key study area 2, crop out in some areas of Banifing shear zone, and extent to depth. These mafic rocks correspond to the calc-alkaline volcanics of the Upper Birimian Supergroup described by Baratoux et al. (2010) for the southwest of Burkina Faso in the Houndé greenstone belt.

The Bougouni and Kolondieba fold-thrust volcanic belt trends northwest, which is similar in orientation to that described by Tshibubudze and Hein (2009; 2013) and Hein (2010) for the northeast of Burkina where several greenstone belts were deformed during the Tangaean Event at 2170 -2130 Ma (Hein, 2010), and thus represent older tectonic remnants. The Tangaean Event is interpreted in the study area by the presence of syn-tectonic granitoids along the Banifing shear zone, and is similar to those described by Tshibubudze and Hein (2013) in the northeast of Burkina Faso along the Markoye Shear Zone; these plutons should be dated using absolute geochronologically to constrain the age of the shear zone. However, the relative chronology clearly shows that dextral strike-slip activity on the Banifing shear zone, and emplacement of crosscutting plutons, took place before the Eburnean orogeny (2130-1980 Ma) as a unique oceanic arc accretion tectonic event. The Banifing shear zone is thereby interpreted as a Dl structure in the southwest of Mali.

Structures that formed during the Eburnean orogeny are also characterised in the study area. The presence of Yanfolila shear zone and the secondary splay shears of Yanfolila shear zone agree with the current research that the Eburnean orogeny is divided into at least two sub-events (Feybesse et al., 2006a ; Hein, 2010; Baratoux et al., 2011), namely, $D2_A$ and $D2_B$. The sub-events of the Eburnean Orogeny are the result of progressive deformation across West Africa (Allibone et al., 2002; De Kock et al., 2011, 2012) and mark a shift from compressive tectonics to strike-slip transpressive tectonics. Gold mineralisation is hosted in late $D2_B$ structures (secondary splay shears) that correspond to tip damage structures.

Additionally, the Menankoro and Koumantou-Morila faults that are orientated north-northwest in the study area are similar to structures that formed during the Wabo-Tampelse (D3) (Hein, 2010) at approximately 1.1 Ga (Baratoux et al., 2011), or during the Pan African Orogeny at ca. 500 Ma. However, the structures have yet to be investigated through geometric, kinematic and dynamic structural analytical studies, or constrained in age. Furthermore, based on the results of this study:

1. The Banifing shear zone is older than Yanfolila shear zone.
2. Archaean basement and CAMP intrusions are located in the south of Siguiri basin as opposed to the north of the Siguiri basin.
3. The north of Siguiri basin is largely composed of sedimentary rocks and bordered to the north by the sediments of Taoudenni basin.
4. The margin of the Archaean basement can be defined if the signatures of the CAMP intrusions can be removed from the south Siguiri basin.

7.4. New interpretation of the study area

A comparison of the results of this study with the work of previous researchers has shown that;

1. The Yanfolila shear zone corresponds to the position of the Siekorole shear zone of Miller et al. (2013) who concluded the shear zone as having formed in third deformation (D3). The use of the name "Siekorole shear zone" should therefore be abandoned.
2. The Banifing shear zone corresponds to same structure as reported by Milési et al. (1989), SIGAFRIQUE (2000), Randgold (2007), Parker and Wilkinson (2011) and Miller et al. (2013). The Banifing shear zone is a dextral strike-slip shear zone based on the orientation of splay shears and evidence of clockwise block (domain) rotation. In this study the Banifing shear zone resolves as at least two parallel strike-slip shears and is subtended by secondary splay shears.
3. The Fatou shear zone has been reported by Girard et al. (1998) and Sigafrique (2000) as the "Kolondieba accident" and "dextral strike-slip structure". However, this study suggests it is a sinistral strike-slip shear.
4. The Yanfolila belt as reported by Randgold (2008); Miller et al. (2013); Sigafrique (2000) is arcuate and trends north-northeast at it southern end and north-northwest at it northern end.
5. The Menankoro fault was reported by Sigafrique (2000). In this study the Menankoro fault is a sinistral strike-slip fault. It is crosscut and offset by the northeast trending Madina fault. The Madina fault was not recognised in previous studies and is clearly younger than the Menankoro fault. Both structures need focussed structural study.
6. The Mandiana-Yanfolila fault was reported by Sigafrique (2000) as a sinistral strike-slip fault. However, it crosscuts the Yanfolila shear zone and formed after the Yanfolila shear zone and Yanfolila belt.
7. The Koumatou-Morila fault corresponds to the Sanso and Massigui faults of Sigafrique, (2000) and were mapped as dextral faults. In this study, the Koumantou-Morila fault resolves as a single feature that crosscuts the Banifing and Fatou shear zones. It is therefore younger than those structures. Importantly, it hosts the decommissioned Morila gold mine that is situated in the tip damage zone of Banifing shear zone. Clearly, the structural and metallogenic relationships need further investigation to understand the tectonic history of the shear-fault complexes.
8. The Kadiolo-Fourou fault has not been identified in previous studies, but is resolved in this study as a third-order structure that crosscuts the Syama-(Bananso) shear zone in its southern extent.

9. The Syama-(Bananso) shear zone is described by Milési et al. (1989), Girard et al. (1998), Sigafrique (2000), Randgold (2008), Miller et al. (2013) and Ballo et al. (2016) as a sinistral strike-slip shear along its main branch, which is confirmed in this study. The northwestern branch of the Syama-(Bananso) shear zone is a fault.

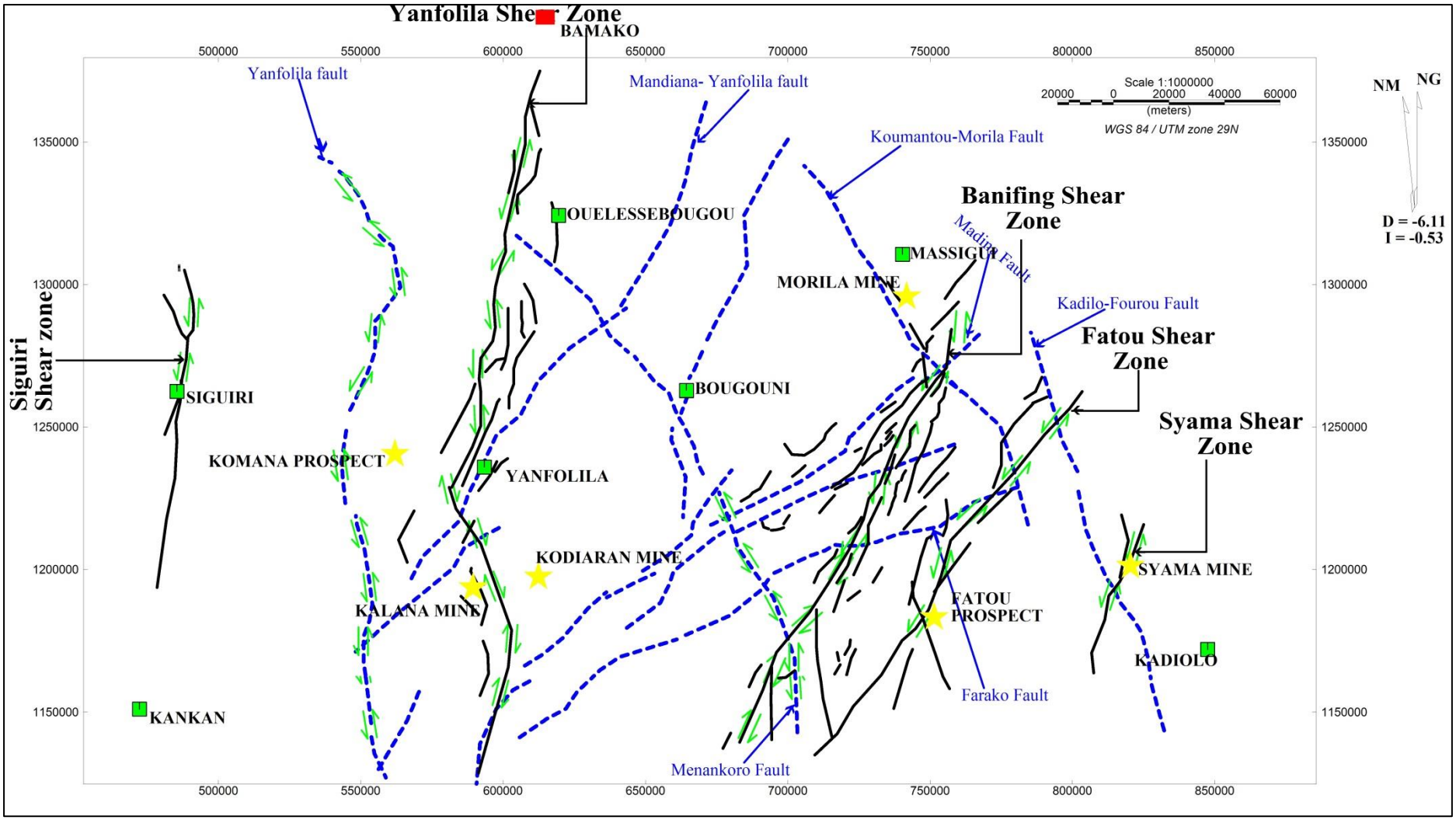

Figure 7.1*: The interpreted structural map of the study area using magnetic, gravity and radiometric data in combination and using fact data as a constraint. The image shows the probably displacement sense of shear zone and faults using the combination of geophysical images processing, forward and inverse modelling with fact and petrophysical data as constraint.*

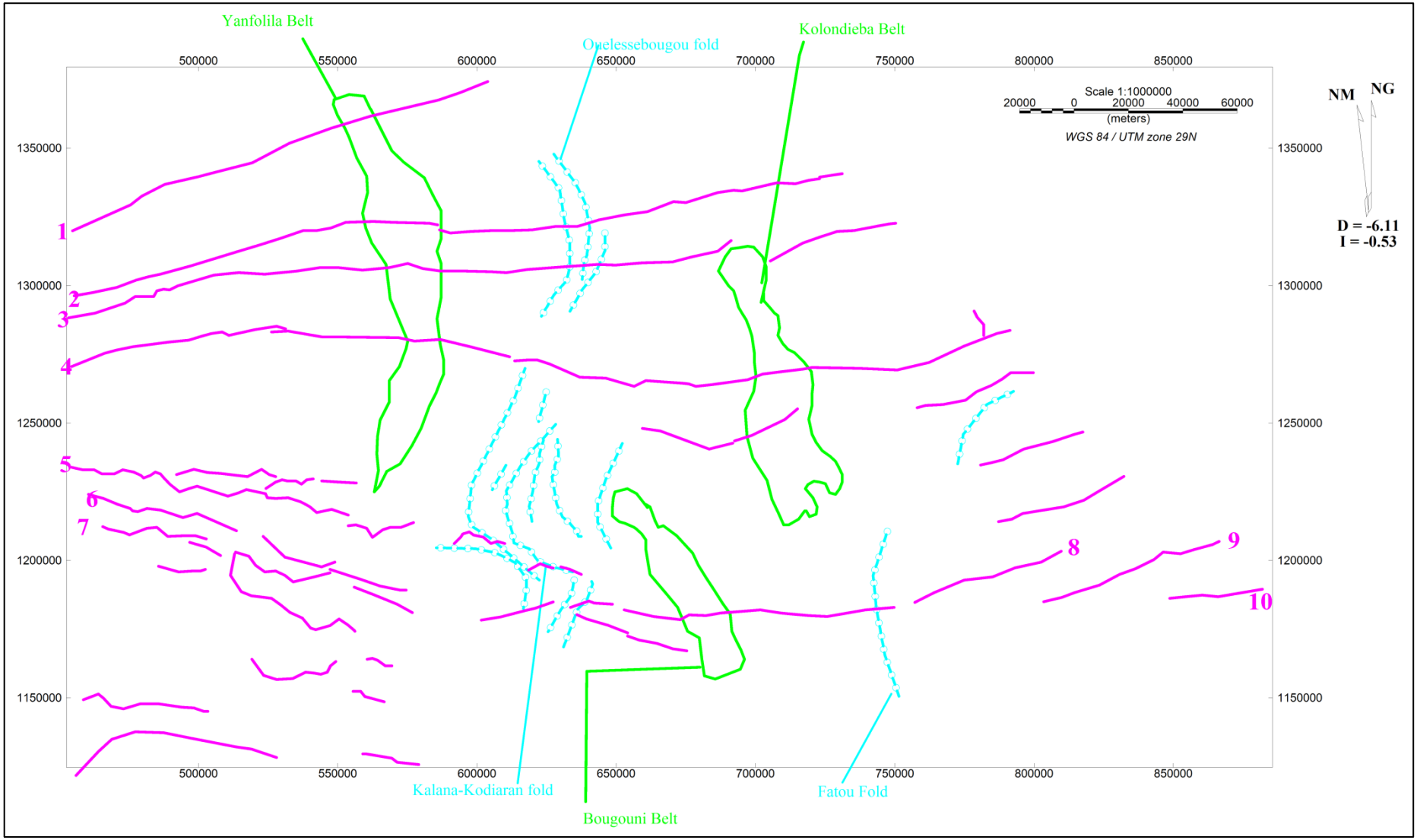

Figure 7.2: *The interpreted structural map of the study area using magnetic, gravity and radiometric data. The image show folds (marked in blue), greenstone belts (marked in green) and dykes (marked in pink) using geophysical processing images, modelling with fact and petrophysical data as constraint.*

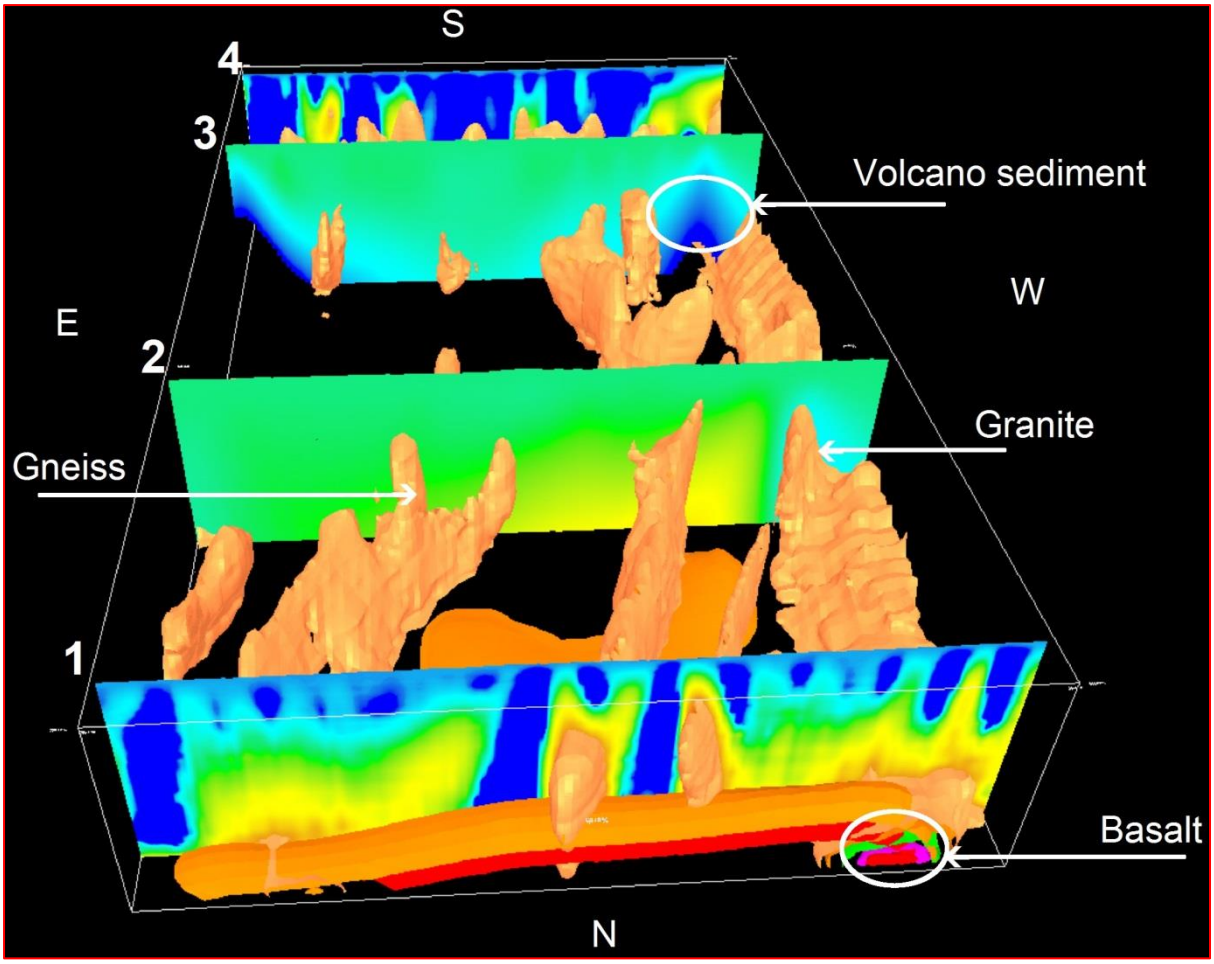

***Figure 7.3**: The image shows the different type of rock in the key area 1. The section 2 and 3 correspond to the gravity section, the numbers 1 and 4 correspond to the magnetic sections. Basalt is located at depth in the northwest of the model. The southern part of the key area resolves volcano-sedimentary rocks at depth.*

8. CONCLUSIONS

The geophysical data processing and modelling performed in the study area for structural and geological interpretation resolved structures and rock volumes at depth. This study showed that inversion modelling with petrophysical data adds important information about rock volumes at depth, but has limitations. The quality of inversion can be tested using analogue modelling to interpret the result of inversion and constrains the solution derived from inversion.

The inversion resolved the complex architecture at depth of first-order structures, which was interpreted from the geophysical map plan view. The Banifing Shear Zone is well defined using the inversion modelling. The inversion resolved different metamorphic grades along the Banifing shear zone. High metamorphic grade is interpreted in the middle of the shear zone (Inversion Zone 5) where the shear zone is wide. The tip area of the shear zone presents low to moderate metamorphic grade. The gold mineralisation systems of the study area are localised at tip damage structures including the Morila mine in the damage area of Banifing shear zone, the Kalana mine in the damage area of Yanfolila shear zone, and the Fatou deposit in the Fatou shear zone.

The rocks that generally make up the study area include granitoid, basalt, gneiss, migmatite, volcano-sedimentary rocks, sandstone and greywacke. Two types of basalt were resolved, namely, basalt in greenstone belts; the second type of basalt is crystallised from young magmatism of the CAMP. The dykes located in the northern part of the study area are interpreted as young dykes compared with dykes of the Central Atlantic Magmatism Province.

The structures of the study area can be classified as first-order structures, second-order structure and third-order structures according to length, width, depth and the complexity. The first-order structures include the Banifing and Yanfolila shear zones. The second-order structures include; 1) the Siguiri, Syama and Fatou shear zones, 2) the Menankoro and Mandianan-Yanfolila faults, and 3) the Kalana Kodieran fold. The third order structures include the Yanfolila fault, Koumantou–Morila fault, Kadiolo-Fourou fault, Kadiolo shear zone and Farako fault.

The Kolondieba volcano-sedimentary belt was recognised for the first time in this study, as was the Kalana-Kodieran fold. The Siguiri basin is divided into two major zones, namely intrusions and basic igneous rocks in the south, and volcano-sedimentary and sedimentary rocks in the north.

The inversion geophysical modelling in this study combined several geophysical and geological parameters including geophysical data, physical property data of rocks, geological fact data, structural parameters and analogue models. The combination helps to interpreted consistently the inversion modelling in the study area.

The petrophysical data is more useful in constraining the inversion than fact data in the study area with the surface mapping data. The analogue models are limited in terms of quality control of the inversion if the structures are not a complex, as is the case of Yanfolila and Banifing shear zones.

REFERENCES

Albouy, Y., Boukeke, D., Legeley-Padovani, A., Villeneuve, J., Foy, R., Bonvalot, S., El Abbass, T., Poudjhom, Y., 1992. ORSTOM Gravity survey Africa and Madagascar. Report presented to the Congres Exploration Minière, Recherches d'Eau et Environnement by the Laboratoire de Géodynamique Interne France, 15p.

Allibone, A., Teasdale, G.C., Ethridge, M., Uttley, P., Soboh, A., Appiah-Kubi, J., Adanu, A., Arthur, R., Mamphey, J., Odoom, B., Zuta, J., Tsikata, A., Pataye, F., Famiyeh, S., Lamb, E., 2002, Timing and Structural Controls on Gold Mineralisation at the Bogoso Gold Mine, Ghana, West Africa, Economic Geology 97, 949-969.

Ballo, I., Hein K.A.A., Traore, A., Sanogo, L., Daou, G., Guindo, B., Ouologuem Y., 2016. The Syama and Tabakoroni goldfields, Mali. Ore Geology Reviews Special Volume 78, 578-585.

Baratoux, L., Metelka, V., Naba, S., Jessell, W.M., Grégoire, M., Ganne, J., 2011. Juvenile Palaeoproterozoic crust evolution during the Eburnean orogeny (~2.2-2.0 Ga), western Burkina Faso. Precambrian Research 191, 18-45.

Beauvais, A., Ruffet, G., Hénocque, O., Colin, F., 2008. Chemical and physical erosion rhythms of the West African Cenozoic morphogenesis: The ^{39}Ar-^{40}Ar dating of supergene K-Mn oxides. Journal of Gophysical Research 113 F04007, doi: 10.1029/2008JF000996, 2008.

Bentley, P.N., Venter, L., Moolman, R., Henry, G., Heidstra, P., Reading, D., 2000. Geological review, gold target prioritization and recommendations for future exploration work. Unpublished report to Randgold Resources Ltd.

Bergen, K. J., Shaw, J. H., 2010. Displacement profiles and displacement-length scaling relationships of thrust faults constrained by seismic-reflection data. The Geological Society of America 122, 7-8; 1209-1219, doi: 10.1130/B26373.1.

Bessoles, B., 1977. Geologie de l'Afrique, Le Craton Ouest Africain. Memoires du BRGM, N° 88. 410p.

Blot, B., 2004. Caractérisation des chapeaux de fer en milieu latéritique cuirassé. Comptes Rendu Géoscience 336, 1473-1480.

Bonvalot, S., Villeneuve, M., Albou, Y., 1991. Interprétation gravimétrique de la Sierra-Leone: mise en évidence d'une suture de la collision dans la chaine panafricaine des Rokelides. Compte Rendus Académie des Sciences de Paris 312 (II), 841-848.

Bonvalot, S., Villeneuve, M., Legeley, A., Albou, Y., 1988. Levé gravimétrique du sud-ouest du Craton Ouest-Africain. Compte Rendus Académie des Sciences de Paris 307 (II), 1863-1868.

Brown, E.T., Bourlès, D. L., Colin, F., Sanfo, Z., Raisbeck, G. M., Yiou, F., 1994. The development of iron crust lateritic systems in Burkina Faso West Africa examined with in-situ-produced cosmogenic nuclides. Earth and Planetary Science Letters 124, 19-33.

Claessens, L.W., Camara, D.M., Van Osta, P., 1988. DNGM, BME, MRAC, Carte geologique du Mali au 1/200 000 Feuillet NC-29-XXIV de Massigui. Ministère du développement industriel et du Tourisme.

Cooper, G.R.J., 2007. Enhancing geophysical datasets using frequency domain techniques. Fugro short course. School of Geosciences, University of the Witwatersrand, Johannesburg, 50p.

Costea, C. A., Deynoux, M., Diallo, S., Diallo, A., Egal, E., 1999. BRGM, DNRGH. Carte géologique de la Guinée à 1/200 000, Feuille n° 27-28, Sirakoro-Bamako Ouest – Conakry (GIN); Ministère des Mines, de la Géologie et de l'Environnement.

Davis, D.W., Hirdes, W., Schaltegger, U., Nunoo, E.A., 1994. U-Pb age constraints on deposition and provenance of Birimian and gold-bearing Tarkwaian sediments in Ghana, West Africa. Precambrian Research 67, 89-107.

De Kock G.S., Théveniaut, H., Botha, P.M.W., Gyapong, W., 2012. Timing the structural events in the Palaeoproterozoic Bolé-Nangodi belt terrane and adjacent Maluwe basin, West African craton, in central- west Ghana. Journal of African Earth Sciences 65, 1-24.

De Kock, G.S., Armstrong, R.A., Siegfried, H.P., Thomas, E., 2011.Geochronology of the Birim Supergroup of the West African craton in the Wa-Bolé region of west-central Ghana: Implication for the stratigraphic framework. Journal of African Earth Sciences 59, 1- 40.

Dooley, T. P., Schreurs, G., 2012. Analogue modelling of intraplate strike-slip tectonics: A review and new experimental results. Tectonophysics 574-575, 1-71.

Egal, E., Lacomme, A., Coatea, C.A., Diabaté, B., Diallo, A., Diallo, A. B., Diallo, S., Gaye, F., Iliescu, D., Minthé, D., 1999a. BRGM, DNRGH. Carte géologique de la Guinée à 1/200 000, Feuille n° 12, Siguiri – Conakry (GIN); Ministère des Mines, de la Géologie et de l'Environnement, 25 p.

Egal, E., Deynoux, M., Costea, C. A., Lacomme, A., Le Berre, P., Diallo, A., Diallo, A. B., Diallo, S., Feybesse, J. L., 1999b. BRGM, DNRGH. Notice explicative de la Carte géologique de la Guinée à 1/200 000, Feuille n° 27-28, Sirakoro-Bamako Ouest – Conakry (GIN); Ministère des Mines, de la Géologie et de l'Environnement, 22 p.

Egal, E., Thieblemont, D., Lahondère, D., Guerrot, C., Costea, C-A., Iliescu, D., Delor. C., Goujou, J-C., Lafon, J-M., Tegyey, M., Diaby, S., Kolié, P., 2002. Late eburnean granitization and tectonics along the western and north-western margin of the Archean Kénéma-Man domain (Guinea, West African Craton). Precambrian Research 177, 57-84.

Féménias, O., 2008. What about the Banifing Lineament? (Southern Mali) Short keynote for IAMGOLD Corporation, December 2008, 20p.

Feybesse, J.L, Bangoura, A., Billa, M., Costea, C.A., Diabaté, B., Diaby, S., Diallo, A., Diallo, S., Diallo, A.B., Égal, E., Gaye, F., Guerrot, C., Iliescu, D., Lacomme, A., Lahondère, D., Le Berre, P., Milési, J.P., Minthé, D., Soumah, D, 1999. Notice explicative de la carte géologique

de la Guinée à 1/200 000, Feuille n° 19, Kankan. Published by the Ministère des Mines, de la Géologie et de l'Environnement, BRGM, DNRGH, 27 p.

Feybesse, J.L., Milési, J.P., 1994. The Archean/Proterozoic contact zone in West Africa: a mountain belt of décollement trusting and folding on a continental craton? Precambrian Research 69, 199-227.

Feybesse, J.L., Sidibe, Y.T., Konate. C.M., Lacomme, A., Lambert, A., Miehe, J.M., Zammit, C., Guindo, L., Dembele, D., Chene, F., 2006a. Carte geologique du Birimien Malien a l'echelle 1/200 000. Published by the Ministere des mines, de l'Energie et de l'Eau, avec appui technique du groupement BRGM-Maps Geosystems et le soutien financier de l'Union Europeenne, dans le cadre du project FED N°7 ACP MLI 117-SYSMIN.

Feybesse, J.L., Billa, M., Guerrot, C., Duguey, E., Lescuyer, J.L., Milési, J.P., Bouchot, V., 2006b. The Paleoproterozoic Ghanaian province: Geodynamic model and ore controls, including regional stress modelling. Precambrian Research 149, 149-196.

Gilbert, D., Galdeano, A., 1985. A computer program to perform transformations of gravimetric and aeromagnetic surveys. Computers and Geosciences 11, 553-588.

Girard, P., Goulet, N., Malo, M., 1998. Synthèse des données géologiques et cartographie Amélioration et Modernisation du centre de documentation. Géologie du Mali. Rapport final partie II. Projet d'assistance technique au secteur minier du Mali crédit 2390-M11.

Giroux, B., Chouteau, M., 2007. Géophysique appliquée, Note de cours- Magnétique. Ecole Polytechnique Montréal, Laboratoire de géophysique appliquée GLQ2200, 111p.

Giroux, B., Chouteau, M., 2008. Géophysique appliquée I, Note de cours- Gravimétrie. Ecole Polytechnique Montréal, Laboratoire de géophysique appliquée GLQ2200, 118p.

Hasting, D.A., 1982. On the tectonics and metallogenesis of West Africa: A model incorporating new geophysical data. Geoexploration 20, 295-327.

Hein, K.A.A., 2010. Succession of structural events in the Goren greenstone belt (Burkina Faso): Implications for West African tectonics. Journal of African Earth Sciences 56, 83-94.

Hein, K.A.A., Morel, V., Kogoné, O., Kiemde, F., Mayes, K., 2004. Birimian lithological succession and structural evolution in the Goren segment of the Boromo-Goren greenstone belt, Burkina Faso. Journal of African Earth Sciences 39, 1-23.

Hirdes, W., Davis, D.W., 2002. U-Pb Geochronology of Paleoproterozoic rocks in the Southern part of the Kedougou-Kéniéba Inlier, Senegal, West Africa: Evidence for diachronous accretionary development of the Eburnean Province. Precambrian Research 118, 83-99.

Hirdes, W., Davis, D.W., Lüdtke, G., Konan, G., 1996. Two generations of Birimian (Paleoproterozoic) volcanic belts in north eastern Côte d'Ivoire (West Africa): consequences for the Birimian controversy. Precambrian Research 80, 173-191.

Institut Géographique National (France), 1993.

Iliescu, D., Costea, C.A., Diabaté, B., Dupuy, J.L., Gaye, F., Lahondère, D., Minthé, D., Picot, J.C., 1999. Carte géologique de la Guinée à 1/200 000, Feuille No. 20-21, Falama-Manankoro. Published by the Ministère des Mines, de la Géologie et de l'Environnement, Guinea Conakry.

Jessell, M., 2001. Three dimensional geology modelling of potential field data. Computers and Geosciences 27, 455-465.

Kearey, P., Brooks. M., Hill. I., 2009. An Introduction to Geophysical Exploration, 3rd Edition. Blackwell, UK, 281p.

Kim, Y.S., Sanderson, D.J., 2005. The relationship between displacement and length of faults: Review. Earth- Science Review 68, 317-334.

Kušnir, I., 1999. Gold in Mali. Acta Montanistica Slovaca Ročnik 4, 311-318.

Kušnir, I., Coulibaly, M., Diallo, M., 1989. Carte géologique du Mali au 1/200 000, feuille NC-29-XVIII, Kadiana. Published by the Direction Nationale de la Géologie et des Mines et le programme des Nations-Unies pour le développement.

Kušnir, I., Keita, N.D., Diallo, M., 1986. DNGM, Carte geologique du Mali au 1/200 000 Feuillet NC-30-XIII de Kadiolo. Published by the Direction Nationale de la Géologie et des Mines et le programme des Nations-Unies pour le Développement.

Lahondère, D., Lacomme, A., Le Berre, P., Coastea, C.A., Égal, E., Iliescu, D., Guerrot, C., Diabaté, B., Gaye, F., Minthé, D., Feybesse, J-L., 1999b. BRGM, DNRGH, Notice explicative de la carte géologique de la Guinée à 1/200 000, Feuillet No. 13, Faraba-Conakry (GIN) : Ministère de Mines, de la Géologie et de l'Environnement, 21p.

Lahondère, D., Lacomme, A., Le Berre, P., Iliescu, D., Guerrot, C., Diabaté, B., Gaye, F., Minthé, D., Feybesse, J-L., 1999a. BRGM, DNRGH, Notice explicative de la carte géologique de la Guinée à 1/200 000, Feuillet No. 20-21, Falama-Manankoro. Conakry (GIN): Ministère de Mines, de la Géologie et de l'Environnement, 21p.

Lahondère, D., Thièblemont, D., Tegyey, M., Guerrot, C., Diabate, B., 2002. First evidence of early Birimian (2.2 Ga) volcanic activity in Upper Guinea: The volcanic and associated rocks of the Niani suite. Journal of African Earth Sciences 35, 417-431.

Lelievre, P.G., 2003. Forward modelling and inversion of geophysical magnetic data. Unpublished Master of Science Thesis, University of British Columbia, 223p.

Lelievre, P.G., 2009. Integrating geologic and geophysical data through advanced constrained inversions. Published Doctor of Philosophy thesis, University of British Columbia, 177p.

Li, Y., Oldenburg, D.W., 1996. 3-D inversion of magnetic data. Geophysics 61, 394-408.

Li, Y., Oldenburg, D.W., 1998. 3-D inversion of gravity data. Geophysics 63, 109-119.

Li, Y., Oldenburg, D.W., 2000. Incorporating geological dip information into geophysical inversions. Geophysics 65, 148- 157.

Liegeois J.P., Claessens W., Camara D., Klerkx, J., 1991. Short-Lived Eburnian orogeny in southern Mali: Geology, tectonics U-Pb and Rb-Sr geochronology. Precambrian Research 50, 111-136.

Lompo, M., 2009. Geodynamic evolution of the 2.25-2.0 Ga Palaeoproterozoic magmatic rocks in the Man-Leo Shield of the West African Craton. A model of subsidence of an oceanic plateau. Geological Society, London, Special Publications 323, 231-254.

Lompo, M., 2010. Paleoproterozoic structural evolution of the Man-Leo Shield (West Africa). Key structures for vertical to transcurrent tectonics. Journal of African Earth Sciences 58, 19-36.

Macleod, I.N., Jones, K., Dai, T.F., 1993. 3D Analytical signal in the interpretation of total magnetic field data at low magnetic latitudes. Exploration Geophysics 24, 679-688.

McClay, K., Bonora, M., 2001. Analog models of restraining step overs in strike-slip fault systems. American Association of Petroleum Geologist, 85-2, 233-260.

Metelka, V., Baratoux, L., Naba, S., Jessell, M. W., 2011. A geophysically constrained litho-structutral analysis of the Eburnean greenstone belts and associated granitoid domains, Burkina Faso, West Africa. Precambrian Research 190, 48-69.

Mickus, K., 2008. Regional gravity analysis of Burkina Faso: implications for the location of metallic ore deposits. Journal of Africa Earth Sciences 50, 55-66.

Milési, J., Ledru, P., Feybesse, J., Dommanget A., Marcoux, E., 1992. Early Proterozoic ore deposits and tectonics of the Birimian orogenic belt, West Africa. Precambrian Research 58, 305-344.

Milési, J.P., Feybesse, J.L., Ledru, P., Dommanget, A., Ouedraogo, M.F., Marcoux, E., Prost, A., Vinchon, C., Sylvain, J.P., 1989. Lithostratigraphy and evolution of the Birimian cycle of West Africa; assessment of its mineral potential. BRGM Chronique de la Recherche Minière 497, 3-98.

Miller, H.G., Singh, V., 1994. Potential field tilt-a new concept for location of total magnetic field sources. Journal of Applied Geophysics 32, 213-217.

Miller, J., Davis, J., McCuaig, C., 2013. Kinematics of large-scale fault in southern Mali, WAXI 2 poster.

Milligan, P.R., Gunn, P.J., 1997. Enhancement and presentation of airborne geophysical data. AGSO Journal of Australian Geology and Geophysics 17, 63-75.

Naba, S., 2007. Propriétés magnétiques et caractères structuraux des granites du Burkina Faso oriental (Craton Ouest Africain, 2.2- 2.0 Ga): implications géodynamiques. Unpublished Doctor of Philosophy thesis, Université de Toulouse, 175p.

Naba, S., Lompo, M., Debat, P., Bouchez, J.L., Béziat, D., 2004. Structure and emplacement model for late-orogenic Paleoproterozoic granitoids: the Tenkodego-Yamba elongate pluton (Eastern Burkina Faso). Journal of African Earth Sciences 38, 41-57.

Parasnis, D.S., 1996. Principles of Applied Geophysics, 5th Edition. Published by Chapman and Hall, 456p.

Parker, R., Wilkinson, A., 2011. A technical review of the Yanfolila gold concession, Mali, West Africa New Resource Management Services Ltd. Report to Compass Gold Corporation, 97p.

Perrouty, S., Aillères, P., Jessell, M.W., Baratoux, L., Bourassa, Y., Crawford, B., 2012. Revised Eburnean geodynamic evolution of the gold-rich southern Ashanti Belt, Ghana, with new field and geophysical evidence of pre-Tarkwaian deformations. Precambrian Research 204-205, 12-39.

Pigois, J.P., Groves, D.I., Fletcher, I.R., McNaughton, N.J., Snee, L.W., 2003.Age constraints on Tarkwaian palaeoplacer and lode-gold formation in the Tarkwa-Damang district, SW Ghana. Mineralium Deposita 38, 695-714.

Rajagopalan, R., Milligan, P., 1995. Image enhancement of aeromagnetic data using automatic gain control. Exploration Geophysics 25, 173–178.

Randgold Resources, 2007. Exploration review. Annual report, 11p.

Randgold Resources, 2008. Delivering profits, growth and new opportunities. Denver Gold Forum, September, 27p.

Reeves, C., 2005. Aeromagnetic surveys: principles, practice and interpretation. E-published by GEOSOFT (*http://www.geosoft.com/knowledge*), 155p.

Ritz, M., 1984. A high conductivity anomaly on the West African craton (Mali). Journal of Geophysical 55, 182-184.

Roddaz, M., Debat, P., Nikiéma, S., 2007. Geochemistry of Upper Birimian sediments (major and trace elements and Nd-Sr isotopes) and implications for weathering and tectonic setting of the Late Paleoproterozoic crust. Precambrian Research 159, 197-211.

Scales, J.A., Smith, M.L., Treitel, S., 2001. Introductory Geophysical Inverse Theory. Published by Samizdat Press; Available via FTP from samizdat.mines.edu, Colorado, 208p.

Sheriff, R.E., 2001. Encyclopaedic dictionary of applied geophysics, 4th Edition. Society of Exploration Geophysics, 441p.

SIGAfrique, 2000. ASIF Afrique mapping program (2000), BRGM (France).

Standing, J., 2006. Structural geology of the Tabakoroni prospect, and detailed mapping in the quartz vein hill-chert ridge-A21 pit area, Syama-Finkolo project, Mali, West Africa. Fluid Focus Pty Ltd, A.C.N. 094 880 627.

Stewart, J. R., Betts, P. G., 2010. Implication for Proterozoic plate margin evolution from geophysical analysis and crustal scale modelling within the western Gawler Craton, Australia. Tectonophysics 483, 151-177.

Sun, J., Li, Y., 2011. Geophysical inversion using petrophysical constraints with application to lithology differentiation. SEG San Antonio 2011 Annual Meeting, doi/138.67.176.183.

Tarantola, A., Valette B., 1982. Generalized Nonlinear Inverse Problems Solved Using the Least Squares Criterion. Reviews in Geophysics and Space Physics 20, No. 2, 219–232.

Telford, W.M., Gerldart, L.P., Sheriff, R.E. 1990. Applied Geophysics, 2nd Edition, Cambridge University Press, 792p.

Tidjani, M. E-H., Affaton, P., Louis, P., Lesquer, A., Socohou, A., Caby, R., 1993. Gravity characteristics of the northern part of the Dahomeyides continental aggregation - Collision orogen and gravity smoothing in the Pan-African (600±100Ma). Journal of African Earth Sciences 17, 203-211.

Tikhonov, A.N., Arsenin, V.Y., 1977, Solutions of Ill-Posed Problems, Halsted Press, New York, 258p.

Toft, P.B., Taylor, P.T., Jafar, A-H., Haggerty, S.E., 1992. Interpretation of satellite magmatic anomalies over the West African Craton. Tectonophysics 212, 21-32.

Tshibubudze, A., 2015. Integrated strato-tectonic, U-Pb geochronology and metallogenic studies of the Oudalan-Gorouol volcano-sedimentary Belt (OGB) and the Gorom-Gorom granitoid terrane, (GGGT), Burkina Faso and Niger, West Africa. Unpublished Doctor of Philosophy thesis, University of the Witwatersrand Johannesburg, 292 p.

Tshibubudze, A., Hein, K.A.A., 2013. Structural setting of gold deposits in the Oudalan-Gorouol volcano-sedimentary belt east of the Markoye Shear Zone, West African craton, African Journal Earth Sciences 80, 31-47.

Tshibubudze, A., Hein, K.A.A., Marquis, P., 2009. The Markoye Shear Zone in NE Burkina Faso. Journal of African Earth Sciences 55, 245-256.

Tunks, A.J., Selley, D., Rogers, J.M.R., Brabham, G., 2004. Vein mineralization at the Damang Gold Mine, Ghana: controls on mineralization. Journal of Structural Geology 26, 1257-1273.

Vidal, M., Gumiaux, C., Cagnard, F., Pouchet, A., Ouattara, G., Pichon, M., 2009. Evolution of a Paleoproterozoic “weak type” orogeny in the West African Craton (Ivory Coast). Tectonophysics 477, 145-159.

Wahr, J., 1996. Geodesy and Gravity class notes. Published by Samizdat press, Colorado Boulder, 304p.

WAXI, 2013. Final report, P934A West African Exploration Initiative, Stage 2, 924pp (with 917 pages of appendices).

Whiteside, J. H., Olsen, P. E., Kent, D. V., Fowell, S. J., Et-Touhami, M., 2007. Synchrony between the central Atlantic magmatic province and the Triassic-Jurassic mass-extinction event? PALAEO 244, 345-367.

Wijns, C., 2004. Exploring Conceptual Geodynamic Models, Numerical Method and Application to Tectonics and Fluid Flow. Unpublished Doctor of Philosophy thesis, University of Western Australia, 114p.

Williams, N., Oldenburg, D., Lelièvre, P., 2009. Constraining gravity and magnetic inversion for mineral exploration using limited geological data. 20th ASEG conference in Adelaide. Extended abstracts.

WinDisp®, 2012. Scientific computing and application user manual.

APPENDICES

Appendix A: Gravity method theory.

The gravity method is a passive geophysical method. It is based on the measurement of the Earth's gravitational field to locate denser bodies than the surroundings environment. Gravity is considered to be a force, which obeys to the Newton first law, it is the universal attraction of the Earth. According to the Newton's second law, the gravitational field forces can be considered as gravitational acceleration if the force exerted on a mass causes a motion as the principle of the free-fall of a body. The acceleration value is in part, produced by the Earth's core (0.30%), and only 0.05% is produced by the Earth's crust about the first 5 km Wahr (1996). The contribution of rocks (minerals) to the acceleration value is only 10^{-5}. Rocks that contribute more are generally mafic igneous rocks (e.g., ultramafic and mafic rocks) with less silicate content.

A .1: Earth gravitational field

The Earth gravitational field values become according to Telford et al. (1990), Wahr (1996), Giroux and Chateau (2007), Giroux and Chouteau (2008) and Kearey et al. (2009).

$$\boldsymbol{F = \frac{\gamma(m_1 m_2)}{r^2}\vec{r}}$$

F correspond to the gravitational forces expressed in Newton, it is always attractive; **γ** is the constant of universal gravitation equal to 6.672×10^{-11} N m^2/kg^2 in SI, or 6.672×10^{-8} dyne cm^2/g^2 in cgs; $\mathbf{m_1}$ and $\mathbf{m_2}$ are the mass and **r** is the distance between these mass.

A 2: The gravitational field forces

$$\boldsymbol{g = \left(\frac{\gamma M_e}{R_e^2}\right)\vec{r}}$$

This is an acceleration of gravity and corresponds to the gravitational forces per unit mass and equal to 980cm/s^2; $\mathbf{M_e}$ is the Earth mass; $\mathbf{R_e}$: the Earth radius.

Measurements of the gravity acceleration data values can be done on sea, ground and air. The technique calculates the components of the gravitational field at each measurement point, which corresponds to the sum of the vectors accelerators at this point. There are two types of gravity measurements: (1) Absolute values, which are complicated and take a long time to acquire. (2)

Relative values, that are the contrast measured between two points. The relative values are used in geophysical exploration.

After gravity data collected, it must be corrected from the non-geological effects such as altitude, plateau and latitude, topography, the position of the Sun and moon effect, and instrumental drift.

A 3: The density value determination

$$\Delta g = 2\pi\gamma\rho t$$

Δg:Gravitational variation measured on the Earth; **ρ** correspond to the density; **γ**: Universal gravitational constant; t is the thickness of the body.

The gravitational acceleration vector is influenced by several factors including the referential, shape of the earth (topography), gravitation of the Earth (Newton's law), the Earth's rotation, and the density of the rocks. Rock density property is the most important factor in geophysical exploration because it depends to the mineralogical composition, porosity, pore saturation and the degree of rocks compaction. Rock density is proportional to the variation of gravitational acceleration (Δg) measured on the Earth. Rock density can be also measured directly on the drill core.

A 4: Gravitational potential

$$\nabla^2 U = \frac{\partial^2 U}{\partial x^2} + \frac{\partial^2 U}{\partial y^2} + \frac{\partial^2 U}{\partial z^2} = 0$$

Using the divergence theorem of Gauss, this formula corresponds to Laplace's equation in the Cartesian coordinate in free space. U is the potential.

A 5: Earth gravitational acceleration

$$\nabla . g = -4\pi\gamma\rho \qquad (a)$$

Equation in (a) correspond to the potential form of the gravitational field.

$$\nabla^2 U = 4\pi\gamma\rho \qquad (b)$$

If the space contains a particle, the equation (A 3.1.4) becomes Poisson's equation. U: Potential, ρ the density of the point; γ: gravitational constant.

A 6: Gravity data correction

$$BA = g_{obs} - g_{\phi} + FAC \pm BC + TC(\pm EC)$$

BA: Bouguer anomaly, $\mathbf{g_{obs}}$: gravity observed, **FAC**: free air correction, **BC**: Bouguer correction, **TC**: Tidal correction, **EC**: EÖTVÖ correction; $\mathbf{g_{\phi}}$: latitude correction.

After corrected the data from non-geological noise, image, profile and contours can be produce and a processing phase can begin. The image processing filters such as edge detection, linear and nonlinear filter and the vertical continuation can be applied to highlight geological targets like lineaments and geological domains on the images. From these images, it is possible to extract:

1. Volcano-sedimentary or greenstone belts that are characterised by the high density values.
2. Shear zones located at the contact between the high and low values of gravity, although strong gravity variation is not always enough to determine the location of shear zone.
3. Dense mafic rocks (high value of gravitational field) versus less dense sedimentary rocks (low gravitational field).
4. Sedimentary basins or granitoids may be determined by their low density values (low gravitational field zone).
5. Faults are characterized by linear discontinuity with low gravity value observed on the lithological trends.

Appendix B: Magnetic method theory

The magnetic formulas were established using the formula from Telford et al. (1990), Giroux and Chateau (2007), Giroux and Chouteau (2008) and Kearey et al. (2009).

The magnetic method is the oldest methods used in exploration geophysics. It was first implemented in the 14th century for metal deposits exploration. Like the gravity method, the objective of the magnetic method is to investigate the subsurface of the Earth. The method measures the changes of magnetic field values in the Earth's which is due to the geomagnetic properties of the Earth subsurface. The technique can be implemented if there is a difference of magnetic susceptibility values between the target and surrounding medium. However, noise caused by man-made sources such as power lines and boreholes, should be avoided and removed from the data after the survey.

B 1: Physical theory of magnetic method based on Coulomb's law

$$F = \frac{P_1 P_2}{\mu r^2}\,\vec{r}$$

F: Coulomb's law Forces emu in the cgs; $\mathbf{P_1}$ and $\mathbf{P_2}$: the magnetic poles expressed in dynes; **r**: distance between pole in cm; and**μ**: magnetic permeability in the vacuum μ= 1 and in air μ≈1.

The physical theory of the magnetic method is derived from the magnetic force (F), which is based on Coulomb's law. The magnetic field is defined as being the magnetic force per unit of pole.

Rocks affect the magnetic field variation through magnetic induction and intensity of magnetization. They are affected by the magnetic susceptibility values in the rock (i.e., minerals). The physical property of certain minerals, such as magnetite, ilmenite and chromite, can contribute more to the variation of the magnetic field.

B 2: Magnetic field

$$\Delta \boldsymbol{H} = \left(\frac{\boldsymbol{I\Delta l}}{\boldsymbol{4\pi r^2}}\right)\vec{\boldsymbol{r}}$$

With ΔH correspond to the magnetic field variation in amperes per meter, I+ the current in amperes, Δl length of the conductor in meters.

The value of the magnetic field is influenced by the subsurface body parameters (including bodies geometry, and his orientation, direction of polarization, magnetic susceptibility), inclination and declination of the magnetic field, and the survey lines orientation relative to the body.

The magnetic field is measured in all point on the Earth surface to determine the total field (induced magnetic B) value in taking account the inclination and declination, i.e. the magnetic field value with all the effects involved in the total field variation. The measures can be done in water, ground and air like in gravity, but using always two magnetometers (base and mobile). Actually, the devices used for ground survey determine the total field.

After data surveyed, the data should be corrected to eliminate the non-geological effects. To remove the non-geological effects, the following corrections must be applied to the magnetic data:

The diurnal correction is to eliminate the effect of the secular variations (change in time) which is less important in geophysical exploration. The diurnal correction allows the elimination of magnetic field daily variations. This correction is realised by using the base magnetometer (very important in geophysical exploration). Altitude correction is to eliminate the elevation effects, used generally for airborne survey (Reeves, 2005).

The IGRF (International Geomagnetic Reference Field) correction is using generally in the airborne survey. It relocated (Longitude and latitude) of the measurements points and eliminate long period variations. After all the correction, the data can be reduced using the filters to highlight the target.

B 3: Intensity of magnetization and magnetic susceptibility formula

In magnetic exploration, magnetics susceptibility is the most important factor. The magnetic method is highly dependent in magnetic susceptibility because it determines the composition of the rock, however it can characterise the behaviour of the rocks inside the Earth. The intensity of magnetization is:

$$\boldsymbol{M = \frac{m}{V} = kHcos\theta} \qquad (\boldsymbol{a})$$

M corresponds to the magnetization intensity, **m**: the moment magnetic dipolar (A.m^2), **V** is the volume, **H**: magnetic field, **θ** is the angle between **H** and the surface in degree. Equation (a) become the following if the field is normal to the Earth surface then **θ** = 0

$$\boldsymbol{M = k.H} \qquad (\boldsymbol{b})$$

This magnetization is done by polarization (magnetization intensity, or dipole moment per unit volume) and noted **M**; ***k*** is the magnetic susceptibility in ***SI*** system.

The type of magnetization depends to the magnetic susceptibility values. It determines the types of magnetism as listed below:

1. Diamagnetic if magnetic susceptibility k according to the formula in Table 3.1, Equation 15 is negative or very small, the minerals concerned are generally the quartz, gold, galena, cuprite, zinc, or salt (in salt domes).
2. Paramagnetic, magnetic susceptibility in which k in Table 3.1, Equation 15 is positive but very small may correspond to the minerals such as pyroxene, biotite, siderite (FeCO3), chalcopyrite, and/or rocks such as gneiss, pegmatite, and syenites.
3. Ferrimagnetism where the magnetic susceptibility k in Table 3.1, Equation 15, is very high, corresponding to the minerals such as magnetite, (magnetic pyrrhotite) and ilmenite.

The ferromagnetism corresponds to the magnetism of mineral like iron, cobalt. The anti-ferromagnetism is the specific magnetism of the hematite. This type of magnetism is the particular case which corresponds to the magnetism of the specific mineral.

B 4: Magnetic induction using magnetic susceptibility

$$\boldsymbol{B = \mu_0(H + M) = \mu_0(1 + k)H = \mu\mu_0 H}$$

B: magnetic induction express in gauss (G) with cgs system, and Tesla (T) in SI system; H: magnetic field A/m in SI and Œrsted (Œ) in cgs; μ_0: the magnetic permeability in the vacuum; μ: permeability in the medium.

B 5: Relation between SI and cgs magnetic susceptibility measurement

Susceptibility values can vary according to the system used (SI or cgs) and susceptibility in the international system (SI) is according to Giroux and Chouteau (2008).

$$\boldsymbol{k_{SI} = 4\pi k_{cgs}}$$

With k_{SI}: the magnetic susceptibility in SI, k_{cgs}: magnetic susceptibility in the cgs.

B 6: Magnetic potential

The magnetic field is a vector which should be reduced in the potential field to facilitate the information interpretation.

By expressing the dipole moment formula in the Cartesian system, it can be deducted that the magnetic potential equation satisfies to the Laplace and Poisson equation by the relation of Telford et al. (1990). From the potential equation, the magnetic and gravity data can be easily handled to get more detail about the subsurface behaviour.

$$\boldsymbol{U(r) = -\int_{\infty}^{r} H(r).dr = \frac{P}{r}} \qquad (\mathbf{18})$$

U(r) corresponds to the magnetic potential; r: distance, P: magnetic pole; H: magnetic field.

$$\boldsymbol{U = -\int_{V} M(r).\nabla\left(\frac{1}{|r_0 - r|}\right)dv} \qquad (\mathbf{19})$$

U corresponds to the magnetic potential; $\mathbf{r_0}$-**r**: distance; **M**: intensity of magnetization.

B 7: Magnetic field using potential formula

$$\boldsymbol{H(r_0) = \nabla\int_{V} M(r).\nabla\left(\frac{1}{|r_0 - r|}\right)dv} \qquad (\mathbf{20})$$

$\mathbf{H(r_0)}$ corresponds to the magnetic field at r_0; **$\mathbf{r_0}$-r**: distance; **M**: intensity of magnetization.

$$\nabla^2 U = 4\pi\mu\nabla . M(r) \qquad (a)$$

And

$$\nabla^2 U = 0 \qquad (b)$$

U: potential of the magnetic field in (a), and magnetic potential in the nonmagnetic corresponding to Laplace's equation.

The rock signals which contribute to the magnetic field variation can lead to the determination of the subsurface behaviour. It allows to the magnetic method to be a good methods for the geological structures definition using the form of anomaly (elongated, linear or circular), from that, it can be distinguished:

1. Dykes, faults and shear zones that are generally characterized by linear feature on the total magnetic field maps.
2. Magmatic intrusions are characterised by circular features, with strong magnetism value generally at the limits of the intrusion.
3. The folds are characterized by linear structures folded, which can often indicates the constrain direction applied on the rocks during the tectonic event.
4. The volcanic belts are characterized by elongated features trending in one direction. The value of the total field is disturbed in these areas of the fact that they are made up by several types of rocks that may have different magnetic field values.
5. Sedimentary basins are represented by wide area magnetically quiet.
6. The metamorphic zones are characterised by the strong field signature, that can be explained by the fact that metamorphism can transform non-magnetic minerals in high magnetic minerals due to the substitution of chemical elements which composed the minerals.
7. Fracture zones are different to the linear and narrow shape by the variation in magnetism due to the fact that these zones can undergo through alteration, and leading to the oxidation of the magnetic minerals giving the low values of magnetic field in these zones.

These characterisations are just for qualitative interpretation, for more detail of these structures parameters, a quantitative interpretation must be done. For this kind of interpretation, the modelling of the gravimetric and magnetic potential field data are performed for more detail on these structures parameters.

Appendix C: Gravity data station points

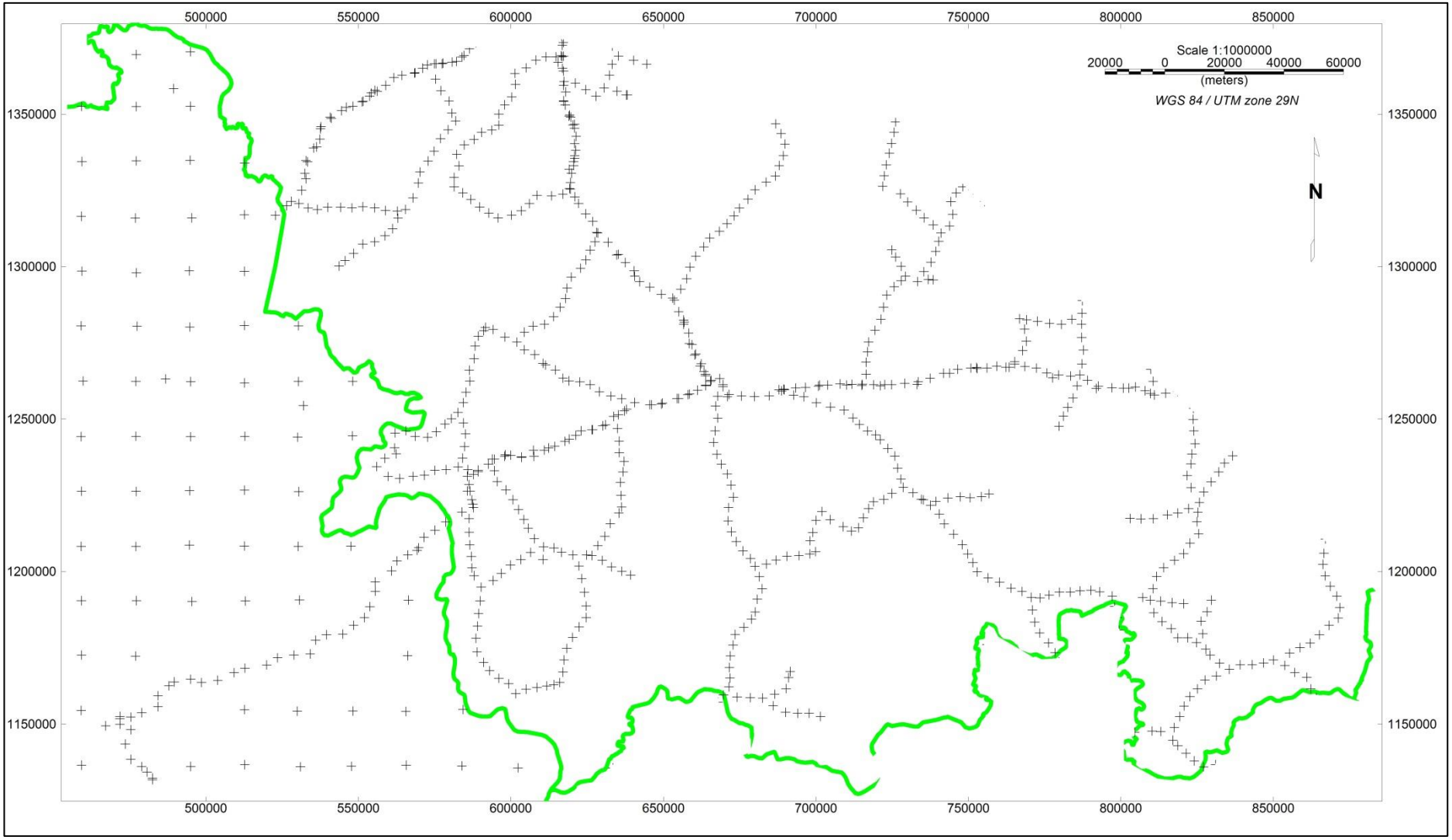

C: The map of the study area showing the gravity station points in cross point and the country boundary in green.

Appendix D: Inversion algorithm used is the code developed by UBC-GIF

D 1: Unconstrained objective function

$$\Phi(m) = \Phi_d(m) + \mu\Phi_m(m)$$

Where **Φ**: is the unconstrained objective function, $\mathbf{\Phi_d}$: is related to errors which corresponds to the difference between the data observed and the data calculated (predicted), $\mathbf{\Phi_m}$: is the objective function of the model, **m**: is the vector model, **μ**: is the parameters of regularization determining the exchange between the error on the data and the objective function of the inversion function (Li and Oldenburg, 2000).

D 2: Errors function

$$\Phi\mathbf{d}(\mathbf{m}) = \sum_{\mathrm{i}=1}^{\mathrm{N}} \left(\frac{\mathbf{di^{obs}} - \mathbf{di^{pre}}}{\in_{\mathbf{i}}} \right)$$

The errors function is expressed by $\mathbf{\Phi_d}$ (m); where $\mathbf{di^{obs}}$ and $\mathbf{di^{pre}}$ correspond respectively to the data observed and data calculated (predict); $\in_{\mathbf{i}}$ is the standard deviation.

D 3: Discrete form of misfit function

$$\mathbf{\Phi}_{\boldsymbol{d}} = \left\| \boldsymbol{W}_{\boldsymbol{d}} \left(\boldsymbol{F}[\boldsymbol{m}] - \boldsymbol{d}^{\boldsymbol{obs}} \right) \right\|^2$$

The discrete form of the errors function is $\mathbf{\Phi_d}$; with **F[m]** function of forward modelling $\mathbf{W_d}$ is the data diagonal weighting matrix for the uncertainty associated with each datum and correlation between data (Sun and Li, 2011).

The error function calculated from each data point is constant and equal to 0.5in the inversion.

D 4: The objective function of the model

$$\mathbf{\Phi_m} = \boldsymbol{\alpha s} \int_{\mathbf{Vol}} \{\boldsymbol{m}(\vec{\boldsymbol{r}}) - \mathbf{mo}\}^2 \boldsymbol{dv} + \boldsymbol{\alpha x} \int_{\mathbf{Vol}} \left\{ \frac{\boldsymbol{\partial}[\boldsymbol{m}(\vec{\boldsymbol{r}}) - \boldsymbol{mo}]}{\boldsymbol{\partial x}} \right\} \boldsymbol{dv}^2 + \boldsymbol{\alpha y} \int_{\mathbf{Vol}} \left\{ \frac{\boldsymbol{\partial}[\boldsymbol{m}(\vec{\boldsymbol{r}}) - \boldsymbol{mo}]}{\boldsymbol{\partial y}} \right\}^2 \boldsymbol{dv} + \boldsymbol{\alpha z} \int_{\mathbf{Vol}} \left\{ \frac{\boldsymbol{\partial}[\boldsymbol{m}(\vec{\boldsymbol{r}}) - \boldsymbol{mo}]}{\boldsymbol{\partial z}} \right\}^2 \boldsymbol{dv}$$

In this equation, $\mathbf{\Phi_m}$ is the objective function; **m** represent the model to be found; **mo.** is the reference model; αs, αx αy and αz are the coefficients which controls equation terms and they are positive (Li and Oldenburg, 2000); αs afford to smooth the model, and is always smaller than other coefficients.

The variations of the other coefficients (αx αy and αz) allow smoothing the structures in one or two direction to the detriment of other directions, then: if αz » αx= αy the model produces the structures stretch vertically, if αx= αy »αz thus the model will be smoothed according to the horizontal directions to the profit of the vertical direction. It was 50m for αx= αy and 25m for αz.

D 5: Depth weighting function

$$\boldsymbol{W(Z) = \frac{1}{(Z - Zo)^{\chi/2}}}$$

W(Z) correspond to the weighting function, expressed by Li and Oldenburg, (1996), (1998) where $\boldsymbol{\chi}$ (χ= 3 in magnetic data and χ=2 in gravity data) depend to the cell size of the discrete model and the height on observation point. Z_0 is a constant depending to the flight height and the cell size.

D 6: The objective function of the model with depth weight function

$$\mathbf{\Phi_m = \alpha s \int WsW^2(Z)(m - m_{ref})^2 dv + \alpha x \int Wx \left(\frac{\partial \{W(Z)(m - m_{ref})\}^2}{\partial x} \right) dv + \alpha y \int Wy \left(\frac{\partial \{W(Z)(m - m_{ref})\}^2}{\partial y} \right) dv + \alpha z \int Wz \left(\frac{\partial \{W(Z)(m - m_{ref})\}^2}{\partial z} \right) dv}$$

The objective function of the model by introducing the depth weight function $\mathbf{\Phi_m}$ according to (Williams et al, 2009); with $\boldsymbol{m}$ the model to be found, $\boldsymbol{m_{ref}}$ is the reference model constructed on the basis of the geology data or preview geophysical study in the area or others information; **α**s, **α**x **α**y and **α**z are the parameters of smoothing and closeness between the model reconstructed and the reference model; **Ws**, **Wx**, **Wy**, and **Wz**, represent the functions of moderation and are spatially dependent, they reflect the confidence in the reference model, indicating the importance of the closeness and the smoothness of the model.

The depth weighting value in the inversion could be 0, 1 or 2. The 0 correspond to the default weighting values. The values used for the inversion were set at 1 which concerns the depth weighting for surface and airborne data.

D 7: Discrete form of the model objective function

$$\boldsymbol{\Phi_m = \alpha_s \left\| W_s W_r (m - m_{ref}) \right\|^2 + \alpha_x \left\| W_x W_r (m - m_{ref}) \right\|^2 + \alpha_y \left\| W_y W_r (m - m_{ref}) \right\|^2} \qquad (a)$$

Or

$$\boldsymbol{\Phi_m = \left\| W_m (m - m_{ref}) \right\|^2 = (m - m_{ref}) W_m^T W_m (m - m_{ref})} \qquad (b)$$

Objective function discrete form is $\boldsymbol{\Phi_m}$, with $\boldsymbol{m}$ the vector model of the physical property value, $\boldsymbol{m_{ref}}$ is the reference model; $\mathbf{W_s}$, $\mathbf{W_x}$, $\mathbf{W_y}$ and $\mathbf{W_z}$ are the matrices of weighting and spatially dependent; $\mathbf{W_r}$ is the depth weighting matrix. In the second discrete form, $\mathbf{W_m}$: matrix of weighting and $\boldsymbol{\alpha}$ is a coefficient. The $\mathbf{W_s}$ term is a diagonal matrix with the elements $\sqrt{W_i V_i}$ with $\mathbf{V_i}$ the volume of the $\mathbf{i^{eme}}$ cell and $\mathbf{W_i}$ is the weight which can be increased in the zone with large degree of confidence (Lelievre, 2003).

D 8: Fuzzy C Means objective function of the model

$$\boldsymbol{\Phi_{fcm} = \sum_{j=1}^{N} \sum_{k=1}^{C} u_{jk}^{q} \left\| m_j - v_k \right\|_2^2}$$

The Fuzzy C Means objective function according to Sun and Li (2011) is $\boldsymbol{\Phi_{fcm}}$; **N** the number of cell model, **C** the number of group; $\mathbf{m_j}$ is the $\mathbf{j^{th}}$ data entry (i.e. the value of the physical parameter in the $\mathbf{j^{th}}$ cell); $\mathbf{V_k}$ is the middle of the group. The parameter **q** is the fuzzification parameters that control the degree of fuzziness.

D 9: Function of optimization of the opposite problem minimizing the objective function

$$\boldsymbol{\Phi(m) = \Phi_d + \beta \Phi_m + \lambda \left(\sum_{j=1}^{N} \sum_{k=1}^{C} u_{jk}^{q} \left\| m_j - v_k \right\|_2^2 + \eta \sum_{k=1}^{C} \left\| v_k - t_k \right\|_2^2 \right)}$$

The optimization form of Fuzzy objective function of the model is presented by ($\boldsymbol{\Phi(m)}$**;** with $\boldsymbol{\lambda}$ and $\boldsymbol{\eta}$ are the weighting coefficients, $\mathbf{t_k}$ is the value of the given physical property from measurements made directly on the sampled rocks.

This function facilitated to creation of bound model using the physical property data. The bound model is used to constrain the inversion with physical properties.

D 10: The orientation and dip parameters which can be introducing into the objective function

$$\boldsymbol{R} = \begin{pmatrix} \boldsymbol{cos\varphi\, cos\psi - sin\varphi\, cos\theta\, sin\psi} & \boldsymbol{sin\varphi\, cos\psi + cos\varphi\, cos\theta\, sin\psi} & \boldsymbol{sin\theta\, sin\psi} \\ \boldsymbol{-sin\varphi\, sin\theta} & \boldsymbol{cos\varphi\, cos\theta} & \boldsymbol{-cos\theta} \\ \boldsymbol{-cos\varphi\, sin\psi - sin\varphi\, cos\theta\, cos\psi} & \boldsymbol{sin\varphi\, sin\psi + cos\varphi\, cos\theta\, cos\psi} & \boldsymbol{sin\theta\, cos\psi} \end{pmatrix}$$

$$= \begin{pmatrix} \boldsymbol{r_{11}} & \boldsymbol{r_{12}} & \boldsymbol{r_{13}} \\ \boldsymbol{r_{21}} & \boldsymbol{r_{22}} & \boldsymbol{r_{23}} \\ \boldsymbol{r_{31}} & \boldsymbol{r_{32}} & \boldsymbol{r_{33}} \end{pmatrix}$$

$\boldsymbol{R}$ is the matrix of rotation; $\boldsymbol{\varphi}$, $\boldsymbol{\theta}$, $\boldsymbol{\psi}$ correspond respectively to the orientation, dip and azimuth angle (Li and Oldenburg, 2000).

The surface fact data were used for reference model. The physical properties were also added to these fact data to construct the reference model.

D 11: The objective function using orientation and dip parameters.

The objective function becomes Φ_m using the rotation matrix R (Li and Oldenburg, 2000). The objective function using the orientation and dip parameters are used for reference model construction by using the geometries of rocks and structures.

$$\begin{aligned} \boldsymbol{\Phi_m} = & \int_{\boldsymbol{Vol}} \boldsymbol{\alpha_s m^2 dv} + \int_{\boldsymbol{Vol}} \left(\boldsymbol{\alpha_{x'} r_{11}^2 + \alpha_{y'} r_{21}^2 + \alpha_{z'} r_{31}^2}\right) \left(\frac{\boldsymbol{\partial m}}{\boldsymbol{\partial x}}\right)^2 \boldsymbol{\partial v} \\ & + \int_{\boldsymbol{Vol}} \left(\boldsymbol{\alpha_{x'} r_{12}^2 + \alpha_{y'} r_{22}^2 + \alpha_{z'} r_{32}^2}\right) \left(\frac{\boldsymbol{\partial m}}{\boldsymbol{\partial y}}\right)^2 \boldsymbol{\partial v} \\ & + \int_{\boldsymbol{Vol}} \left(\boldsymbol{\alpha_{x'} r_{13}^2 + \alpha_{y'} r_{23}^2 + \alpha_{z'} r_{33}^2}\right) \left(\frac{\boldsymbol{\partial m}}{\boldsymbol{\partial z}}\right)^2 \boldsymbol{\partial v} \\ & + \int_{\boldsymbol{Vol}} \boldsymbol{2}\left(\boldsymbol{\alpha_{x'} r_{11} r_{12} + \alpha_{y'} r_{21} r_{22} + \alpha_{z'} r_{31} r_{32}}\right) \frac{\boldsymbol{\partial m}}{\boldsymbol{\partial x}} \frac{\boldsymbol{\partial m}}{\boldsymbol{\partial y}} \boldsymbol{\partial v} \\ & + \int_{\boldsymbol{Vol}} \boldsymbol{2}\left(\boldsymbol{\alpha_{x'} r_{12} r_{13} + \alpha_{y'} r_{22} r_{23} + \alpha_{z'} r_{32} r_{33}}\right) \frac{\boldsymbol{\partial m}}{\boldsymbol{\partial y}} \frac{\boldsymbol{\partial m}}{\boldsymbol{\partial z}} \boldsymbol{\partial v} \\ & + \int_{\boldsymbol{Vol}} \boldsymbol{2}\left(\boldsymbol{\alpha_{x'} r_{11} r_{13} + \alpha_{y'} r_{21} r_{23} + \alpha_{z'} r_{31} r_{33}}\right) \frac{\boldsymbol{\partial m}}{\boldsymbol{\partial x}} \frac{\boldsymbol{\partial m}}{\boldsymbol{\partial z}} \boldsymbol{\partial v} \end{aligned}$$

Appendix E: Comparison between unconstraint inversion and constraint inversion with the bound model in the study area.

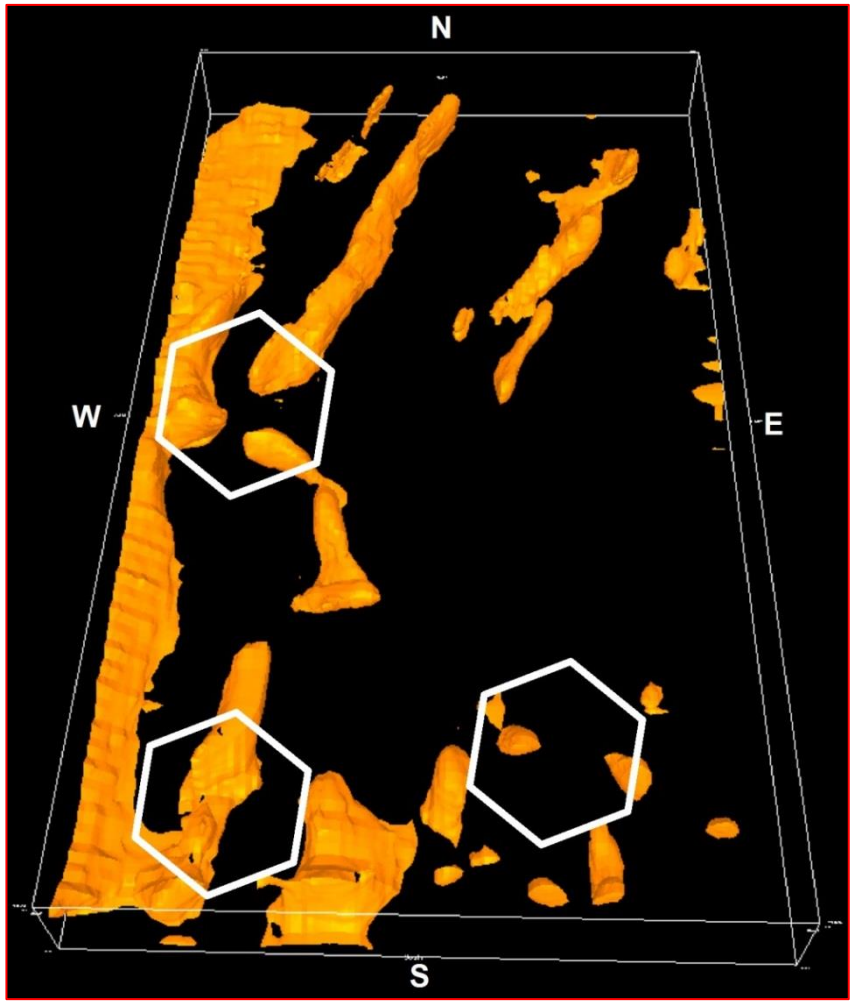

Unconstraint inversion, the white circle show the comparison point

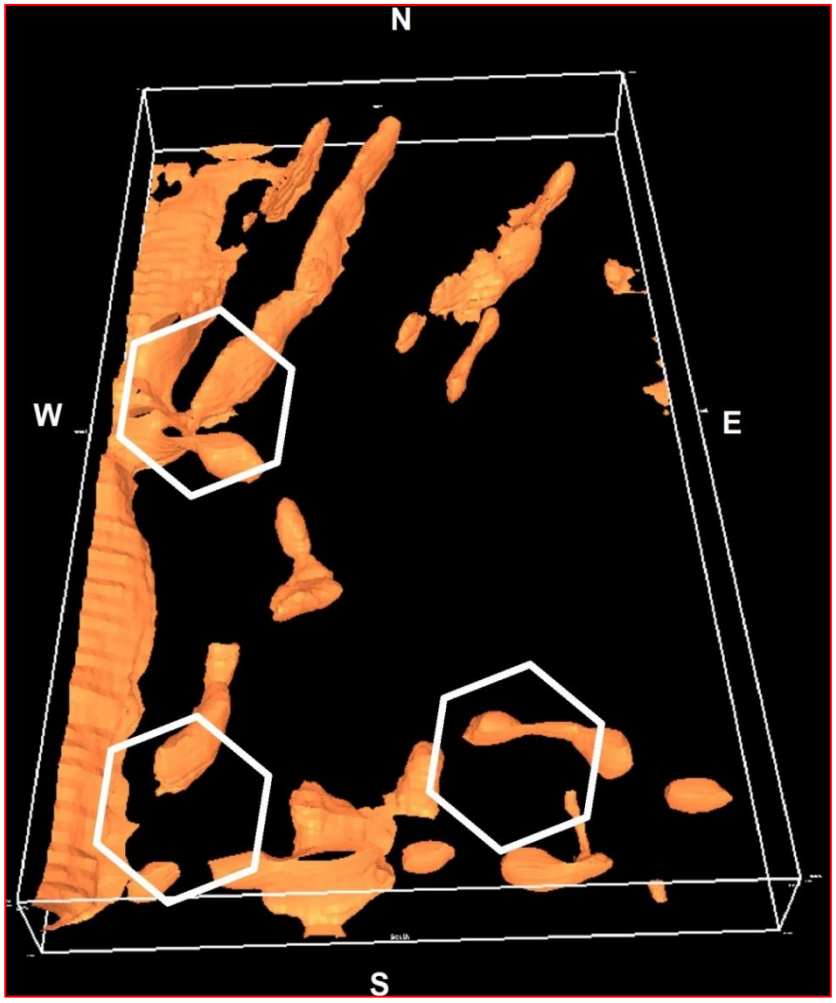

Constraint inversion, the white circle show a comparison point